Dislocation-Based Functionality in Ferroelectric Perovskites

Versetzungsbasierte Funktionalität in Ferroelektrischen Perowskiten

Fachbereich Material- und Geowissenschaften, Technische Universität Darmstadt

Dissertation zur Erlangung des akademischen Grades Doktor-Ingenieur (Dr.-Ing.)
von Marion Anita Höfling

Erstgutachter: Prof. Dr. Jürgen Rödel
Zweitgutachter: Prof. Dr. Hans-Joachim Kleebe

Darmstadt, Mai 2021

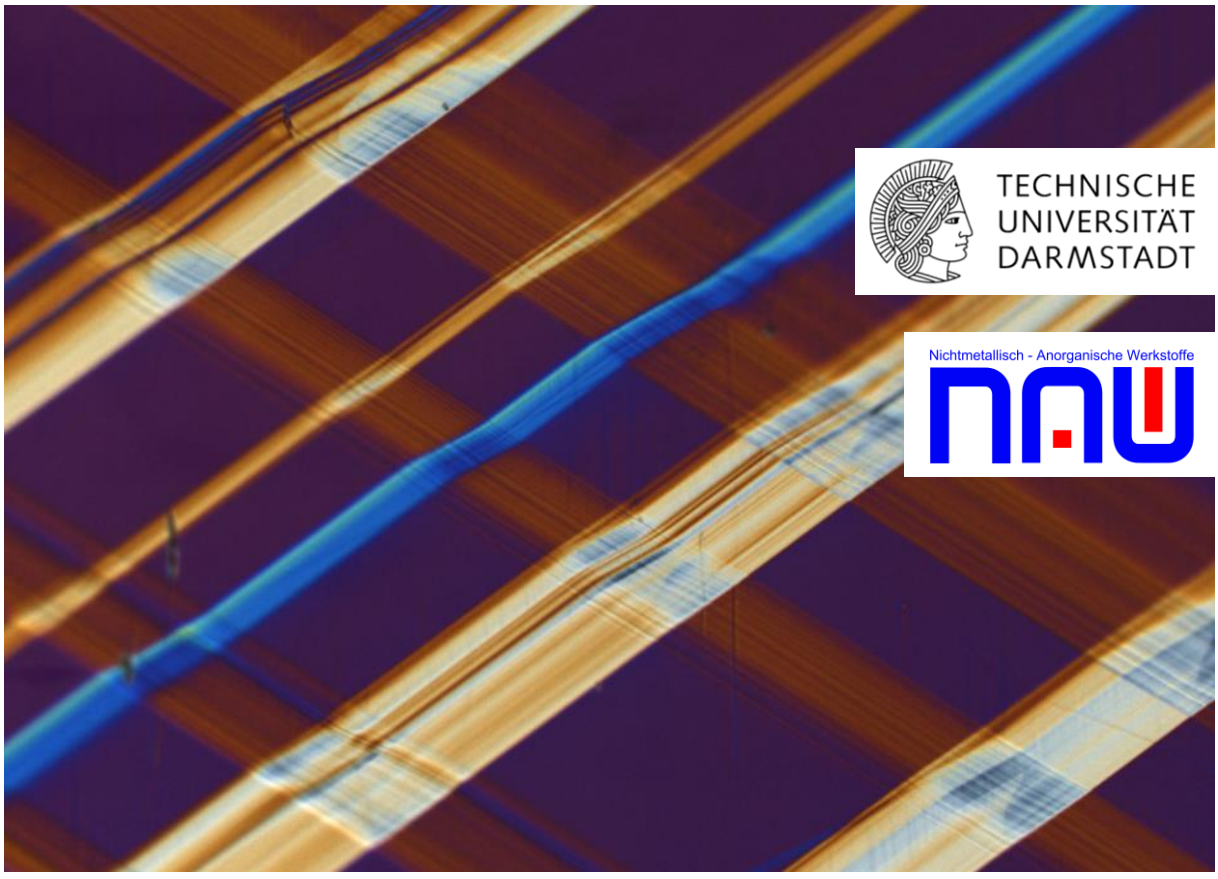

Dissertation

Dislocation-Based Functionality in Ferroelectric Perovskites

von Marion Anita Höfling, M. Sc.
geboren am 05.08.1991 in Erlenbach am Main.

Erstgutachter: Prof. Dr. Jürgen Rödel
Zweitgutachter: Prof. Dr. Hans-Joachim Kleebe

Beisitzer: Prof. Dr. Karsten Durst
Beisitzer: Prof. Dr. Ralf Müller

Tag der Prüfung: 03. Mai 2021

Fachbereich Material- und Geowissenschaften
Technische Universität Darmstadt
Alarich-Weiss-Straße 2
64287 Darmstadt

Bitte zitieren Sie dieses Dokument als:
urn:nbn:de:tuda-tuprints-186538
http://tuprints.ulb.tu-darmstadt.de/18653/

Dieses Dokument wird bereit gestellt von tuprints,
E-Publishing-Service der TU Darmstadt

Declaration of Authorship

Thesis Statement pursuant to § 22 paragraph 7 and § 23 paragraph 7 of APB TU Darmstadt

I hereby formally declare that I, Marion Anita Höfling, have written the submitted thesis independently pursuant to §22 paragraph 7 of APB TU Darmstadt. I did not use any outside support except for the quoted literature and other sources mentioned in the thesis. Furthermore, I state that all passages which have been taken out of publications of all means or unpublished material either whole or in part, in words or ideas, have been marked as quotations in the relevant passage. This thesis has not been handed in or published before in the same or similar form.

In the submitted thesis the written copies and the electronic version for archiving are pursuant to § 23 paragraph 7 APB identical in content

Darmstadt, 04.03.2021

Marion Anita Höfling

Content

Symbols and Abbreviations

Techniques

BSE	Backscattered Secondary Electron
C-DIC	Circular Differential Interference Contrast (Zeiss)
DART	Dual AC-Resonance Tracking mode
DIC	Differential Interference Contrast
DFT	Density Functional Theory
ECCI	Electron Channeling Contrast Imaging
NMR	Nuclear Magnetic Resonance Spectroscopy
OLM	Optical Light Microscopy
PFM	Piezoresponse Force Microscopy
PLM	Polarized Light Microscopy
SEM	Secondary Electron Microscopy
TEM	Transmission Electron Microscopy
TSSG	Top-Seeded Solution Growth
U-DICR	Circular Differential Interference Contrast (Olympus)

Chemical Formula

KN	$KNbO_3$
PMN-PT	$0.65Pb(Mg_{1/3}Nb_{2/3})O_3$-$0.35PbTiO_3$
PZT	$Pb(Zr,Ti)O_3$
STO	$SrTiO_3$
WC	Tungsten Carbide

Other Abbreviations

bcc	Body centered cubic
C	Sample name “Creep”
CRSS	Critical Resolved Shear Stress
DLD	Dislocation Linear Density (Phase-field parameter)
DLS	Dislocation
DS	Sample name “deformation stepwise”
fcc	Face centered cubic
LVDT	Linear Variable Differential Transducer
pc	Pseudo cubic
SF	Stacking fault

Temperature

C	Curie Constant
RT	Room temperature
T	Temperature
T_0	Curie Weiss temperature
T_c	Curie temperature
T_m	Melting temperature

$T_{o\text{-}t}$	Phase transition temperature (orthorhombic to tetragonal), increasing T
$T_{t\text{-}o}$	Phase transition temperature (tetragonal to orthorhombic), decreasing T
$T_{o\text{-}r}$	Phase transition temperature (orthorhombic to rhombohedral), decreasing T

Energy, Enthalpy, Work

ΔA	Helmholtz free energy
E_{pin}	Critical electrical pinning strength (Phase-field parameter)
E_p	Peierls energy
E_{pot}	Potential energy
F	Mechanical force
ΔG^*	Gibbs fee activation energy
H	Activation enthalpy
Q	Activation energy
W	Work

Stress

σ	Stress
$R_{p0.2}$	Stress value at 0.2% of plastic deformation
R_c	Compressive strength
σ_{jk}	Mechanical stress
σ_{crit}	Critical stress
σ_{pin}	Critical pinning stress (Phase-field parameter)
σ_{ys}	Yield strength
τ	Shear stress
τ_p	Peierls-Nabarro stress (short: Peierls stress)
τ^*	Effective shear stress

Dislocation Characteristics

a	Interplanar spacing of slip planes
$\vec{b}$	Burgers vector
$\lvert\vec{b}\rvert$	Magnitude of the Burgers vector
d_{dis}	Dissociation distance
h	Dislocation spacing (Phase-field parameter)
λ	Angle between Burgers vector and line vector
ρ_{DLS}	Dislocation density
$\vec{t}$	Line vector
ξ	Dislocation velocity

Mechanical Deformation-Related

m	Schmid factor
n	Stress exponent
ψ	Angle between slip plane normal and applied force

τ^*_{therm}	Thermal stress component
V_A	Activation volume
χ	Angle between slip plane direction and applied force
γ_{kl}, γ	Mechanical strain caused by compression
$\dot{\gamma}$	Strain rate
$\dot{\gamma}_0$	Prefactor
γ_{plast}	Plastic strain

Electric Parameter, Electromechanical Response

d_{ijk}	Piezoelectric coefficient
d_{33}	Piezoelectric coefficient (Berlincourt)
d_{33}*	Piezoelectric coefficient (large-signal)
$d_{int}(0)$	Intrinsic contribution
E_j	Electric field
E_c	Coercive field
E_c^*	Apparent coercive field at 1 kV/mm
k	Electromechanical coupling factor
$\overrightarrow{P_l}$	Polarization
P_{max}	Maximum polarization
P_{max}*	Apparent maximum polarization
P_r	Remnant polarization
P_r^*	Apparent remnant polarization
P_{max}-P_r	Back-switching polarization
P_s	Spontaneous polarization
S_{jk}	Elastic strain
S_{max}	Maximum strain
S_r	Remnant strain

Dielectric Properties, Permittivity

α	Rayleigh coefficient
$\overrightarrow{D_l}$	Dielectric displacement
ε_0	Vacuum permittivity
ε'	Real part of the permittivity
ε''	Imaginary part of the permittivity
ε_r	Relative permittivity
ε_r'(max)	Maximum permittivity
ε_r'(RT)	Permittivity at room temperature
ε_{ij}^T	Permittivity (unclamped)
ε_{ij}^S	Permittivity (clamped)
ε_{dw}	Dielectric permittivity, domain wall polarization contribution
ε_{elec}	Dielectric permittivity, electronic polarization contribution
ε_{ion}	Dielectric permittivity, ionic polarization contribution
ε_{or}	Dielectric permittivity, orientation polarization contribution
ε_{sc}	Dielectric permittivity, space charge polarization contribution

$tan\delta$	Dielectric loss
χ_{ij}	Dielectric susceptibility

Others

A	Area
A_0	Initial area
c_{ijkl}	Elastic stiffness
d	Lattice distance
d_{GS}	Grain size
δ_{ij}	Kronecker's delta
η	Constant
f	Frequency
k_B	Boltzmann constant
k	Material parameter
l_0	Initial length
μ	Elastic shear modulus
ν	Poisson ratio
p_i	Pyroelectric coefficient
r	Distance, radius
R	Ideal gas constant
ρ_{rel}	Relative density
x	Lattice position
O, T, C	Orthorhombic, tetragonal, cubic
q	charge
ς	Geometric constant
$t_{T=const}$	Time (Temperature constant)
t_{cool}	Time (Decreasing temperature)
Y	Youngs modulus
Y_{RT}	Youngs modulus at room temperature
Z'	Real part of the impedance
Z"	Imaginary part of the impedance

Point Defects

Fe'_{Ti}	Titanium site occupied by an iron ion
$Nb^{\cdot}_{Ti}$	Titanium site occupied by a niobium ion
$V_O^{\cdot\cdot}$	Oxygen vacancy
V''_{Pb}	Lead vacancy

Abstract

Dislocations have been severely underestimated as a tool for tailoring the functional properties of ferroelectric materials, which are essential electroceramic components in many applications. Recently, numerical simulations have predicted strong ferroelectric dislocation–domain wall interactions. However, little is known about the plastic deformability of bulk ferroelectrics to introduce dislocations and the ability of dislocations to tune electromechanical properties.

In this work, these issues are addressed for the ferroelectric single crystal materials $KNbO_3$ and $BaTiO_3$. Furthermore, the obtained knowledge is applied to fine-grained polycrystalline $BaTiO_3$.

The anisotropic deformation behavior of $\langle 010 \rangle_{pc}$ and $\langle 101 \rangle_{pc}$-oriented $KNbO_3$ single crystals is studied by uniaxial compression at room temperature. The activation of the $\{110\}\langle 110 \rangle$ slip system and the observed low critical resolved shear stress of 20–30 MPa cause a large plastic deformation of 4.6% and allow the determination of the resulting slip band structures. A reduction in domain size from the initial 1.8 μm to 0.5 μm and local switching experiments confirm that dislocations act as nucleation and pinning sites for domain walls.

The dislocation-induced change in functional behavior was examined in detail using $\langle 001 \rangle$-oriented $BaTiO_3$ single crystals. Creep experiments at high temperature cause a mechanical imprint, leading to rhombic domain structures. Moreover, a huge increase in dielectric and electromechanical response ($\varepsilon_r \approx 5800$ and $d_{33}^* \approx 1890$ pm/V) was observed in the subcoercive field region. Based on these results, we propose an extension of the concept of local domain wall pinning at dislocations towards a macroscopic restoring force acting against the domain wall motion. The mechanical imprint and the resulting pinning force (Peach Koehler force) stabilize an *a*-*c*-domain configuration. The application of an electric field causes strain incompatibilities between pinned and switched domains, which result in the macroscopic restoring force preventing the switching of further domains or causing already switched domains to switch back. Since plastic deformation is anisotropic, a brief outlook to the deformability of $\langle 110 \rangle$-oriented $BaTiO_3$ is given, indicating that $BaTiO_3$ and $SrTiO_3$ behave similarly at high temperatures and high stresses.

This mechanism provides a deeper understanding of the dislocation–domain wall interaction on a macroscopic level and paves the way for anisotropy studies in single crystals, as well as the transfer to polycrystalline ceramics.

A creep deformation map for polycrystalline $BaTiO_3$ is then developed. The influence of dislocation- and diffusion-based creep mechanisms on the microstructural and electromechanical properties is discussed. An increase in the phase transition temperature of $\Delta T = 5$ °C, a decrease in the maximum polarization by 10% and an electromechanical strain by 30% were observed. Moreover, the different creep mechanisms are discussed.

In this work, the foundations are laid to better understand the plastic deformability of $KNbO_3$ and $BaTiO_3$ single crystals and the resulting consequences of the mechanical imprint on the ferroelectric domain structure and the dielectric and ferroelectric behavior. Thus, the dislocation-based functionality approach was established on the macroscopic scale, which could facilitate the further implementation of dislocations as functional property-tuning defects in ferroelectric bulk materials.

1 Introduction

The ability to tailor functional properties of a material is an essential feature of all cooperative phenomena, including superconductivity, multiferroics, magnetism, and ferroelectricity. For each phenomenon and application field, the strategy varies slightly with form of the material, for example, thin films or bulk materials. Strain engineering is a common approach to tune the properties of functional materials. For thin films, this is often achieved through epitaxial strain from the substrate, resulting in high-performance ferroic [1-3] or superconducting materials [4]. Other approaches are required for bulk materials, including point defects [5], grain boundaries [6] and phase engineering [7]. Although property tuning with dislocations is less well established, it has been used in some complex materials, including superconducting $YBa_2Cu_3O_{7-\delta}$ [8], thermoelectric bismuth antimony tellurides [9], and ionic materials such as LiF [10]. Dislocations provide tensile and compressive strain fields, which pin vortexes in high-temperature superconductors [8] and reduce thermal conductivity [9]. The combination of a strain field together with a charged dislocation core and a surrounding space charge layer not only enables the modification of thermal properties in oxides [11], but also offers additional transport pathways through the core [12, 13] or the space charge layer [14], thus affecting the electrical conductivity of the material.

Ferroelectrics are among the most versatile functional ceramics because they exhibit a combination of various physical properties such as switchable polarization, high permittivity, pyroelectricity, and piezoelectricity [15]. Tuning these properties is essential for a wide range of applications from sensors, transducers, actuators and capacitors to data storage [15, 16]. Ferroelectric materials are mainly defined by switchability of spontaneous polarization. Regions with similar polarization orientation are referred to as ferroelectric domains, whereas the boundaries between regions with divergence in polarization direction are called domain walls.

Controlling the movement of the domain walls allows the tuning of properties of ferroelectrics, and it is an essential part of their applicability. The main challenge for bulk materials is achieving high temperature and cycling stability, as well as high electromechanical response. Control of domain wall motion is typically achieved by strain engineering [1], phase boundary engineering [17], point defect doping [5, 18], texturing [19-21], domain engineering [22, 23] and required poling procedure [24]. Nevertheless, limited temperature- and field-stability and point defect mobility offer potential for improvement [25-27]. For example, when using acceptor-doped piezoelectrics in resonant drive mode, the heat generation limits the applicability of the point-defect doping approach [15, 28, 29]. This is where, dislocations come into play as a defect type, due to their thermal stability up to 600 °C [30].

Dislocations are intrinsic and temperature-stable defects. Their strain field, charged dislocation core, and surrounding space charge layer offer an opportunity to affect and control the ferroelectric domain wall motion. They combine the potential of electrostatic interaction and a strain field for elastic interaction similar to the strain engineering approach in thin films. In addition, because dislocations are intrinsic defects, no further introduction of potentially toxic materials (e.g., lanthanides) is necessary. Dislocations can stabilize the ferroelectric phase [1, 31], act as nucleation and pinning sites for domain walls [32] and locally alter polarization [32-38]. Nevertheless, dislocations in ferroelectrics remain underestimated and underinvestigated.

The introduction of dislocations in oxide materials is not a trivial challenge owing to the limitation of slip systems because of covalent and ionic bonding, the low dislocation density [39] and higher Peierls stress [40] compared to metals [41, 42]. Therefore, most studies on ferroelectric materials focus on indentation [43-45] or are related to viscosity of the lower Earth's mantle in the context of geological studies but do not focus on the ferroelectric properties [46, 47]. Until now, the influence of dislocations on ferroelectric domain wall motion has been studied mainly theoretically [32, 33, 36, 38, 48, 49] and in thin film model systems [34, 50-57]. As a result, the detailed knowledge and understanding of how dislocations impact the electromechanical response on the macroscopic scale remain limited.

In this study, the effect of artificially introduced dislocations on ferroelectric functionality in bulk materials was investigated, in order to extend the understanding of dislocations to the macroscopic scale. As a starting point, ferroelectric single-crystalline $KNbO_3$ was chosen as one of the rare perovskite materials deformable at room temperature [39]. $KNbO_3$ is used as a photocatalyst [58] and electrooptic material [59] and is the basic component of $(K,Na)NbO_3$, which is one of the most promising lead-free ferroelectric systems. Uniaxial compression experiments were performed to investigate the plastic deformability of $KNbO_3$ along the $[010]_{pc}$ and $[101]_{pc}$ orientations and the dislocation-based changes in the domain structure were investigated. Special attention was given to the slip band formation and distribution, which is rarely discussed for oxides in the literature. The temperature- and locally DC field-dependent domain structures of $KNbO_3$ were investigated to provide evidence that dislocations affect domain formation and arrangement on the microscopic and macroscopic scales.

In the second part, the dislocation-based changes in the electromechanical behavior are discussed. For this purpose, the ferroelectric model material $BaTiO_3$ was used, which is an important electroceramic material in applications [60]. Single crystals were deformed along the $\langle 001 \rangle_{pc}$ orientation by high-temperature creep, causing a mechanical imprint in the $BaTiO_3$ single crystals. The electromechanical properties were studied to investigate the influence of the dislocations on the dielectric, piezoelectric and ferroelectric properties in the subcoercive and supercoercive electric field regimes, indicating a unique potential of dislocation–domain wall interaction.

In addition, an outlook on the high-temperature deformability of $\langle 110 \rangle_{pc}$-oriented single crystals is provided to address the orientation dependence and a comparison to the high-temperature deformability of $SrTiO_3$ is given.

The concept of mechanical-imprint was then extended to polycrystalline bulk materials, which are commonly used in applications. Thus, high-temperature creep was applied to fine-grained polycrystalline $BaTiO_3$ and a deformation map was developed to determine the dislocation creep regime and to investigate the resulting microstructural and electromechanical changes in the material.

The concept of dislocation-based engineering enables the modification of domain structure and domain wall mobility. The demonstrated impact on functional properties shows that bulk ferroelectrics can strongly benefit from dislocations as internal defects.

2 Theory and Literature Review

This chapter summarizes the basics of dislocations and ferroelectrics to explain the introduction of dislocations into ceramics and their interaction with domain walls. In the first section (2.1), the most relevant knowledge about dislocations and dislocation-based deformation mechanisms is presented, focusing on the deformability of perovskites. This information is followed by an overview of the fundamentals of ferroelectrics (Section 2.2). The last section (2.3) highlights the state-of-the-art knowledge on dislocations in ferroelectrics.

2.1 Dislocation-Based Deformation in Ceramics

Dislocations are commonly seen as the major crystal defect type contributing to plastic deformation in metals. However, the term plastic deformation covers several partially competing mechanisms ranging from dislocation-based plastic deformation ($\sigma > \sigma_{crit}$), dislocation creep and diffusion creep to grain boundary sliding [61-65].

The introduction and motion of dislocations in ceramics is more intricate than in metals. The ionic charges and the often more complex crystal structure are two of the main reasons impeding plastic deformation of ceramics. During dislocation motion the system still has to fulfill the charge neutrality condition. Contact between ions of the same charge is undesired. Therefore, easy glide is only possible on a limited amount of planes (slip planes).

In metals, the atoms share an electron cloud. Thus, the atom arrangement does not affect the charge distribution in the same way as ions in ceramics do. As a result, the number of active slip systems in metals is not as severely limited by the atom arrangement, like it is the case for ceramics. In addition, typical dislocation densities in ceramics are lower compared to metals. A dislocation density in the range of 10^9–10^{10} 1/m² [41] can be reached for a well-annealed metallic crystal, while for a cold-worked metal even 10^{14}–10^{16} 1/m² [42] is possible. Several orders of magnitude lower are dislocation densities in ceramic single crystals with 10^8 1/m² or below [39, 66]. The dislocation core structure can be more complex in ceramics, as well. The increased stacking fault energy for ceramics [67] leads to higher energies of dislocations in oxides than in metals [67]. Generally, higher stresses and higher temperatures are thus needed to plastically deform a ceramic and it is likely that the ceramic will fracture before the critical stress for plastic deformation is reached.

To understand the deformation mechanisms in ceramics, a summary of the physical background for dislocation characteristics and motion (Section 2.1.1 and 2.1.2) is given below. The concept of plastic deformation above the yield strength σ_{ys} and creep are presented in Sections 2.1.3 and 2.1.4, respectively. This is followed by a literature review on plastic deformation experiments from ambient to high temperatures for selected ceramics (Section 2.1.5).

2.1.1 Dislocation Characteristics

Dislocations can be described by the insertion of half planes into the regular crystal lattice. Their character is described by the Burgers vector $\vec{b}$, a line vector $\vec{t}$ and the angle λ between both [64, 65]. The Burgers vector, depicted in red in Figure 2.1, is defined by the extent of the additional

lattice plane and the direction of the distorted lattice, visualized as an additional step to close the Burgers circuit (Figure 2.1). The Burgers vector is perpendicular to the line vector for an edge dislocation (Figure 2.1a) and is parallel to the line vector for a screw dislocation (Figure 2.1b) [64, 65, 68].

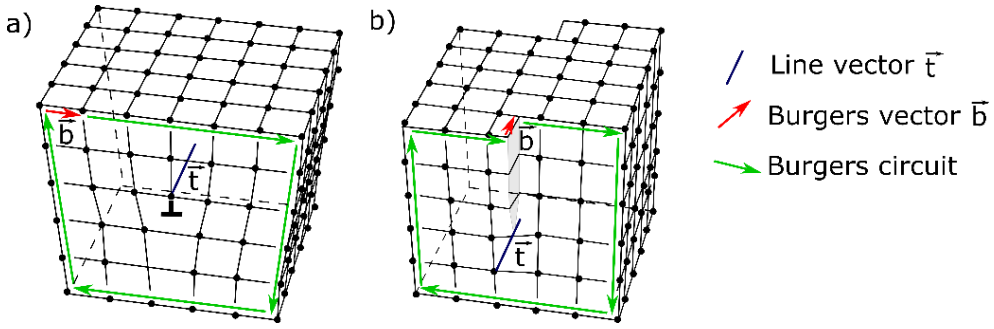

Figure 2.1: Schematic of the Burgers circuit and the Burgers vector of an edge (a) and a screw (b) dislocation (Redrawn from Ref. [68]).

Dislocations distort the crystal lattice, leading to an elastic strain field and an elastic stress field in the surroundings. The shape of the elastic stress and strain fields depends on the dislocation character and affects the dislocation motion, as well as the interaction with other defects and external stresses.

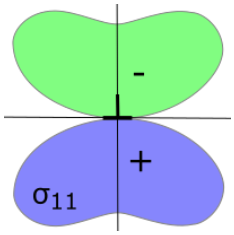

Figure 2.2: Tensile (+) and compressive (-) stress fields around an edge dislocation.

The most common representation of the tensile (+) and compressive stresses (-) σ_{11} around an edge dislocation is shown in Figure 2.2 [64]. The stress field σ of a dislocation is directly proportional to the elastic shear modulus μ and the Burgers vector $\vec{b}$. σ decays with the reciprocal of the distance r [69].

$$\sigma \propto \frac{\mu \vec{b}}{r} \qquad 2\text{-}1$$

The decay of the stress field with increasing distance is among the smallest for dislocations compared with that for other defect types such as point defects ($1/r^2$); the decay is slower only for cracks ($1/\sqrt{r}$). Therefore, dislocations provide a long-range stress field and can interact with other dislocations and defects. The interaction between ferroelectric domains and the strain and stress fields of dislocations will be discussed again in Section 2.3.

Apart from strain and stress fields, excess of charges of the same kind may result in a charged dislocation core in ionic crystals [10]. A charged dislocation may be caused by several different aspects, such as a charged end of the inserted half-plane, charged steps in the dislocation line (jogs and kinks), variations in the vacancy formation energy at the core and by the accumulation of vacancies at the dislocations during dislocation motion [10, 70]. Charged dislocations are addressed in detail for alkali halides by Whitworth [10] and summarized for TiO_2 and $SrTiO_3$

in the review article by Szot [71]. A deficiency of oxygen and strontium was determined at the dislocation core in $SrTiO_3$, indicating a positively charged dislocation core [72, 73]. In contrast to $SrTiO_3$, TiO_2 has a negatively charged dislocation core [74]. In both cases, space charge layers are formed in the surrounding [14, 75]. Whether the core is charged positively or negatively depends on, among other aspects, the complexity of the material, available ions, point defect doping, slip system and dislocation type. It was shown that the dislocation type (e.g., screw, edge and partials) affects the cation concentration [76, 77]. Such variations in charge conditions in the core and in the space charge layer offers huge interaction potential with other defects and can alter electrical properties. Specifically, the conductivity of the core and the space charge layer have been studied in detail in recent years [71, 75, 78-81].

2.1.2 Dislocation Motion

The following descriptions are based on the textbooks by Poirier [69], Messerschmidt [64], Hull [65] and Suzuki [40].

The crystal structure, bonding nature and periodicity of a crystal lattice define the intrinsic resistance of a dislocation to glide. The bonds at the dislocation core have to be broken and rebuilt for dislocation motion. The Peierls potential E_p (Figure 2.3a; also known as Peierls energy) is the periodic lattice potential E, that needs to be overcome. The periodic lattice potential determines the potential energy of the dislocation at a certain lattice position x and depends on the bonding nature of the lattice atoms. The Peierls potential E_p is the peak of the potential curve presented in Figure 2.3a and can be determined with Equation 2-2:

$$E_p = \frac{\mu \vec{b}^2}{\pi(1-\nu)} exp\left(\frac{-2\pi a}{|\vec{b}|\,(1-\nu)}\right) \qquad 2\text{-}2$$

The Peierls potential depends on the shear modulus μ, Poisson ratio ν, magnitude of Burgers vector $|\vec{b}|$ and interplanar spacing of the slip plane a. To overcome the Peierls potential, the Peierls-Nabarro stress τ_p is required, as indicated in Figure 2.3b. Peierls-Nabarro stress is correlated, among other parameters, with the maximum slope (critical force per unit length) of the Peierls potential divided by $\vec{b}^2$. The relationship between Peierls-Nabarro stress and Peierls potential is given in Equation 2-3.

$$\tau_p = \frac{2\pi}{\vec{b}^2} E_p \qquad 2\text{-}3$$

Inserting Equation 2-2 into Equation 2-3 gives the Peierls-Nabarro stress for an edge dislocation, which is defined as follows [40]:

$$\tau_p = \frac{2\mu}{1-\nu} exp\left(\frac{-2\pi a}{|\vec{b}|\,(1-\nu)}\right) \qquad 2\text{-}4$$

The ratio $a/|\vec{b}|$ substantially influences the Peierls stress and can be used to qualitatively predict material behavior. A large $a/|\vec{b}|$ ratio ($a/|\vec{b}| = 1$) leads to a low τ_p ($\tau_p \propto 10^{-4}\mu$), whereas a

small $a/|\vec{b}|$ ratio ($a/|\vec{b}| = 1/3$) has a high τ_p ($\tau_p \propto 10^{-1}\mu$). Face-centered cubic metals (fcc) have a large $a/|\vec{b}|$ ratio owing to their close-packed structures and metallic bonding (small $|\vec{b}|$), resulting in low Peierls stress of $\tau_p \propto 10^{-5}\mu$. This leads to an easier dislocation glide than body-centered cubic (bcc) metals and ceramics. For most ceramics, τ_p is high owing to covalent or ionic bonds, with small $a/|\vec{b}|$ ratios and in the range of $\tau_p \approx 10^{-3} - 10^{-1}\mu$ [82-84]. Perovskites have an $a/|\vec{b}|$ ratio of 0.2–0.5, depending on the slip plane and the Burgers vector [82]. In the case of a small $a/|\vec{b}|$ ratio, the fracture stress is often reached before the dislocation can overcome the Peierls potential [40].

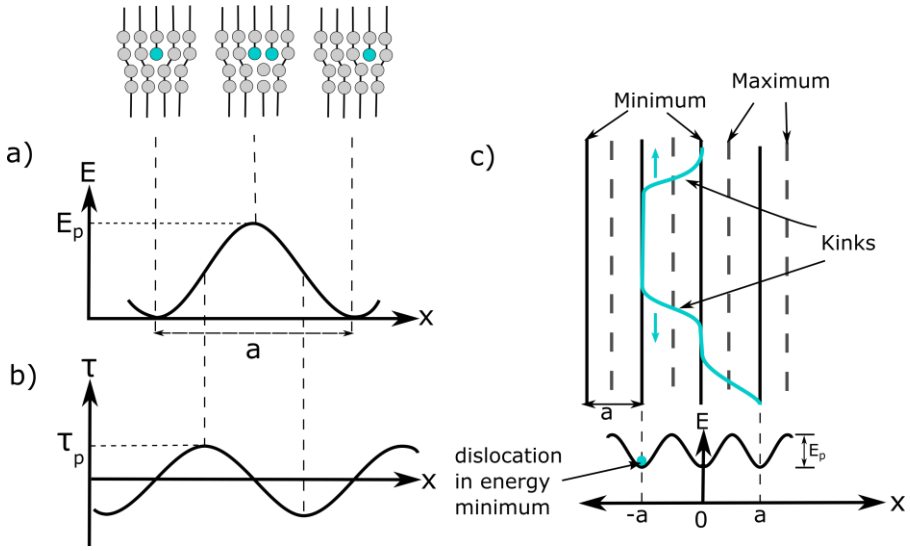

Figure 2.3: Simplified schematic for the dislocation motion and the resulting (a) Peierls energy, E_p, and (b) Peierls-Nabarro stress, τ_p.(Redrawn from Ref. [85]) Kink formation in dependence on the position x is given in (c). Kink migration is indicated with an arrow (cyan; redrawn from Ref. [65]).

With the assistance of thermal activation, the energy potential can be surmounted by the formation of a kink pair. The so-called Peierls mechanism describes the motion of the dislocation in a slip plane (glide mechanism) by the formation of two kinks (kink-pair formation) and migration of the kinks with applied stress. The two kinks have opposite signs and are spread laterally, as indicated in Figure 2.3c. Kink migration (cyan arrow in Figure 2.3c) is the prolongation of the line connecting the two kinks and occurs along the dislocation line. Owing to the periodicity of the lattice the migration of kinks has an energy barrier as well [64]. Only in a few ceramics E_p is low enough for dislocation glide at room temperature. If the kink-pair mechanism is the dominant process, both migration and nucleation can be the rate-limiting step. Another option for a rate-controlling mechanism is overcoming local obstacles (e.g. voids, precipitates, point defects and other dislocation loops), which was first described by Orowan. The Orowan mechanism describes the overcoming of local obstacles by glide (inside a slip plane) or by climb (moving to another slip plane) of dislocations.

The plastic strain rate $\dot{\gamma}_p$ (Orowan equation; Equation 2-5) is correlated with the dislocation density ρ_{DLS}, Burgers vector $\vec{b}$ and the average dislocation velocity $\bar{\xi}$, which is affected by the temperature T and the thermal stress component τ^*_{therm} [69, 86]:

$$\dot{\gamma}_p = \rho_{DLS}\vec{b}\,\bar{\xi}(T, \tau^*_{therm}) \qquad 2\text{-}5$$

For Equation 2-5, it is assumed that the dislocation density is constant, which is the case for quasi-steady-state deformation (regime II, see Section 2.1.4) [69].

Both Orowan and kink-pair mechanisms are thermally activated and, therefore, follow an Arrhenius-type behavior for the strain rate [86]:

$$\dot{\gamma} = \dot{\gamma}_0 exp\left(-\frac{\Delta G^*(\tau^*)}{k_B T}\right) \quad 2\text{-}6$$

$\dot{\gamma}_0$ is a prefactor, $\Delta G^*(\tau^*)$ is the Gibbs free activation energy (indicated in Figure 2.4), k_B is the Boltzmann constant and T is the temperature [87].

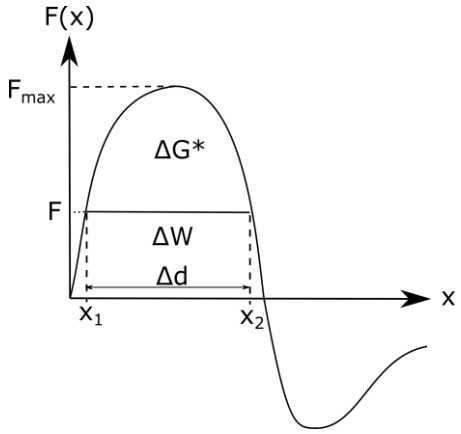

Figure 2.4: a) Overcoming a Peierls barrier (localized obstacle) in dependence of the applied mechanical contribution ΔW and the free energy of thermal activation (Gibbs free activation energy) ΔG^*. This schematic is also valid for kink-pair mechanism (Redrawn from Ref. [64]).

The energy ΔG^* necessary to overcome the localized obstacle is partly provided by the mechanical contribution ΔW, which acts as additional driving force and reduces the required thermal contribution between the states x_1 and x_2 (at the same applied stress and temperature) [65].

$$\Delta G^* = \int_{x_1}^{x_2} F(x)dx - (x_2 - x_1)F \quad 2\text{-}7$$

ΔG^* is indicated in the upper part of the barrier, presented in Figure 2.4a [64, 87]. By integrating Equation 2-7, the Helmholtz free energy $\Delta A(\tau^*)$ (Equation 2-8) and the activation volume V_A (Equation 2-9) can be determined with the force $F(x)$, the positions $x_1$and x_2, the activation distance Δd and the bow-out dislocation segment of length l [64]:

$$\Delta G^* = \Delta A(\tau^*) - \Delta d l|\vec{b}|\tau^* \quad 2\text{-}8$$

$$\Delta G^* = \Delta A(\tau^*) - V_A * \tau^* \quad 2\text{-}9$$

The activation volume V_A is thermodynamically defined as

$$V_A = \left[-\frac{\partial \Delta G^*}{\partial \tau^*}\right]_T. \quad 2\text{-}10$$

Arrhenius relationships are often used to describe dislocation dynamics or creep in general. Hereby, the microscopic interpretation of the thermodynamic parameters can differ between the mechanisms. For example, determining the activation volume as $V_A = \Delta dl\left|\vec{b}\right|$ is only valid for the description of overcoming localized obstacles. Schoeck [87] experimentally determined the activation energy Q_{DLS} for the dislocation motion and the activation enthalpy ΔH.

$$Q_{DLS} = k_B T^2 \left(-\frac{\partial \ln \frac{\dot{\gamma}}{\dot{\gamma}_0}}{\partial T} \right)_\sigma \tag{2-11}$$

$$= \Delta G - T\left(\frac{\partial \Delta G}{\partial T}\right)_\sigma = \Delta H \tag{2-12}$$

The activation energy Q_{DLS} can be determined with a temperature change test at constant stress. At this point, the change of the entropy is disregarded for the motion of dislocations and, therefore, is equal to the activation enthalpy ΔH.

In the literature, a simplified empirical equation of an Arrhenius-type relationship is often applied to experimental data to determine the activation energy Q (or ΔH [88]), which is applicable for dislocation dynamics and creep considerations but thermodynamically erroneous.

$$\dot{\gamma} = \dot{\gamma}_0 exp\left(-\frac{Q}{k_B T}\right) \tag{2-13}$$

These variations in the use of Arrhenius-type relationships can result in an inconsistent terminology for the activation energy and activation enthalpy of experimental data.

Nevertheless, the activation volume and activation enthalpy together facilitate an interpretation of the deformation mechanism [86, 88]. The kink-pair mechanism has an activation volume in the range of 1– $10^2 \cdot b^3$. Localized obstacles, in contrast, have an activation energy in the range of eV and $V_A \approx 10 - 10^4 \cdot b^3$. For $SrTiO_3$ single crystals, the activation volume and activation enthalpy decrease with increasing critical resolved shear stress below room temperature (RT) [86]. With increasing temperature from 1300 K to 1800 K the activation volume increases up to $120 \cdot b^3$ for the ⟨110⟩-oriented single crystals; see Figure 2.5. The activation enthalpy can reach several eV and depends on the single crystal orientation [88]. For $SrTiO_3$, different kink-pair mechanisms are assumed, depending on the temperature range [89, 90].

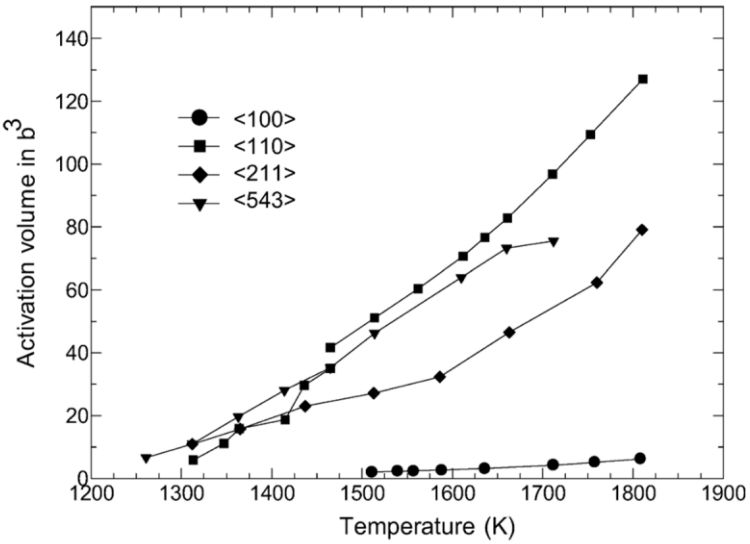

Figure 2.5: Activation volume as a function of temperature T for different orientations in a $SrTiO_3$ single crystal at T > 1227 °C (Reprinted from Ref. [88] © Carl Hanser Verlag GmbH & Co.KG, München).

2.1.3 Concept of Plastic Deformation ($\sigma > \sigma_{crit}$)

Plastic deformation of crystalline materials is typically described with a stress-strain curve. In the linear-elastic regime, the material deforms linearly according to the generalized form of the Hooke's law [61, 91]:

$$\sigma_{ij} = c_{ijkl}\gamma_{kl} \qquad 2\text{-}14$$

c_{ijkl} is the elastic stiffness of the material [91] and it is the proportionality factor between applied stress σ_{ij} and the resulting mechanical strain γ_{kl} at constant temperature. The elastic stiffness is referred to as Young's modulus, denoted by Y in this thesis [91].

Above a certain critical stress, the yield strength σ_{ys}, the material starts to plastically deform. The critical stress is experimentally determined as the mechanical stress value at 0.2% of plastic deformation, $R_{p0.2}$ [92]. In most cases, the yield strength in ceramics is higher than the fracture stress. Therefore, plastic deformation is rarely observed in oxides at RT. Some exceptions are MgO [62], $SrTiO_3$ [93, 94], $KNbO_3$ [95], LiF [96], ZnO [97, 98], ZnS [99, 100] and ZrB_2 [101].

The activation of the slip system does not only depend on a low Peierls stress (highest package density in metals) and a low lattice friction, whose maximum is correlated in metals to the Peierls stress [102], but also on the applied stress and the angle between slip plane and applied stress:

$$\tau = \frac{F}{A}\cos\psi\cos\chi \qquad 2\text{-}15$$

The angle ψ between the slip plane normal and force F and the angle χ between slip direction and force have to be chosen in such a way that the Schmid factor $m = \cos\psi\cos\chi$ is maximal. The angles are shown schematically in Figure 2.6. Multiplication of the resolved shear stress

with the Schmid factor leads to the critical resolved shear stress (CRSS), which has to be exceeded to start the slip motion [65].

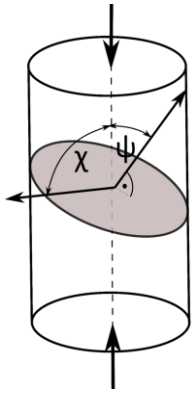

Figure 2.6: Illustration of the relation between the slip direction, the slip plane normal and the applied compressive force, as described in Schmid's law (Redrawn from Ref. [65]).

An example of the relation between the compression axis and a certain slip plane for two orientations of $SrTiO_3$ is given in Figure 2.7 [88]. Up to approximately 900 K, the $\{110\}\langle 1\bar{1}0\rangle$ slip system is the easiest activated slip system in $SrTiO_3$. Compression experiments in [100] direction reach a Schmid factor of $m = 0.5$, which is the highest possible value. Compression in [110] direction leads to a Schmid factor of $m = 0.25$ for the same slip system. The difference in the resolved shear stress is shown for both compression directions in Figure 2.7. The CRSS is for both directions the same, which points out that only one slip system is active [88]. In single crystals the resolved shear stress varies with crystal orientation [88], temperature [39, 93], point defect concentration [103], phase structure [39], initial strain rate [88, 104, 105] and with changing light conditions [100].

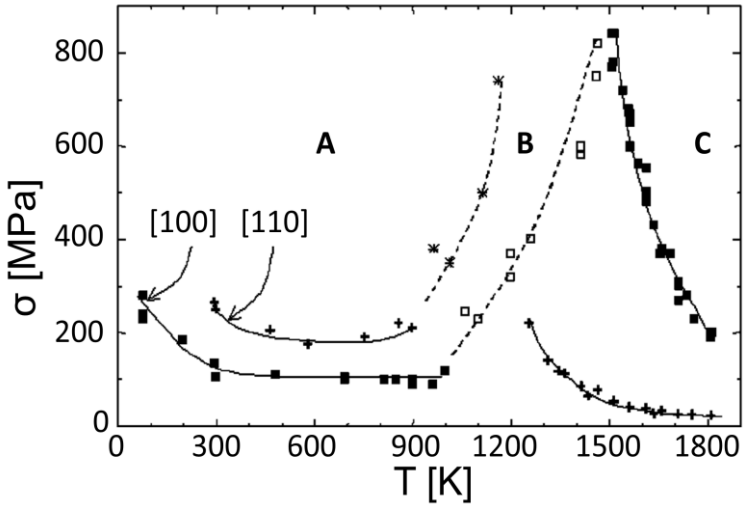

Figure 2.7: Applied shear stress of $SrTiO_3$ as a function of temperature and compression direction. **A** and **C** indicate the ductile temperature ranges. The filled squares indicate the compression along the [100] orientation and the crosses along the [110] orientation. **B** indicates the intermediate temperature range, where the fracture stress is reached before plastic deformation occur. The fracture stresses are indicated with open squares and stars. Reprinted from Ref. [94], with permission of American Physical Society.

In perovskites the amount of available slip systems is limited. However, for a successful deformation of a polycrystalline ceramic at least five independent slip planes are necessary. The easiest activated slip system does not provide enough independent slip planes in most ceramics to fulfill this Taylor criterion. Therefore, higher stresses and temperatures are needed to activate another slip system with a less preferred orientation, as well [68]. In metals, the Taylor criterion is not such a critical parameter due to the availability of sufficient independent slip planes, which makes the plastic deformability in metals much easier.

2.1.4 Creep

Creep describes the time-dependent plastic deformation of a material. In ceramics, creep typically takes place at temperatures above 50% of the melting temperature T_m [63]. Commonly, creep is a complex process with several involved mechanisms, which can occur simultaneously or competitively [69, 106-108].

Creep tests can be carried out in tension or compression. The uniaxial stress is kept constant in both cases and the strain γ is measured as a function of time. The creep strain rate $\dot{\gamma}$ ($\dot{\gamma} = \frac{d\gamma}{dt}$, σ=const.) is defined as the slope of the creep curve, which can be seen in Figure 2.8a or as derivative in Figure 2.8b. If the strain rate or the crosshead speed (depending on the compliance of the testing device) is kept constant, then this test is called a constant strain rate test, in which the force is measured as a function of time.

The creep curve can be divided into three regimes (Figure 2.8a): primary, secondary and ternary creep. The strain rate decreases with time in the primary creep regime, $\dot{\gamma}$ is constant in the secondary regime (steady-state creep) and increases again in the ternary creep regime.

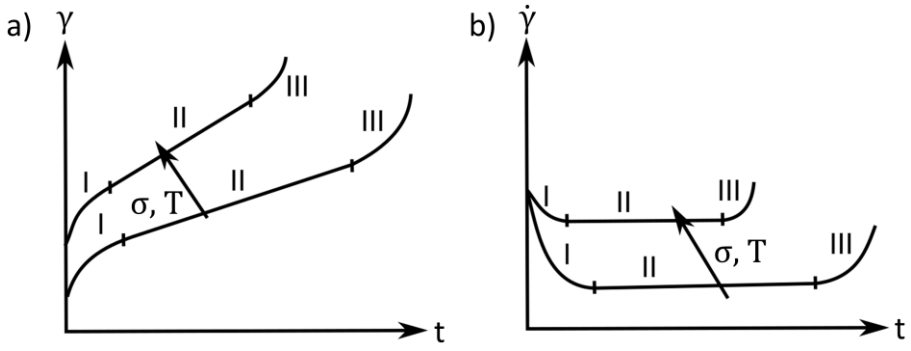

Figure 2.8: a) Creep curves with primary (I), secondary (II) and ternary creep regimes (III). In (b) the strain rate as a function of time emphasizes the steady-state creep regime with constant strain rate. The increase in strain and strain rate with temperature and stress are indicated with arrows (Redrawn from Ref. [85]).

On the assumption that the creep process is, in this specific case, a dislocation-based mechanism, dislocations are generated in the primary creep regime and cause hardening. An equilibrium is reached between dislocation generation by plasticity and annihilation by recovery in the steady-state creep regime. The ternary creep regime leads to failure [68].

The creep rate in the steady state creep regime is a thermally-activated and stress-dependent process (indicated in Figure 2.8), which can be described by the empirical power-law [69]:

$$\dot{\gamma} = \dot{\gamma}_0 \sigma^n exp\left(-\frac{Q}{RT}\right) \quad 2\text{-}16$$

$\dot{\gamma}_0$ is a proportionality factor, σ is the applied stress, n and Q are the stress exponent and the apparent activation energy, respectively, R is the ideal gas constant and T is the temperature. The stress exponent can give an indication for the creep-controlling mechanisms, like diffusion-controlled ($n = 1$) or dislocation-controlled creep ($n > 1$). An alternative to the empirical power-law creep equation is the use of Equation 2-17, which is based on Equation 2-6 and Equation 2-9.

$$\dot{\gamma} = \dot{\gamma}_0 exp\left(-\frac{\Delta A(\tau^*) - V_A \tau^*}{k_B T}\right) \quad 2\text{-}17$$

An activation energy can be gained for both strain-rate equations (2-16 and 2-17). Equation 2-17 offers the benefit that the calculation of the activation volume allows basically the differentiation between kink-pair ($V_A \propto |\vec{b}|^3$) and obstacles ($V_A >> |\vec{b}|^3$), and simplifies the estimation of the related deformation mechanism. If only one thermally activated strain-rate controlling process is active, the Arrhenius plot is linear and the activation energy can be assigned to this process. In cases where several independent processes take place in series or in parallel, the curvature of the Arrhenius plot changes [69].

Dislocation creep can be separated into thermally-activated and indirectly thermally-activated creep processes. In the first case, obstacles in similar dimensions as the dislocation core are overcome due to thermal activation and applied stress. This process's characteristic is the stress-dependence of the activation enthalpy and covers in principle both glide-controlled creep (overcoming Peierls hills) and cross-slip of screw dislocations [69]. In the second case, the obstacles are too large to be overcome by glide, but they can be overcome by diffusion-controlled climb. Climb is a non-conservative motion based on diffusion. Diffusion itself is a thermally-activated process. Thus, this creep mechanism is a directly thermally-activated process but only an indirect thermally-activated dislocation mechanism. As a result, the activation energies for dislocation creep (climb) and self-diffusion are similar. Diffusion-controlled climb can be separated into a stress-independent activation enthalpy process of recovery-controlled creep and the stress-dependent power-law creep [69].

Further creep mechanisms become relevant when considering polycrystalline materials. These mechanisms include grain boundary sliding and the grain size dependence of the diffusion processes: Nabarro-Herring [109] and Coble creep [110]. Nabarro-Herring creep describes the diffusion of vacancies and ions through the lattice, see Figure 2.9a. The strain rate is indirectly proportional to the inverse of the square of the grain size (d_{GS}^{-2}). Coble creep describes the diffusion along the grain boundary (Figure 2.9b) and has a strain rate dependence of d_{GS}^{-3}. Deformation mechanisms maps visualize the regions where a certain creep mechanism takes place. The strain maps for two different grain sizes in TiO_2 are shown in Figure 2.9c and d to emphasize the changes in the stress and temperature range of the creep mechanisms [74, 111].

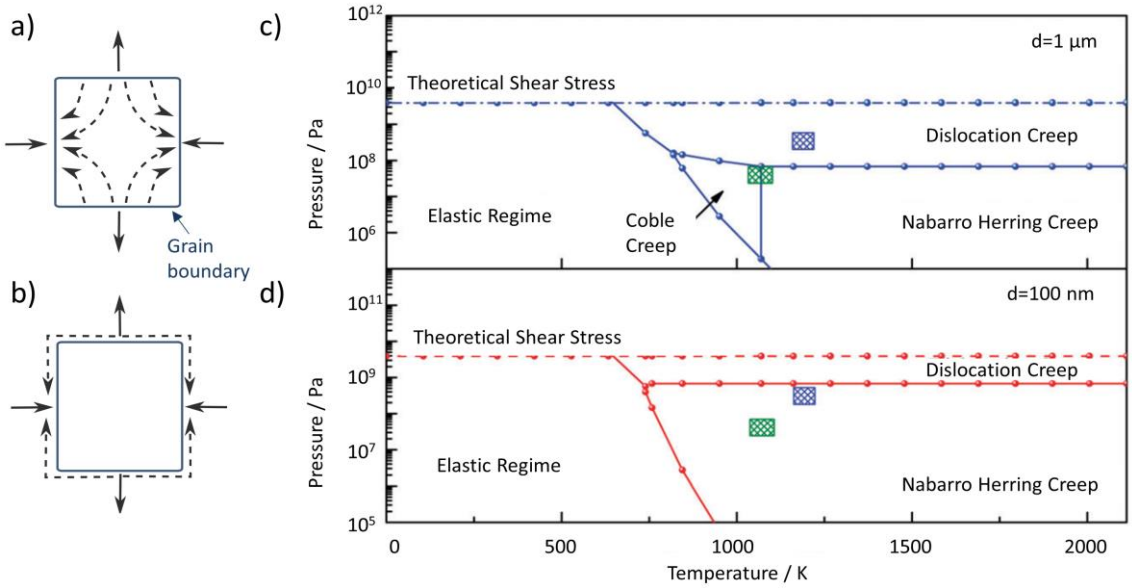

Figure 2.9: Schematics for (a) Nabarro-Herring creep by lattice diffusion and (b) Coble creep by grain boundary diffusion (Redrawn from Ref. [61]). The diffusion paths are indicated with dashed arrows. Grain-size-dependent deformation mechanism maps for polycrystalline spark-plasma sintered TiO_2 with a grain size of (c) 1 μm and (d) 100 nm. The spark plasma sintered (SPS) samples are indicated with a blue-shaded box (SPS sintered at 400 MPa) and a green-shaded box (SPS sintered at 40 MPa). Note that in (c) and (d) dislocation creep only considers dislocation climb-processes. Adapted from Ref. [74], with permission from the Royal Society of Chemistry.

For polycrystalline samples the ratios between grain size, sample dimensions and the aspect ratio are essential for a creep experiment with no or limited cleavage and cracking. The grain size should be at least one order of magnitude smaller than the sample size. The best aspect ratio for the dimensions is in the range of 3:1 to 2:1. For both polycrystals and single crystals, the usage of a lubricant can prevent barreling or rotation of the samples during compression tests [69].

A detailed description of the creep mechanisms and examples for deformation maps can be found in the textbooks of Pelleg [63], Poirier [69] and several review articles [106, 107, 111, 112].

2.1.5 Plastic Deformation of Perovskites

Different methods have been applied to deform perovskites and to investigate the resulting dislocation structures over the past decades. Surface treatments like microscratching on $BaTiO_3$ and $CaTiO_3$ [113], as well as polishing on $SrTiO_3$ [114] are easy and fast methods to introduce dislocations [113]. Surface treatments can, together with indentation [44, 45, 115-117], provide insights into the deformation behavior at room temperature. Although these methods substantially enhance the dislocation density, the plastic zone is limited by the indenting parameters or the polished surface. An interpretation of the interaction between dislocations and ferroelectric domain walls is difficult, especially for random dislocation arrangements, as they occur during polishing. Therefore, macroscopic plastic deformation experiments and creep experiments are the preferred methods to introduce a well-structured dislocation network, which is also distributed over the whole bulk material.

2.1.5.1 Slip System and Deformation Mechanism (RT–900 °C)

In the early 1980s, Poirier et al. reported that the $\{110\}\langle 1\bar{1}0\rangle$ slip system is the easiest one to activate at room temperature for the perovskite $KZnF_3$ [118], even though the slip planes are less dense-packed than the highest-packed {111} planes. The concept of the shortest lattice translation (highest dense-packed plane) would bring ions with the same charge close together during shearing [113, 119]. Therefore, Amodeo proposed that the "dense planes and directions paradigm" is not valid for oxides due to the ionic character of the ceramic crystals [119]. The interpretation that the $\{110\}\langle 1\bar{1}0\rangle$ slip system is the easiest to activate was confirmed by atomistic simulations [95, 120] and experimentally for several other oxides [93, 113, 119].

The $\{110\}\langle 1\bar{1}0\rangle$ slip system has a comparably large Burgers vectors (small $a/|\vec{b}|$ ratio), resulting in high Peierls stresses (Equation 2-4). Thus, the dislocation tends to dissociate into partial dislocations according to Equation 2-18, to reduce the required energy to overcome the Peierls barrier and to enable dislocation motion [47, 82, 121-125]:

$$\langle 110\rangle \rightarrow \frac{1}{2}\langle 110\rangle + \frac{1}{2}\langle 110\rangle + (\mathrm{SF}) \qquad 2\text{-}18$$

A stacking fault (SF) can be formed between the two partial dislocations, as indicated in Equation 2-18. Hirel et al. identified a local energy minimum (Figure 2.10a) of the generalized stacking fault (GSF) energy surface, which corresponds to the ½[110] stacking fault in accordance with the dislocation dissociation given in Equation 2-18 [95]. The distance between two partials is called dissociation distance, d_{dis}, of the dislocation and can be determined by the stacking fault energy [95, 126].

Atomistic simulations were conducted to investigate the dislocation core, mobility, mechanisms and the generalized stacking fault energy surface in $SrTiO_3$, $BaTiO_3$, $PbTiO_3$ and $KNbO_3$. The focus was laid on identifying possible dislocation reactions, the energy of the stacking faults and the favorable glide systems [95, 120].

The dissociation distance d_{dis} is 3 nm for screw dislocations in $KNbO_3$ and is smaller than d_{dis} = 6 nm for edge dislocations [95]. The Peierls stress of the edge dislocation is with $\tau_{p(edge)}$ = 0.57 GPa considerably smaller than the Peierls stress of the screw dislocation $\tau_{p(screw)}$ = 3.42 GPa [95]. The differences in Peierls stresses in $SrTiO_3$ ($\tau_{p(\mathrm{screw})}$ = 2.64 GPa, $\tau_{p(\mathrm{edge})}$ = 1.5 GPa) are not as large as in $KNbO_3$ [95]. A direct comparison of τ_p for edge dislocations indicates that they are more mobile in $KNbO_3$ than in $SrTiO_3$, whereas screw dislocations are less mobile in $KNbO_3$. Additionally, $KNbO_3$ has a strong coupling between the partials, which is weaker in $SrTiO_3$ [93, 95]. Therefore, it was concluded that the mobility and the dislocation core in perovskites are more complex, as described by the theory of elasticity [95]. Nevertheless, atomistic simulations provide evidence that the $\{110\}\langle 1\bar{1}0\rangle$ slip system is the easiest one to activate for perovskites, even if the mobility and dislocation core differences are not fully understood.

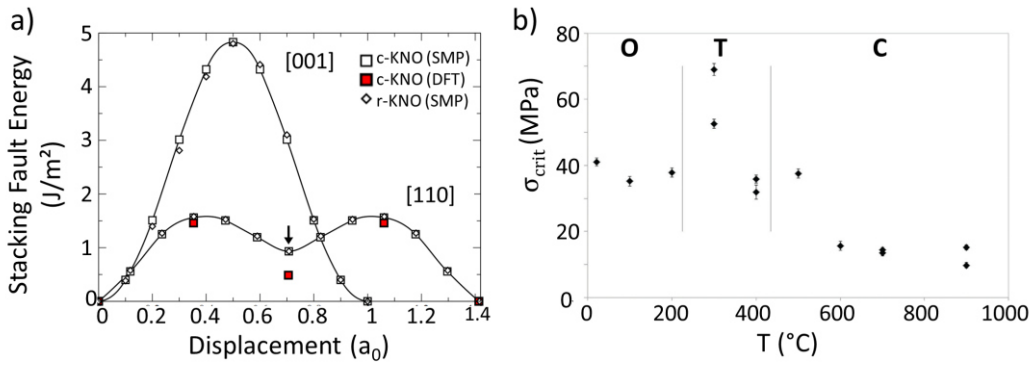

Figure 2.10: a) Simulated generalized stacking fault (GSF) energy in $KNbO_3$ as a function of the displacement. The empty symbols correspond to the cubic and rhombohedral $KNbO_3$ GSF results using the ionic shell-model potential. Density functional theory (DFT) was used to compute the GSF for cubic $KNbO_3$ along the [110] direction. The arrow indicates an antiphase boundary. b) Temperature-dependent critical stress for $KNbO_3$. The different phases (O, T, C) are separated with vertical lines. Reprinted or adapted from Ref. [39, 95], with permission from American Physical Society and Elsevier.

After the identification of the easiest slip system $\{110\}\langle 1\bar{1}0\rangle$ at room temperature, the next step is to identify the deformation mechanisms in a broader temperature range. Therefore, a closer look into the deformation experiments of $KNbO_3$ is given and the results are compared with the model material $SrTiO_3$. Deformation experiments for $KNbO_3$ single crystals were conducted along the $\langle 100\rangle_{pc}$ direction between 21 °C and 900 °C with a strain rate of $8.3{\cdot}10^{-6}$ 1/s (2.5 μm/min) [39, 95]. In this temperature range, $KNbO_3$ has two phase transitions ($T_{o\text{-}t}$ = 225 °C and T_c = 435 °C). Mark et al. separated the critical stress values (Figure 2.10b) in two ranges, from room temperature to 400 °C and above 400 °C. The critical stress at low temperature is approximately 30–45 MPa, while above 600 °C the critical stress lies within the range of 10–15 MPa. The origin of the jump in stress at 300 °C is not clear yet. It is either a measurement artifact or an abrupt increase related to the phase transition ($T_{o\text{-}t}$ = 225 °C). The overall trend indicates a change in deformation mechanisms.

Mark et al. proposed three possible reasons for the jump in stress at 300 °C: I) A change of the amount of active slip systems, II) different influence of the domain walls on the dislocation slip and III) a change in the dislocation mechanism.

Dislocations, which belong to the $\{110\}\langle 1\bar{1}0\rangle$ slip system, were identified over the whole temperature range. At higher temperatures, the $\{100\}\langle 100\rangle$ slip system is active, too. This supports statement I that the critical stress decreases due to the activation of a second slip system. The activation of the $\{100\}\langle 100\rangle$ slip system is to this point surprising due to the Schmid factor of 0 for the [100]-oriented single crystal. Mark et al. assumed that the presence of cracks changed the local stress fields, which leads to the activation of both slip system $\{110\}\langle 1\bar{1}0\rangle$ and $\{100\}\langle 100\rangle$ [39]. Statement II implies a change of the yield strength because of the pinning of domains at dislocations; the pinning effect will be discussed in chapter 2.3.

Straight and long dislocations point towards dislocation motion mainly by Peierls mechanisms [39]. Besides, they indicate a slower kink-pair nucleation than kink-pair migration and high lattice friction. Ferré et al. argued that the orthorhombic distortion increases the lattice friction compared to pseudo-equivalent slip systems in the cubic phase [127], which could explain the hindering of the kink-pair nucleation. Kink-pair nucleation and migration are thermally-

activated processes, therefore at intermediate temperatures, the kink-pair nucleation is accelerated, and the Peierls potential can be surmounted. Above 600 °C, the dislocations easily overcome the Peierls barrier due to kink-pair nucleation and migration [39].

The Peierls mechanism is a strain rate and temperature sensitive process [128]. A strain rate sensitivity was observed in $KNbO_3$ at 100 °C, which seems negligible at 700 °C. From these results it was concluded that there is a change in the dislocation mechanism in $KNbO_3$ and that neither Peierls mechanisms, nor the lattice friction are the rate-controlling mechanisms for deformation at high temperatures [39].

A more detailed study was conducted of the kink-pair mechanisms and the strain-rate sensitivity over a wide temperature range on $SrTiO_3$ [86, 88-90, 129]. At room temperature, the influence of the strain rate on the critical resolved shear stress is negligible. A strain-rate and temperature dependency of the CRSS is obvious above 1227 °C. Within this temperature range, a ductile-brittle-ductile transition takes place in $SrTiO_3$, impeding an interpretation of the mechanisms [93, 94]. One explanation is that a change in the dislocation cores facilitates the difference in temperature regimes [88], but a change in the kink-pair mechanisms is conceivable as well [89]. It has to be considered that also at room temperature the strain rate sensitivity varies for $SrTiO_3$ and $KNbO_3$, which could be related to the difference in phase structures. As in other perovskites, e.g., $BaTiO_3$ and $GdFeO_3$, both slip systems $\{110\}\langle 1\bar{1}0\rangle$ and $\{100\}\langle 100\rangle$ are active in $KNbO_3$ at high temperatures [46, 71, 95, 113]. To this point, it seems that $KNbO_3$ has no ductile-brittle-ductile transition like in $SrTiO_3$ [95]. The melting point of $KNbO_3$ is 1039 °C [47, 130], therefore, it is possible that in $KNbO_3$ such a transition cannot be found due to this temperature limit.

Even though until now, only creep experiments were carried out at temperatures above 1000 °C for $BaTiO_3$, the knowledge gained from $SrTiO_3$ single crystals can help to understand the thermal activation process for dislocation motion in $BaTiO_3$.

2.1.5.2 High-Temperature Deformation

In the late 1980s and early 1990s, Beauchesne and Poirier performed a series of creep studies on $BaTiO_3$, $KZnF_3$, $KTaO_3$ and $KNbO_3$ single crystals to investigate whether a superordinate coherence exists in the deformation behavior of perovskites at high temperatures [46, 47, 131]. $\langle 110\rangle$-oriented $BaTiO_3$ single crystals were compressed uniaxially in the temperature range 1150–1570 °C. The compressive stress was in the range 9–25 MPa and remained constant during deformation in argon atmosphere. The strain rate increases with temperature at constant stress, leading to a strain rate in the range $3\cdot10^{-8}$–$5\cdot10^{-5}$ 1/s [46].

The creep experiments and the TEM results were separated into two categories according to the temperature of phase transition from the cubic to the hexagonal phase (1470 °C) [46]. In the cubic phase, different microstructural features such as scallops, debris, black dots and second phases were observed [46, 113]. An example of a dislocation decorated with scallops for a sample deformed at 1334 °C is given in Figure 2.11a. The overall dislocation loop has a Burgers vector of [010]. A closer look at Figure 2.11b points to the dissociation of the loop into partial dislocations (scallops) with a Burgers vector of $\frac{1}{2}[01\bar{1}]$ and $\frac{1}{2}[011]$, as given in Equation 2-19.

$$[010] = \frac{1}{2}[01\bar{1}] + \frac{1}{2}[011] + (SF) \qquad 2\text{-}19$$

The change in Burgers vector indicates a climb dissociation on the (010) plane. In addition, dislocations in glide configuration appear occasionally on the slip system $\{110\}\langle 1\bar{1}0\rangle$.

Climb involves the diffusion of point defects, which is facilitated by high temperatures. The deformation mechanism changes from glide in $\{110\}\langle 1\bar{1}0\rangle$ at lower temperatures to climb (and glide) of $\langle 100\rangle$ dislocations at higher temperatures, similar to the behavior of $KZnF_3$ [118]. Note that the scallops may also be formed during cooling by dislocation climb owing to the agglomeration of point defects at the dislocation loops [113]. Such scallops (Figure 2.11a) were also found in samples deformed at 1153–1296 °C and 1380–1403 °C. Therefore, the climb dissociation of the dislocations with $\vec{b} = [010]$ into $\frac{1}{2}[01\bar{1}]$ and $\frac{1}{2}[011]$ partial dislocations seems to be a common process. Moreover, stacking faults are formed at partials, as shown in Figure 2.11c, in a polycrystalline $BaTiO_3$ sample. The arrows in Figure 2.11d correspond to the same partials shown in another perspective, to emphasize the stacking fault length of several hundred nanometers and the stacking fault sequence of the TiO_2 and BaO layers (Figure 2.11e) [132]. Debris were found in the same high-temperature range, which indicates glide on the $\{001\}\langle 100\rangle$ slip system [46]. These debris consist of several trapped dislocation parts in adjacent planes, forming a dipole. If the thermal activation is high enough, these dipoles can climb and form elongated loops.

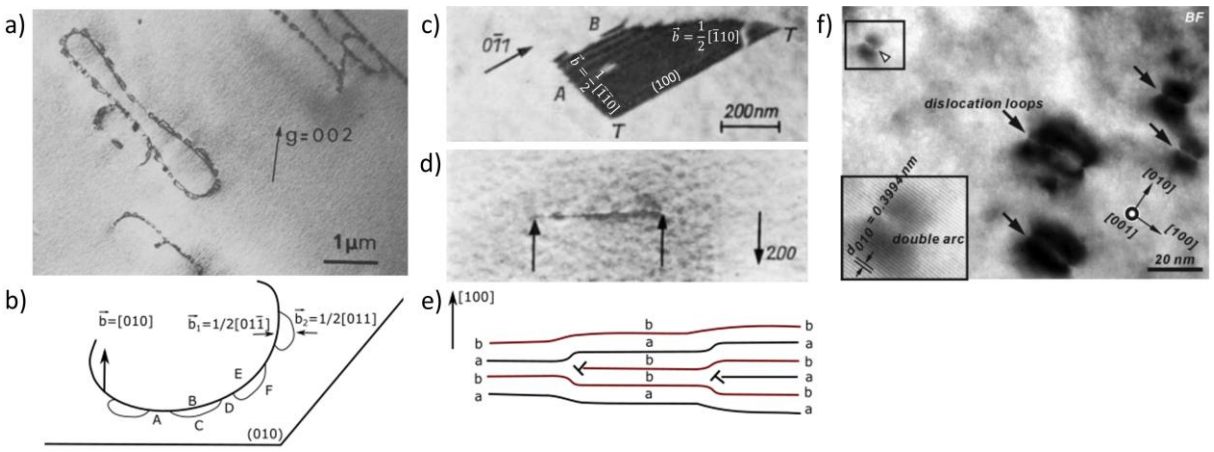

Figure 2.11: a) Dislocation loop decorated with scallops in a 1% deformed $BaTiO_3$ sample at 1334 °C [113]. b) Schematic of the climb dissociation of the partial dislocations in (a) and equation 2-19. Non-dissociated parts A and D are shown between the scallops; the scallop partials with $\vec{b} = \frac{1}{2}[011]$ are highlighted as B, C, E and F [113]. c) Stacking fault on a (100) plane is bordered by two partial dislocations. T corresponds to the top of the foil. The same stacking fault is shown from another perspective in (d). The stacking fault lies parallel to the beam to emphasize the partial dislocations, which are marked with arrows. The resulting stacking sequence is schematically represented in (e) with TiO_2 (labelled with **a**) and BaO layers (labelled with **b**) [132]. f) Coffee-bean like dislocation loops in pressure-less sintered $BaTiO_3$ samples [133]. Reprinted or adapted from Ref. [113, 132, 133], with permission from Springer Nature and John Wiley and Sons.

In the cubic phase (0.71–0.9 T_m), the power-law equation (Equation 2-16) is valid, and a stress exponent of $n = 3.6 \pm 0.3$ is achieved with an activation energy of 469 ± 27 kJ/mol [46]. This indicates a dislocation-based deformation mechanism. The activation energy of creep is in the

same range as the activation enthalpy for pressureless-sintering (ΔH = 396 ± 16 kJ/mol) [134] and hot pressing (ΔH = 400 kJ/mol) [135], indicating that Ba^{2+} lattice diffusion is the rate-determining step for the climb-controlled dislocation mechanism [124]. The creep behavior of $KNbO_3$ single crystals was investigated in the temperature range 870–1030 °C (0.84–0.99 T_m) with 19–47 MPa, resulting in a strain rate of $2.4 \cdot 10^{-9}$–$1.9 \cdot 10^{-7}$ 1/s [47]. These strain rates are two orders of magnitude lower than those for $BaTiO_3$ [46]. The activation energy was 415 ± 103 kJ/mol, and the stress exponent was 3.7 ± 0.4. $KNbO_3$ follows the power-law creep equation and has a stress-independent activation energy [47], indicating a climb-controlled creep mechanism, where edge dislocations with ⟨100⟩ Burgers vector climb, and screw dislocations slip on {100} planes.

A common characteristic of $BaTiO_3$ and $KNbO_3$ is that both materials deform according to the power-law creep behavior. Additionally, the primary {001}⟨100⟩ slip system and the secondary $\{110\}\langle 1\bar{1}0\rangle$ slip system are active for both materials at high temperatures. Poirier et al. [131] pointed out that other perovskites ($KTaO_3$ and $KZnF_3$) do not follow this trend. No reliable deformation system has been established for perovskites until now [131].

Similarly, dislocations can be introduced into polycrystalline materials by creep, as into single crystals [136, 137]. Additionally, several sintering techniques, non-stoichiometry [124, 132, 133, 138-142] and electron radiation [143] result in a variety of dislocation structures. Creep experiments on polycrystalline materials are partly dependent on grain size [74, 144]. With increasing grain size, the dislocation creep regime and the diffusion creep regime are shifted to higher temperatures but lower stresses; see Figure 2.9c and Figure 2.9d [74]. The grain size in creep studies varies from 0.45 μm [136] to 19.3–52.4 μm [137] for $BaTiO_3$. The fine-grained $BaTiO_3$ (0.45 μm) samples were deformed at 1150–1250 °C in the range of 5–60 MPa in argon atmosphere; 0.5% plastic deformation was reached without texturing. The strain rate increases with increasing temperature and a change in the stress exponent from $n = 3$ to $n = 2$ was found for high and low stress, respectively [136]. The stress exponent of 2 in the high-stress region and a decrease in activation energy from 1200 kJ/mol to 800 kJ/mol indicated superplasticity in $BaTiO_3$ [136].

Coarse-grained $BaTiO_3$ samples (19.3–52.4 μm) were deformed at 1200–1300 °C at different oxygen partial pressures (10^2–10^5 Pa) to investigate the rate-controlling diffusion species [137]. A stress exponent of $n = 1$ and a grain size exponent of 2 indicated diffusion creep in combination with grain boundary sliding as the dominant deformation process. An activation energy of 720 kJ/mol points toward Ba ions or Ti cations as rate-controlling species [137]. Ba^{2+} lattice diffusion was also confirmed as the rate-determining step for climb-controlled glide mechanisms during sintering [124, 134].

The experimental conditions varied for both experiments with the type of loading history (stress or strain rate controlled), grain size and oxygen partial pressure. A direct comparison is, therefore, not straight forward. In general several different dislocations structures were found in polycrystalline $BaTiO_3$, varying from vacancy-type partial dislocations [133], which look like coffee beans [140, 142] (Figure 2.11f), over stacking faults bordered by partial dislocations [132] (Figure 2.10c), to low-angle grain boundaries [138] and can belong to different slip systems [138].

2.2 Fundamentals of Dielectric, Piezo- and Ferroelectric Materials

This chapter introduces the fundamental principles of polar oxide materials and is based on references [16, 145-148].

2.2.1 From Dielectrics to Pyroelectrics

Dielectrics are electrical insulators. Applying an external electric field to a dielectric material results in short-range displacements of charges. Consequently, dipole moments are formed and the material is polarized [146]. The dielectric displacement

$$D_i = \varepsilon_0 E_i + P_i \qquad 2\text{-}20$$

increases linear with the applied electric field E_i and the induced polarization P_i [16]. Here, ε_0 is the permittivity of vacuum. For a dielectric response under non-vacuum condition the relative permittivity ε_{ij} has to be considered [148] (in this thesis ε_r is used instead of ε_{ij}) :

$$D_i = \varepsilon_0 \varepsilon_{ij} E_j \ . \qquad 2\text{-}21$$

The dielectric permittivity is a complex parameter with a real part ε'_{ij} and an imaginary part ε''_{ij}, like it is given here:

$$\varepsilon_{ij} = \varepsilon'_{ij} + \sqrt{-1}\varepsilon''_{ij} \ . \qquad 2\text{-}22$$

The dielectric loss

$$tan\delta = \frac{\varepsilon''_{ij}}{\varepsilon'_{ij}} \qquad 2\text{-}23$$

is the ratio between the imaginary and real parts and describes the dissipation of electrical energy. ε_r can vary with temperature, mechanical stress, electric field and frequency.

$$P_i = \varepsilon_0 \chi_{ij} E_j \qquad 2\text{-}24$$

describes how the polarization changes with applied electric field and depends on the dielectric susceptibility χ_{ij} :

$$\chi_{ij} = \varepsilon_{ij} - \varepsilon_0 \delta_{ij} \ . \qquad 2\text{-}25$$

δ_{ij} is Kronecker's delta with $\delta_{ij} = 1$ for $i=j$ and $\delta_{ij} = 0$ for $i \neq j$.

These equations are only valid for small electric fields [148].

The overall polarization has several contributions [16, 148]. Electronic polarization describes the displacement of the electron shell against the charged core and is common in all dielectrics. Ionic polarization is a field-induced displacement of cations and anions in an ionic crystal [148, 149]. Orientation polarization is the alignment of permanent dipoles due to an applied electric field. The spatial separation of positively and negatively charged species caused by a difference in charge carrier densities can lead to a space charge.

Crystalline, dielectric materials can be sorted into the 32 point groups according to their crystallographic structure (Figure 2.12). Piezoelectric materials build a subgroup of dielectrics and include only materials with non-centrosymmetric point groups (except point group 432). Piezoelectric materials show a linear coupling of the mechanical and electrical fields. This behavior can be found in 20 of the 21 non-centrosymmetric point groups [148]. Applying an external mechanical stress σ_{jk} causes a change in electric polarization P_i or dielectric displacement:

$$D_i = d_{ijk}\sigma_{jk} \ . \qquad 2\text{-}26$$

Respectively, an electric field E_k results in an elastic strain S_{jk} (inverse piezoelectric effect) [148].

$$S_{jk} = d_{ijk}E_i \qquad 2\text{-}27$$

The piezoelectric coefficient d_{ijk} (C/N) is a third rank tensor and describes the relationship between the mechanical and electrical variables. d_{ijk} is identical for Equation 2-26 and Equation 2-27 [145, 148, 150]. Additionally, the electromechanical coupling factor k is used to describe the system. k is the relation between the converted energy (electrical/mechanical) and the input energy (mechanical/electrical) [145].

Ten of the 21 non-centrosymmetric point groups have a unique polar axis and form a spontaneous dipole moment, which is referred to as spontaneous polarization [148, 150]. The center of positive and negative charges does not overlap. The temperature dependency of the spontaneous polarization and the resulting change in the density of charges at the surface is called pyroelectricity [145, 146]. The last subgroup of dielectrics (Figure 2.12) are ferroelectrics, which will be explained in chapter 2.2.2.

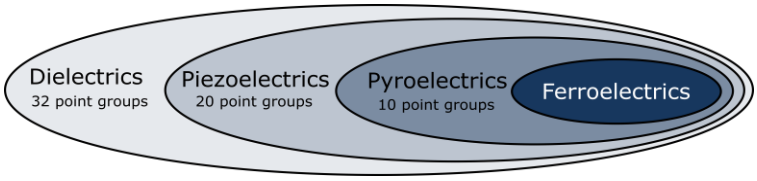

Figure 2.12: Dielectric subgroups: From dielectrics to ferroelectrics.

2.2.2 Ferroelectrics

The field of ferroelectricity was born with the discovery of switchable polarization in Rochelle salt in the early 1920s by Joseph Valasek [151]. In 1946 van Hippel showed that polycrystalline $BaTiO_3$ is ferroelectric too [152, 153], and since then, $BaTiO_3$ became one of the model materials for ferroelectrics. Therefore, the basics of ferroelectricity are explained in this chapter for $BaTiO_3$ and in parts for $KNbO_3$, mainly based on the text books of Jaffe [145], Waser [148] and Rabe [154] and review articles of Damjanovic [150] and Haertling [153].

Ferroelectricity is defined as the ability of a material to switch the spontaneous polarization with an applied external electric field [145]. Ferroelectric materials possess two or more energetically equivalent spontaneous polarization directions. Applying an electric field can switch the spontaneous polarization towards another equivalent direction. $BaTiO_3$ is both ferroelectric and ferroelastic. Therefore, switching of the spontaneous polarization is possible with applied electric field and with applied mechanical stress.

2.2.2.1 Barium Titanate

$BaTiO_3$ (ABO_3) is a polymorphic perovskite with large cations on the A-site (Ba^{2+}), a smaller cation on the B-site (Ti^{4+}) and oxygen ions (O^{2-}) in the centers of the faces (Figure 2.13). In the cubic phase (highest symmetry) the Ti-ion is placed in the center. During phase transition to lower symmetry the polar structure causes a displacement of the Ti-ion, resulting in a spontaneous polarization (indicated as a red arrow in Figure 2.13).

The phase transition from the paraelectric phase to a ferroelectric phase takes place at the Curie temperature T_c (T_c = 130 °C) [150]. Followed by further phase transitions at $T_{t\text{-}o}$ = 0 °C and $T_{o\text{-}r}$ = -90 °C to the orthorhombic and rhombohedral ferroelectric phases, respectively [155].

A phase transition of 1st order takes place at T_c, which is accompanied by a discontinuity in polarization, lattice constant and relative permittivity, indicated in Figure 2.13 [148, 154, 156]. The changes in the dielectric permittivity with temperature T can be described with the Curie-Weiss-law (Equation 2-28).

$$\varepsilon \geq \frac{C}{T - T_0} \qquad 2\text{-}28$$

where C is the Curie constant, T is the actual temperature and T_0 is the Curie-Weiss temperature.

The lattice constants differ for the lower symmetry crystal structure (Figure 2.13a), which results in an anisotropy of the permittivity (Figure 2.13c).

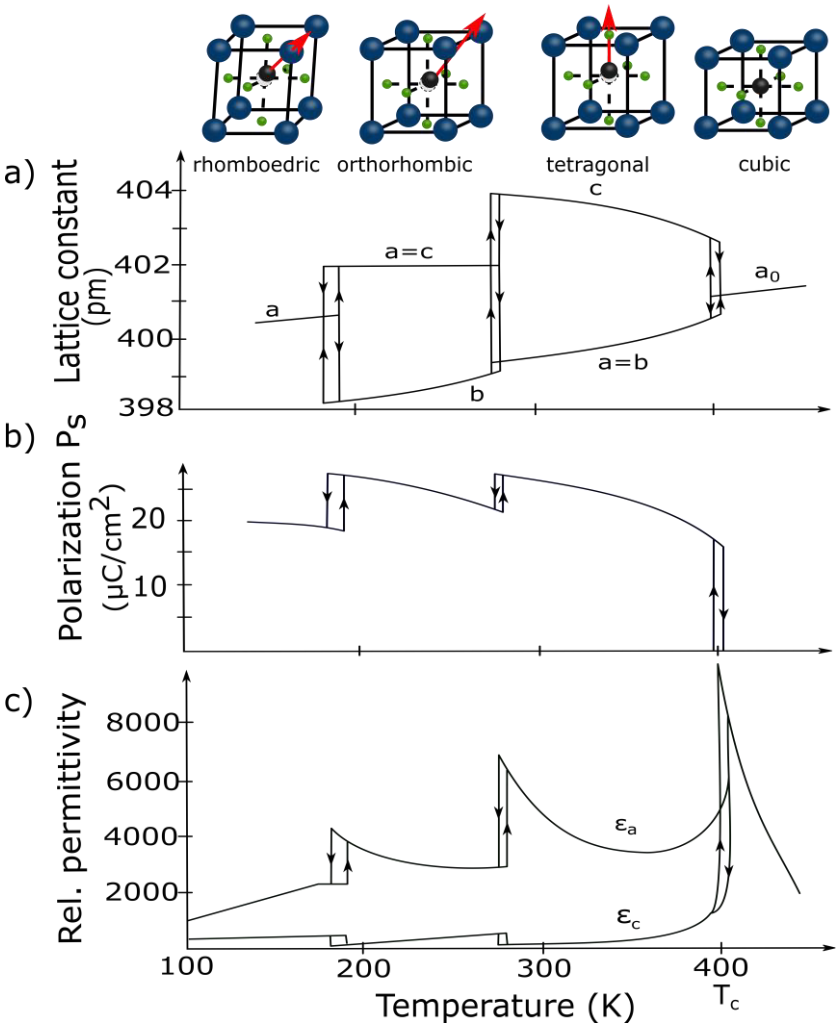

Figure 2.13: Polymorphs of $BaTiO_3$ with spontaneous polarization vectors and the temperature dependency and phase transitions in lattice constant (a), spontaneous polarization (b) and relative permittivity (c) for $BaTiO_3$. Anisotropy of the properties is indicated with a, b and c (Redrawn from Ref. [148]).

2.2.2.2 Potassium Niobate

Similar to $BaTiO_3$ also $KNbO_3$ is a ferroelectric perovskite, but the phase transitions (T_c = 435 °C, $T_{t\text{-}o}$ = 225 °C, $T_{o\text{-}r}$ = -10 °C) take place at higher temperatures [95]. At room temperature $KNbO_3$ is orthorhombic with lattice parameters a = 5.697 Å, b = 3.971 Å and c = 5.722 Å [157]. The anisotropy is evident in the variation of the dielectric constants $\varepsilon_{11}^T = 160 \pm 10$, $\varepsilon_{22}^T = 1000 \pm 80$ and $\varepsilon_{33}^T = 55 \pm 5$ (T: unclamped) [158]. At 100 °C a spontaneous polarization of 22 μC/cm² was reported for $KNbO_3$ single crystals grown with the Remeika method [159]. $KNbO_3$ is also considered for nonlinear-optical and electro-optical applications because of the spontaneous polarization and the oxygen octahedral [59]. It should be noted, that $KNbO_3$ is hygroscopic due to a high surface energy (2.95 J/m²), leading to an affinity to water and sensitivity to ambient conditions [58].

2.2.2.3 Domain Classification and Formation

During cooling below T_c, a surface charge is formed due to the formation of the spontaneous polarization, resulting in the depolarizing field E_d. In addition, the anisotropy of the lattice constants causes a mechanical constraint resulting in a spontaneous strain and an increase in elastic energy. Both elastic energy and depolarizing field can be minimized by the formation of domains like it is indicated in Figure 2.14 for 180° domain wall and 90° domain wall formation.

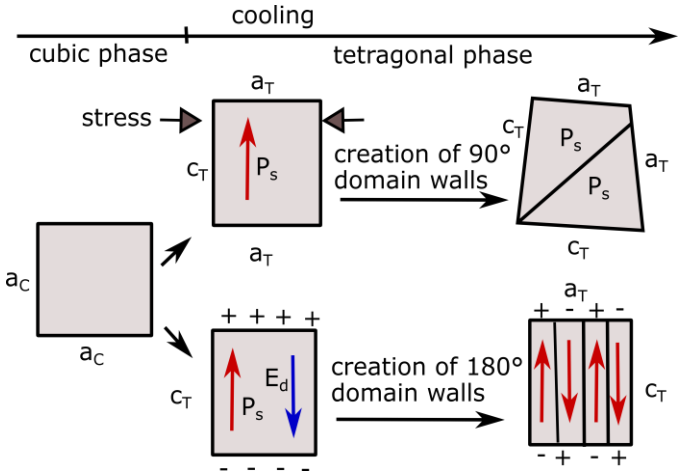

Figure 2.14: Formation of 90° and 180° domains during cooling from cubic into tetragonal phase (Redrawn from Ref. [150]).

Domains are regions with uniform spontaneous polarization with the same spontaneous polarization direction. Depending on the crystal structure, the spontaneous polarization can be oriented along with several energetically equivalent crystallographic directions (Table 2.1) [160, 161]. The borders between the domains are domain walls, defined by the relative orientation of the spontaneous polarization vectors of adjacent domains.

The mechanical constraints result in a preferred choice of the crystallographic planes for the formation of non-180° domain walls [162]. As a result, 90° domain walls are formed at the $\{101\}_{pc}$ crystallographic planes [161] in the tetragonal phase and at the $\{001\}_{pc}$ planes [163, 164] in the orthorhombic phase. 60° domain walls are located at the $\{011\}_{pc}$ planes [165, 166]. A slight misorientation from the expected planes cannot be ruled out in small samples and due to defects [167]. 180° domain walls are not affected by mechanical constraints [161].

An overview of the domain wall types, the spontaneous polarization direction and the number of the spontaneous polarization directions are given in Table 2.1 for the tetragonal, orthorhombic and rhombohedral phases. Note, the domain walls are named after the angle of the spontaneous polarization vectors between two neighboring domains.

Table 2.1: Overview on the domain structures in different ferroelectric phases [149, 168, 169].

Ferroelectric phase	Tetragonal	Orthorhombic	Rhombohedral
P_s directions	⟨001⟩	⟨110⟩	⟨111⟩
Number of P_s directions	6	12	8
Domain wall types	90°, 180°	60°, 90°, 120°, 180°	71°, 109°, 180°

Examples for 90° domain walls in $BaTiO_3$ and for 60° and 90° domain walls in the orthogonal phase for $KNbO_3$ are given in Figure 2.15. The schematics in in Figure 2.15b and d illustrate the relative orientation of the spontaneous polarization for the 90° domain walls in $BaTiO_3$ and 60° and 90° domain walls in $KNbO_3$.

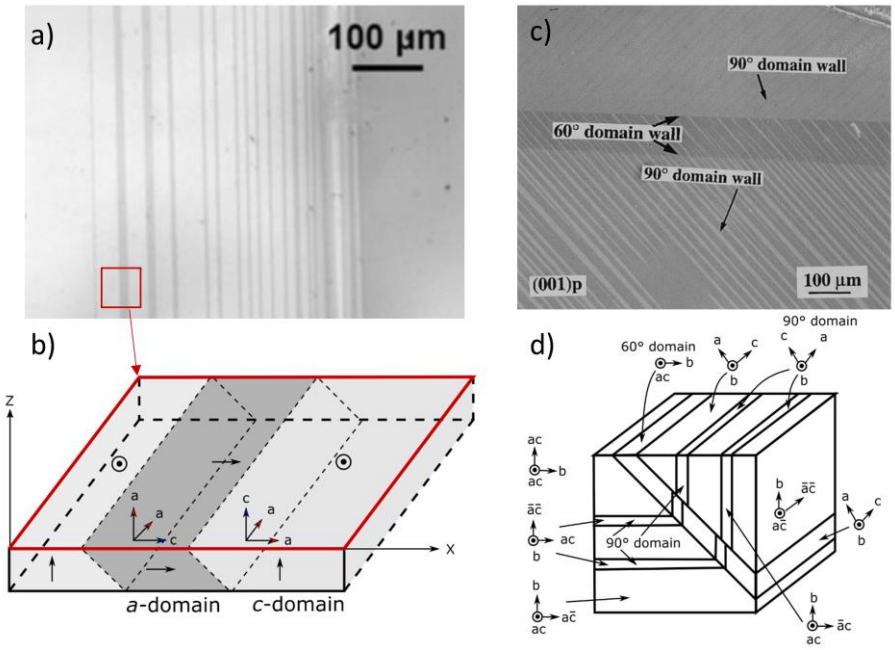

Figure 2.15: a) Light microscope image of a $BaTiO_3$ single crystal with 90° domain walls. The domains lie either in-plane (*a*-domain) or out of plane (*c*-domain); see schematic in (b) [170]. c) Photomicrograph and schematic (d) of the corresponding 60° and 90° domain walls in a $KNbO_3$ single crystal in the orthorhombic phase [171]. Adapted or reprinted from Ref. [170, 171], with permission from Springer Nature and AIP Publishing.

2.2.2.4 Reversible and Irreversible Domain Wall Contributions

The unique feature of ferroelectrics is that the domain walls can move, which gives rise to an increase in properties such as permittivity and piezoelectric constants. In this section, the static domain wall response and the dynamic response based on an applied electric field are explained.

Domain walls can be described by their potential energy E_{pot} which differs for different types of domain walls (90° or 180°) [167, 172, 173] and is a function of the domain wall position x (Figure 2.16). The potential energy is a superposition of the Peierls potential of the lattice and the potential energy contribution by defects. This change in the potential energy landscape is an indication that defects act as pinning sites for domain walls, which will be explained in Section 2.2.2.5. The displacement of the domain wall along the x-axis depends on the energy, which is brought into the system by external stimuli and is either reversible or irreversible. The energy can be provided by an applied electric field, mechanical stress, or increased temperature.

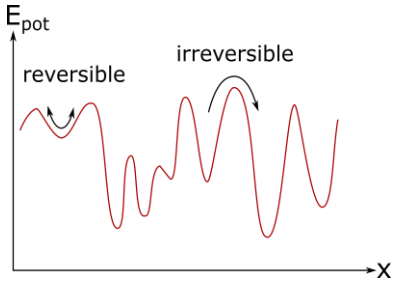

Figure 2.16: Potential energy E_{pot} curve as a function of the domain wall position x (Redrawn from Ref. [150]).

The reversible contribution to permittivity (Figure 2.17) refers to the domain wall displacement inside the potential well of a local energy minimum. Bending and vibration around the equilibrium position in the potential well (extrinsic), as well as the distortion of the unit cell (intrinsic) are reversible mechanisms [150, 174]. At sufficiently high electric fields the introduced energy is high enough to overcome the potential barrier, leading to an irreversible displacement of the domain wall into another local energy minimum [150]. This extrinsic response based on the domain wall displacement is an essential difference between ferroelectrics and dielectrics. In dielectrics, only the lattice response (intrinsic) contributes to the permittivity; therefore, in ferroelectrics, a higher permittivity is reachable.

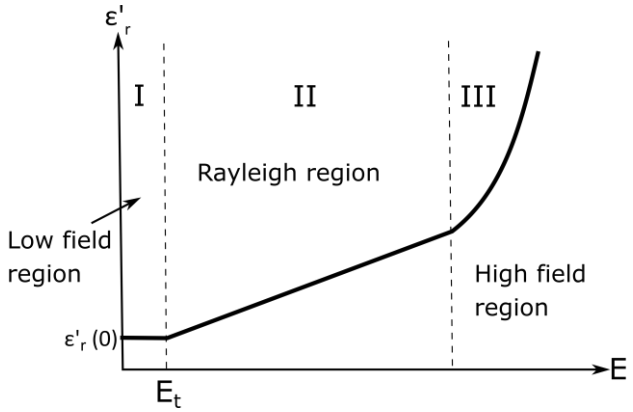

Figure 2.17: Schematic view of the three electric field regions in the field-dependent relative permittivity plot: I. low-field region, II. Rayleigh region, and III. high-field region (Redrawn from Ref. [174]).

The electric field dependent behavior can be classified into three regions (Figure 2.17): I. low-field region, II. Rayleigh region and III. high-field region [174].

In the low-field region the domain wall displacement is reversible and the permittivity response is either independent or weakly dependent on the applied electric field [174]. In medium electric fields, the Rayleigh region is reached [175], and the domain wall displacement is controlled by reversible and irreversible contributions. Damjanovic et al. proved that the Rayleigh law, which describes the behavior of the magnetic materials at low electric fields, is applicable for certain ferroelectrics as well [150, 175, 176]. The linear dependency of permittivity in the Rayleigh region (and the piezoelectric coefficient) on the applied electric field is seen as a result of the irreversible domain wall displacements [176, 177]. The field-dependent permittivity is described by the Rayleigh equation:

$$\varepsilon_r'(E) = \varepsilon_r'(0) + \alpha(E - E_t) \qquad 2\text{-}29$$

where $\varepsilon_r'(0)$ and α are related to the reversible and irreversible contributions (Rayleigh coefficient), respectively [174].

Equation 2-30 is based on the original one derived for ferroelectrics by Damjanovic et al. describing the piezoelectric response as a function of the applied electric field amplitude [176, 178]:

$$d(E) = d_{int}(0) + \alpha(E - E_t) \qquad 2\text{-}30$$

with $d_{int}(0)$ as low field contribution to the intrinsic contribution and the irreversible contribution as slope α.

The electromechanical response becomes non-linear at high electric fields owing to irreversible domain wall displacement, domain switching along the applied electric field direction and domain nucleation. The polarization increases non-linearly with increasing electric field until the saturation polarization (maximum polarization, P_{max}, or maximum strain, S_{max},) point (b) (in Figure 2.18) is reached. The reduction in the electric field to zero leads to the back-switching of some domains, delineated as remnant polarization P_r (c). Applying an opposite directed electric field leads to a further decrease in polarization until a net polarization of zero is reached. At the coercive electric field E_c (d), the domain arrangement is random again. The continuation of this cycle leads to a polarization hysteresis curve, such as that shown in Figure 2.18a, and it is a result of the reversible and irreversible domain wall displacements. The alignment of the domains along the electric field causes mechanical strains, leading to a hysteretic strain behavior (Figure 2.18b) [179].

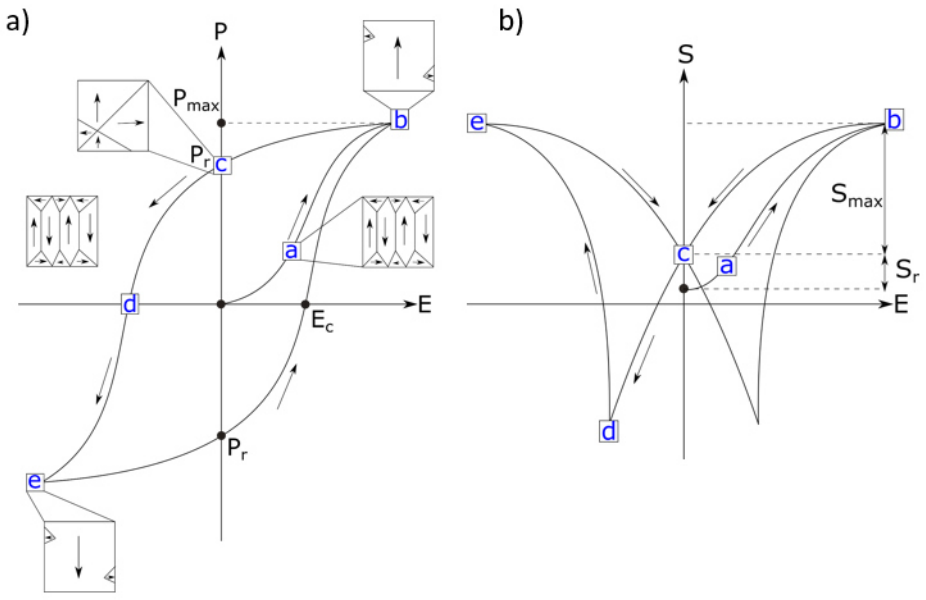

Figure 2.18: (a) Polarization and (b) strain hysteresis of a ferroelectric material (Redrawn from the PhD thesis of Matias Acosta).

2.2.2.5 Extrinsic Domain Wall Contribution

Domain wall movement (reversible and irreversible) is one of the most relevant extrinsic contributions to the dielectric, piezoelectric and ferroelectric properties of perovskite ferroelectrics [180-182]. The mobility of the domain walls is highly affected by defects, external stimuli (e.g., electric field), temperature and other boundary conditions [150, 183].

Pinning the domain walls by defects is a crucial method to manipulate the extrinsic domain wall contribution. A schematic of the pinning of a 180° domain wall between two pinning sites is given in Figure 2.19; the pinning was directly observed experimentally with near-field scanning optical microscopy and later confirmed qualitatively through simulations [184, 185]. Applying a small electric field leads to a bowing of the domain wall between two pinning defects, which were, in this case, narrowed down to screw dislocations or point defects [184] until the curvature reaches a material-dependent radius (Figure 2.19). The estimated domain wall energy of 0.2–0.4 J/m² was approximately one order of magnitude larger than the theoretically calculated domain wall energy of 0.046 J/m² for 180° domains in $BaTiO_3$ [172, 184], supporting the prediction that defects increases the domain wall energy.

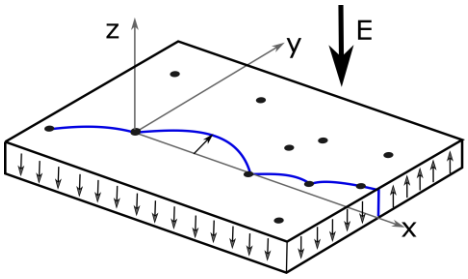

Figure 2.19: Pinning and bowing of a domain wall at defects. Adapted from Ref. [184], with permission from the American Physical Society.

The domain wall pinning strength of point defects (charged defects) was theoretically determined for 90° and 180° domain walls [186]. Kinking and pinning of both domain wall types were found in the vicinity of the charged defects. This kinking increases the extrinsic contribution to the dielectric properties and leads to a change in the polarization distribution close to the charged defects. The domain wall can break through the defect barrier only after a critical electric field is reached [186].

The principle of acceptor-doping (soft) and donor-doping (hard) of ferroelectrics was established on the basis of the pinning potential of point defects and the concept of point defect doping by Carl and Härdtl [5, 187].

Lead-zirconate-titanate (PZT) is one of the model materials to explain the concept of hard and soft doping. By replacing the B-cation Ti^{4+} with Fe^{3+} an additional oxygen vacancy ($V_O^{\cdot\cdot}$) is formed for two Fe^{3+}, leading to the defect pair $(Fe'_{Ti}–V_O^{\cdot\cdot})^{\cdot}$ (Figure 2.20a) [188, 189]. The ordered alignment of this defect pair along the bulk polarization is caused by electrostatic and elastic effects. The oxygen vacancy migrates inside the oxygen octahedra to compensate for these effects, which leads to ferroelectric “hardening” [189, 190], indicated in Figure 2.20b with the increased potential energy landscape barrier. Oxygen vacancies are highly attracted by the domain walls, especially to 180° domain walls [189]; therefore, they are strong pinning centers. As a consequence, the domain wall mobility is reduced, resulting in low coupling and piezoelectric coefficients, reduced ferroelastic strain response, a pinched hysteresis loop (Figure

2.20c), and smaller electromechanical losses, but also higher mechanical quality factors [145, 191-195]. Moreover, hard doping reduces the electric field dependency (Figure 2.20d) and frequency dependency of relative permittivity [190, 196].

Soft doping is achieved by the replacement of A-cations or B-cations in the perovskite, for example, with Bi^{3+}or Nb^{5+}. This leads to the formation of $(Nb_{Ti}^{\cdot}-V_{Pb}^{\prime\prime})^{\prime}$ defect pairs in PZT with a disorder of the pinning sites, indicated in Figure 2.20e and Figure 2.20f with a non-uniform potential energy landscape barrier. Owing to the donor doping the number of oxygen vacancies is reduced and a ferroelectric "softening" is achieved. As a consequence, the domain wall mobility is increased, leading to a higher remnant polarization (Figure 2.20c), a strong electric field sensitivity in the Rayleigh region (Figure 2.20d) and a low mechanical quality factor. The differences in the polarization loop for soft and hard doped PZT are indicated in Figure 2.20c.

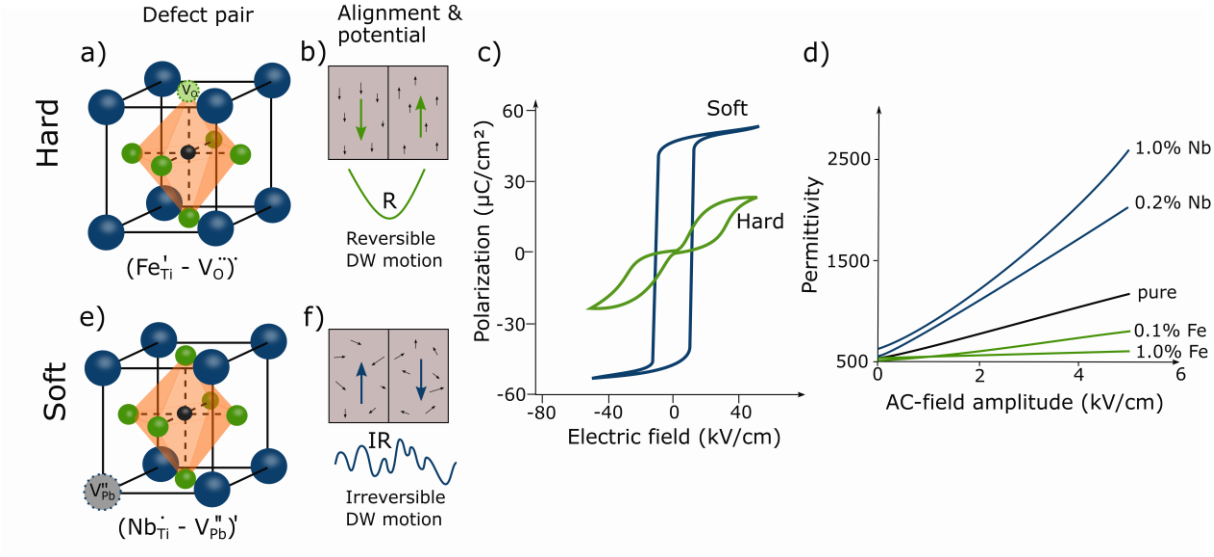

Figure 2.20: Hard and soft doping of lead zirconate titanate (PZT). Formation of defect pairs in hard doped PZT (a) and soft doped PZT (e) (Redrawn from Ref. [197]). Defect dipoles (black arrows) with an elastic component are aligned relative to the spontaneous polarization (blue arrow) and the resulting change of the energy landscape is schematically shown in (b) and (f)[1]. Influence of the point defect doping on (c) P(E) loops [194] and (d) field-dependent permittivity [190]. Adapted from Ref. [190, 194, 197], with permission from AIP Publishing and Elsevier.

2.2.2.6 Domain Engineering

Domain engineering describes controlled change in the domain orientation and domain size to optimize the domain wall density and to adjust the ferroelectric properties [198-202]. Originally, this term was used to describe a poling process in a direction that does not belong to one of the zero-field polar axes, conceiving domains with a minimized angle between polar axis and polarization vector [201]. The resulting domain configuration depends on the direction of the applied electric field and the domain state (monodomain or polydomain). The resulting electromechanical response is determined by the intrinsic anisotropy of the single crystals and

[1] Personal correspondence with Dragan Damjanovic, EPFL, Lausanne.

the ferroelectric phase [203, 204]. Therefore, it is an intrinsic contribution, and the domain walls are considered as stationary [205].

In a broader sense, domain wall engineering considers static domain wall-based modifications of the properties, which widens the field beyond the poling approach.

Wada et al. used both anisotropy in orthorhombic $KNbO_3$ single crystals and non-polar axis poling to investigate the piezoelectric coefficients of a $[001]_{pc}$- and $[111]_{pc}$-oriented $KNbO_3$ and $BaTiO_3$ single crystals [206, 207]. With decreasing domain size (increasing 90° domain wall density), an increase in piezoelectric coefficients d_{33} and d_{31} was determined, leading to the conclusion that a stationary polydomain state with a high domain density is beneficial to gain high piezoelectric properties [207]. Moreover, the permittivity and piezoelectric and coupling coefficients are affected by the orientation [208], domain wall type, domain state, domain pattern and domain size [22, 23, 209, 210].

2.3 Dislocations in Ferroelectrics

The lattice potential and the extrinsic domain wall contribution are affected not only by point defects, but can also be altered by dislocations. The interaction between dislocations and ferroelectrics materials is summarized in this chapter. The first part describes the characteristics of the nucleation of domains at dislocations [32, 113, 211], formation of dislocations at the domain walls [143] and dislocation formation during electric poling or cycling [212, 213]. It also provides an overview of the dislocation–domain wall configuration (Section 2.3.1). The stability to external stimuli, as well as the pinning potential are highlighted in Section 2.3.2. The last part (Section 2.3.3) summarizes the effects of dislocations on the dielectric, piezoelectric and ferroelectric properties.

2.3.1 Dislocation and Domain Wall – Nucleation and Configuration

In most studies, dislocations in ferroelectric materials were formed above T_c by creep [113], plastic deformation ($\sigma > \sigma_{ys}$) [39, 95], during thin-film growth [35, 214], during crystal growth [211], sintering [139] or were implemented in the simulation as defects [32, 36, 38, 49]. The main part of this chapter will review the literature describing the domain wall nucleation and configuration at dislocations, which occur mainly during the phase transition from the cubic to the tetragonal phase [31, 49, 120, 214]. A smaller part addresses the formation of dislocations in the ferroelectric phase by electric poling [212], or cycling [213] or at domains due to point defect agglomeration [143].

2.3.1.1 Phase Transition

Misfit dislocations that form at the interface between the substrate and a thin film to reduce the lattice mismatch are common during film growth [215, 216]. During cooling below T_c in epitaxial $BaTiO_3$ thin films [214], the thermal mismatch causes an additional strain component at the interface between substrate and film owing to phase transition, which is reduced by domain formation. The 90° domain wall points towards the dislocation core at the interface,

indicating that the strain fields of the dislocation and the 90° domain wall counteract each other, which lowers the energy [214]. Hu et al. simulated such a domain formation process around interfacial dislocations [49]. A spatially inhomogeneous eigenstrain was chosen for the random dislocation distribution with respect to elastic fields. For simplicity, the dislocation core energy and changes in local bonding were disregarded, and a static dislocation position was assumed. The cooling of $PbTiO_3$ was simulated from the cubic phase (paraelectric) into the tetragonal phase (ferroelectric). The inhomogeneous strain fields of the dislocation cause a spatial variation in transition temperatures, which resulted in the existence of a ferroelectric phase at temperatures higher than the dislocation-free T_c. The nucleated domain type and domain growth rate varied for the different dislocations simulated either in climb or glide configuration. Either the *a* or *c*-domains nucleated, but no mixed domain structures were identified. The position of domain nucleation varied from nucleation at one side of the dislocation (glide) to nucleation on both sides (for climb). It seems that dislocations are positioned inside the domains and not at the domain wall, which is contrary to the experimental findings of Dai et al. [214].

In bulk materials, several different configurations of domains and dislocations were found, varying from dot-shaped dislocations and triangles to partials with stacking faults [66, 211, 213]. A domain was localized close to dot-shaped dislocations on the $(110)_{pc}$ plane. The dislocation density in Remeika-grown $BaTiO_3$ single crystals was approximately $2{\cdot}10^8$ $1/m^2$ (Figure 2.21a) [66], which is lower than that in $KNbO_3$ and $SrTiO_3$ single crystals (10^9–10^{12} $1/m^2$) [11, 39, 104]. Thus, fewer nucleation sites were available in the Remeika-grown $BaTiO_3$ sample. Nevertheless, a domain was pinned by dislocations, as indicated in Figure 2.21a. As shown in Figure 2.21a, unstable domains were nucleated in the scallops, which decorated the dislocation loops. Additionally, unstable domains were formed or nucleated at dislocation lines reaching the TEM-sample surface (Figure 2.21b). These dislocations were initially created during high-temperature creep [113]. In temperature-dependent plastic deformation experiments (see chapter 2.2.4.1), it was observed that the number of domains and dislocations varied significantly with phase structure during deformation [39, 95]. $KNbO_3$ single crystals deformed in the tetragonal phase had the highest number of domains and slightly higher dislocation density than the samples deformed in the orthorhombic or cubic phase. A high dislocation density is preferred for domain nucleation owing to many nucleation sites [95]. In in-situ temperature-dependent TEM experiments, the domains were reported to have formed at screw dislocations with $\vec{b} = [1\bar{1}0]$ [31]. In $KNbO_3$ single crystals (Czochralski growth method), domain walls were formed at the (110) plane in the tetragonal phase and at the (133) and (277) planes in the orthorhombic phase. This finding indicates a relationship between the 90° and 60° formation of domains and the slip planes and emphasizes the role of phase transitions in the nucleation of domains at dislocations.

2.3.1.2 External Stimuli and Point Defects

Moreover, domains with a 90° domain wall were nucleated at the dislocation by varying the electron beam conditions [211]. An isosceles triangle was formed, consisting of a dislocation as the base and 90° domain walls as the sides, as shown in Figure 2.21c and schematically represented in Figure 2.21d. This triangle separated two regions with different polarization directions on the inside and outside of the triangle. The polarization change is likely caused by

the strain fields of the dislocation-domain-triangle [211]. In a further study, Ingle and Kokate investigated the switching behavior of KN single crystals under applied DC field [217], emphasizing the role of dislocations in domain nucleation [217-219].

Therefore, nucleation of domains at dislocations was considered. However, domain walls can also lead to the formation of dislocations, which was experimentally shown by Buck et al. for $BaTiO_3$ [143]. Dislocation loops and stacking faults were formed at domain walls owing to the agglomeration of point defects of a similar kind during electron beam irradiation, as shown in Figure 2.21e [143]. The nucleation rate of the dislocation loops is strongly associated with the mobility of the slowest species; therefore, nucleation is a temperature-dependent process. During electron beam radiation, the temperature increases locally, which is beneficial for the agglomeration of the point defects. Nevertheless, most dislocation loops were predominately formed at 90° domain walls. Only a small number of dislocation loops were found inside the domains and above T_c [143]. Below T_c, elastic strains promote dislocation loop formation at the domain walls. A distortion in the domain facilitates the dislocation nucleation inside the domain. Above T_c, the migration energy is low enough such that the dislocation loops or point defects can move to and disappear at the grain boundary or TEM-sample surface.

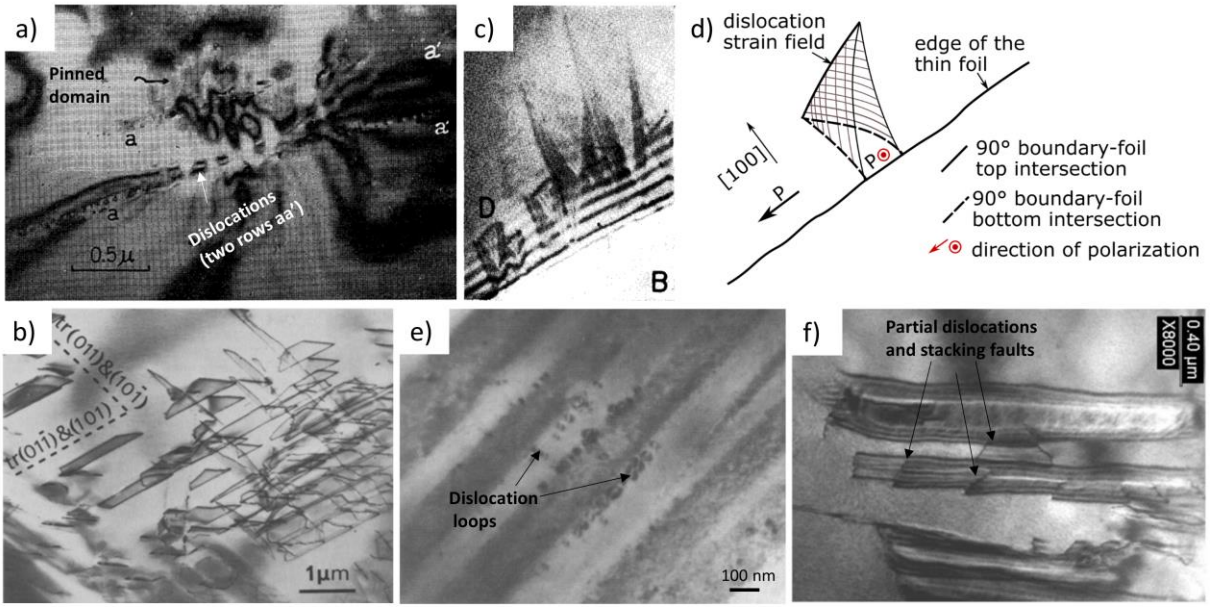

Figure 2.21: a) Dot-shaped dislocations and a pinned domain are identified in a $BaTiO_3$ single crystal [66]. b) Domains are pinned at dislocations in 1% deformed $BaTiO_3$ single crystals [113]. c) The image shows an isosceles triangle formed by the dislocation-pinned domain wall in $BaTiO_3$ [211]. d) Schematic of the triangle shown in (c); redrawn from Ref. [211]. e) Dislocation loops are formed by point defect agglomeration at the domain walls [143]. f) Partial dislocations and stacking faults are found in a ⟨001⟩-oriented $0.65Pb(Mg_{1/3}Nb_{2/3})O_3$-$0.35PbTiO_3$ single crystal [213]. Adapted or reprinted from Ref. [66, 113, 143, 211, 213], with the permission from © (1964) The Physical Society of Japan, Springer Nature, AIP Publishing, Taylor and Francis and IOP Publishing.

An alternative approach to form dislocations in ferroelectric materials is electric poling [212] or electric cycling [220]. Balzar et al. studied the stress and strain components of the polycrystalline $BaTiO_3$ samples during poling by X-ray diffraction [212] and determined a dislocation density of 10^{13} $1/m^2$. This density is five magnitudes larger than the dislocation density in a Remeika-grown $BaTiO_3$ single crystal [220]. Notably, no direct evidence of dislocations was presented, and the calculated dislocation density may have been overestimated

[221]. Another approach is electric field cycling of 0.65Pb($Mg_{1/3}Nb_{2/3}$)O_3-0.35$PbTiO_3$ (PMN-PT) single crystals [213]. During this process, partial dislocations and stacking faults were formed at the intersection of 90° domain walls (Figure 2.21f). Prior to electric cycling, the as-grown single crystals were almost completely free of dislocations. The TEM investigation indicated that partial dislocations with $\vec{b} = \frac{1}{2}[101]$ were formed on $(\bar{1}01)$ planes to balance shear displacements in the sample caused by switching. In contrast to the findings of Bradt and Ansell [211] for $BaTiO_3$, the partials in the PMN-PT sample formed during the cycling are temperature stable (irradiation with an electron beam) or locked within the domain intersection [213].

2.3.2 Domain Wall Pinning at Dislocations

Dislocations not only provide a nucleation site for domains but also pin the domain walls [32, 211]. The pinning was experimentally shown for 90° domains during electron beam radiation in TEM [211]. In contrast to freely movable domains, pinned domains withstand longer variations in the electric field and beam conditions [211]. The strain fields of the dislocations and the 90° domain wall in thin films negate each other, which leads to a lower energy and to domain wall pinning at the dislocations [214]. For 180° domain walls in Pb(Zr,Ti)O_3 thin films (PZT), the pinning was shown to occur at interface dislocations and at threading dislocations. It was argued that the pinning results from the disorder in the area leading to a locally reduced energy owing to the non-charged and non-ferroelastic character of the 180° domain walls. Pinning is caused for both domain types by the reduction in energy. The position of the dislocations seems to be determined by the elastic energy as well [214]. The elastic energy excess as a function of the dislocation and domain wall position suggested that the dislocation-domain combination depends on the dislocation configuration, as indicated in Figure 2.22a. Glide dislocations G_I seem to be more stable in *c*-domains than in *a*-domains and vice versa for G_{II} dislocations. For one of the glide configurations an energetically stable configuration at the domain wall was identified, similar to the experimental results in thin films, but dislocations inside the domains are energetically possible, as well [214].

Kontsos and Landis focused on their phase-field simulations on the electromechanical coupling and interaction between different configurations of dislocations and 90° and 180° domain walls in ferroelectric single crystals [32]. They used $BaTiO_3$ as the model material with 180° domain walls on (100) planes and 90° domain walls (head to tail) on (110) planes. In contrast to thin films [57, 123], dislocations are implemented as displacement discontinuities in the single crystals, and are not based on isotropic elasticity [32]. 180° domain walls were combined with a dislocation array with $\vec{b} = \frac{b}{\sqrt{2}}[110]$ (b = dislocation size) and the 90° domain walls with $\vec{b} = \frac{b}{\sqrt{2}}[110]$ and $\vec{b} = \frac{b}{\sqrt{2}}[\bar{1}10]$. Both 180° and 90° domain walls were straight without dislocations. The introduction of a dislocation array results in a kinking of the domain wall, which was also shown in $KNbO_3$ single crystals [31], and a shift in the equilibrium position. The larger the dislocation size and Burgers vector, the more kinked the domain wall becomes.

An increase in the Burgers vector leads to an increase in the critical electrical pinning strength E_{pin}. The pinning strength depends on the orientation of the applied electric field (towards or away from the dislocation) and decays inversely with the dislocation spacing h (Figure 2.22b).

Applying an electric field and a shear stress can cause a similar trend in the pinning behavior of 90° domain walls on the dislocation array in the chosen configurations. A similar behavior was determined for charged point defect arrays as well [186]. A linear relationship between the critical pinning stress (σ_{pin}) and E_{pin} was identified for both defect types (dislocations and point defects). The switching surface separates the areas of pinning (below E_{pin} and σ_{pin}) and overcomes the pinning of the dislocations (above E_{pin} and σ_{pin}) for a constant dislocation spacing and dislocation size (Figure 2.22c). However, the calculated E_{pin} for 180° domain walls is higher than that for two 90° domain wall configurations [32]. This prediction contradicts the assumption by Gao et al., who estimated an even larger elastic interaction for non-180° domain walls [35]. Note that it is beyond the scope of the studies by Kontsos and Landis [32] and Gao et al. [35] to encompass the overall complexity of the dislocation core, Burgers vector, domain structure and energy distributions. Therefore, a direct comparison between a thin film study and a bulk simulation could be misleading. Far away from the phase transition temperatures in the ferroelectric phase the internal stresses can differ significantly for different regions in the material. Therefore, the domain structures and types can spatially vary even if they are pinned at the same dislocation type [31]; similar results were obtained for 90° and 180° domains and edge dislocations in simulations [32].

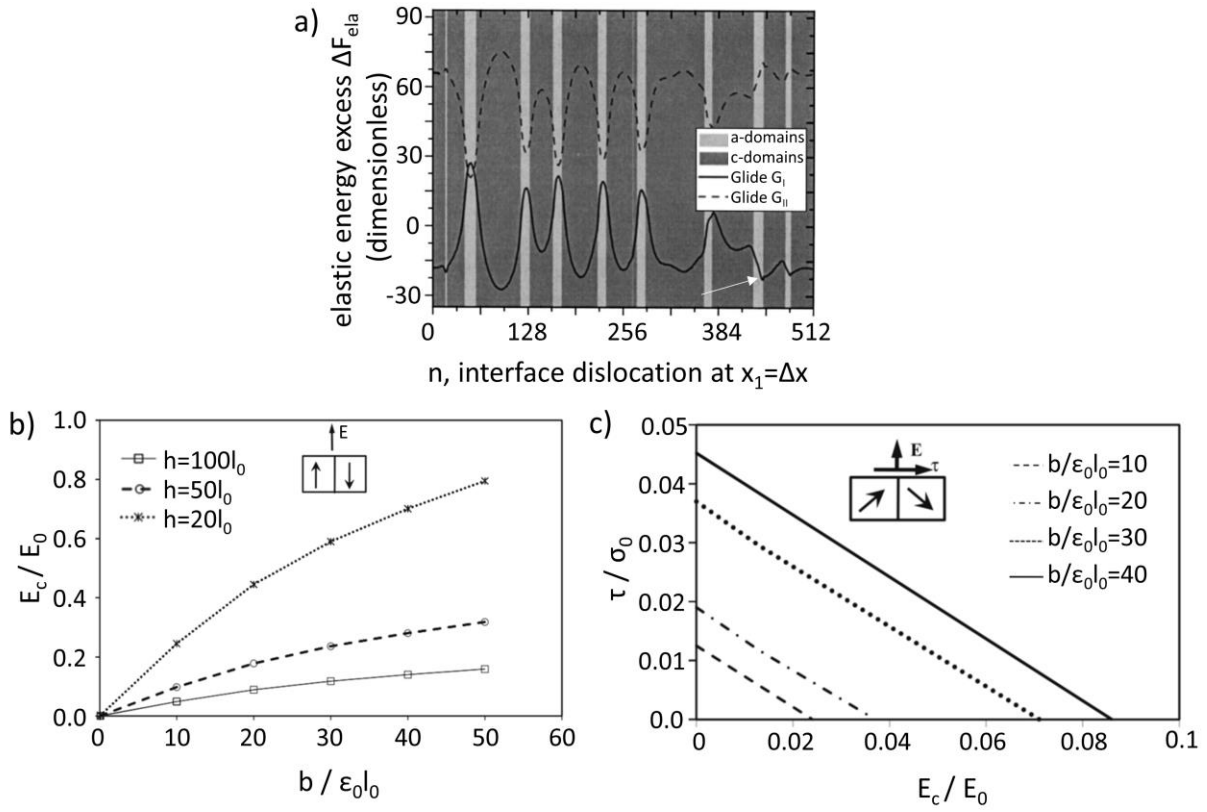

Figure 2.22: a) Elastic energy as a function of domain wall (bright/dark area) and dislocation (glide) position. Negative elastic energy values correspond to a preferred position of the dislocation. The white arrow indicates the position at the domain wall [49]. b) Critical electric field necessary for a 180° domain wall to overcome the pinning and break through the dislocation barrier for different Burgers vector values and dislocation spacing (h) values. c) Linear relation between the shear stress and the critical electric field forming a switching surface for a 90° domain wall pinned at a dislocation array in [$\bar{1}$10] direction [32]. Adapted from Ref. [32, 49], with the permission from AIP Publishing and Elsevier.

Above a critical field E_{pin}, the domain wall can overcome the pinning of the dislocation. This effect could explain the unstable domains found in scallops by Doukhan and Doukhan [113], who questioned a pinning effect based on their results in the unstable domains. Such a depinning was indirectly depicted by electron irradiation experiments on $KNbO_3$ [31]. Remarkably, the material behavior shown in Figure 2.23 indicates that, initially (Figure 2.23a), the mobility of the dislocations is hindered owing to the induced domains. Only after the domain disappears (Figure 2.23b), the dislocation can move further (Figure 2.23c) [31].

This behavior is beyond the frequently discussed unilateral pinning behavior in the literature. Note that in addition to the pinning of domains at dislocations, domain walls can also act as an obstacle, hindering the glide of dislocations and causing a pile-up at the domain wall, which has been experimentally shown in $KNbO_3$ [31].

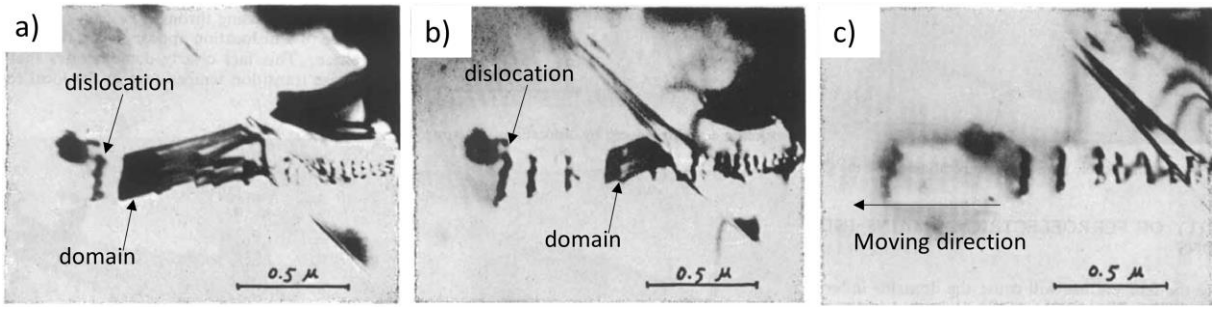

Figure 2.23: a) Initial domain and dislocation configuration, domains with a 60° domain walls are pinned at the dislocation. b) Domain disappears during electron irradiation. c) Dislocations move to the left [31]. Adapted from Ref. [31], with permission from Taylor & Francis.

For the sake of completeness, it should be mentioned that the stress fields of edge dislocations can lead to point defect diffusion towards the dislocation to relieve the stress [222]. Such an impurity-dislocation arrangement can prevent the formation of 60° domain walls at the dislocations, which would otherwise enclose the dislocation array to reduce the stress field. Although no domain walls are formed at such impurity-dislocation arrangements, these are still able to hinder the domain wall motion of the domains [222]. This indicates that the domain wall–dislocation pinning relationship is more complex and can also depend on the point defect concentration in the material.

2.3.3 Effects of Dislocations on the Dielectric, Piezoelectric and Ferroelectric Properties

This section summarizes the most relevant influence of dislocations on the phase transition temperature [31, 49], permittivity [48], local polarization distribution around a dislocation [95, 123] and overall electromechanical response and ferroelectricity [35-38, 49, 53].

2.3.3.1 Phase Transition

The inhomogeneous strain fields of the dislocation cause a spatial variation in Curie temperature, which results in a ferroelectric phase at a temperature higher than the dislocation-free T_c [49]. In-situ temperature-dependent TEM investigations show that, on the one hand, domains at the dislocations disappear long after the rest of the sample has reached the

paraelectric phase; on the other hand, with decreasing temperature, domain walls are formed first at the dislocations, indicating a local shift to higher Curie–Weiss temperature surrounding dislocations. This finding supports the calculation of Hu et al. for the spatial variation of T_c around dislocations [49]. Additionally, for randomly distributed edge dislocation, it was simulated that the Curie-Weiss-temperature increases with increasing dislocation density [48]. An increase in dislocation density may reduce the permittivity and cause a broadening of the phase transition region, depicted as diffuseness [48].

2.3.3.2 Piezoelectric and Ferroelectric Properties

The coupling between the stress field of a dislocation and polarization was demonstrated for thin films with a modified Landau–Devonshire formalism [223]. It was concluded that the stress fields of the dislocations induce a polarization instability, leading to a local depolarizing field. As a consequence, the ferroelectricity is locally suppressed, which was observed in PZT nanoislands with piezoresponse force microscopy [53]. This phenomenon is limited to thin films, where in-plane and out-of-plane strains and stresses substantially affect the dislocation formation and polarization [53]. Li et al. reported a polarization of 120 μC/cm² in the tensile region and 21 μC/cm² in the compressive strain region of a PZT-STO thin film, which supports the suggestion that dislocation orientation influences the local polarization [224]. In bulk materials, atomic-scale calculations were used to determine the polarization vector field around edge and screw dislocations in $KNbO_3$, as shown in Figure 2.24a and Figure 2.24b. A local change in the polarization field was determined in the surrounding of the dislocation cores. Whereas, edge dislocations have a short-range effect on the polarization field, the effect of screw dislocations has a more extended range, as indicated in Figure 2.24a and Figure 2.24b. Such perturbation indicates strong electromechanical coupling, which is discussed in more detail below.

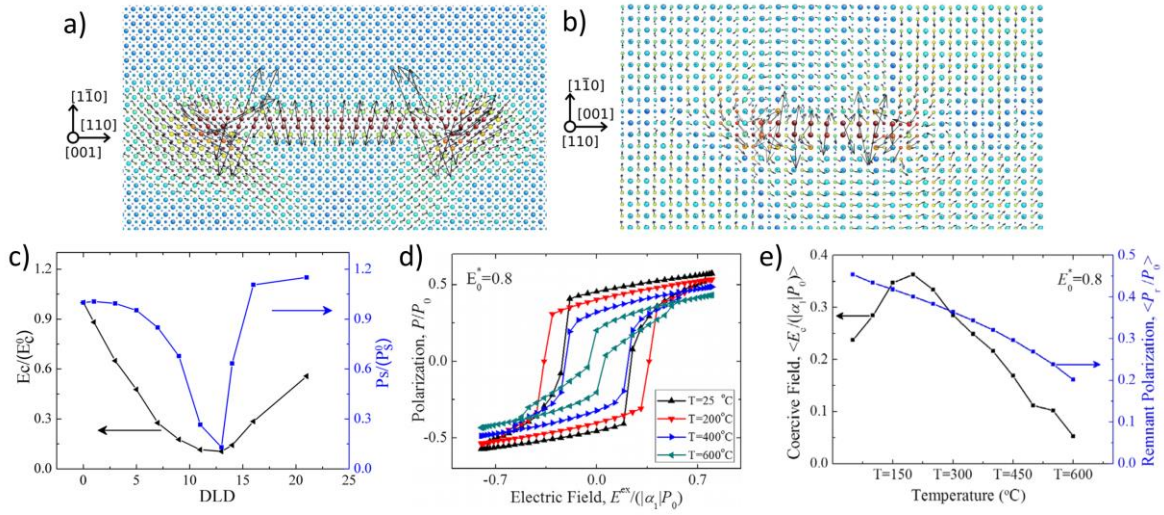

Figure 2.24: Simulated local polarization fields around an (a) edge dislocation and (b) a screw dislocation [95]. c) The coercive field and remnant polarization are presented as a function of the dislocation line density, normalized to the values of DLD = 0 [38]. d) Polarization depicted as a function of the dimensionless applied electric field for different temperatures [37]. e) The coercive field and remnant polarization are given as a function of temperature based on the hysteresis loops in d) [37]. Adapted or reprinted from Ref. [37, 38, 95], with permission from AIP Publishing and IOP Publishing; copyright (2015) by the American Physical Society.

The effect of dislocations on the domain structure and hysteresis loops depends on, among other parameters, the dislocation linear density (DLDs, similar to dislocation density) [36], dislocation character [34, 38], domain type [35] and temperature [37].

The DLD of a dislocation array with a Burgers vector of $\vec{b} = \frac{\Delta x_1^*}{2}[100]$ in $PbTiO_3$ single crystal [38] affects not only the stress field of the dislocation array but also the domain structure, shape of the polarization hysteresis loop [38], coercive field and remnant polarization [37]. In a dislocation-free single crystal, new domains nucleate, and domain walls move during the switching process homogeneously. In contrast, in a crystal with dislocations, a multi-domain state is reached. Some, but not all, domains are pinned at the dislocations, and under certain conditions, the dislocation stress field favors domain nucleation and leads to inhomogeneous switching behavior. As a result, remnant polarization and the coercive field decrease until a minimum is reached (at DLD = 13, see Figure 2.24c) and afterwards, with increasing DLD, both parameters increase [38].

The coercive field and remnant polarization are affected by all types of dislocations. During ferroelectric polarization switching in $Pb(Zr,Ti)O_3$ thin films, an attraction of the 180° domains towards the dislocation in the positive switching branch and a repulsion in the negative switching branch were observed in TEM [35]. It was emphasized that non-180° domain walls most likely provide a larger elastic interaction owing to the ferroelastic contribution [35]. The relative orientation of the stress fields around the different dislocation types and the polarization result in a decrease or an increase in remnant polarization and a reduction in the coercive field (e.g., more nucleation sites) [49]. The hysteresis behavior was investigated for stationary misfit dislocations (interface dislocations) and threading dislocations [225, 226] with a Burgers vector of $\vec{b} = \langle 100 \rangle$ and $\vec{b} = \langle 1\bar{1}0 \rangle$. The dislocations were introduced periodically into a cubic perovskite film [33]. A decrease in average polarization, and changes in remnant polarization and the coercive field were detected spatially and at high temperatures, owing to stress relaxation caused by interfacial dislocations [34].

Simulation predicts the formation of hysteresis loops even far above the Curie temperature, which indicates that dislocations stabilize the ferroelectric phase at higher temperatures [37] as it was experimentally shown by Qi et al. for $KNbO_3$ [31] and simulated for thin films [49]. The maximum polarization and remnant polarization decrease with increasing temperature, as shown in Figure 2.24d and Figure 2.24e (DLD = 21). Notably, the behavior for remnant polarization varies with maximum applied electric field amplitude, which indicates that the coupling is more complex [37]. The coercive field increases when the temperature increases from RT to a critical temperature and decreases with further increasing temperature (Figure 2.24e). Such a temperature trend is contrary to dislocation-free materials and thus, is attributed to the pinning of domains by the dislocation arrays until a certain threshold temperature is reached [37].

On the one hand, a high dislocation density (or DLD) favors the nucleation of domains during phase transitions, leading to a higher domain wall density. On the other hand, dislocations pin domains, which could hinder ferroelectric switching [95]. These competing mechanisms for the switching behavior are associated with the dislocation characteristics, density and strength of the coupling between dislocations and domain walls. This has already been emphasized by phase-field simulations and led to the assumption that the role of dislocations could be material dependent and, most likely, related to phase structure [95, 220].

3 Concept and Aim

Little is known on the plastic deformability of bulk ferroelectrics and the interaction between dislocations and domain walls on a macroscopic scale. Thus, in this work, the following topics are addressed:

1. Plastic deformability of ferroelectric perovskite single crystals
2. Dislocation-induced changes of domain structures
3. Modification of dielectric and electromechanical response at a macroscopic scale due to activation of dislocation slip systems
4. Effect of competing creep mechanisms in polycrystalline ferroelectric on microstructure and functional properties.

In the first part of this thesis, the deformability, introduction of dislocations and characterization of the resulting microstructure are discussed. For this purpose, single-crystalline $KNbO_3$ was used because it is one of the rare perovskite materials plastically deformable at RT. In addition to improving the degree of plastic deformation and identifying critical deformation parameters, the variation of orientation was also considered. On the basis of different degrees of deformation, the dislocation structure, slip bands and domain configurations were analyzed with complementary characterization methods. $KNbO_3$ is a good material of choice for deformation studies, but it is inferior to other ferroelectrics such as $BaTiO_3$, partly because of its hygroscopic nature and more complex orthorhombic structure.

Therefore, ⟨001⟩-oriented $BaTiO_3$ single crystals were chosen to investigate the dislocation-based modifications in dielectric and electromechanical properties. Unlike $KNbO_3$, $BaTiO_3$ tends to crack severely at RT, when a mechanical uniaxial compressive load is applied over the entire sample. Indentation introduces dislocations, and domain formation can be studied, but higher temperatures are required for a more detailed understanding of the dislocation-based functionality. Therefore, high temperature creep was the method of choice. Creep experiments allow not only the introduction of dislocations into $BaTiO_3$ but also the study of domain patterns before and after deformation and the study of changes in the extrinsic domain wall contribution. Thus, a study of the extrinsic domain wall contribution was used to investigate the pinning of domain walls by dislocations on a macroscopic scale.

Next, the thesis provides an outlook on high-temperature plastic deformation of ⟨110⟩-oriented $BaTiO_3$ single crystals to gain a deeper understanding of the deformation mechanism in $BaTiO_3$ and pave the way for further coarse-grained polycrystalline deformation experiments.

The last section includes the transition from single crystalline creep to polycrystalline creep. From an application point of view, polycrystalline materials are more economically suitable. Thus, the applicability of the dislocation concept is discussed for fine-grained $BaTiO_3$. For this purpose, a deformation map was constructed, and the influence of the different regimes on the structure and dielectric and electromechanical behavior was investigated.

4 Materials and Methods

4.1 Materials

4.1.1 Single Crystals: $BaTiO_3$ and $KNbO_3$

High-purity top-seeded solution-grown $BaTiO_3$ and $KNbO_3$ single crystals with dimensions of $4\times4\times8$ mm³ were purchased from FEE GmbH, a division of Electro-Optics Technology GmbH (Germany). The tetragonal $BaTiO_3$ single crystals were oriented along the 8-mm axis either in the $\langle001\rangle_{pc}$ direction or in the $\langle110\rangle_{pc}$ direction, respectively. $KNbO_3$ single crystals were oriented along the 8-mm axis in $\langle010\rangle_{pc} = \langle010\rangle_{ortho}$ or $\langle101\rangle_{pc}$ directions. The single crystals were polished to optical grade on four or six sides by the supplier. The crystallographic planes and directions are given in this thesis for both $KNbO_3$ and $BaTiO_3$ single crystals in pseudocubic notation.

4.1.2 Polycrystalline $BaTiO_3$

The polycrystalline $BaTiO_3$ powder was prepared via the conventional solid-state reaction. The starting powders were TiO_2 (purity ≥ 99.6%, Sigma-Aldrich, USA) and $BaCO_3$ (purity ≥ 99.8%, Sigma-Aldrich, USA). TiO_2 and $BaCO_3$ were mixed according to the stoichiometric formula and ball-milled for 12 h with ethanol and zirconia balls in a planetary ball mill (Fritsch Pulverisette 5, Germany). Afterwards, the powders were dried, calcined at 1100 °C for 6 h and re-milled for 24 h. Cylindrical green bodies were pressed with a die of 6.5-mm diameter and compacted under 200 MPa using a cold isostatic press (KIP 100E, Weber, Germany). The samples were sintered at 1350 °C for 6 h.

Cylindrical samples with a diameter of about 4.8 mm and a height of 16.5 mm were produced (Figure 4.1). Each cylinder was cut into two smaller ones using a diamond wire saw, and the diameter was reduced to 4 mm ± 0.05 mm using a lathe. Plan-parallel samples with a final height of 8 mm ± 0.02 mm were ground to ensure a homogeneous stress distribution between the sample and the pressing dies during the creep experiments. After the creep experiment, the sample was cut into several pellets (t = 1 mm), electroded and electrically measured together with the reference samples (as indicated in Figure 4.1c; modified from Ref. [227]).

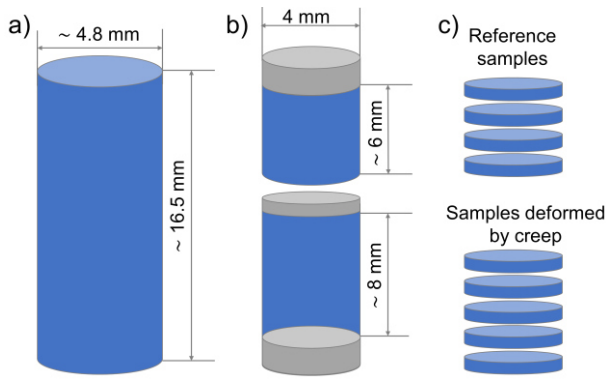

Figure 4.1: Schematic of the sample preparation for creep experiments on polycrystalline $BaTiO_3$.

Powders were provided by Lalitha Kodumudi Venkataraman. Sample preparation and creep experiments were carried out by Pengrong Ren. Data analysis, discussion and interpretation were performed jointly.

4.2 Plastic Deformation and Creep Experiments

The plastic deformation and creep tests were carried out under compression using a screw-driven load frame (Z010, Zwick GmbH & Co. KG, Germany) equipped with a linear variable differential transducer (LVDT) for displacement measurement. Two different materials were used for the pressing dies, depending on the temperature range. Experiments between ambient temperature and 300 °C were performed using a set of tungsten carbide (WC) dies (Figure 4.2a). Above 800 °C, the Al_2O_3 setup (Figure 4.2b) was used, due to the temperature stability of alumina. An integrated furnace (LK/SHC 1500-85-150-1V-Sonder, HTM Reetz GmbH, Germany) was placed around the experimental setup, marked with red dashed lines in Figure 4.2a and Figure 4.2b. Platinum foils (at high temperatures) and PTFE (Teflon tape; at room temperature) were placed between the sample and the pressing dies to reduce friction and reduce the cracking of the samples.

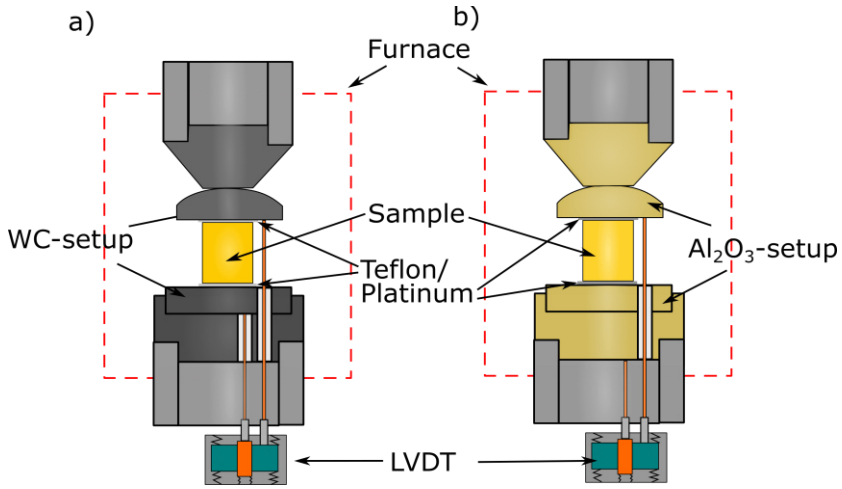

Figure 4.2: Schematic of the deformation setups consistent of WC pressing dies at ambient temperature (a) and Al_2O_3 dies for high-temperature experiments (b). The use of Teflon or platinum is optional.

The samples were positioned with centering tools to achieve a precise alignment. A preload was applied to ensure contact throughout heating, testing and cooling. The preload was 20 N (1.2–5 MPa) for the single crystals and polycrystals. This chosen value was as low as possible to avoid ferroelastic switching and cracking during the application of the preload, but it was high enough to have a constant contact between the sample and the pressing dies.

The stress σ and strain γ data presented in the experimental section are given as engineering stresses and strains. In the results and discussion section, they are converted to true stresses and true strains according to Equations 4-1 and 4-2 [228], where F is the applied force, A_0 the initial area, Δl the length difference and l_0 the initial length of the sample.

$$\gamma_{true} = -\ln\left[1 - \frac{\Delta l}{l_0}\right] \qquad 4\text{-}1$$

$$\sigma_{true} = \frac{F}{A_0}(1 + \gamma_{eng}) \qquad 4\text{-}2$$

4.2.1 Deformation Experiments on $KNbO_3$ Single Crystals

$KNbO_3$ single crystals were deformed in the loading frame equipped with tungsten carbide dies. The single crystals were deformed with a displacement rate of 1.9–8 μm/min at room temperature (RT), corresponding to an initial strain rate of $8.3 \cdot 10^{-6}$ 1/s and $1.7 \cdot 10^{-5}$ 1/s, respectively. Teflon tape was inserted between the tungsten carbide pressing dies and the sample (as indicated in Figure 4.2a) to avoid friction due to shear and to counteract small misfits in surface roughness. The $KNbO_3$ single crystals were deformed in either [010] or [101] orientation. The [010] samples had a geometry of about 4×4×8 mm³ and the [101] samples of about 4×4×4 mm³. For the [101] samples, a [010] single crystal of 4×4×8 mm³ was cut into two pieces, polished and deformed along the [101] orientation.

A typical RT deformation experiment for $KNbO_3$ can be divided into five regions, given in Figure 4.3a for a deformation in the [010] direction (see schematic in Figure 4.3b). In the first step (I), a preload of 20 N was applied for several seconds to a few minutes to ensure proper contact between the sample and the dies. This step is a safety step to ensure the system is working properly. In regions II and III, the sample was loaded at a displacement rate of 1.9–8 μm/min. The deformation parameters for selected samples are given in Table 4.1. The measurement was stopped manually (end of the region III) after a certain initial strain value (more precisely, a certain LVDT-displacement value) was reached. Region IV is a special feature of the loading frame and enables one to stop the measurement (fixed position of the pressing tool), while data points are still recorded during the relaxation of the sample at constant cross-head position. Severe cracking often occurs during unloading. Therefore, this relaxation is a gentle unloading procedure. As soon as the material-dependent load decrease slowed down, Step V with a controlled unloading rate began. This step was either load-controlled with 0.2–1 N/s or displacement-controlled with 8 μm/min.

The critical compressive stresses were determined according to the $R_{p0.2}$-criterion, describing the stress at which 0.2% plastic deformation was reached [85]. The true plastic strain values were obtained by subtracting the elastic strain values at $R_{p0.2}$ from the maximum total strain values at the end of the applied force plateau (i.e., the end of Step III).

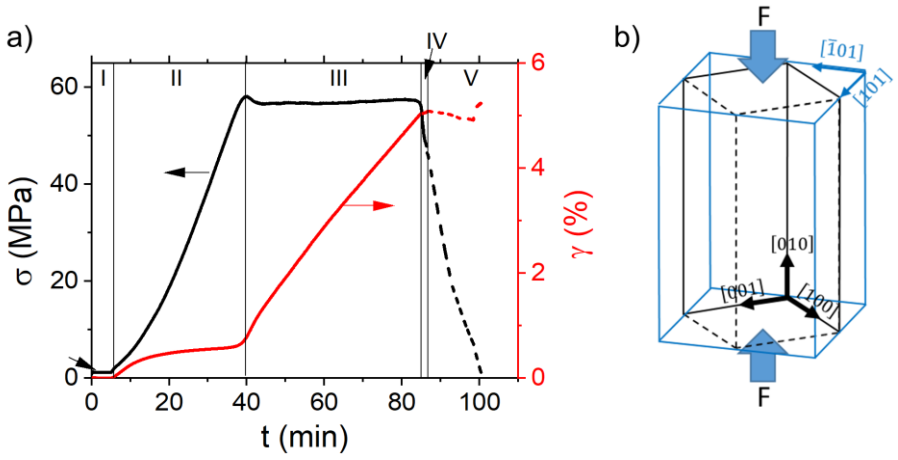

Figure 4.3: Typical deformation experiment for $KNbO_3$ at room temperature (sample KN-010-3).

Table 4.1: Room temperature deformation of $KNbO_3$ single crystals. The samples are named after the material (KN = $KNbO_3$) and the deformation direction (010 = ⟨010⟩ and 101 = ⟨101⟩). The numbering of the samples is sorted by strain rate.

Sample	Orientation	Loading rate (μm/min)	Strain rate (1/s)
KN-010-1	⟨010⟩	4	$8.3 \cdot 10^{-6}$
KN-010-2	⟨010⟩	4	$8.3 \cdot 10^{-6}$
KN-010-3	⟨010⟩	4	$8.3 \cdot 10^{-6}$
KN-010-4	⟨010⟩	8	$1.7 \cdot 10^{-5}$
KN-010-5	⟨010⟩	8	$1.7 \cdot 10^{-5}$
KN-101-1	⟨101⟩	1.9	$8.3 \cdot 10^{-6}$
KN-101-2	⟨101⟩	3.8	$1.7 \cdot 10^{-5}$

The influence of commercial PTFE (Teflon) as protective layer on the RT deformation results is discussed in the following paragraph. An Al_2O_3 reference sample was compressed with and without Teflon tape on top and on bottom of the sample (Figure 4.2a). In the first experiment, the Al_2O_3 reference (with and without Teflon) was loaded initial strain-rate-controlled with $1.7 \cdot 10^{-5}$ 1/s to 60 MPa, given in Figure 4.4. In the second experiment $8.3 \cdot 10^{-6}$ 1/s and a load of 30 MPa were chosen. The maximum loads correspond to the expected yield stresses of [010]-oriented $KNbO_3$ single crystals.

The contribution of the Teflon tape to the plastic strain rate was defined as the difference in strain between the experiment with and without Teflon under the same experimental conditions. This leads to a strain contribution of 0.15% and 0.38% for prior slightly or non-stretched Teflon tape. The majority of the strain contribution took place in the low-stress range, 0–20 MPa. This result leads to two conclusions. First, the plastic strain values are not directly affected because the Teflon contributes mainly to the non-linear low stress and linear elastic stress region. Second, the Teflon compression and ferroelastic switching take place in the same stress region. Therefore, a superposition of both strain contributions impedes a clear separation of the two processes. To reduce this strain contribution, the Teflon tape was stretched prior to the $KNbO_3$ deformation experiments. Despite the additional strain contribution, Teflon protects the sample surface from surface damage.

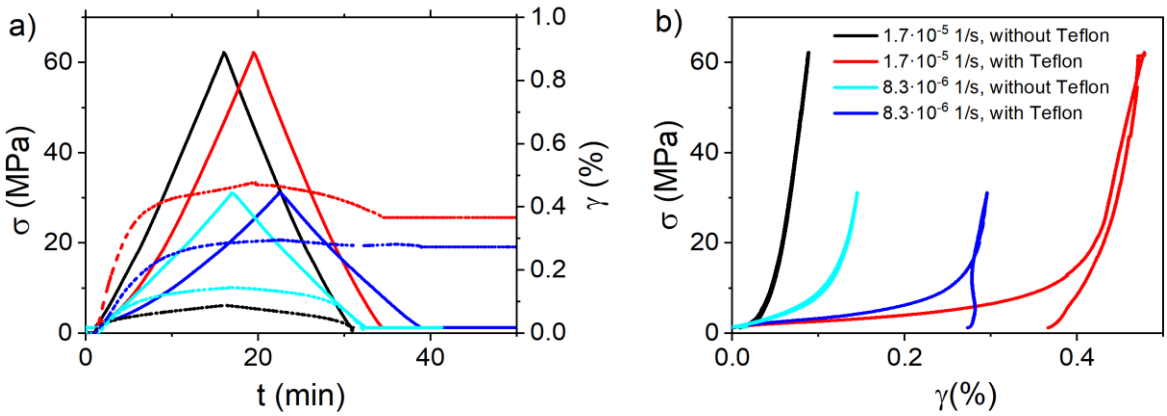

Figure 4.4: Reference experiments on Al_2O_3 to evaluate the influence of Teflon. a) Stress (strain) as a function of time and (b) stress-strain curve for compression experiments with a strain rate of $1.7 \cdot 10^{-5}$ 1/s and $8.3 \cdot 10^{-6}$ 1/s, in agreement with $KNbO_3$ deformation strain rates.

Without Teflon (Figure 4.5a), the surface is covered with grooves, non-controlled indents and scratches which come from the contact with the WC dies. Such features can be avoided with use of Teflon. More important is, that after deformation slip bands are visible on the bottom and top surface of the sample, as indicated in Figure 4.5b.

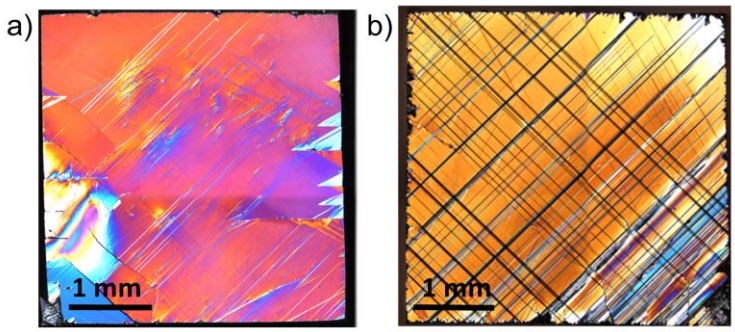

Figure 4.5: Differential interference contrast optical light microscopy images of the top surface after compression along the [010] axis of a $KNbO_3$ single crystal without (a) and with (b) Teflon as a protection layer.

4.2.2 Deformation Experiments on $BaTiO_3$ Single Crystals

4.2.2.1 Creep Experiments on $BaTiO_3$ Single Crystals

High-temperature (HT) creep experiments were performed on [001]-oriented $BaTiO_3$ single crystals using the Al_2O_3-setup at temperatures of 1050 °C and 1150 °C with a cooling and heating rate of 1 K/min. The temperatures were chosen with respect to the device temperature limit of 1200 °C. Microcrack formation was reduced by the use of protective platinum foils at contact areas and low heating and cooling rates.

The high-temperature experiment can be divided into seven regions, as shown in Figure 4.6. In the first region, a constant compression pre-load of 1.2–1.3 MPa (20 N) was applied to maintain contact between samples and dies during heating at 1 K/min. On the one hand, this pre-load was crucial to avoid sample damage due to thermal expansion of the setup and the sample, which would lead to an uncontrolled increase of force. On the other hand, the contact between sample and die could be lost without the pre-load, due to the phase transition into the cubic phase and the resulting change in the sample geometry. In the second region, the set temperature was reached and kept constant for 20–30 min to ensure a temperature equilibrium in the surrounding of the sample. The compressive stress was kept constant at 1.2–1.3 MPa (20 N). Afterwards, the force was increased in a manner either displacement controlled, corresponding to an initial strain rate of $8.3 \cdot 10^{-6}$ 1/s or force controlled with 0.2 N/s until a compressive stress of 20–50 MPa was reached (see Table 4.2). The actual experiment (Step IV) started as soon as the set load was reached. The compressive load was kept constant for 1–4 h at constant temperature in Step IV. In Step V the applied force was maintained during cooling at 1 K/min until a temperature of approximately 1000 °C was reached (t_{cool}= time span for cooling in Step V). Step V should minimize recovery of the dislocations and avoid the elimination of dipoles, which would lead to the annihilation of the dislocations [108]. At lower temperatures (Regions VI and VII), the force was released in a force-controlled manner with 0.2 N/s and a pre-load of 1.2–1.3 MPa (20 N) was kept until the system cooled at 1 K/min to RT. A safety protocol was followed for each measurement to protect the setup from damage. This protocol included a measurement stop, to be carried out if a force-drop of $\Delta F = \pm 30$–50% or a displacement drop of Δl = 2–4 mm was reached. The limitations were chosen according to the sample geometry (max. 50% of the sample height), including a buffer for thermal heating and the setup accuracy.

Reference sample “reference 1150 °C” was placed on a platinum foil in the Zwick furnace (no load applied) and thermally treated at 1150 °C for 3 h to exclude an influence of the heating on the measurement results.

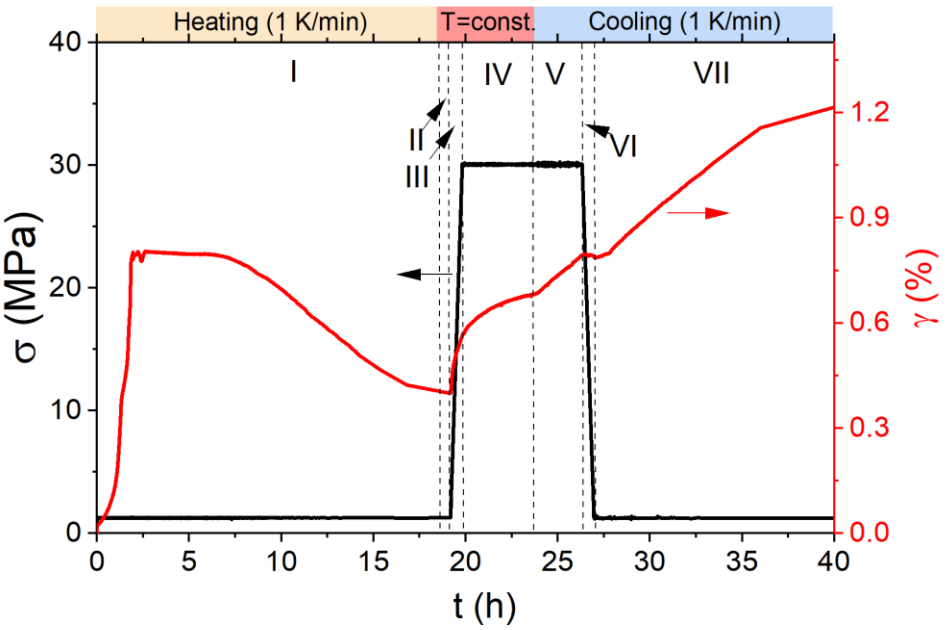

Figure 4.6: Creep experiment can be divided into seven regions (I–VII). Region IV is the actual creep experiment.

A typical HT-experiment takes at least 39 h, which is beyond the data storage capacity of 100,000 data points. In the range of 99,900 data points (already reached in the heating region), the system drastically increases the time interval between the data points. This increase leads to the loss of the most relevant data points during the creep experiments. To avoid such data loss, the experiment was divided into two partial experiments. The first was stopped after the equilibrium temperature was reached (region II), and the second part was started immediately after the first one was stopped.

Table 4.2: High-temperature creep experiment parameters for selected $BaTiO_3$ single crystal samples in [001] orientation. Only parameters for the loading (Step III), actual experiment (Step IV) and time during cooling at constant set stress (Step V) are provided. The samples are labeled according to the deformation process (C for creep), the set temperature and the maximum applied initial stress.

Sample	**T (°C)**	**Loading condition**	**Applied initial load (MPa)**	**Holding time** $t_{T=const}$ **+(**t_{cool}**)**
C-1050-30	1050	0.2 N/s	30	2 h (50 min, 1000 °C)
C-1150-20	1150	4 µm/min	20	1 h (/)
C-1150-30-1	1150	0.2 N/s	30	2 h (150 min, 1000 °C)
C-1150-30-2	1150	0.2 N/s	30	4 h (50 min, 1000 °C)
C-1150-35	1150	0.2 N/s	35	2 h (150 min, 1000 °C)
C-1150-40-1	1150	0.2 N/s	40	3 h (250 min, 900 °C)
C-1150-40-2	1150	0.2 N/s	40	4 h (150 min, 1000 °C)
C-1150-50	1150	0.2 N/s	50	4 h (150 min, 1000 °C)
Reference 1150	1150	/	/	3 h (/)

4.2.2.2 Plastic Deformation Experiments at High Temperatures (Orientation-dependent)

Compression experiments were carried out on [001]-oriented and [110]-oriented $BaTiO_3$ samples at 1150 °C (at a heating rate of 1 K/min), to determine the stress at which the yield stress or the fracture stress is reached.

The heating procedure was identical across Regions I and II of Figure 4.6. The load was increased until either the predefined force was reached, a plastic deformation of several percentages was reached, or the sample broke (**A** in Figure 4.7 for [110] orientation). Region **B** in Figure 4.7 corresponds to a measurement sequence whereby the position of the loading head is fixed and the sample shows relaxation behavior. After the relaxation, the force was reduced with a constant loading rate (not presented in Figure 4.7). The loading and unloading took place at constant temperature.

In contrast to the creep experiments, no platinum was used in this experiment, and considerably higher force was applied. The samples had a geometry of 2×2×4 mm^3. This geometry is more economical, which was important due to a delivery bottleneck. Additionally, higher loads could be applied due to the smaller sample area. The disadvantages were that the alignment and centering of the sample were more difficult and that more samples showed severe cracking due to the missing protective layer of platinum.

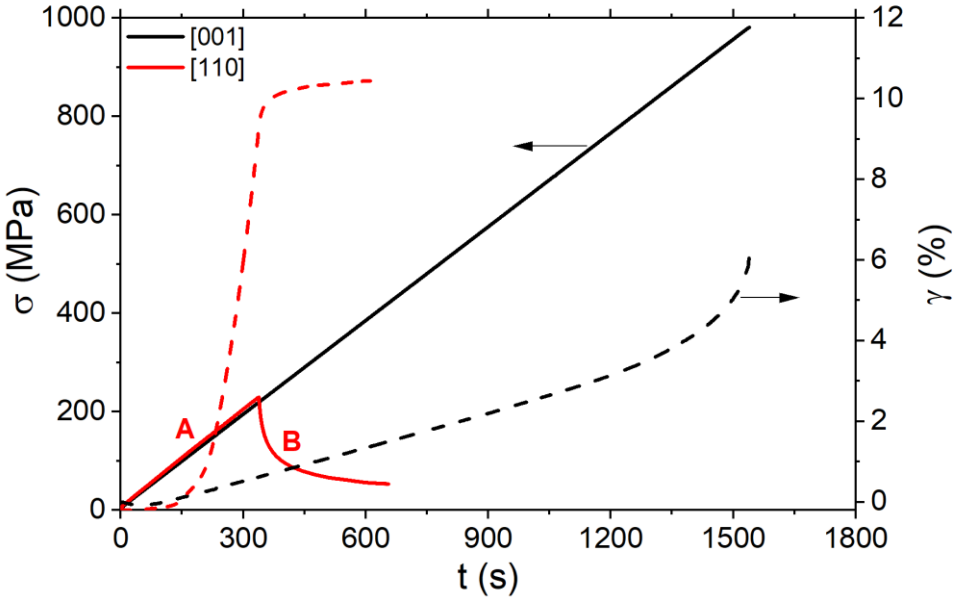

Figure 4.7: High-temperature deformation experiment for a [001]- and a [110]-oriented $BaTiO_3$ single crystal. The [100] curve (black) stopped due to sample failure. Strain as a function of time curves are given as dashed lines. The continuous lines are the corresponding stress curves. At **A**, the compressive stress increases constantly. In **B**, the cross-head position was maintained.

4.2.2.3 Plastic Deformation at High Temperatures on [110]-Oriented $BaTiO_3$

Stepwise deformation experiments (stress-intervals, Figure 4.8) were carried out for [110]-oriented $BaTiO_3$ single crystals to determine the strain rate at different stress levels. The load was increased by 2 N/s, and the time spans decreased with increasing load to avoid failure of the sample. The chosen step loads are listed for 1100 °C, 1150 °C and 1170 °C in Table 4.3. For

these experiments, the Al_2O_3 dies were used without platinum. The sample geometry was $2\times2\times4\ mm^3$.

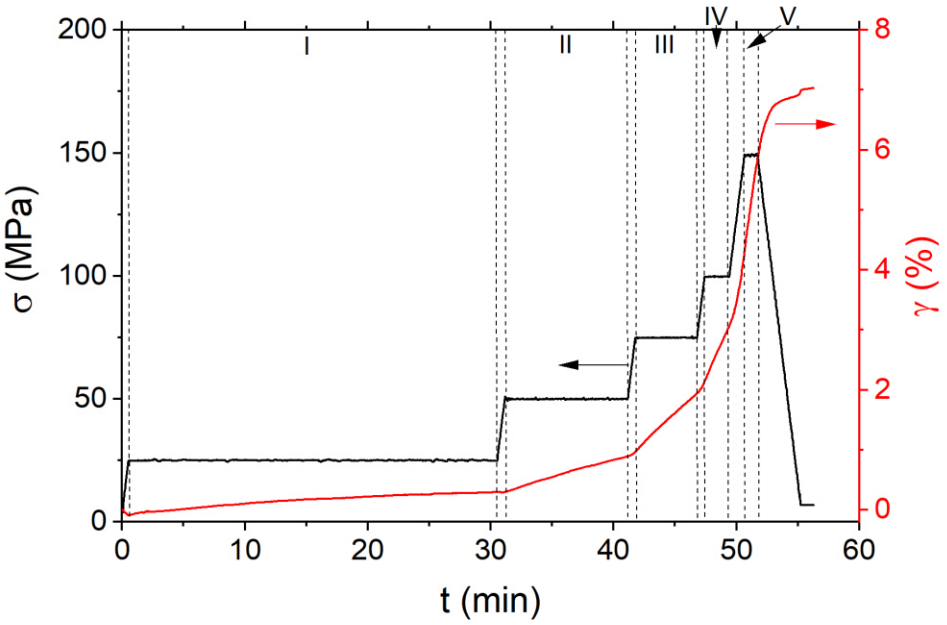

Figure 4.8 Stepwise experiment with 2 N/s at 1150 °C for a [110]-oriented $BaTiO_3$ single crystal.

Moreover, deformation experiments with a constant initial strain-rate of 10^{-4} 1/s, 10^{-5} 1/s or constant load-rates of 0.5 N/s and 1 N/s were carried out at 1150 °C.

Table 4.3: Stepwise deformation experiments for 1100 °C, 1150 °C and 1170 °C. The samples are labeled based on the deformation procedure (D: Deformation, S: Stepwise), compression direction [110] and set temperature.

Sample	T (°C)	Step I (MPa)	Step II (MPa)	Step III (MPa)	Step IV (MPa)	Step V (MPa)	Step VI (MPa)
DS-110-1100	1100	-	-	-	100	150	200
DS-110-1150	1150	25	50	75	100	150	-
DS-110-1170	1170	25	50	75	100	-	-

4.2.2.4 Influence of Platinum

Platinum foils with a thickness of 0.11–0.16 mm were used to protect the surface from damage and to counteract small misfits in the sample roughness. Without platinum, the sample surface was heavily damaged during the loading experiment, due to the different hardness of $BaTiO_3$ and Al_2O_3 and the slight irregularities at the contact area. Furthermore, the cleavage of the sample and the complete destruction of the samples were observed several times without the usage of platinum, especially for the [001] orientation. The disadvantage was that platinum creep occurred at high temperatures and affected the initial strain values (Figure 4.9). The creep of platinum results in a plastic strain of approximately 0.5% after 4.5 h at 40 MPa, and it flattens the slope of the stress-strain curve of Al_2O_3 in the linear stress regime (Figure 4.9b). A comparison between the sample geometry before and after deformation was not feasible,

because the sample and the platinum stuck together after the creep experiment and the samples had to be cut out.

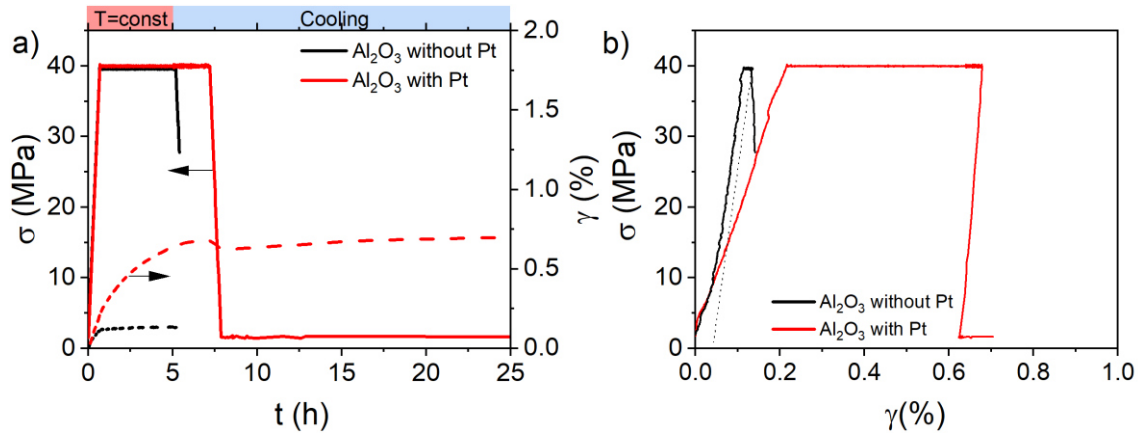

Figure 4.9: Reference creep experiment on Al_2O_3 without and with platinum. a) Stress and strain curves as a function of time. b) Stress as a function of strain curve with and without Pt.

4.2.3 Creep Experiments on Polycrystalline $BaTiO_3$

The creep study can be separated into two parts. In the first, the different creep mechanisms were determined, to construct a map of deformation mechanisms. In the second, the knowledge gained from that map was used to deform the cylindrical samples at a certain stress and constant temperature and to investigate how the selected creep regimes influence the microstructure and electrical properties. For both parts, the Al_2O_3 dies were used without platinum, and a pre-stress of approximately 1.6 MPa (20 N) was applied during heating at 5 K/min, to prevent damage of the sample due to thermal expansion. The target temperature was above $0.5 \cdot T_c$ [106] and was maintained for 30 min to ensure temperature equilibrium.

Interval experiments to determine the deformation map were carried out at temperatures of 950 °C, 1000 °C, 1050 °C and 1100 °C, respectively. The uniaxial compressive stress was increased in 25 MPa steps from 100 MPa to 225 MPa with a loading rate of 1 MPa/s. Each interval was held for 30 min. Afterwards, the stress was sustained until the temperature was decreased to 1000 °C to minimize the recovery and annihilation of the dislocations [108]. Finally, the samples were cooled to RT with an applied stress of 1.6 MPa.

The single-stress experiments were carried out at 1000 °C for 15 min and at 1050 °C for 15, 22 and 30 min, respectively (labeled as 'PC-1000-15', 'PC-1050-15', 'PC-1050-22' and 'PC-1050-30'; PC: polycrystalline creep). A load of 200 MPa was applied for all samples, with a loading rate of 1 MPa/s, and maintained for at least 15 min to ensure that the steady-state creep regime could be reached. The chosen temperatures, times and stress levels provide a balance between increasing the dislocation density [108], avoiding vast cavitation or cracking, and reducing the probability of grain growth.

The creep experiments were performed on polycrystalline $BaTiO_3$ together with Pengrong Ren.

4.3 Microstructural Investigations

4.3.1 Laue Diffraction

The *back-scattering Laue method* was applied to confirm the orientation of the single crystals. Single crystals were mounted on a goniometer head (Type 1001, Huber Diffraktionstechnik GmbH & Co. KG, Germany) and placed at a distance of approximately 32–34 mm in front of the image plate (or charge-couple-device (CCD) camera), as indicated in Figure 4.10. Silver or Molybdenum was used as an X-ray source. A collimator with a diameter of 0.5 mm was mounted to bundle the beam and transform it into a parallel beam before it hits the single crystal.

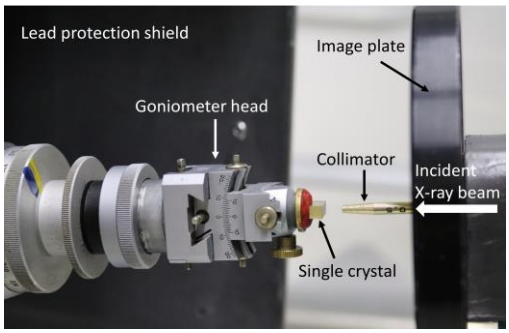

Figure 4.10: Laue setup with goniometer head, collimator and image plate. The X-ray source is located outside of the viewer's field to the right.

The back-scattered Laue pattern was collected with the image plate or a CCD camera. The image plate was read out with a scanner (CR 35 Bio, Dürr Medical, Dürr NDT GmbH & Co. KG, Germany) through the "CR Scan Config" software, and it was post-processed with ImageJ. For the Peltier-cooled CCD camera, the "Artemis Capture" software was used, and the images were post-processed with ImageJ. The orientations were determined with the Cologne Laue Indexation Program (clip). To achieve good contrast, a current of 38 mA and a voltage of 25 kV were applied for $BaTiO_3$ single crystals, and 16 mA and 16 kV, for $KNbO_3$.

4.3.2 Light Microscopy

Optical light microscope (OLM) images were taken either with a 3D-Laser-Scanning microscope (LEXT OLS4100, Olympus, Japan) or an OLM (Zeiss Axio Imager2, Zeiss, Germany). Overview pictures of the 4×4×8 mm^3 samples were taken with a stitching (LEXT) or tiles mode (Zeiss) to capture images of the whole single crystal before and after deformation. For the polarized light pictures, a differential interference contrast (U-DICR, Olympus) or a circular differential interference contrast (C-DIC [229], Zeiss) and a polarizer were used. Due to the combination of several images into one, some of the differential interference contrast (DIC) images have artificial horizontal and vertical lines. These lines are equally distributed and are unrelated to the domain structure.

Temperature-dependent light microscopy was performed with an optical microscope (PSM1000, Motic, Hong Kong) equipped with a temperature-controlled stage (THMS 600 System, Linkam Scientific Instruments, UK). Thin $KNbO_3$ samples with {101} surface were cut and polished to an optical grade and heated from room temperature up to 600 °C at a heating rate of 1–2 K/min. Images were taken during heating and cooling.

4.3.3 Secondary Electron Microscopy and Electron Channeling Contrast Imaging

Scanning electron microscopy (SEM) investigations were conducted with a Philips XL30 FEG (Philips, Germany). The polycrystalline $BaTiO_3$ samples were ground and polished to a 0.25 μm finish, thermally etched at 1250 °C for 10 minutes and investigated in secondary electron imaging mode (SE). $KNbO_3$ single crystals were etched with a concentrated solution (volume ratio 1:2)[222] of ammonium acetate in water (7.4 g CH_3COONH_4, 4.99 g distilled H_2O) and hydrogen peroxide (H_2O_2) for 1 h and investigated in SE-mode.

In *Electron channeling contrast imaging* (ECCI) the change in the backscattered electron intensity with changing crystallographic orientation is used to capture the image of the sample [230, 231]. Dislocations cause a local disruption of the crystallographic orientation and can therefore be visualized with ECCI. For $BaTiO_3$ and $KNbO_3$ single crystals, ECCI was performed using a MIRA3-XMH SEM (TESCAN, Czech Republic) equipped with a four-quadrant solid-state backscattered secondary electron (BSE) detector (DEBEN, UK). The channeling contrast was maximized by tilting the sample and rotating it to an intensity minimum corresponding to the backscattered Kikuchi pattern acquired with a rocking beam.

The ECCI experiments were carried out by Enrico Bruder (PhM, TU Darmstadt).

4.3.4 Piezoresponse Force Microscopy

Piezoresponse force microscopy (PFM) was carried out with an MFP-3D AFM (Asylum Research, Oxford Instruments, United Kingdom) to determine the changes in the domain structure due to plastic deformation. Changes in the surface topography cause a deflection or torsion of the tip, leading to a relative displacement of the laser signal on the photo detector. With this signal, the topography can be determined with an atomic force microscope (AFM), but irregularities on the surface are also emphasized in the deflection image (derivative of the topography). Such irregularities can be surface steps caused by plastic deformation or scratches. In the dual AC-resonance tracking (DART) mode of the PFM, an electric field is applied on the tip to track the domain reaction beneath the tip. Extension and contraction of the domains can be measured in the vertical (bending of the tip) and lateral direction (torsion of the tip) with this method. The response is afterwards transferred to amplitude and phase signals, based on the local piezoelectric response (amplitude) and the orientation of the spontaneous polarization (phase) [232].

Either the sample surfaces of the $KNbO_3$ single crystals were polished in-house or the sample surfaces were already polished to optical grade by the EOT GmbH prior to deformation experiments. For the in-house polishing, the surfaces were polished with different diamond pastes (6 μm, 3 μm, 1 μm and 0.25 μm), followed by a final polishing step with a non-crystallizing amorphous colloidal silica suspension (MasterMet2, 0.02 μm, Buehler, Germany). An AC sinusoidal signal was applied to measure the reference and deformed samples with an amplitude of 5–30 V and 345–360 kHz. To investigate the local domain switching, a DC field of +150 V was applied in a square of 30×30 μm^2 for an undeformed sample, with −150 V/+150 V for KN-010-2 (+150 V: 20×10 μm^2 and −150 V: 20×10 μm^2) and −150 V/+150 V for KN-010-4 (two triangles together forming an area of 30×30 μm^2). The PFM was operated mainly by

Matija Buljan, Mateo Miličevič and myself. Hana Uršič from the Jožef Stefan Institute in Ljubljana (Slovenia) supervised the PFM operation.

4.4 Electrical Measurements

The $BaTiO_3$ single crystals were mainly cut out of the middle part of the deformed 4×4×8 mm^3 single crystals to reach a final thickness of 0.5–1.2 mm. The area of the samples varies from 2.3 mm^2 to 16 mm^2, depending on the single crystal quality after deformation. Afterwards, the samples were annealed at 400 °C for 2 h at 1 K/min and sputtered with Au electrodes on the corresponding {010} faces. The electric fields were applied in the loading direction, and the samples were annealed at 200 °C for 2 h (1K/min) between individual measurements.

Sputtered Pt electrodes were used for polycrystalline $BaTiO_3$ samples. $KNbO_3$ single crystals were coated with Pt or Au.

4.4.1 Temperature, Electric Field and Frequency Dependent Electrical Properties

Electric-field-dependent and *frequency-dependent permittivity* data were recorded for [001]-oriented $BaTiO_3$ single crystals at room temperature with an impedance analyzer (Alpha Analyzer, Novocontrol Technologies, Germany) equipped with a 150 V amplifier. The measurements were carried out at 1 kHz in the linear or intermediate electric-field region (below E_c). The samples were measured in unpoled and poled states. For the electric-field-dependent permittivity measurements, $BaTiO_3$ samples were poled at 1 kV/mm for 10 min at RT.

The small-signal room-temperature permittivity of poled $BaTiO_3$ single crystals was measured with a lock-in amplifier (SR830, Stanford Research System, USA) [196]. The voltage was amplified by a voltage amplifier to provide an AC electric field, while signals were read out with a second lock-in amplifier. The LabVIEW program was written by Lukas M. Riemer and the measurements were performed at the École Polytechnique Fédérale de Lausanne (Group of Ferroelectrics and Functional Oxides, Prof. Damjanovic, EPFL, Lausanne, Switzerland) in parallel to the d_{33}* measurements.

The *temperature-dependent dielectric properties* of of $BaTiO_3$ single crystals were evaluated with a Precision LCR meter (HP 4284 A, Hewlett Packard, USA) and a switch control unit (HP 3488 A, Hewlett Packard) in the temperature range from RT and up to 160 °C. The environmental test chamber was equipped with an additional Pt100 resistance temperature detector (RTD), monitored by a multimeter (HP34401A, Hewlett Packard, USA). The frequencies were chosen in the range of 0.1 kHz to 800 kHz.

The temperature-dependent permittivity of the $KNbO_3$ single crystals and of the polycrystalline $BaTiO_3$ samples was determined at selected frequencies in the range between 100 Hz and 1 MHz with the HP 4284A LCR meter (Hewlett Packard Corporation, USA) equipped with a furnace (Nabertherm LE4/11/R6, Nabertherm GmbH, Germany). The undeformed and deformed $KNbO_3$ samples were measured from room temperature to 550 °C with an increase of 1 K/min, while the polycrystalline $BaTiO_3$ measurements were performed up to 250 °C at 2 K/min.

4.4.2 Electrochemical Impedance Spectroscopy (EIS)

Impedance measurements were carried out on polycrystalline $BaTiO_3$ with a Novocontrol Alpha-A High Performance Frequency Analyzer (Novocontrol Technologies, Germany) equipped with a tube furnace in a frequency range of 0.1 Hz to 3 MHz at 400 °C.

4.4.3 Large Signal Measurements

The *subcoercive field polarization measurements* were performed with a function generator (Agilent Technologies, USA) in combination with a voltage amplifier (Model 7602M Wideband, Krohn-Hite Corporation, USA), a charge amplifier (Type 5011, Kistler, Switzerland) and an oscilloscope (Tektronix 3014, Tektronix, USA). All measurements were completed at room temperature at the selected frequencies. The sine function (burst mode, 3 cycles) of the function generator was amplified by the voltage amplifier by a factor of 20. The bottom of the sample holder acted as contact. The oscilloscope recorded both the function generator signal and the charge amplifier signal, as schematically visualized in Figure 4.11a.

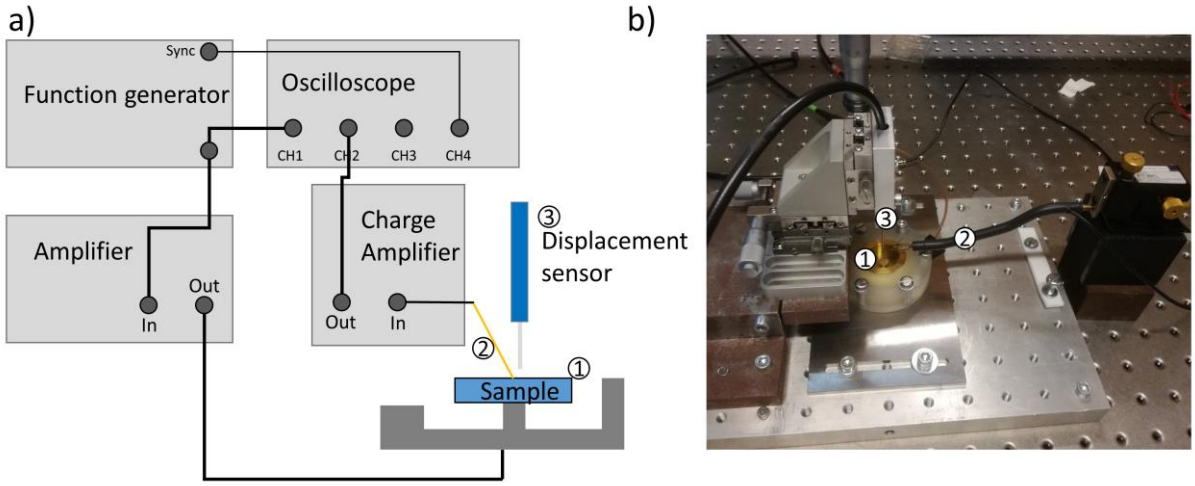

Figure 4.11: a) Schematic of the subcoercive field polarization setup with function generator, voltage amplifier, charge amplifier and oscilloscope. The displacement sensor is not used in this method and is, therefore, not in contact with the sample. b) Sample holder for the measurement. Setup and software were built and programmed by members of the "Group of Ferroelectrics and Functional Oxides" at the EPFL.

The *large-signal measurements* were performed at unpoled [001]-oriented $BaTiO_3$ single crystals with a modified Sawyer–Tower setup. A triangular DC signal is provided by a signal generator (33220A, Agilent, USA) and amplified by a TREK high-voltage generator (20/20C, Trek Inc., USA). The displacement was tracked simultaneously with a fiber optical displacement sensor (Philtec Inc., USA). $BaTiO_3$ single crystals were examined at 1 Hz in the range of 0.5 kV/mm to 3 kV/mm. Unipolar loops were investigated for polycrystalline $BaTiO_3$ samples at 10 Hz and 4 kV/mm.

The *piezoelectric coefficient,* d_{33}^* was determined for poled [001]-oriented $BaTiO_3$ single crystals with a lock-in amplifier (SR830, Stanford Research System, USA) combined with a voltage amplifier (Model 7602M Wideband, Krohn-Hite Corporation, USA). The polarization was either derived from a charge amplifier signal [196] or from the voltage measured across a resistor

connected in series to the sample. The displacement measurement of the samples was carried out with a displacement sensor (MTI 2000 Fotonic Sensor, MTI Instruments INC., USA). Signals were read out either with a lock-in-amplifier or an oscilloscope (Tektronix MDO 3014, Tektronix, USA). The sample holder in Figure 4.11b was also used. The setup was calibrated with a bismuth titanate (PZ46, Meggitt) reference sample prior to measurement. The $BaTiO_3$ single crystals were poled at 0.5 kV/mm for 20 min. The experiments were performed during my research visit at the EPFL.

5 Results and Discussion

5.1 Room-Temperature Deformation and Domain Structure of $KNbO_3$

5.1.1 Domain Structure of As-Received Single Crystals

All single crystals were oriented as indicated in the schematic in Figure 5.1a by the blue cuboid. In Figure 5.1b, a single crystal is shown for the deformation along the [010] axis, whereas Figure 5.1c corresponds to a single crystal deformed along the [101] axis. The respective orientation of the single crystals was confirmed by the back-scattering Laue pattern shown in Figure 5.1d and e.

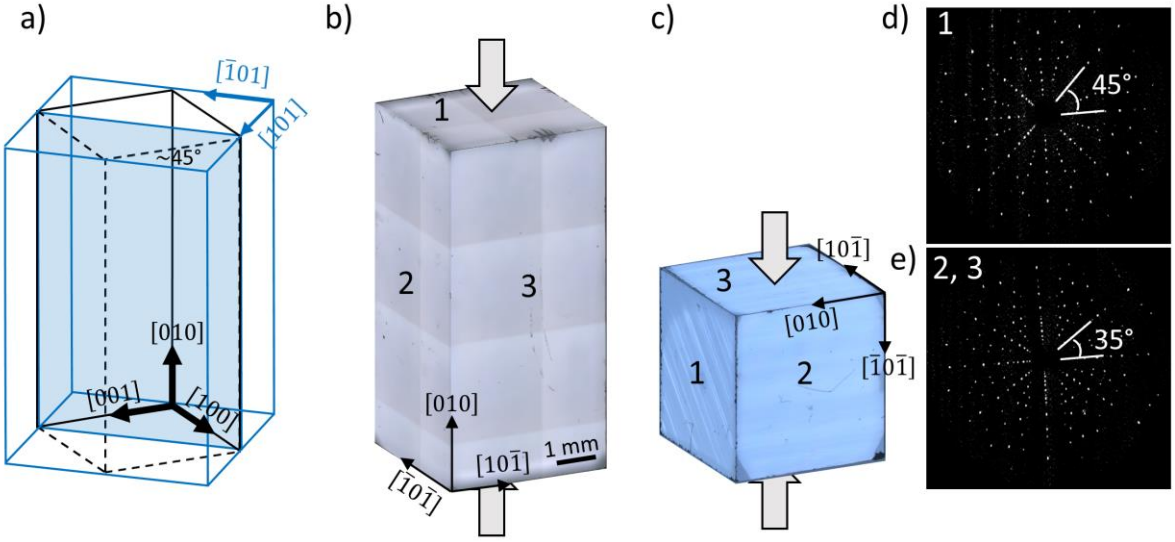

Figure 5.1: Single crystal orientation in the pseudocubic nomenclature (a). Confirmation of the $KNbO_3$ single crystal orientation prior to deformation along (b) the [010] direction and (c) the [101] direction with optical light microscopy. The deformation directions are indicated with grey arrows. The numbers 1-3 in (b) and (c) correspond to the Laue patterns in (d) [010] and (e) [101] [233].

The domain structure was documented for every single crystal before deformation (a selection is presented in Figure 7.1). Most of the initial single crystals had no visible domain structure, as indicated in Figure 5.2a, whereas a few had an obvious domain structure (Figure 5.2b and Figure 5.2c). Most of the domain walls were aligned parallel to the [010] direction, as highlighted in Figure 5.2d and Figure 5.2e with PFM. The PFM scan of a side face of undeformed KN-010-4 demonstrated that the change in topography contrast was accompanied by a change in PFM amplitude contrast. This finding emphasized that domain walls were located at the position of changed topography. Based on previous studies [234], it is known that ferroelastic domain walls result in a topographical change of the surface. Therefore, surface roughness in the nanometer range suggests non-180° domain walls. This was supported by the optical light microscopy images, which showed only non-180° domain walls. Another possibility is that the surface was chemically etched during the polishing process. The polishing suspension used by the single crystal supplier is unknown; nevertheless, own experiments have shown that $KNbO_3$ single crystals are not as sensitive to polishing suspensions as $BaTiO_3$. The fact that the as-received single crystals provided a height contrast in the nanometer range is important for subsequent considerations (Section 5.1.3).

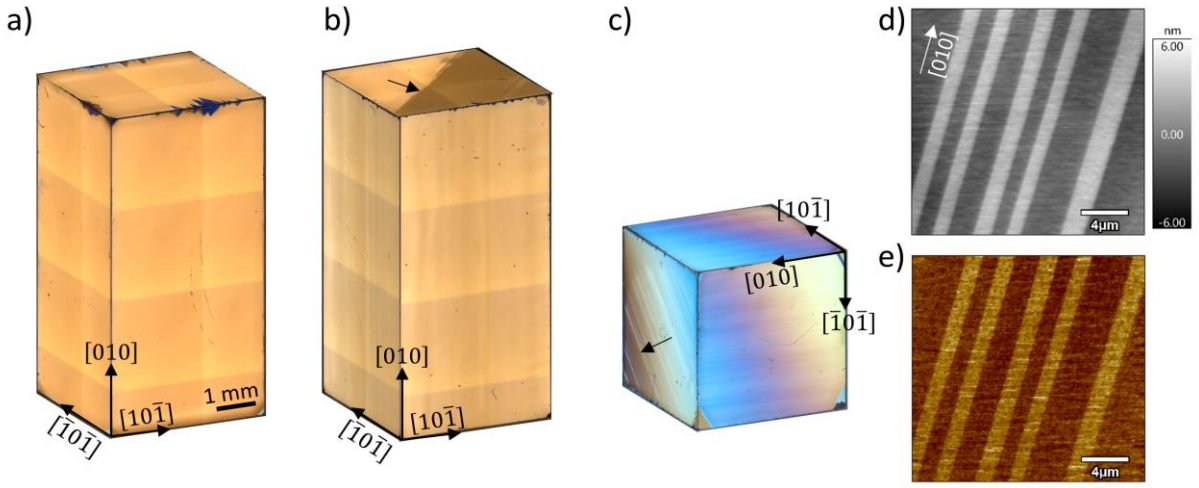

Figure 5.2: Initial domain structures of undeformed single crystals: a) Undeformed KN-010-2 without visible domain walls and two undeformed single crystals with local optical cloudy regions ((b) undeformed KN-010-4 and (c) undeformed KN-101-1). Piezoresponse force microscopy images of (d) the topography and (e) amplitude highlight the domains at the side face of the single crystal in (b). The images in (a), (b) and (c) were gained in differential interference contrast mode (LEXT or Zeiss). Black arrows in (b) and (c) indicate the cloudy region.

5.1.2 Plastic Deformation in the Orthorhombic Phase

The compressive stress-strain curves of $KNbO_3$ single crystals deformed in [010] and [101] directions are depicted in Figure 5.3a. Several mechanisms contribute to the stress-strain curves at RT. To elucidate the different contributions in detail, the curves were separated into three regimes: low-, medium- and high-stress regimes.

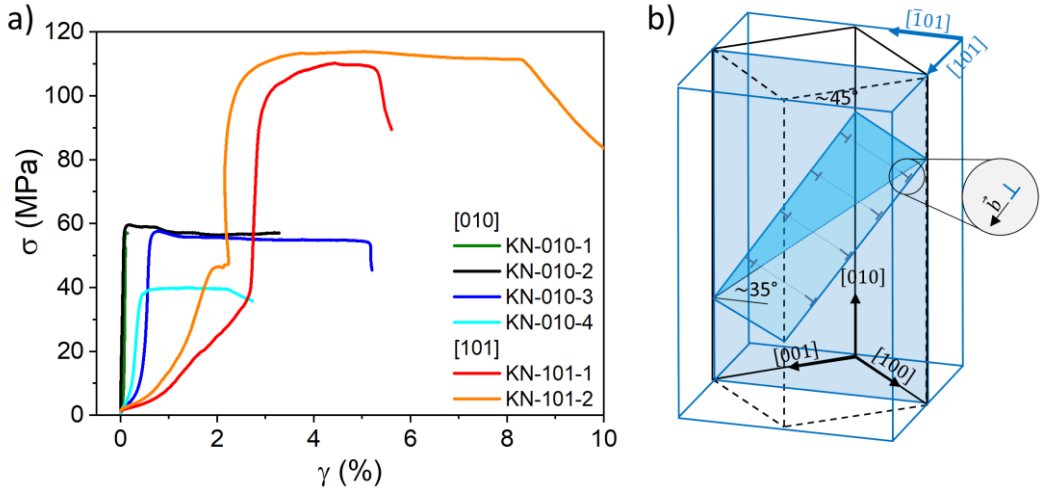

Figure 5.3: a) Compressive stress-strain curves of $KNbO_3$ single crystals in the orthorhombic phase at room temperature. The compression axis was either in [010] or in [101] orientation. b) Schematic of the single crystal's orientation (blue cuboid). The middle blue and bright blue triangles form a slip plane in $\{011\}\langle 0\bar{1}1\rangle$ direction; the dashed line indicates the dislocation line, connecting edge dislocations (⊥), which run in the direction of the Burgers vector along the slip plane. The cutting surface between sample surface and slip plane is indicated with the hypotenuse of the triangles, forming a 35° angle with the dark blue reference surface.

Between 0 and 20 MPa, the slope first slowly increased before a substantial increase in slope was observed with increasing stress. In this low-stress regime, (magnified in Figure 5.4a), ferroelastic switching and deformation of the Teflon protection layer occurred. The [101]-oriented single crystal indicates a more pronounced non-linear range in the stress regime from 0 MPa to 20 MPa than the [001]-oriented crystals, as indicated in Figure 5.4a. The coercive stress, at which the maximum domain switching was achieved was estimated by the inflection point in the low-stress regime of the stress-strain curve in Figure 5.4a. For both orientations, the coercive stresses were in the range of 3–5 MPa, which is in agreement with the findings of Prasad and Subbaro for [001]-oriented $KNbO_3$ [235]. The ferroelastic switching contribution to the strain value depends on the initial domain configuration and the orientation of the single crystals. Applying a mechanical stress along the [010] (Figure 5.4b) and [101] (Figure 5.4c) directions led to switching of the spontaneous polarization vector into the (010) plane (45°) and (101) plane (90°), respectively. Owing to the larger switching angle, the compression in [101] results in a larger ferroelastic strain contribution, explaining the higher strain.

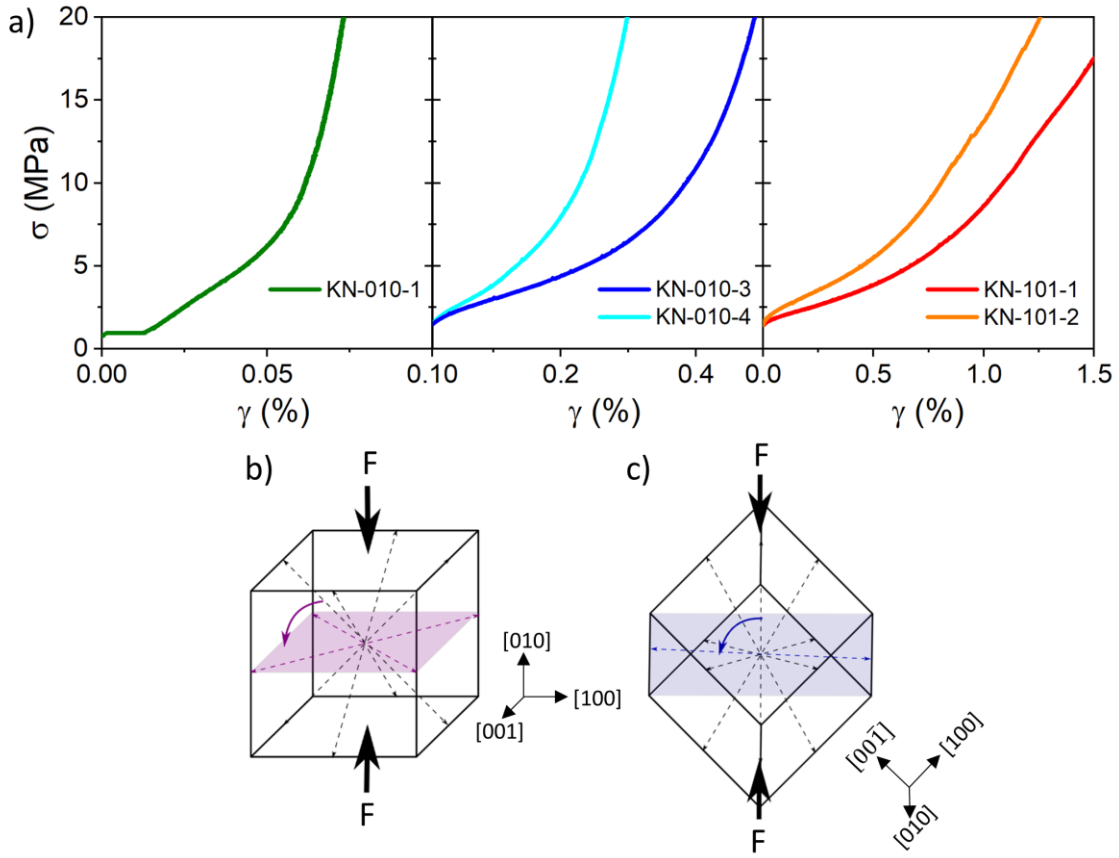

Figure 5.4: (a) Low-stress regime of the compressive stress-strain curves for selected samples; note the change of scale on the x axis in (a). Possible directions of spontaneous polarization for the two different sample orientations are displayed in (b) and (c). The arrows indicate the equivalent switching directions of spontaneous polarization, whereas the favored polarization directions are displayed by the plane.

A visible initial domain structures with domain walls aligned parallel to the [010] direction, as for KN-010-4, KN-101-1 and KN-101-2 (see Figure 5.2b-c for KN-010-4 and KN-101-1) tend to a more pronounced ferroelastic domain switching during compression. Samples with an inconspicuous initial domain structure (e.g. KN-010-1 and KN-010-2, Figure 7.1a and b), a predominant 180° domain wall configuration and only a few visible domain walls or inclusions

on top of the single crystal (KN-010-3; Figure 7.1c) indicate no extensive ferroelastic domain switching (like KN-010-2; which was omitted from Figure 5.4a) or limited domain switching. Nevertheless, not only the domain structure but also the Teflon protection contribute to the total strain. Which could explain why samples with only a few visible domains on the top face (KN-010-3) indicate with 0.3% at 5 MPa a more pronounced strain than a sample with a larger number of visible domain walls (KN-010-4) at the same deformation stress. The Teflon strain contribution (max. 0.38%) varies between the measurements owing to the manual stretching of the Teflon prior to the deformation experiments. For KN-010-1 no Teflon was used in contrast to the other KN single crystals, which can partly explain the lower strain values in Figure 5.4a. However, the orientation-dependency of the strain values at low stresses is attributed to the anisotropy of the material and not to the Teflon strain contribution.

In the intermediate-stress regime from 20 MPa until the bending of the curve at the critical stress ($R_{p0.2}$) occurs, the stress-strain curves were almost linear. This is mainly defined by the anisotropy of the elastic stiffness compliance of $KNbO_3$ single crystals [59, 158]. A deviation in the ideal elastic behavior indicated microcrack formation, similar to that in KN-101-2, or it was caused by a stiffness contribution of the setup.

The last and most relevant stress regime is the plastic deformation regime, which is reached for stresses above the critical stress $R_{p0.2}$ value, where dislocation motion and multiplication occur. The determined $R_{p0.2}$ values are listed in Table 5.1. The samples deformed along the [010] axis had a $R_{p0.2}$ in the range of 39–59 MPa. The variation in the values was mainly due to crack formation or tilting of the sample during the deformation process. A higher $R_{p0.2}$ value of 101 to 107 MPa was found for the [101] samples. For KN-010-1 the plastic strain was below 0.2%, which is the benchmark strain for the $R_{p0.2}$ determination. Therefore, the listed stress value in Table 5.1 corresponds to the kink at high stresses before a plateau was reached.

The multiplication of the $R_{p0.2}$ values with the Schmid factor for the {110}⟨110⟩ slip system gives the critical resolved shear stress. Both [101] samples had a Schmid factor (m) of 0.25, whereas all [010] samples had a Schmid factor of 0.5. Independent of the orientation, an overall CRSS in the range of 20–30 MPa was obtained, which is in accordance with the previously reported value of 27 MPa for [010]-oriented $KNbO_3$ [39]. With 20 MPa, the KN-010-4 sample seemed to be an outlier. This is likely related to the tilting of the sample during compression, which indicates that the stress was not applied homogenously over the whole sample area but rather at a smaller area. Therefore, the CRSS value of the KN-010-4 is underestimated. Within the high-stress regime, a stress plateau was formed for all samples. In contrast to the results obtained on $SrTiO_3$ single crystals [88], the stress plateau did not merge into a work-hardening curve (increase in slope). For $SrTiO_3$, it was suggested that the work hardening is caused by an intersection of slip planes, reducing the dislocation-free path [88]. The absence of work-hardening in $KNbO_3$ suggests that the dislocation-free path is still high enough, which indicates that even larger plastic deformation is possible. Each measurement was stopped after a certain strain was reached or a rapid crack growth was observed to avoid a failure of the sample. This manual stop resulted in a decrease in the slope after the stress plateau for KN-010-3, KN-010-4, KN-101-1 and KN-101-2, due to the relaxation of the system. None of the [010]-oriented samples failed, and they showed only limited cracking. In contrast, KN-101-1 and KN-101-2 exhibited severe cracking and cleavage, as indicated in Figure 5.5a for the bottom surface and a side face (Figure 5.5b).

Table 5.1: Compression direction, critical stress ($R_{p0.2}$), plastic strain (γ_{plast}), Schmid factor (m) and critical resolved shear stress (CRSS) for selected $KNbO_3$ single crystals.

Sample label	Compression direction	$R_{p0.2}$ (MPa)	γ_{plast} (%)	Schmid factor	CRSS (MPa)
KN-010-1	[010]	(57)[2]	0.05	0.5	
KN-010-2	[010]	59	3.2	0.5	30
KN-010-3	[010]	58	4.6	0.5	29
KN-010-4	[010]	39	1.8	0.5	20
KN-101-1	[101]	102	2.5	0.25	25
KN-101-2	[101]	107	5.8	0.25	27

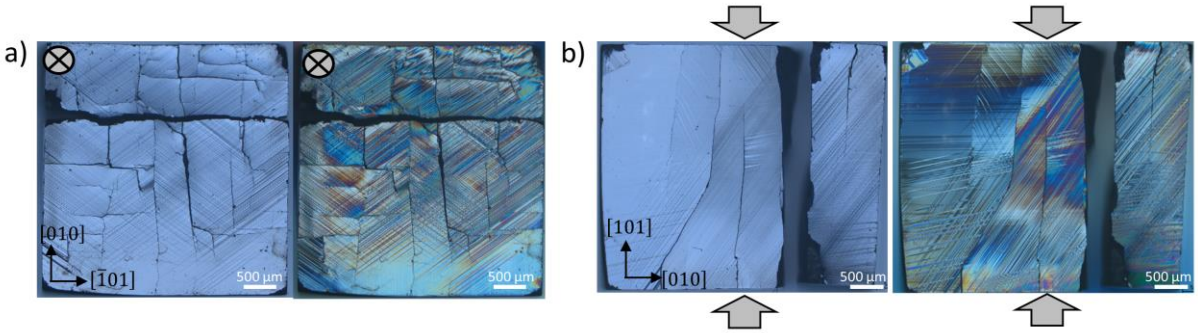

Figure 5.5: Severe cracking of the KN-101-1 sample during compression. Bottom surface (a) and a side surface (b) have cracks running through the whole sample. Cleavage can lead to an uncontrolled load distribution in the sample. Reflected-light bright-field optical microscopy and circular differential interference contrast (C-DIC) mode images are shown in both (a) and (b). Loading directions are indicated with grey arrows (a) in-plane or (b) parallel to the view plane. The bright-field optical microscopy images highlight the cracked structure, whereas the C-DIC images emphasize the domain walls and slip band structure for the different orientations.

The deformation of the [010] samples was stopped after reaching different plastic strain levels to systematically study how the plastic strain affects the domain structure and slip band structures. The deformation of the KN-010-1 and KN-010-5 (not listed in Table 5.1) was stopped immediately after reaching the stress plateau; therefore, the plastic strain is limited to 0.05% or below. KN-010-2, KN-010-3 and KN-010-4 were deformed to realize deformations of 3.2%, 4.6% and 1.8%, respectively. The KN-101-1 and KN-101-2 were deformed to 5.8%, but here the strain contribution of cleavage fracture and cracking could not be separated owing to continuous cracking throughout the experiment [236]. The [010] single crystal achieved, with 4.6% plastic deformation, an approximately 10 times higher plastic strain than that reported by Mark et al. [39] (~0.4% at RT). This result demonstrates that $KNbO_3$ can reach the plastic deformability of $SrTiO_3$ single crystals (~5.5% at RT), which are model materials for RT deformation of perovskites [93].

The evolution of the apparent slip band structure with increasing plastic deformation is depicted in Figure 5.6 for an initial single crystal (a), a 0.05% deformed single crystal (b, KN-010-1), a

[2] Plastic deformation is too small to determine $R_{p0.2}$. Therefore, stress at the transition between elastic and plastic regime of the curve is given.

3.2% deformed sample (c, KN-010-2) and a 4.6% deformed sample (d, KN-010-3). Each black line in Figure 5.6 is considered as an apparent slip band. The images are limited by the resolution of the OLM method.

In the initial state (0%) no slip bands and no domain walls were visible. With increasing plastic deformation (Figure 5.6b), domain walls (shadows; red arrows) and the first isolated slip bands (black arrows) appeared. The slip bands formed fine lines at the surface, later discussed as surface steps, which allowed the differentiation between slip bands and domains. Domain walls were often visible as dark shadows beneath the surface with a blurry contrast. At 3.2% (Figure 5.6c), the slip bands were mainly distributed at the top and bottom of the single crystal, which indicates that the surface and edges provide the preferred starting points for plastic deformation, which may be related to a slight miscut of the initial single crystals. This slip band distribution changed with increasing plastic deformation (4.6%), where most of the slip bands were concentrated in the middle part of the sample (Figure 5.6d).

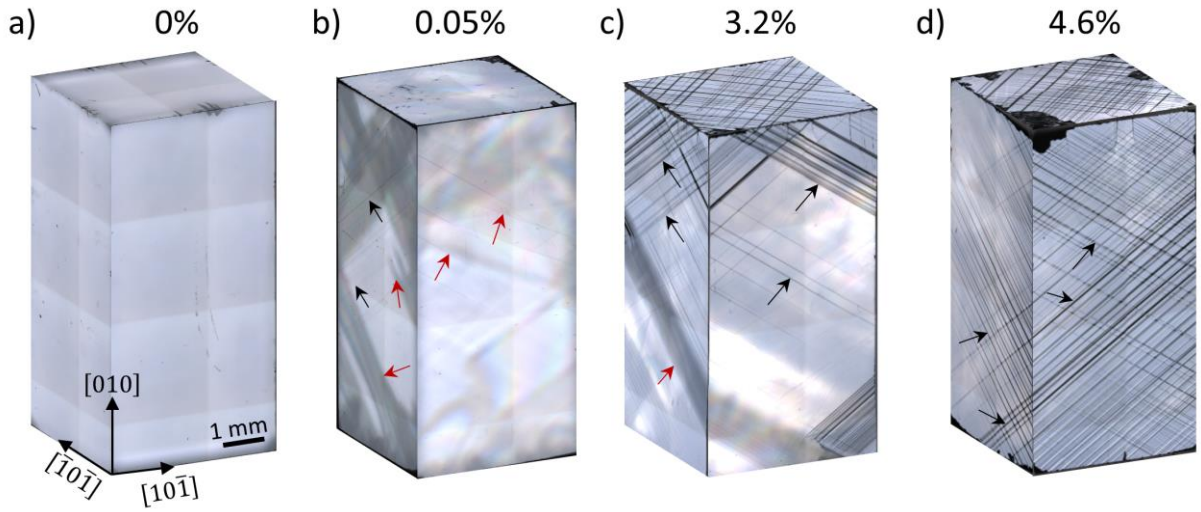

Figure 5.6: Slip band distribution in $KNbO_3$ single crystal deformed by (a) 0%, (b) 0.05%, (c) 3.2% and (d) 4.6%. The reflected light microscopy images correspond to KN-010-2 (initial state), KN-010-1, KN-010-2 and KN-010-3, respectively. Slip planes and slip bands are marked with black arrows, whereas domains and domain walls are marked with red arrows. Images were taken with an optical light microscope.

5.1.3 Identification of Slip Bands, Dislocations and Domains in $KNbO_3$

5.1.3.1 (010) Surface

Plastic deformation above 0.5% and the use of Teflon facilitated the appearance of slip bands at the top and bottom surfaces of single crystals deformed along the [010] orientation. As shown in the DIC-images in Figure 5.7a_2 and b_1, the slip bands in the KN-010-2 sample with 3.6% deformation formed a 45° angle with the edges of the samples. This angle corresponds well with the orientation of the $\{011\}\langle 0\bar{1}1\rangle$ slip system, as indicated in Figure 5.3b, and was subsequently verified with TEM. Moreover, the 90° and 60° domain walls were also found at the top and bottom surface (Figure 5.7a_1 and b_2), forming angles of 45°. Lines that formed an angle other than 45° to the edges were easily recognized as domain walls; however, a precise statement of the orientation of the spontaneous polarization vector is not possible without polarized light microscopy or vector PFM analysis. The dark features in Figure 5.7b_2 can be

identified as domains, owing to their needle-like shape [209]. Note that slip bands follow predefined crystallographic orientations; thus, they cannot form needle-like contrast in the C-DIC mode. The local variation of regions with primary domain walls (Figure 5.7a_1 and b_2) and slip bands (Figure 5.7a_2 and b_1) suggest a local variation of the stress state of the sample during compression, caused by a slight miscut of the initial crystal or cracking during the experiment.

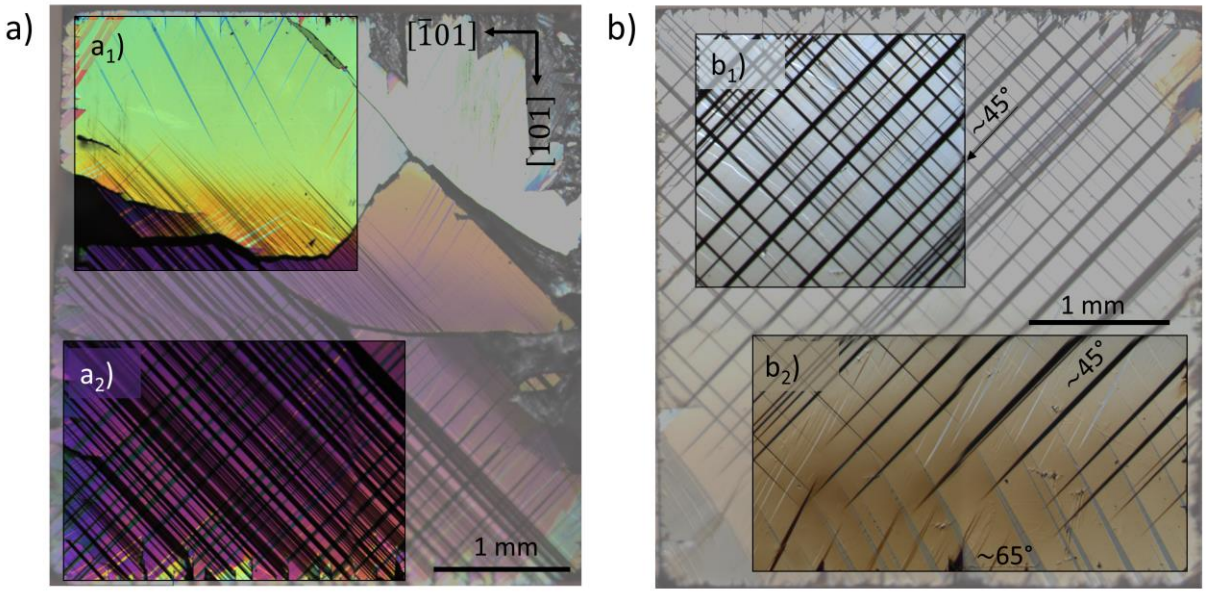

Figure 5.7: Optical images of the bottom (a) and top (b) surfaces of the deformed KN-010-4 sample. Slip planes (a_2) and (b_1) and domain walls (a_1) and (b_2) are highlighted in separate regions with DIC-mode.

Chemical etching of the surface (Figure 5.8a and b; KN-010-2) visualized the slip band alignment and distribution. Etching of the domains depends on the spontaneous polarization orientation and would lead to an etching effect on the whole domain and not only the domain walls [163]. The etch patterns in Figure 5.8 disclose two sets of parallel lines aligned along the [001] and [100] directions. Each line consists of a row of etch pits. Such patterns are atypical for etched domains but common for dislocation etching [237]. The slip band in Figure 5.8b is 12 μm wide and thus broader than the smaller slip bands of width 0.3–1.2 μm in Figure 5.8a, indicating that the dislocation motion and multiplication were not equally distributed over the sample. Multiplication of dislocations causes widening of the slip bands, like that observed in LiF single crystals [238], and it is proportional to the total plastic strain [239]. The difference in the slip band width in Figure 5.8a and b indicates that the apparent stress varied locally and that regions with broad slip bands were deformed more strongly. This could either indicate an inhomogeneous stress distribution caused by the off-centering of the sample, a sample miscut or local inhomogeneities in the sample. Sharp and straight edges of the slip bands indicate no pronounced cross-glide, which was found in LiF, where dislocations moved out of the slip bands shortly after deformation [238]. The distance between the etched lines in Figure 5.8b was in the range of 0.1–1 μm, which is in good agreement with the spacing in aluminum single crystals (0.2 μm) and in copper (0.3–2.5 μm [240]. In metals, smaller spacings are expected for larger deformation strains [240]. Nabarro clarified that “slip markings provide evidence of the dislocations, which have left the crystal and of dislocation lines intersecting the surface” but they are “no direct evidence of the dislocation array present within the crystal” [241]. The formation of surface steps or slip markings in the other orientation will be discussed.

Nevertheless, the etch patterns on the top surface confirm the dislocation-based plastic deformation and point towards dislocation motion in both ($\langle 0\bar{1}1\rangle$ and $\langle 011\rangle$) directions.

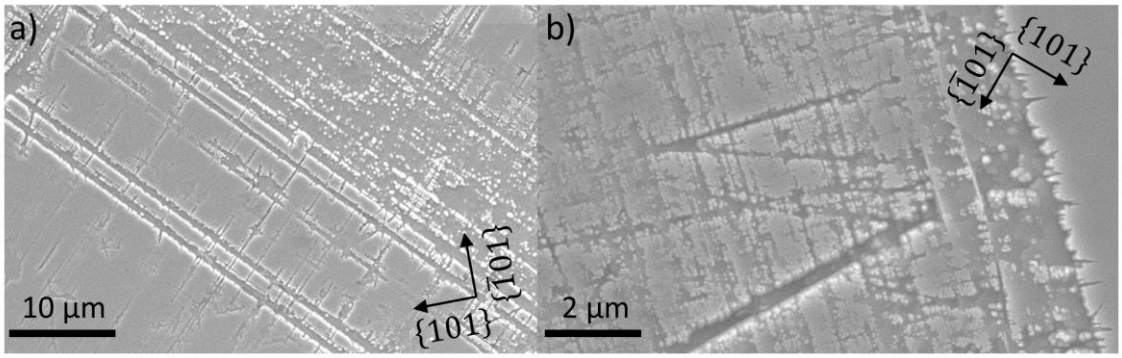

Figure 5.8: Top surface of the KN-010-2 sample. Subfigures (a) and (b) represent different positions of the chemically-etched top surface in secondary electron imaging mode.

5.1.3.2 {110} Surface

The slip band structure was investigated for the {110} side surfaces of the KN-010 single crystals. During the discussion of the stress-strain curves, a point was raised that the slip band distribution depends on the deformation degree, as shown in Figure 5.6. Only a few single slip planes reached the surface at low plastic deformation of 0.05%, as indicated with black arrows in Figure 5.9a. The distance between different slip bands was in the range 12–60 μm, and the slip band width is limited to less than 5 μm, which is comparable to the slip band structures reported for $SrTiO_3$ [242]. The density of slip planes and slip bands increases with increasing plastic deformation [240]. Regions with high slip band density achieved an expansion up to 130 μm. The outer edges of a slip band region or a broad slip band are marked with black arrows in Figure 5.9b and c. In contrast to LiF, which is one of the rare ceramic materials deformable at RT, the slip bands in $KNbO_3$ seem to consist of several slip planes separated in the submicrometer range. In LiF, the widened slip band has indistinguishable slip planes, which may be related to the cross-slip behavior and the motion of dislocations inside and away from the slip bands [238]. A clear separation of the slip band into slip planes point towards a planar alignment of the dislocations and supports the assumption that cross-slip is limited in $KNbO_3$.

Slip occurred along the slip plane, which may be related to the relatively high stacking fault energy in ceramics and the high Peierls stress in oxides, as discussed in Section 2.1.2. Moreover, the slip behavior is influenced by the density of the dislocation sources, which are in the case of Frank–Read sources in ceramics limited or pinned at impurities, the atomic-bonding-related stacking fault energy and temperature [96]. Several regions depicted no slip bands at all, marked with an **x** in Figure 5.9b and c. Nucleation and motion of dislocations were limited to certain areas in the sample, which resulted in a non-uniform appearance of slip bands with a variation in width. Additionally, the point defect concentration, for example, due to non-stoichiometry, affects the slip band distribution, similar to the findings in stoichiometric and Sr-excess $SrTiO_3$ single crystals [243]. For example, an Sr/Ti ratio of 1 results in more visible slip bands distributed in the sample than in single crystals with an Sr/Ti ratio of 1.04, which is likely associated with a reduction in Sr vacancies in samples with a high Sr/Ti ratio. Nevertheless,

with increasing plastic deformation, the number and width of the slip bands increase in $SrTiO_3$ single crystals. Although $KNbO_3$ showed a planar slip behavior for a plastic deformation up to 4.6%; at higher strains, a transition to cross-slip behavior may occur, as was reported for single-slip-oriented metallic single crystals [244].

A change in the intensity signal inside the broad slip band, running diagonally from bottom left to top right (yellow arrows) in Figure 5.9c indicates a height difference in the sample's surface. This change is associated with the plastic deformation processes and has been widely studied in metals [241, 245, 246]. At the yield stress, dislocation half-loops were created at the surface or reached the surface from inside the single crystal and expanded along the surface, resulting in a surface step (also called a surface terrace) [245].

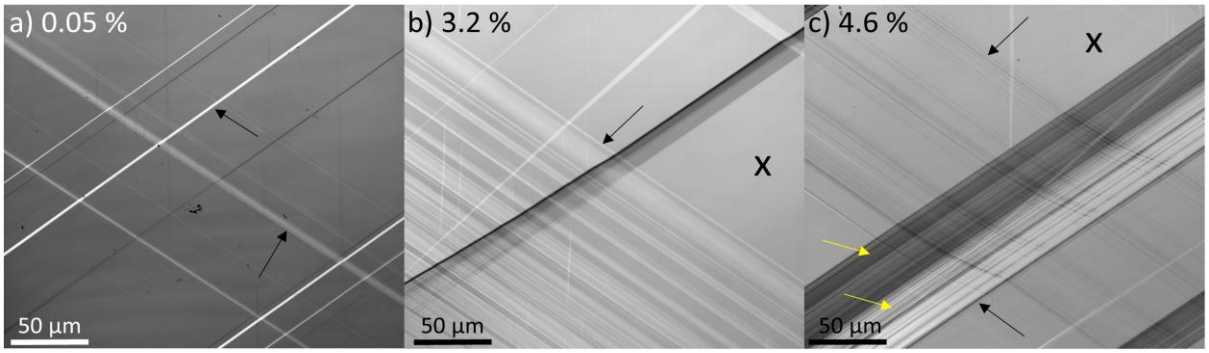

Figure 5.9: Slip band distribution at {110} surfaces for (a) 0.05 %, (b) 3.2% and (c) 4.6% plastic deformation. The images were taken with a laser scanning microscope and represent the intensity signal reflected at the sample surface. Black arrows mark the beginning of regions with high slip band density, yellow arrows the contrast change due to height differences and "x" the regions with no obvious slip bands.

The topographical changes were investigated with atomic force microscopy, presented in Figure 5.10 (a-c) for an undeformed, 0.2% deformed and 3.2% deformed $KNbO_3$ sample.

In the initial state (Figure 5.10a), the surface roughness was in the range of a few nanometers, due to chemical etching of some domains during polishing to optical grade or ferroelastic domains. A plastic strain of 0.2% induced local surface steps and an increase in surface roughness from 6 nm to 60 nm. With increasing deformation, the total height difference from the lowest to the highest position increased from ±60 nm (Figure 5.10b) to ±150 nm (Figure 5.10c). In (b), a terrace-like increase in height was noticeable; it was not as pronounced in (c); however, the total height difference was larger in (c). This may be correlated with the increase in slip band density, as indicated in Figure 5.9a and Figure 5.9c, and the mobility of dislocations on a single slip plane. Assuming that the surface roughness is solely associated with dislocations, the number of dislocations formed during mechanical deformation can be determined. The step formation at the surface is correlated with the Burgers vector's magnitude [247]. The $KNbO_3$ single crystals are orthorhombic, oriented as indicated in Figure 5.3b; therefore, the normal component of $|\vec{b}|$ to the {110} surface varies slightly from the value observed for $BaTiO_3$ {100} surfaces (0.4 nm). A step height of 60 nm corresponds to approximately 150 dislocations under the assumption of a step size of 0.4 nm, whereas 375 dislocations are estimated for a step size of 150 nm (Figure 5.10c). For comparison, in Cu crystals with 7.5 at.% Al, 1700 dislocations cause a step of 270 nm, because of the smaller Burgers vector in metals [245]. The dislocation density, number of dislocations per slip plane and slip plane density affect the step height and

superposition of the steps. Such a superposition is one of the reasons for the wavy landscape presented in Figure 5.10b and c. Dislocation multiplication and pre-existing dislocation sources contribute to the step height as well [248].

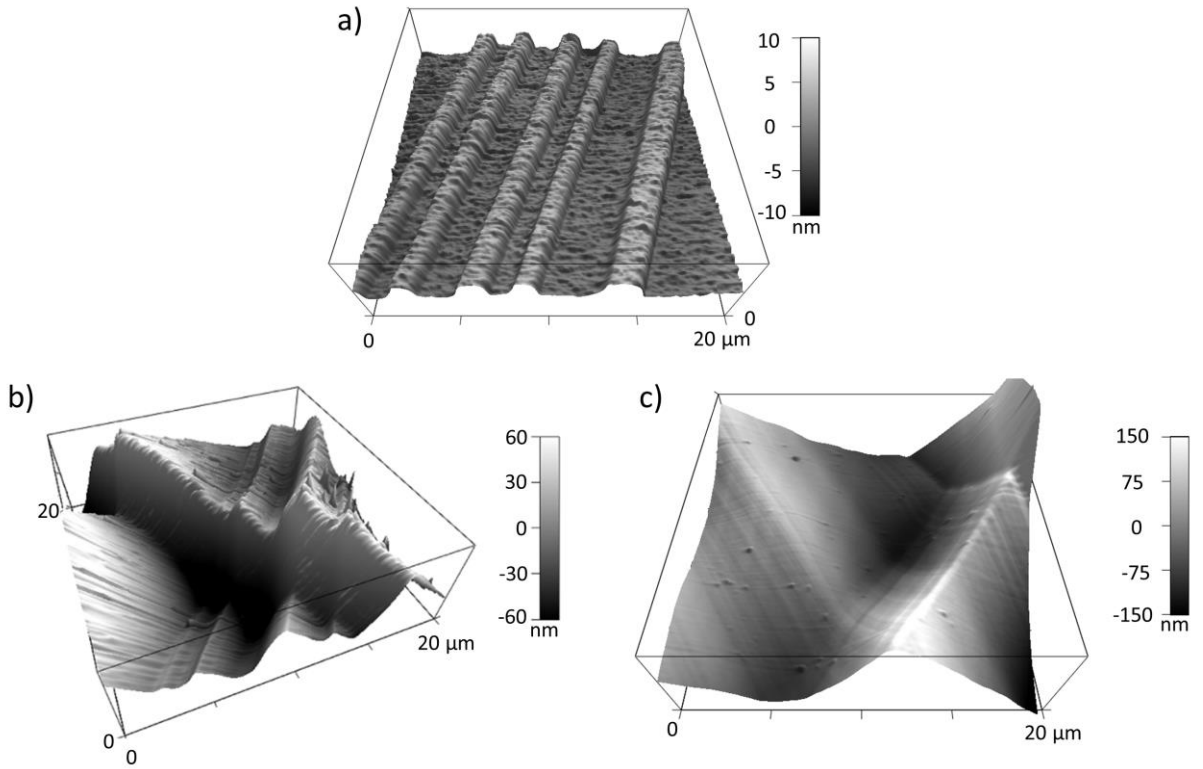

Figure 5.10: Topography (atomic force microscopy) of an undeformed (a), less than 0.2% deformed (b) and a 3.2% deformed (c) $KNbO_3$ single crystal.

For the {101} surfaces of the KN-010 samples Figure 5.11a_1 and a_3 depict that the domain walls formed an angle of approximately 55° or 35° with the edges of the {101} face. These angles (55° and 35°) are either correlated with 60° domain walls (Figure 5.11a_1) or with slip planes (Figure 5.11a_2) of the $\{110\}\langle 1\bar{1}0\rangle$ slip system. In Figure 5.11a_1, the lines have a tapered tip, which indicates a domain wall rather than a slip plane. 90° domain walls can be excluded in Figure 5.11a because 90° domain walls run parallel to the edge of the {101} faces [165, 249]. A closer look into the local domain arrangement was made possible with ECCI (Figure 5.11b) and PFM (Figure 5.11c); the images reveal that in the local scale domain walls run parallel to the ⟨100⟩ sample edges [165]. Nevertheless, the domain size varied and the domains were elongated, which is substantially different from the parallelism of the slip bands, as seen in Figure 5.11b.

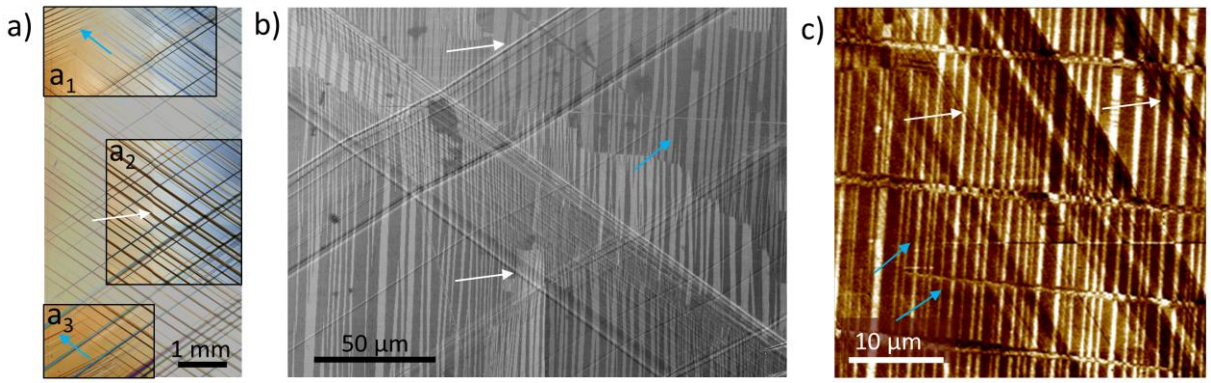

Figure 5.11: Appearance of domain walls and dislocations on a {101} side face as observed on different scales. a) Overview of the KN-010-3 side face with DIC mode. Three regions (a_1–a_3) highlight either domains or slip bands at the surface. b) Electron channeling contrast imaging combines the visualization of a slip band crossing and 90° domain walls. c) Piezoresponse force microscopy amplitude emphasizes the domain structure in the KN-010-2 sample. Blue arrows mark domain walls, whereas white arrows mark slip bands.

A method to further differentiate between slip bands and domains is temperature-dependent optical light microscopy.

At RT, slip bands (white lines) and domains (black arrows, black dashed line) appeared simultaneously (Figure 5.12a). The domain structure included needle-like domains, bands and thin lines. Some of the needle-like domains became smaller during heating from RT to 220 °C, and the thin domain walls also started to disappear (Figure 5.12b, black arrows) before the phase transition temperature of 225 °C to the tetragonal phase was reached. The direction of the spontaneous polarization transformed from ⟨110⟩ to ⟨100⟩ in the tetragonal phase, leading to a parallel alignment of the domain walls, as depicted in Figure 5.12c. At 420 °C, the sample was close to the Curie temperature (435 °C) and the domain walls in the upper left part of Figure 5.12d had already disappeared, whereas some domains were still visible in the lower right part (black arrow). Above T_c, no domains were left in the sample (Figure 5.12e). The slip bands, which are marked with white lines, were visible over the whole temperature range from the orthorhombic to cubic phase. Subsequently, the sample was cooled down, and new domains were formed in the orthorhombic phase (black arrow) but in a simpler structure than that in the domain state in Figure 5.12a. In addition, a crack grew during cooling, as indicated in the lower part of Figure 5.12f. The marker for the slip bands indicates the same position in all images, which was shifted due to thermal expansion and contraction of the sample. The color change in the figures is caused by ambient light conditions.

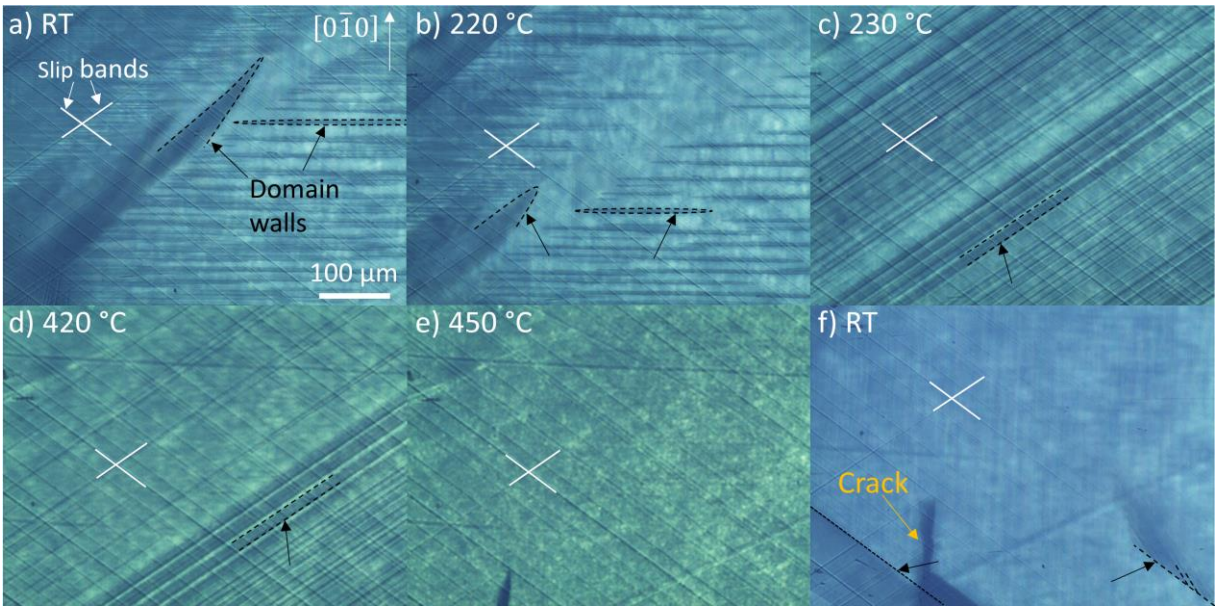

Figure 5.12: Temperature-dependent evolution of the domain structure and slip bands in $KNbO_3$ with optical light microscopy. A {101} surface was heated from the orthorhombic phase (a, b) to the tetragonal phase (c, d) into the cubic phase (e). Afterwards the sample was cooled down to room temperature (f). Domain walls are marked with black arrows and black dashed lines, slip bands with white lines and the crack with a yellow arrow. The sample slightly drifted during the experiment due to thermal expansion and contraction.

It should be noted that reflected-light optical microscopy visualizes slip bands at the sample's surface and does not necessarily provide insights into the whole bulk. For further investigation of slip bands in ferroelectric materials, transmitted-light optical microscopy is suggested.

5.1.3.3 Dislocation Structures in $KNbO_3$

Transmission electron microscopy was performed by Max Trapp and Stefan Lauterbach in order to determine the dislocation density and dislocation structure after plastic deformation. In the initial undeformed state, the dislocations were randomly distributed and no network structure was recognizable (Figure 5.13a). The determined dislocation density of $0.4–1.2 \cdot 10^{12}$ 1/m^2 for the undeformed state was in good agreement with previously reported values for $KNbO_3$ [39]. At low plastic deformation levels (< 0.2%; Figure 5.13b); the dislocations were aligned and some of the dislocations were split, which indicates that dislocation dipoles had formed, see white arrows in Figure 5.13b.

A superordinate dislocation structure was achieved at 1.8% plastic deformation, as depicted in Figure 5.13c. The slip band consisted of dislocations with mainly $(\bar{1}\bar{1}0)[1\bar{1}0]$ and $(101)[10\bar{1}]$ edge character, reaching a dislocation density in the range of $2–5 \cdot 10^{12}$ 1/m^2. The overlap of the dislocations in the TEM image (inset in Figure 5.13c) impeded the determination of the dislocation density. Nevertheless, the estimated density is in accordance with previously reported values of $2.4 \cdot 10^{12} \pm 1.4 \cdot 10^{12}$ 1/m^2 and $7.9 \cdot 10^{12}$ 1/m^2 for deformed $KNbO_3$ [95] and $SrTiO_3$ [104], respectively. Note that $(101)[10\bar{1}]$ edge dislocations belong to a slip plane with a nominal Schmid factor of zero (compare Figure 7.2a and b). Mark et al. have suggested that local stress field changes caused by microcracks can promote a different slip system [39]. In this case, the deformed sample exhibited some cracks and showed a macroscopic tilt after

deformation (Figure 7.2d), likely caused by an initial slight miscut of the crystal. Due to this tilting, a strong variation of the local stress distribution could result in a local nominal Schmid factor higher than zero for the $\{101\}\langle 10\bar{1}\rangle$ slip system. This could explain the presence of the non-preferred edge dislocation orientation. However, the dislocation structure in the slip band was complex; therefore, different dislocation motion and multiplication mechanisms may also be possible reasons for the occurrence of the $\{101\}\langle 10\bar{1}\rangle$ edge dislocations. Straight screw dislocations in $[0\bar{1}1]$ direction were observed outside of the slip band (Figure 5.13d). Both screw dislocations $[0\bar{1}1]$ and edge dislocations $(\bar{1}\bar{1}0)[1\bar{1}0]$ were reported frequently in the literature [39, 88, 95, 250, 251]. In the bulk region not only screw dislocations but also mixed dislocations were found (Figure 5.13e).

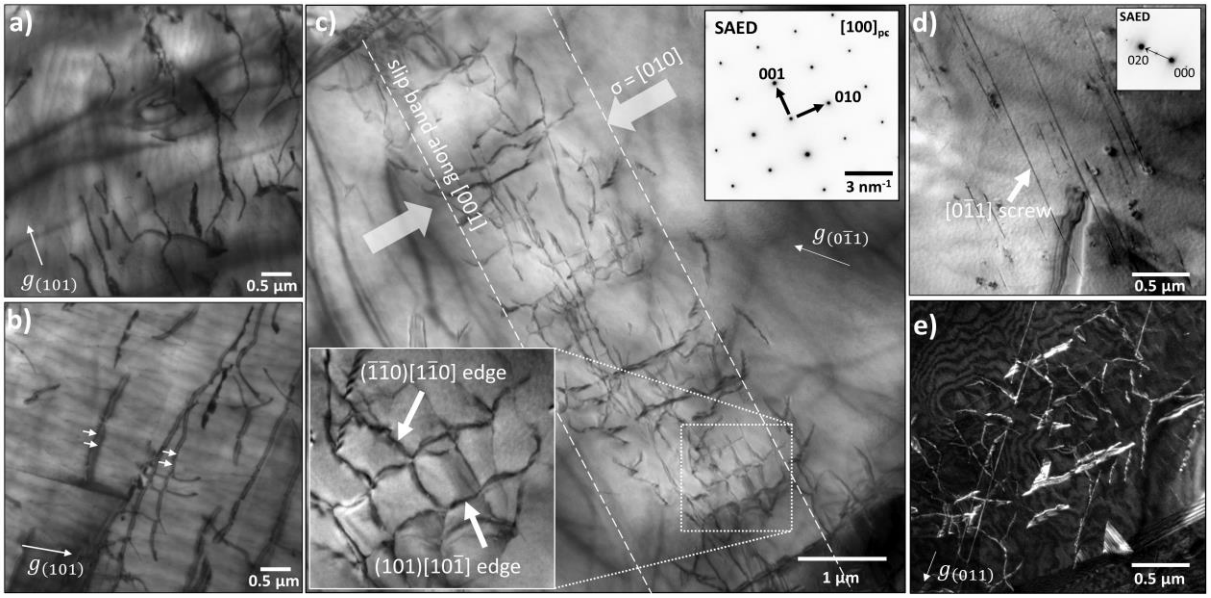

Figure 5.13: Transmission electron microscopy images of an undeformed (a), a less than 0.2% deformed (b) and a 1.8% deformed (c-e) $KNbO_3$ single crystal. Randomly distributed single dislocations with mixed character were found in the undeformed sample (a) and the 0.2% deformed sample (b). In addition, some of the dislocations in the 0.2% deformed sample exhibited a double line, marked with white arrows in (b), suggesting dipole formation. A slip band along the [001] direction composed of $(\bar{1}\bar{1}0)[1\bar{1}0]$ and $(101)[10\bar{1}]$ edge dislocations is shown in (c) for the 1.8% deformed sample (KN-010-4), indicating a large increase in dislocation density. d) Straight $[0\bar{1}1]$ screw dislocations and (e) mixed dislocations were found outside the slip band. The g-vector and the selected area electron diffraction (SAED) insets indicate the orientation. The undeformed sample and the 0.2% deformed sample were cut perpendicular to the [010] direction, whereas the 1.8% deformed sample was cut parallel to the deformation direction along the (100) plane. As indicated by the g-vectors and the small selected area electron diffraction (SAED) insets, subfigures (a) and (b) were taken in two-beam bright-field conditions with g=(101), whereas (c) and (d) were recorded with $g = \{0\bar{1}1\}$ and $g = \{020\}$, respectively. In (e), weak-beam dark-field conditions were applied for $g = \{011\}$. The large SAED inset in (c) represents a [100] zone axis pattern indicating the main directions and general orientation of the investigated crystal

Hirel et al. simulated a Peierls-stress of 0.57 GPa and 3.42 GPa for edge dislocations and screw dislocations in $KNbO_3$, therefore, edge dislocations are considered to be more mobile [95]. The appearance of mainly edge dislocations in the slip plane can be explained by the easier dislocation motion of edge dislocations than screw dislocations. The straight appearance of the

dislocations indicates a low mobility [250] and a limited kink-pair nucleation, which is therefore the rate-controlling mechanism of the whole kink-pair process [39].

5.1.4 Influence of Dislocations on the Domain Structure

The impact of the dislocations on the domain arrangement and domain width was determined with PFM and ECCI. The change in domain structure is illustrated for KN-010-2 (Figure 5.14a), KN-010-4 (Figure 5.14c) and an undeformed sample (KN-010-4 before deformation, Figure 5.14b). While the domain walls in the reference sample ran parallel to the [010] direction, the domain structures in both deformed samples were more complex and varied considerably with the chosen region (Figure 5.14a_2, a_3, c_2, c_3). Figure 5.14a_2 and c_2 demonstrate a pronounced domain structure with needle-like domain walls and wavy domain walls. Both indicate a mixture of 60°, 90° and 180° domain walls. In Figure 5.14a_3, the domain structure was similar to that in the undeformed sample in Figure 5.14b, but the orientation of the domains was tilted by 90°, and the domain size was smaller. Both Figure 5.14 a_3 and c_3 had a distinct slip band appearance in the amplitude image.

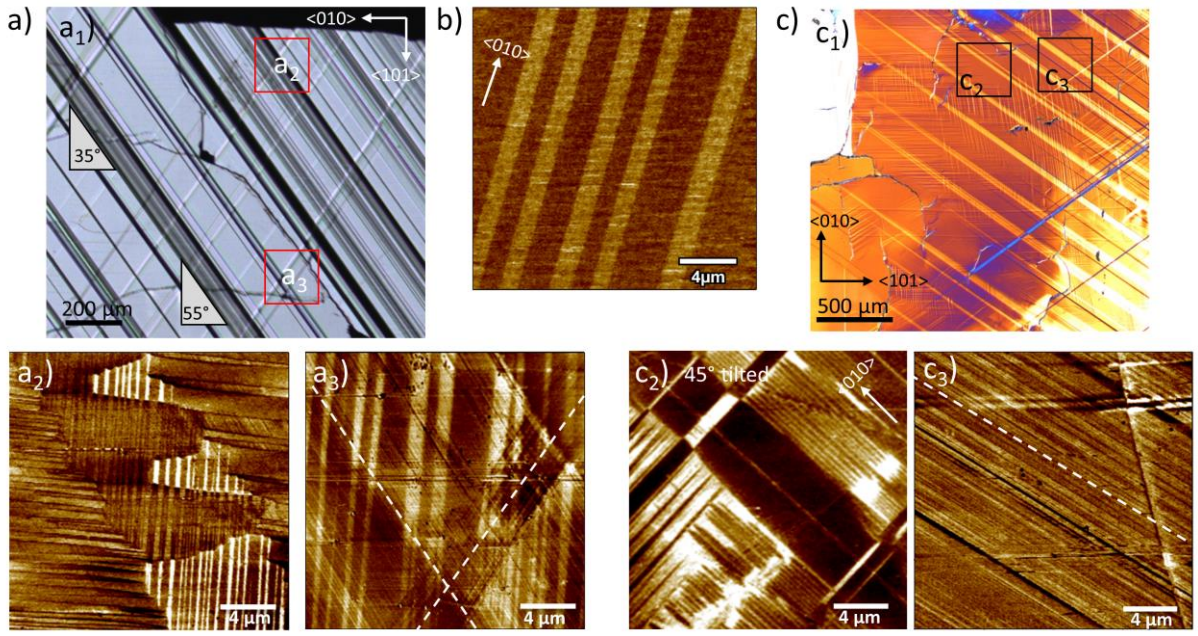

Figure 5.14: Impact of plastic deformation on domain size. a) Optical microscopy overview image (a_1) of the piezoresponse force microscopy (PFM) amplitude in two different regions (a_2) and (a_3) of the KN-010-2 sample. b) Domain structure before deformation of the KN-010-4 sample and after deformation (c). The differential interference contrast optical microscopy image (c_1) emphasizes the PFM amplitude regions (c_2) and (c_3). The white dashed lines indicate the directions in which slip planes intersect with the surface.

A detailed investigation of the domain size from PFM and ECCI images is depicted in Figure 5.15 for KN-010-2 (3.2% deformed), KN-010-4 (1.8% deformed) and a reference surface (KN-010-4 before deformation). Figure 5.15 indicates a considerable reduction of the domain size from 1.8 μm ±1.1 μm in the undeformed sample to 0.5 μm ±0.5 μm in the deformed samples. The domain size of a region without slip bands (Figure 5.15b; cyan) was 1.8 ±1.4 μm, which is in the same range as that in the undeformed sample. Inside and surrounding the slip

bands, the domain size was reduced considerably, and only a few domains showed a size larger than 1 μm.

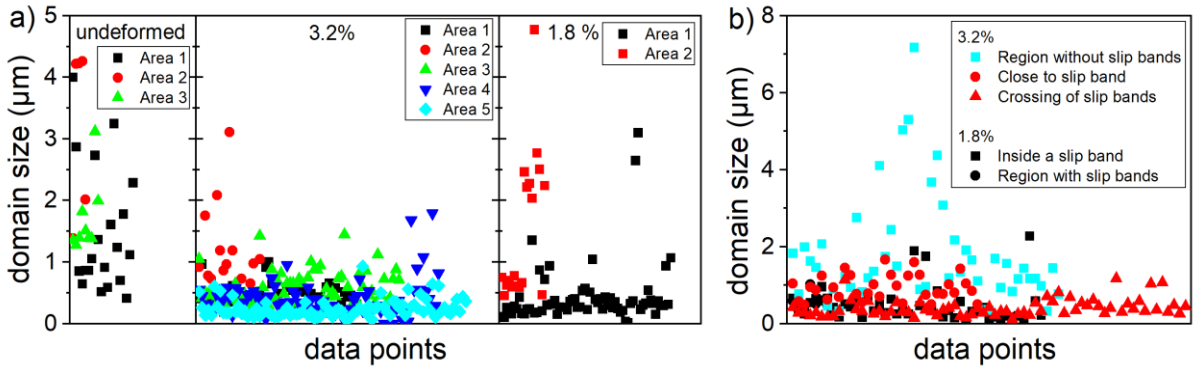

Figure 5.15: Domain size determination based on piezoresponse force microscopy (PFM) (a) and electron channeling contrast imaging mode (ECCI) images (b) at different regions and samples. a) Domain size of the undeformed, 3.2% deformed (KN-010-2) and 1.8% deformed (KN-010-4) samples at several positions on the surface, respectively. b) Differentiation between the regions with and without slip bands to determine the domain size for KN-010-2 and KN-010-4 in ECCI. Data points in (a) represent the measured values, which were determined at different areas for the three samples. Therefore, the colors indicate all values that were taken from the same PFM images, respectively.

The response of the ferroelectric domains was locally investigated by applying a direct-current (DC) electric field on an undeformed, 3.2% deformed (KN-010-2) and 1.8% deformed (KN-010-4) sample, as given in Figure 5.16. The reference sample initially had a typical lamellar domain structure along the ⟨010⟩ direction (Figure 5.16a_1). After applying an electric field of +150 V in the entire area a_1, the domains switched according to the applied electric field as visualized in Figure 5.16a_2. Note that Figure 5.16a_2 depicts a larger area than a_1 and, therefore, also includes the non-switched surrounding. The white arrows mark some of the newly formed domain walls, most of them were parallel to the original domain walls. The domain walls were perpendicular to the walls in the surrounding area only at the edge of the DC imprint. All original and newly formed domain walls behave similar to the domain walls presented in the schematic of Figure 2.15d. The ferroelastic switching of the domains as a function of the applied +150 V caused a slight increase in the surface height. This increase was still in the low nanometer range (see topography image in appendix Figure 7.3), which agrees with the domain height estimated in Section 5.1.1.

Similar DC switching tests were performed on deformed KN-010-2 (3.2% deformed, Figure 5.16b) and KN-010-4 (1.8% deformed, Figure 5.16c) in areas of high slip plane density (see DIC-OLM images in Figure 7.4a and Figure 7.5a). The resulting changes in domain structure were more pronounced in the deformed samples with the application of two opposing DC fields (±150 V) in adjacent regions. KN-010-2 (3.2% deformed) had a parallel alignment of the initial domain walls with a domain size below 1 μm before application of the DC field. The slip bands are highlighted with white dashed lines and formed an angle of about 35° to the deformation axis. After applying the opposite DC field, the slip planes were still visible in the left region in Figure 5.16b_2. The slip planes on the right-hand side were more difficult to see, suggesting expansion of the domains with applied electric field. The ferroelastic switching changes in the topography were negligible compared to the height differences caused by the slip bands (see

Figure 5.10). Nevertheless, the domain structure was more pronounced, especially at the corners of the right side, as indicated by white arrows in Figure 5.16b$_2$. The new domain structure crossed the boundary of the actual imprint and formed several thin domain walls aligned along the ⟨010⟩ direction. These newly formed domains had a domain size in the range of 0.5 μm, which agrees well with the average domain size presented in Figure 5.15. Although the slip planes in this region were not visible, they appear to influence the domain formation. The slip planes oriented along dashed line "2" caused a greater height contrast in topography than those oriented along the dashed line "1". This height difference indicates a higher dislocation density for the slip planes along "2". Remarkably, a comparison of the domain structures indicates that the set of slip planes "2" causes a more pronounced domain structure compared to "1" (white arrows at the top and bottom of the right side Figure 5.16b$_2$). These findings suggest that domains nucleated at dislocations. Perhaps, the locally higher dislocation density caused a more stable and pronounced domain structure.

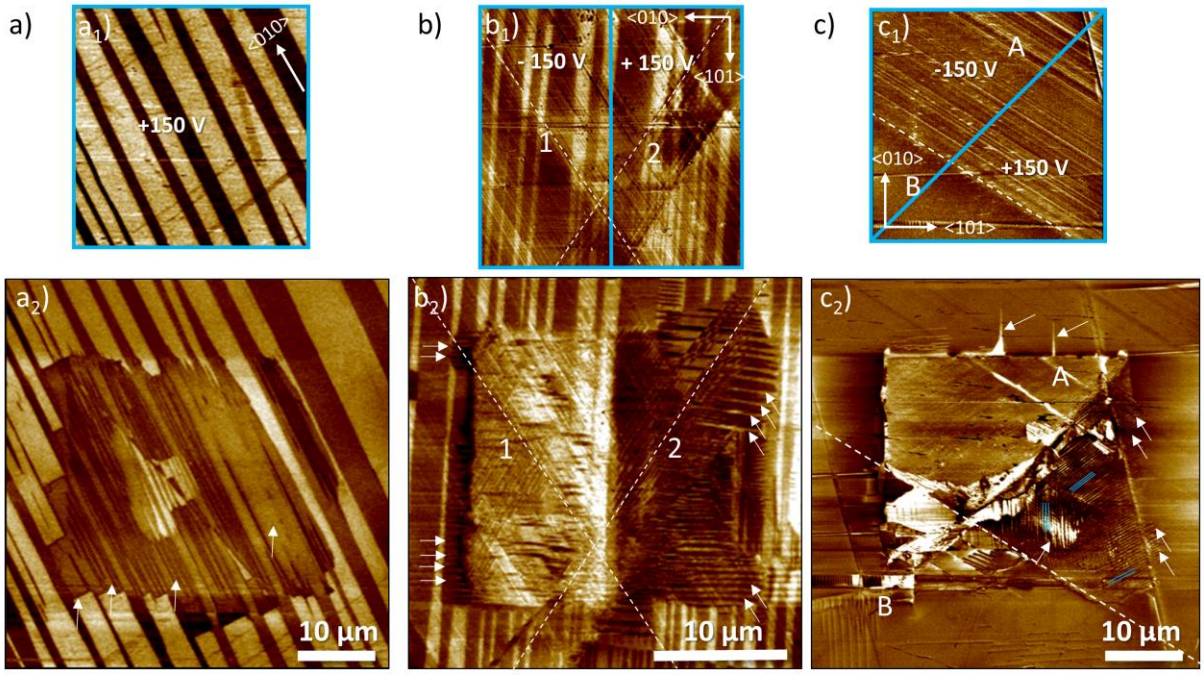

Figure 5.16: Effect of a local DC field application on the domain structure. The domain structure changes are demonstrated in the piezoresponse force microscopy amplitude images for (a) an undeformed sample, (b) KN-010-2 (3.2% deformed) and (c) KN-010-4 (1.8% deformed). In the upper row (a$_1$, b$_1$ and c$_1$) the DC electric field region is indicated with blue lines and the voltage is mentioned in the respective region of the initial domain structure: a$_1$) +150 V for the undeformed (30×30 μm², square), (b$_1$) -150 V/+150 V for KN-010-2 (+150 V: 20×10 μm² and -150 V: 20×10 μm²) and (c$_1$) -150 V/+150 V for KN-010-4 (two triangles forming together an area of 30×30 μm²). The switched regions are embedded in a larger region in (a$_2$), (b$_2$) and (c$_2$) to emphasize the domain changes. White dashed lines correspond to the slip plane orientation and the white arrows correspond to domain walls. In (b) the set of parallel slip planes is marked as "1" or "2", respectively. c) "A" indicates a region with high slip plane density and "B" emphasizes a region without slip bands; blue stripes indicate newly formed small domains. All amplitude images were acquired 15 min after application of the DC field. Topography, amplitude and phase are given in the appendix (Figure 7.3, Figure 7.4 and Figure 7.5). (a$_1$), (b$_1$) and (c$_1$) have the same scale as a$_2$, b$_2$ and c$_2$, respectively.

Another DC switching experiment was conducted in a region with no distinct domain structure and only one orientation for the slip planes (Figure 5.16c$_1$). The boundary between the region with high slip plane density (slip band marked with A) and a region without slip planes (B) is indicated by a dashed line in Figure 5.16c$_1$ and c$_2$. In Figure 5.16c$_1$, two triangles with ±150 V were applied on this slip band. In topography only the boundary between the two DC imprint regions was observed and no further changes appeared (Figure 7.5c$_1$). Applying -150 V resulted in a distinct imprint with straight boundaries, as depicted in Figure 5.16c$_2$. Few domains were formed outside of the DC imprint or in region B without slip planes. The main part of the -150 V region, which overlapped with the slip band, indicated no domain switching in amplitude, but a change in the P_s-orientation (see phase in Figure 7.5c$_3$). The domain structure was disturbed in the +150 V region; and fine lines (blue lines) were formed across the entire +150 V imprint. Moreover, newly formed domains extended across the edges (see white arrows). These fine lines occurred only within the slip band (region A) and were likely 0.2 μm thick domains. The beginning of the slip band was still recognizable after an electric field was applied. In addition, bright domain walls in Figure 5.16c marked particularly pronounced slip planes. These results point towards an alignment of the domain walls along the slip planes, but also the formation of several smaller new domains within the slip band.

In these PFM experiments, a positive DC field affected the domain structure more effectively than a negative DC field, which is related to the orientation of the P_s vector. In addition, the domain wall density was locally increased, and the domain wall orientation near slip planes did not follow the original domain structure before DC was applied. This is in contrast with the reference sample and suggests that the dislocations act as pinning sites and affect the domain wall density.

5.1.5 Permittivity Measurements

Domain structure changes and defects affect the polarizability and the phase transition, which in turn influence, among other parameters, the permittivity of a material (see Section 2.2). Therefore, temperature-dependent permittivity was measured in two deformed samples (KN-010-2 and KN-010-3) and two reference samples. In Figure 5.17, the permittivity and dielectric loss ($tan\delta$) are plotted as a function of temperature. At ambient temperatures, all samples reached permittivities in the range of 810-900, which corresponds well with the permittivity values from the literature [59, 157, 158]. Reported permittivity values in the range of e.g., $\varepsilon_{22}^{s} = 800$ indicate clamping (superscript s) of the sample, which was also the case for all samples in these measurements. With increasing temperature, the permittivity slightly decreased until the first transition from the orthorhombic to the tetragonal phase was reached. KN-010-2 and KN-010-3 have a $T_{o\text{-}t}$ of 220 °C, whereas the reference samples reach the tetragonal phase at a slightly higher temperature, at $T_{o\text{-}t} =$ 222 °C. This value is lower than the previously reported value of 224 °C [252]. Permittivity decreased in the tetragonal phase for all samples with increasing temperature until T_c was reached. T_c varied from 432 °C to 435 °C. The higher value is in good agreement with those reported previously (435 °C [95, 145] and 434 °C [252]). Even though a trend is visible at the first phase transition, no clear trend is apparent for T_c. For all samples, t$an\delta$ is below 0.15 in the orthorhombic phase, exhibits a peek at both phase transitions, and reaches a local maximum in the tetragonal phase in the range 300–350 °C,

which may be related to domain formation. Note that this maximum decreases with increasing frequency for all samples.

Qi et al. [31] identified a local increase in the phase transition temperatures $T_{o\text{-}t}$ and T_c around dislocations with $\vec{b} = [1\bar{1}0]$ during in-situ TEM observation in $KNbO_3$, which is contrary to the observation of $T_{o\text{-}r}$ in Figure 5.17. A point defect contribution can be neglected, because point defect doping leads to a shift of both phase transition temperatures [253], and the initial point defect concentration is assumed to be constant. The lower phase transition $T_{o\text{-}r}$ suggests that the dislocations favor the transition to the tetragonal phase, which would imply that the interaction between 60° domain walls and dislocations is not as strong as that between 90° domain walls and dislocations.

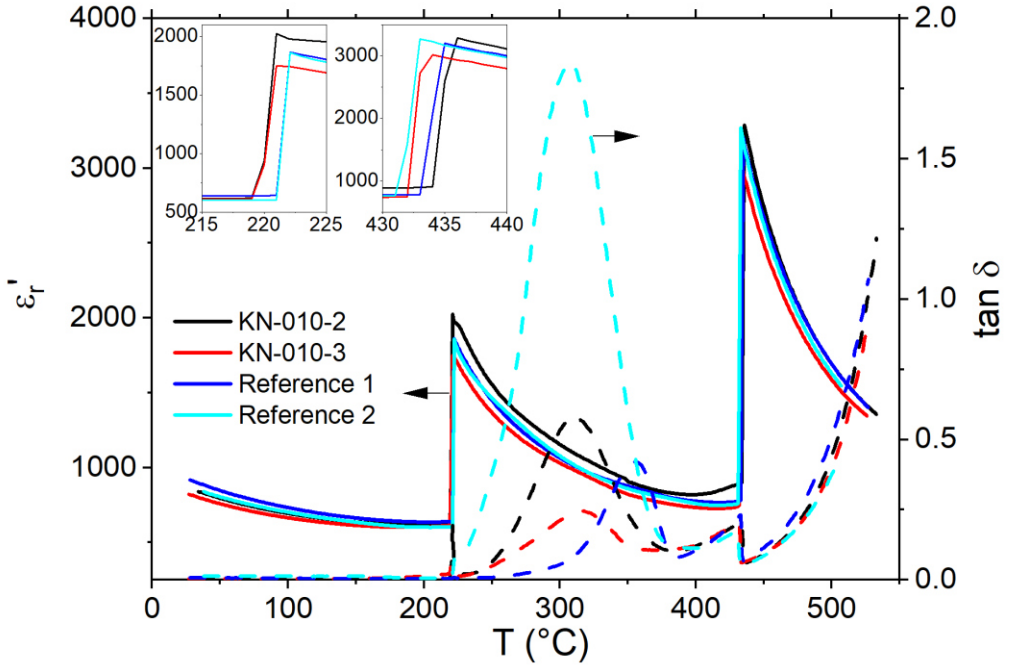

Figure 5.17: Temperature-dependent permittivity (ε_r') and dielectric loss (tanδ) at 10 kHz.

5.1.6 Discussion: Dislocation-Based Slip Band and Domain Wall Arrangement in $KNbO_3$

The onset of dislocation motion was about $R_{p0.2} \approx 39$–59 MPa for the [010]-oriented single crystals, which is in good agreement with the value of 56 MPa reported for $KNbO_3$ in the literature [39]. The [101] direction required almost twice as high compressive stress, $R_{p0.2} \approx 102$–107 MPa, to reach the plastic deformation regime. The $\langle 1\bar{1}0\rangle\{110\}$ slip system is the most active for perovskites at RT, resulting in a Schmid factor of 0.5 for the [010] orientation and $m = 0.25$ for the less suitably oriented [101] crystals. The plastic deformability of a material depends on, among other parameters, the initial dislocation density. With 10^{12} 1/m², the dislocation density in $KNbO_3$ is very high compared to other perovskite materials. Furthermore, the Peierls potential, dislocation mobility [95], dislocation core properties [95], point defect concentration [105, 243] and single crystal orientation [88] influence the deformation behavior. The Peierls stress for edge dislocations in $KNbO_3$ is 0.57 GPa, which is lower than that in other perovskites such as $SrTiO_3$ (1.5 GPa [95]) and $CaTiO_3$ (1 GPa [127]) for the $\langle 1\bar{1}0\rangle\{110\}$

slip system. The formation of partial dislocations further reduces the Peierls stress owing to the smaller Burgers vector (see Equation 2-4), which is one of the reasons why $SrTiO_3$ is deformable at RT. The low Peierls-stress of 0.57 GPa [95] for $KNbO_3$ and the high initial dislocation density are proposed to be the main reasons for its good plastic deformability at RT.

The arrangements of slip planes and slip bands with increasing plastic deformation provide information about the dislocation dynamics and stress distribution in $KNbO_3$. Dislocations move on the crystallographically prescribed slip planes. The slip band distribution and positioning in the deformed specimen suggest that slip bands are preferentially formed on the top and bottom surfaces. With increasing plastic deformation, the slip bands distribute over the whole sample, become wider and areas with high slip band concentration are formed. On the one hand, a width of 130 μm was observed for an area with high slip band concentration for the 3.2% deformed sample; on the other hand, there were also large areas without slip bands nearby. This indicates that slip planes are mainly formed near other slip planes. Etching of the top surface of a [010] deformed $KNbO_3$ depicts a minimum spacing between the etched slip bands (or planes) of 0.1–1 μm within a region with high slip band density, which is in good agreement with values of 0.3–2.5 μm reported for copper single crystals, a typical fcc metal with easy slip behavior [240]. The spacing between slip bands and planes in $KNbO_3$ indicates a planar alignment of the dislocations in the slip plane and limited cross-slip behavior. This is in contrast with the findings in LiF single crystals [238], where an increase in deformation causes a broadening of slip bands with indistinguishable slip planes, suggesting that cross-slip occurs frequently. TEM results confirmed that the dislocation density in a slip band was substantially high ($2–5 \cdot 10^{12}$ 1/m^2), which is in good agreement with values reported in the literature [39, 104]. Moreover, dislocations with $(\bar{1}\bar{1}0)[1\bar{1}0]$ and $(101)[10\bar{1}]$ edge characters were found. For a highly overlapping dislocation structure, such as that in the slip band of the 1.8% deformed sample, the average minimum projected distance between the dislocations can also provide useful information. The minimum projected dislocation distance in the undeformed sample was approximately 0.4 ± 0.3 μm and decreased to 0.13 ± 0.1 μm for the deformed samples, indicating that the dislocations were closer to each other and therefore can interact more easily. Thus, it is hypothesized that despite the limited cross-slip behavior, the increased dislocation density and possible dislocation accumulation or interaction between dislocations on perpendicular slip planes trigger the multiplication and movement of dislocations, paving the way for the formation of more slip planes nearby. With increasing plastic deformation, the number of slip planes and slip bands increased, and topographic steps were formed on the surface of the sample.

Domain walls and dislocations cause similar features on the macroscopic scale, but their appearance and shape can be used to distinguish between the two. Domain walls can have several shapes, from needle-like, S-walls, zig-zag to parallel alignment [163, 254]. Dislocations, in contrast, are strictly defined by their crystallographically prescribed slip planes and depict sharp and thin lines in ECCI or surface steps in AFM topography. In contrast to dislocations, domains in ECCI and PFM cause a contrast change over a broader range. This separation between slip planes and domain walls allows the determination of domain size for different positions and deformed samples in ECCI and PFM. In general, the domain size decreased from an initial 1.8 μm for the undeformed samples to 0.5 μm for the deformed samples. Regions without slip band structures in deformed samples had similar domain size as the undeformed samples. Moreover, the domain size for the undeformed samples varied greatly with a tendency

towards even larger domains. Note that previously reported domain sizes vary even stronger between 0.1-50 μm for $KNbO_3$ single crystals [171, 219, 255, 256]. The reduced domain size within a slip band or near slip bands deviated less, suggesting that the dislocations act as nucleation sites for the domain walls, as has been theoretically predicted [32].

The changes in local domain structures with the application of a DC field were investigated using PFM, indicating that domain structures are mainly affected in regions of high slip plane density or at the intersection of two perpendicular slip bands. Therefore, these DC imprint experiments suggest that the domain structure is affected by the slip bands and that there is a local interaction between the domain walls and the dislocations.

Despite the indication for a local interaction between dislocations and domain walls, no clear trend was observed in the temperature-dependent permittivity after plastic deformation. Moreover, a lower phase transition temperature (orthorhombic to tetragonal; $T_{o\text{-}t}$) was observed in the deformed samples than in the reference sample, and no clear trend was observed for T_c. This finding suggests that the dislocations favor the transition to the tetragonal phase, which would mean that the interaction between 60° domain walls and dislocations is not as strong as the interaction between 90° domain walls and dislocations. Notably, the hygroscopic nature of $KNbO_3$ [58] also affects electrical measurements, and therefore a less hygroscopic material is preferred for this type of experiments.

In conclusion, $KNbO_3$ is a suitable material to study the dislocation-based microstructural changes, but for a detailed study of the dislocation-based functionality the model ferroelectric $BaTiO_3$ is more appropriate.

Some of these results were published in a modified way in Ref. [257].

5.2 Dislocation-Based Functionality of $BaTiO_3$ Single Crystals

5.2.1 Initial Domain Structure and Configuration

The initial domain structure for each single crystal varies slightly. Most of them had a similar (but often less-pronounced) domain structure, as indicated in Figure 5.18a with an arrangement of 90° and 180° domain walls typical for $BaTiO_3$. The spontaneous polarization vectors lie in-plane (*a*-domains) at a 90° angle to each other (left surface in Figure 5.18a), forming a 90° domain wall, as depicted in Figure 2.15b. The front surface in Figure 5.18a features 180° domain wall watermarks. The domain structure in Figure 5.18b is a 90° rotated version of the domain structure in Figure 5.18a. Both single crystals show distinct 90° and 180° domain walls, magnified in Figure 5.18c and Figure 5.18d. The 90° domain walls in Figure 5.18d correspond to a combination of in-plane and out-of-plane (c-domains) spontaneous polarization vectors (see Figure 2.15b). All single crystals were in a polydomain state. The variation in the initial domain structure was related to the use of samples from different boules, a certain inhomogeneity in each boule and different cutting directions. Further examples of the initial domain configuration follow throughout this chapter.

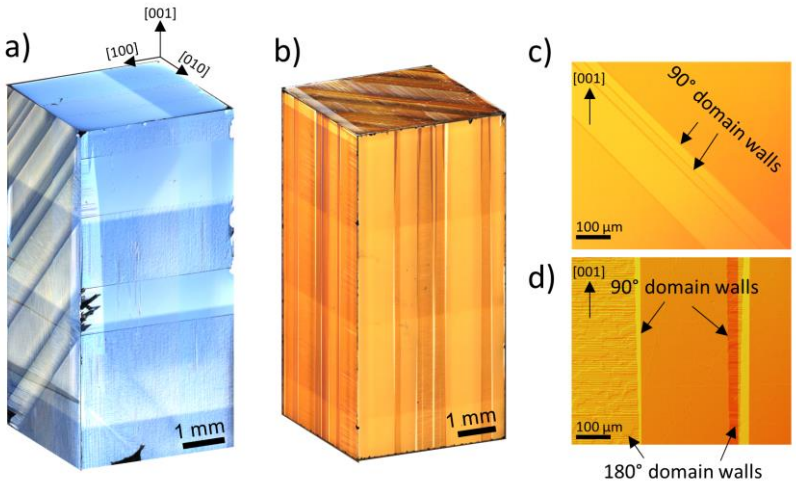

Figure 5.18: Initial domain structure of the [001]-oriented $BaTiO_3$ single crystals. a) A typical initial domain structure. b) An alternative initial domain structure. Examples of 90° domain walls and 180° domain walls are marked with black arrows in (c) and (d). 180° domain walls are visible only due to chemical etching of the surface during polishing, forming in (d) wavy lines and surface reliefs; straight lines between regions with different etching rates indicate 90° domain walls. All images are optical light microscopy images in DIC-mode (reflected light).

To avoid the influence of the initial domain structure, the samples of the same boule were chosen for direct comparison, where possible. Due to the large size of the single crystals and the limited size of the boules, a mixture of several boules could not be completely avoided. Therefore, the domain structure was documented carefully for every single crystal. The orientation of the single crystals was verified with Laue diffraction. The sample height of 8 mm is defined as the [001] orientation.

For the HT creep experiments, an influence of the initial domain structure was ruled out because the deformation was carried out in the cubic phase.

5.2.2 Creep Experiments

Creep experiments were carried out at [001]-oriented $BaTiO_3$ single crystals at temperatures in the range of 1050 °C to 1150 °C with Pt foils to reduce cracking. Selected deformation curves as a function of time are presented in Figure 5.19a and the corresponding stress-strain curves are displayed in Figure 5.19b. All creep experiments in Figure 5.19 were conducted at 1150 °C and a loading rate of 0.2 N/s. C-1150-30-2 has the lowest applied stress at 30 MPa (see Figure 5.19a), and thus also the lowest deformation strain. The creep experiment of C-1150-50 results in a nine-times greater deformation strain. The slope of the stress-strain curves varies for several measurements, which could be related to variations in the strain rate at a constant loading rate of 0.2 N/s. The deformation strain correlates with the applied stress level and the experiment duration. While the qualitative trend is valid, there is no quantitative statement possible for the $BaTiO_3$ due to the strain contribution of the platinum protection foils. As demonstrated by the comparison of the compression experiment of Al_2O_3 with Pt foils and the C-1150-40-2 measurement in Figure 5.19, a larger deformation strain is reached for the Pt-$BaTiO_3$ stack than for the Pt-Al_2O_3 stack (Al_2O_3 reference). Under the assumption that the platinum foil creep behavior is identical for both measurements, the comparison indicates a substantial strain contribution of the $BaTiO_3$ single crystal. This conclusion is reasonable because Al_2O_3 has in general a higher stiffness and compressive strength (R_c) compared to $BaTiO_3$. Values of $Y_{RT} \approx 410$ MPa [258] and $R_c \approx 2$ GPa [259] are reached for dense Al_2O_3, and $Y_{RT} \approx 115$ MPa and $R_c \approx 480$–913 MPa, for polycrystalline $BaTiO_3$ [260], assuming a similar relation at high temperatures. Moreover, single crystals are generally mechanically softer. As a consequence, the deformation of $BaTiO_3$ is qualitatively shown without the option to provide a quantitative deformation-strain value. Due to the overlap of the platinum strain and the $BaTiO_3$, an analysis of the strain rate and a determination of the steady-state creep regime are not feasible.

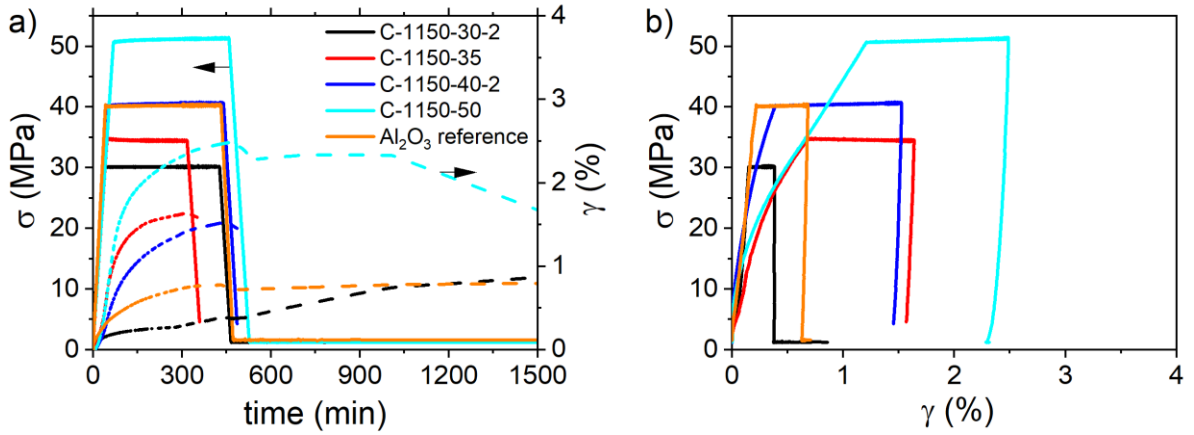

Figure 5.19: Creep experiments on [001]-oriented $BaTiO_3$ single crystals. a) Stress and strain as a function of time and (b) stress-strain curves for selected samples at 1150 °C.

5.2.3 Change of the Ferroelectric Domain Configuration

An overview of several single crystals with the initial domain structure (Figure 5.20a) and after deformation (Figure 5.20b) is presented in Figure 5.20. The presented faces in the 3D plots after deformation are the same as those of the undeformed samples in Figure 5.20a–f.

Therefore, a direct comparison of domain structure is possible. While only few 90° domain walls are visible before deformation with a distance of several hundred micrometers to millimeters (Figure 5.20a and Figure 5.20b), the number of visible 90° domain walls after deformation increases. Several deformed single crystals demonstrate newly formed 90° domain walls or slip planes, as indicated with a white line in Figure 5.20h.

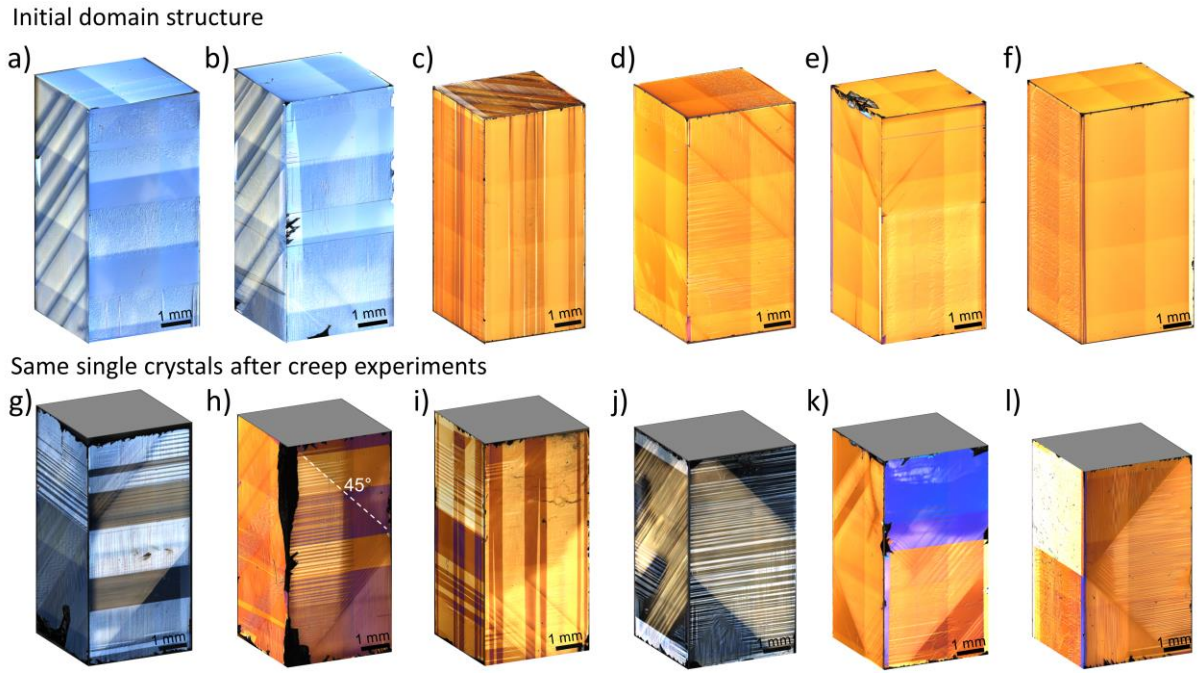

Figure 5.20: Comparison of the domain structure before (a–f) and after creep experiments (g–l). The single crystals positioned on top of each other are the same. The grey areas in g–l indicate that the samples were separated from the platinum protection sheets. The samples were loaded during the creep experiment with (g) 20 MPa, (h-i) 30 MPa, (j) 35 MPa, (e) 40 MPa and (f) 50 MPa. All samples were deformed at 1150 °C except (i), which was deformed at 1050 °C. Note that the DIC settings vary for some images to highlight the domain structure better.

For a better understanding of the polydomain state after deformation, the changes in domain structure are related to the {101}⟨101⟩ slip system available in $BaTiO_3$, schematically demonstrated in Figure 5.21. Four of the six slip planes of the {101}⟨101⟩ family reach a Schmid factor of 0.5. Two of them are marked in Figure 5.21b as blue planes running at a 45° angle inside the single crystals. Edge dislocations with the corresponding dislocation line and the Burgers vector are indicated in Figure 5.21b, sitting on the slip planes. The photography of the C-1150-30 sample in Figure 5.21c was taken shortly after the creep experiment was completed; the Pt protection foil remains visible on the bottom of the sample. The reflected light mode (Figure 5.21a) emphasizes the domain structure of the surface. The photo reveals an unusual, rhombic domain arrangement with clear and cloudy regions in the sample, caused by the mechanical imprint. Plastic deformation of $SrTiO_3$ single crystals in [001] orientation also creates a mechanical imprint of the {101}⟨101⟩ slip system. In the case of $SrTiO_3$ the slip planes are visualized with polarized light microscopy at an angle of 45° to the [001] edges [104]. In $BaTiO_3$ single crystals, no surface steps were observed, indicating that the plastic deformation is substantially lower; nevertheless, the arrangement of the ferroelectric domain walls highlights the mechanical imprint, indicated with the dashed line at a 45° angle in Figure 5.21a and Figure 5.21c. The nucleation and pinning potential of dislocations on domain walls has been suggested by phase-field simulation [32], TEM studies [31, 211] and near-field scanning

optical microscopy [184]. Based on this dislocation-domain wall interaction and the match of the slip plane orientation, the rhombic domain wall alignment correlates with the mechanical imprint, suggesting direct interaction between the dislocations and the domain walls.

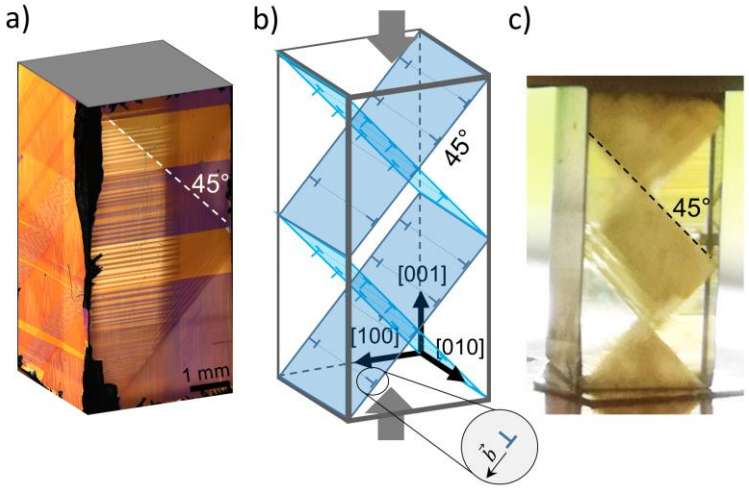

Figure 5.21: Rhombic structure in the deformed single crystals. a) DIC image of the C-1150-30-1 single crystal, (b) schematic of the active slip system with edge dislocations, dislocation line and Burgers vector and (c) photo of the C-1150-30-1 single crystal to highlight the rhombic structure. The white dashed line in (a) and black line in (c) indicate the rhombic structure.

The domain wall density [207] and the domain wall orientations are essential for the dielectric, piezoelectric and ferroelectric properties. Thus, the domain state of the cloudy and clear regions of the rhombic domain structure is depicted in Figure 5.22 for three samples: C-1150-30-1 (Figure 5.22a–e), C-1150-40 (Figure 5.22f–j) and C-1150-50 (Figure 5.22k–o). The rhombic structure is visible particularly in the photographs in Figure 5.22a, Figure 5.22f and Figure 5.22k. None of these single crystals had a cloudy region before deformation (see Figure 5.20b, e and f). The side faces, where the rhombic structure is clearly visible, are marked with A and C for the front and the back, respectively. The positions of the corresponding subfigures (Figure 5.22c–e, h–j and m–o) are sketched in the photos and 3D images (Figure 5.22a–b, f–g and k–l). In the clear regions (e.g. Figure 5.22c, d and o), fewer domain walls are observed, as compared to the cloudy regions. The domain walls that appear in the clear regions are mainly horizontally aligned and needle-like domain walls. In the cloudy region, the domain structure is more complex, as depicted in Figure 5.22I, Figure 5.22m and Figure 5.22g. 90° domain walls at a 45° angle to the compression axis are predominant in all cloudy regions, resulting in a high domain wall density (e.g. Figure 5.22i and m). Aside from the needle-like domains, some fine lines are also visible, marked with white arrows in Figure 5.22i–j and Figure 5.22m.

Domain walls normally nucleate and terminate at defects, inhomogeneities or other domain walls, but no obvious origin of the termination is visible for these fine domain walls. This absence raises the question of whether they are domain walls at all or rather, perhaps, a dislocation arrangement pinning domain walls. 90° domain walls would be visible as a herring-bone pattern, like it is the case in Figure 5.22h or as zig-zag-pattern [261, 262] (Figure 5.22o). Thus, probably the termination of the fine domain walls in Figure 5.22j is either correlated to domains inside the crystal or to slip planes, which are oriented in {101}⟨101⟩ directions and match the orientation of the fine domain lines in the cloudy region. Therefore, the domains were probably formed and pinned at the dislocations, leading to a locally high domain wall density. The clear and cloudy parts of the rhombic structure seem to reflect the internal stress,

strain or defect concentration distribution in the samples, to which dislocations can contribute substantially due to their local tensile and compression stress fields.

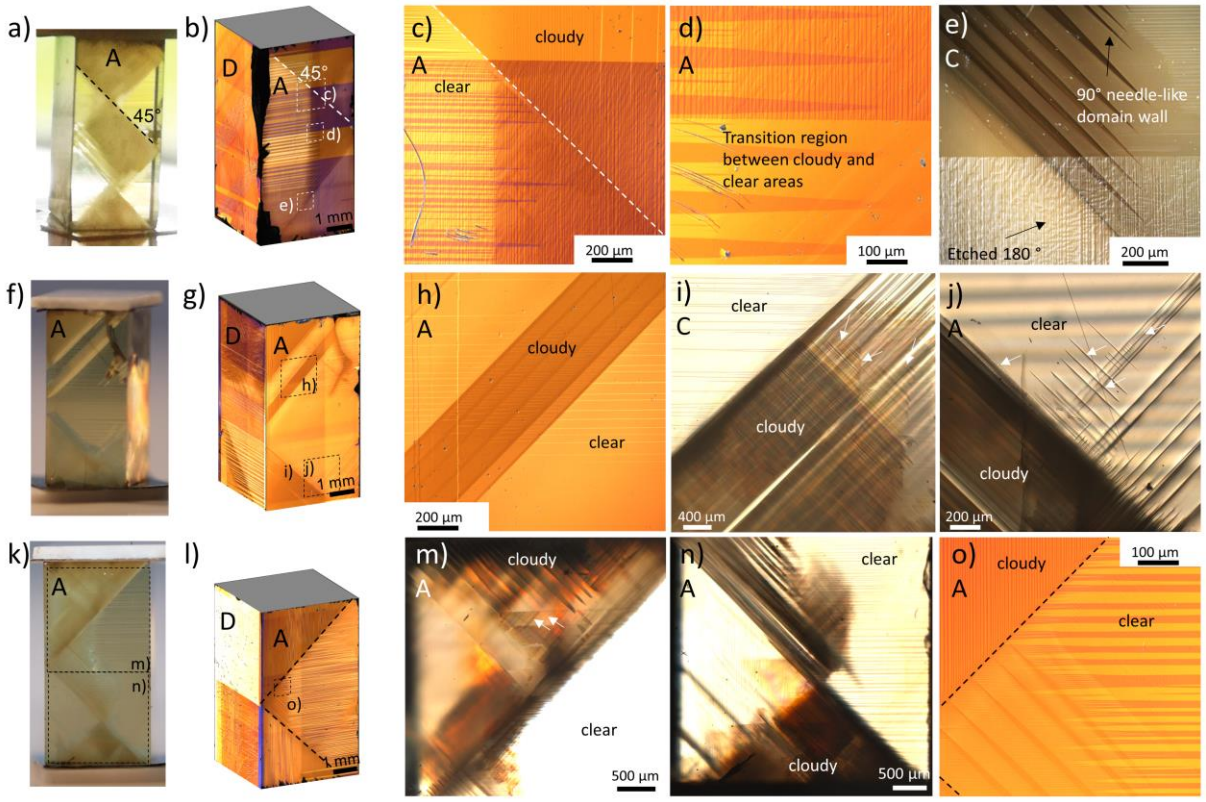

Figure 5.22: Rhombic domain structure of three deformed $BaTiO_3$ caused by mechanical imprint. Photography of the domain structure, a 3D image of the deformed single crystal and selected positions at the side face A (or C) are given for (a–e) C-1150-30-1, (f–j) C-1150-40 and (k–o) C-1150-50. Only the side faces with particularly visible rhombic structures are presented here in DIC or transmitted light mode. Cloudy and clear regions are indicated, and some domains are highlighted with arrows. Side face C corresponds to the back of side face A. The dashed rectangles indicate the regions, but not necessarily the precise position or size of the subfigures (c–e), (h–j) and (m–o).

Changing the perspective from A side (Figure 5.22) to B side, Figure 5.23 features a different view of the domain structure in the deformed samples. While the photos in Figure 5.22a and Figure 5.22k reveal a clear rhombic structure, the photos in Figure 5.23a, Figure 5.23e and Figure 5.23i present no clear domain structure. In contrast those of side A, the surfaces of B are partly covered with reliefs of etched 180° domain walls, which sometimes occur during initial polishing. Examples of the reliefs are marked with black arrows in Figure 5.23g and Figure 5.23l. The domain structure varies from thin horizontal and vertical domain walls (Figure 5.23c–d) to domain walls in a 45° angle in Figure 5.23g, Figure 5.23h, Figure 5.23k and Figure 5.23l. While the horizontal and vertical stripes can be traced back to small 180° domain reliefs, the white dashed lines in Figure 5.23c and Figure 5.23d suggest less dominant domain walls, identified as real domains.

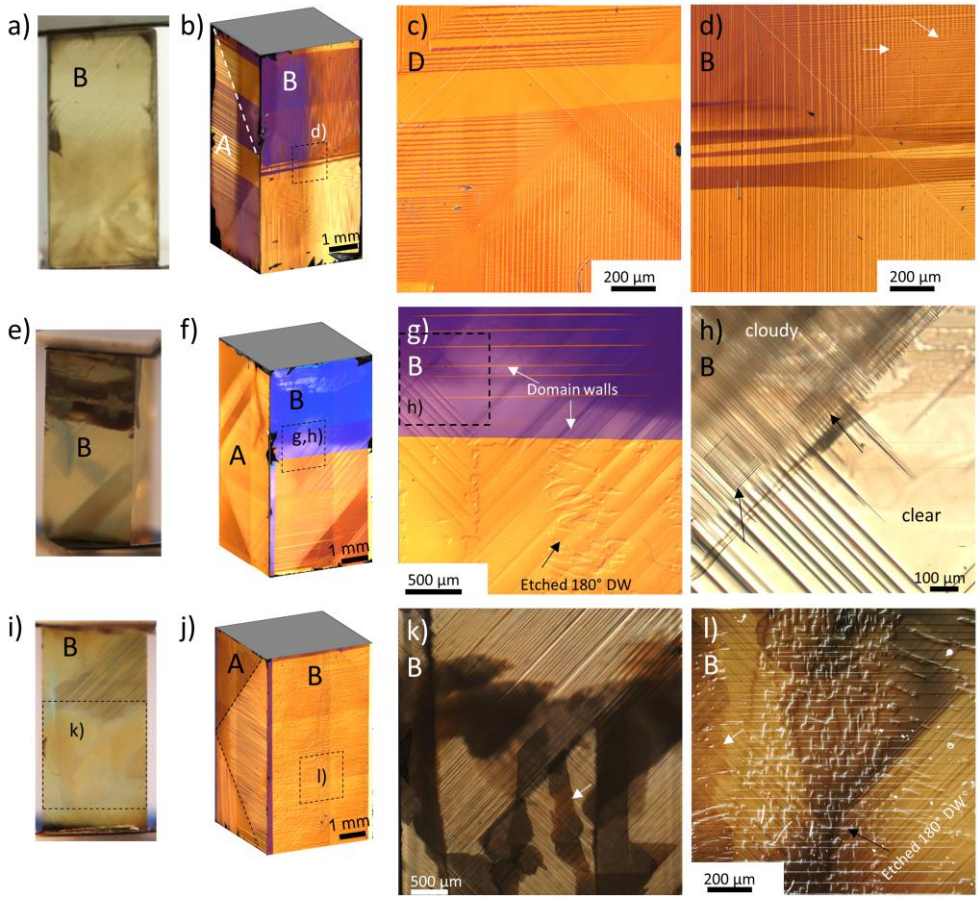

Figure 5.23: Different perspectives on the domain structure of three deformed [001]-oriented $BaTiO_3$ crystals caused by mechanical imprint. Photography of the domain structure, a 3D image of the deformed single crystal and selected regions at the side face B (or D) are given for (a–d) C-1150-30, (e–h) C-1150-40 and (i–l) C-1150-50. Please note that these are the same samples as in Figure 5.22 and that "A" indicates the corresponding surface. The white lines emphasize structures beneath the surface, which are not as obvious as the rest of the domain structure. Arrows point towards domain walls or locations with high domain wall density.

The separation of the surface in an upper part and a lower part, indicated by a color change in the DIC-images (Figure 5.23b, f), occurs regularly and is sometimes accompanied by a thin horizontal edge at the surface in the middle part. The transition between the upper and lower regions is highlighted in Figure 5.23d and Figure 5.23g traced back to a region with out-of-plane etched 180° domain walls and non-etched in-plane domain walls. Interestingly, this transition is, in most cases, more pronounced after deformation than before (e.g. see Figure 5.20e, f). While the transition in the color contrast between the upper and lower region can be neglected, the domain walls in a 45° angle (Figure 5.23g), which surpass this transition region, are correlated to new domain walls formed after deformation and are not affected by the reliefs. The domain structures in Figure 5.23g, Figure 5.23h, Figure 5.23k and Figure 5.23l indicate a predominant formation of domain walls at a 45° angle to the deformation direction. In optical microscopy, 180° domain walls are not visible. Hence, the domain walls with the 45° angle to the applied uniaxial stress are 90° domain walls (*a*-*c*-domain configuration). The 45° angle corresponds well with an optimal Schmid factor concerning the {101}⟨101⟩ slip system. Kontsos and Landis have elucidated in phase-field simulations that 180° and 90° domain walls align at a dislocation array of $\vec{b} = [\bar{1}10]$ [32]. Therefore, dislocations are likely the reason for the preferred orientation of the newly formed domains. Moreover, the face B surfaces display some

cloudy regions with fine domain structures, too, as exhibited in Figure 5.23h and Figure 5.23k. Cloudy regions were frequently reported in KNN-based single crystals [263] and were correlated to differently oriented domain walls in the orthorhombic phase They were also observed in $BaTiO_3$ single crystals [261] due to an overlap of domains. Nevertheless, the origins of those cloudy regions differ from that presented here.

In conclusion, the $BaTiO_3$ domain structure was considerably affected by the deformation process. While the undeformed single crystals were initially transparent and clear, the deformed ones exhibited a rhombic domain structure with clear and cloudy regions. Under consideration of the activated slip systems and the elimination of other effects, dislocations and the resulting internal stress configuration were identified as reasons for the domain-structure changes. Some of the single crystals tilted during deformation, resulting in a non-homogeneous loading condition (e.g., Figure 5.23a), and could favor and disfavor certain slip systems. This tilting led to a locally increased dislocation density. As a result, not all of the four equivalent slip systems with $m = 0.5$ were equally activated, leading to an imperfect rhombic domain structure over the whole sample. Further, the density of the visible 90° domain walls was increased in the cloudy regions, which is expected to affect the piezoelectric properties in the material.

5.2.4 In-Plane and Out-of-Plane Domain Contributions

Nuclear magnetic resonance spectroscopy analysis was carried out by Pedro Groszewicz to determine the relative number of domains before and after deformation. A reference sample with a domain structure similar to that shown in Figure 5.20a–b (inset in Figure 5.24a) was compared to a $4\times1\times8\,mm^3$ large piece of the deformed C-1150-20 sample, given in Figure 5.20g. While the reference sample has a greater tendency to form an in-plane domain arrangement (a_1-a_2), the amount of out-of-plane contributions is increased to more than 65% after deformation, pointing towards an a_1-c or a_2-c-domain arrangement (Figure 5.24). The schematic in Figure 5.24b demonstrates a simplified domain arrangement for 90° domain walls, corresponding to the slip planes of the {101}⟨101⟩ system. Slip planes with a Schmid factor of 0.5 (black) tend to result in a_1-c or a_2-c-domain arrangements, while a Schmid factor of 0 would lead to a_1-a_2 combinations. The observed predominance of out-of-plane c-domains is thus the result of the slip planes with $m \neq 0$. These slip planes are the only active ones, providing dislocations, and they can act as pinning sites for domain walls. Therefore, NMR evaluation supports the observed tendency that domain walls on {101} plane are dominant, as already identified by optical light microscopy.

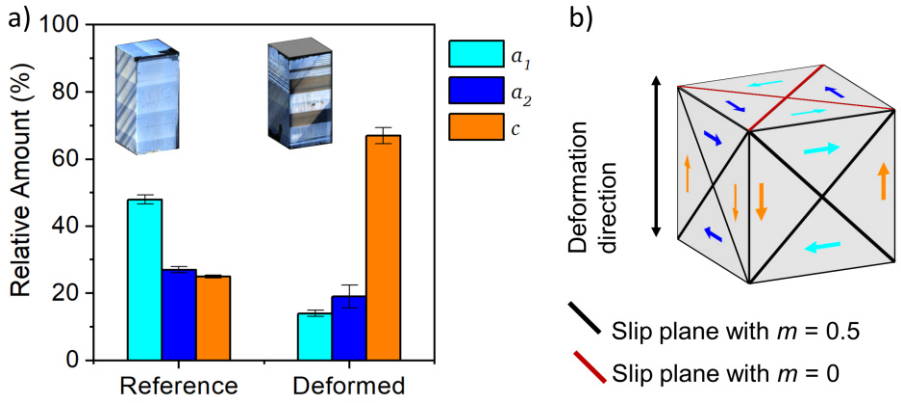

Figure 5.24: a) Nuclear Magnetic Resonance results for a reference and a deformed sample. b) Simplified schematic of a spontaneous polarization vector configuration assuming only 90° domain walls. The black and red lines correspond to different slip planes of the {101}⟨101⟩ slip system with Schmid factors 0.5 (black) or 0 (red). These lines also indicate the orientation of the 90° domain walls for the in-plane polarization vectors (a_1 and a_2) and out-of-plane P_s (c).

5.2.5 Dislocations and Slip Systems in $BaTiO_3$

Although optical light microscopy and NMR spectroscopy suggest the presence of mechanical imprint, direct proof is pending. Thus, ECCI was carried out to provide information on the dislocation orientation and the spacing between the dislocations. The sample was cut out from the inner part of the deformed single crystal, as indicated in the schematic in Figure 5.25a with the dashed square **b**. The (101)[10$\bar{1}$] slip plane is marked in blue with white shading effects indicating the dislocations moving on the slip plane in the [10$\bar{1}$] direction and cutting the ECCI-sample surface along the [0$\bar{1}$0] direction, as indicated in Figure 5.25b. Dislocations (white dots) are marked with arrows and are distributed over the slip plane. Moreover, a reference measurement was performed at a position without slip planes to elucidate the difference between the appearance of domain walls and slip planes in ECCI (Figure 5.25c). The 180° domain wall reliefs provide a sharp black/white contrast, but no color difference is obvious between the domains, which had initially formed the 180° domain walls. Without relief, 180° would not be visible in ECCI, due to the missing contrast in the backscattering response. 90° domain walls, in contrast, are clearly visible as broad lines (marked in Figure 5.25c) running in parallel, as observed in the undeformed BT samples with OLM. The interpretation of dislocation structures with ECCI provides several pitfalls, mainly due to the limited availability of reference options to other perovskites studies. Therefore, benchmarking was performed with indentation experiments on $BaTiO_3$ (100) surfaces. The spherical indent[3] was removed by polishing, and the dislocation structure beneath was examined with ECCI, as presented in Figure 5.25d. Such alignment of the slip planes and dislocations, as shown in Figure 5.25d, is well-known for oxides like MgO [264], $BaTiO_3$ [116, 265] and $SrTiO_3$ [266, 267]. The dislocation spacing in the crept sample is in the range of 80–450 nm (Figure 5.25b), within the same order of magnitude as the dislocation spacing in plastically deformed $SrTiO_3$ single crystals with 225–1000 nm [242]. Indentation creates smaller dislocation spacings directly beneath the indent, as indicated in Figure 5.25d or determined with the etch pit method for $SrTiO_3$ [117].

[3] 20 μm, strain rate controlled 0.05 1/s

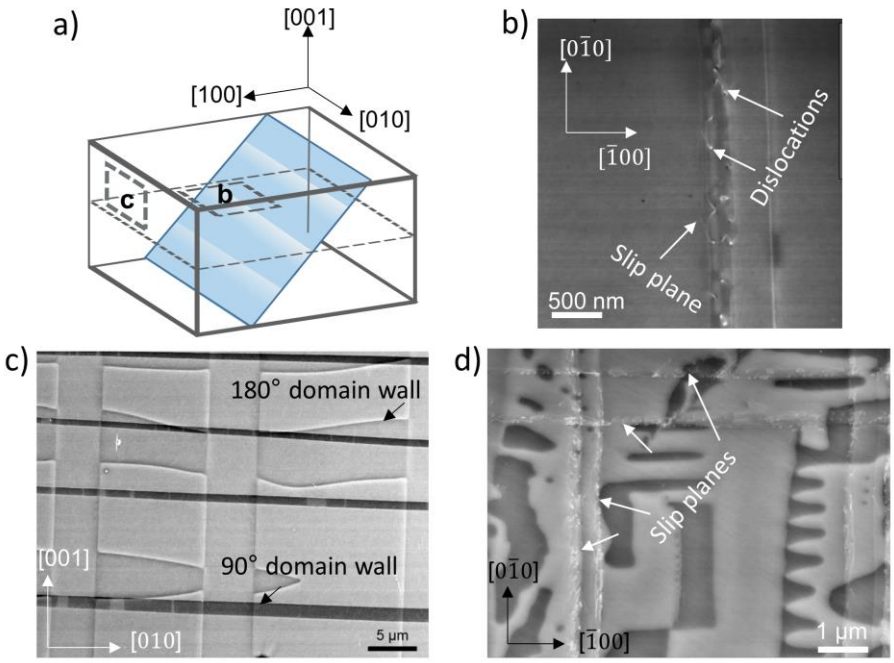

Figure 5.25: Visualization of the dislocation structures with electron channeling contrast imaging (ECCI). a) Schematic of a slip plane. Dislocations are emphasized with white arrows in (b) and ferroelectric domains with black arrows in (c). 90° domain walls have a dark/bright contrast, while 180° domain walls are wavy lines, chemically etched by the polishing suspension. Dislocations form bright spots in the ECCI image (b) and (d), the low contrast trails indicate that the dislocations reach the surface at a 45° angle from underneath. Beneath a spherical indent, the same slip system on a (100) $BaTiO_3$ surface is active. Therefore, such an indent is given for benchmarking in (d).

The {101}⟨101⟩ slip system and edge dislocations with $b = a[101]$ were confirmed with TEM by Xiaoli Tan and his team. The results coincide with the slip system and dislocation type in other perovskite materials [88]. Thus, evidence of dislocations in a specified slip system in $BaTiO_3$ single crystals was provided with ECCI and TEM, supporting the explanation of the rhombic structure formation and the mechanical imprint via dislocation-based creep mechanism.

5.2.6 Electrical Measurements

5.2.6.1 Temperature-, Frequency- and Field-Dependent Permittivity

The dielectric response of a $BaTiO_3$ is affected by the crystal structure [145], grain size [268-270], crystal orientation [271], domain size [209], point defect doping and anisotropy [6, 272]. Therefore, measuring the permittivity and dielectric loss of the single crystals facilitates the evaluation of the influence of dislocations on the dielectric properties. The permittivity (solid lines) and tanδ (dashed lines) are presented in Figure 5.26 at different frequencies as a function of temperature for a reference and a part of the deformed C-1150-20 sample. The permittivity of the reference sample is at room temperature in the range of 2040 for all frequencies, while the deformed sample reaches only 830. $BaTiO_3$ single crystals have a strong anisotropy of the permittivity; along the tetragonal *c*-axis, a value of 130 is reported, while the *a*-axis (and *b*-axis, perpendicular to c-axis) can reach a permittivity of 4000 [6, 271-273]. The single crystals are both unpoled and in a multi-domain state, resulting in permittivity values between the

mentioned literature values. Thus, the single crystal orientation is the same, and only the domain size, density and orientation affect the permittivity. The lower permittivity of the deformed sample (Figure 5.26) suggests a predominant *c*-domain configuration, which is in good agreement to the NMR data.

With increasing temperature, the permittivity first decreases slightly before it increases for the deformed sample until T_c is reached. In the frequency ranges presented here, several mechanisms can contribute to the response, such as ionic polarization, orientation polarization and extrinsic domain wall contributions [274]. With increasing temperature, the extrinsic contribution to the dielectric permittivity increases, while the intrinsic contribution is temperature-independent as long as the lattice parameter is not changing (e.g., due to a phase transition) [275]. The resulting trend between permittivity and 90° domain walls depends also on the ratio between *a*/*c*-domains and is therefore not straightforward to define [6, 276]. The OLM results indicate a substantial amount of 90° domain walls in the deformed sample, but due to the multidomain state, a clear trend is not obvious; this absence of a trend also correlates with a lack of precise knowledge about the domain wall density in the samples. More drastic than the changes in permittivity is the frequency-dependent behavior of tanδ. The dielectric loss of C-1150-20 is always greater than for the reference sample, which is even more pronounced at 0.1 kHz. At such low frequencies, the system has more time to react; therefore, slower defect types can also respond.

The T_c of the reference sample, $T_c = 132$ °C, is in good agreement with the T_c of 132 °C reported by Wada et al. [209]. After deformation, T_c is with 131 °C slightly shifted to lower temperatures for the deformed sample. This trend is contrary to the results of Qi et al., who found indications that the stress-field of dislocations could raise the Curie temperature in $KNbO_3$ single crystals [31].

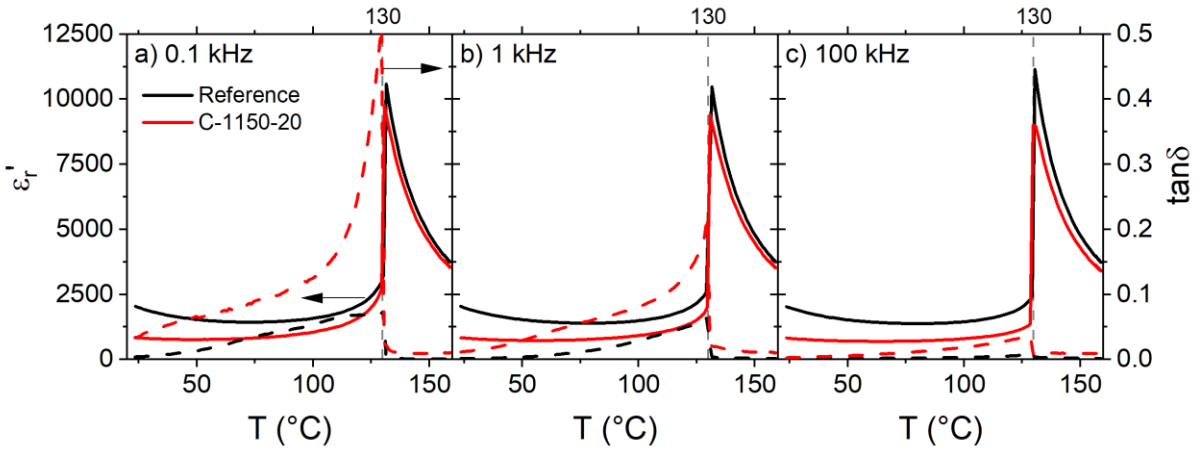

Figure 5.26: Temperature-dependent permittivity and dielectric loss for an unpoled reference and an unpoled deformed sample (C-1150-20) at (a) 0.1 kHz, (b) 1 kHz and (c) 100 kHz. All measurements were carried out at 1 V.

Following the temperature-dependent permittivity measurements, samples were annealed again, and frequency-dependent permittivity measurements were carried out. In the unpoled state (Figure 5.27a), the samples remain in a multi-domain state, but now the permittivity levels are in the range of 2500–3500 for all samples, indicating a change in the domain density or distribution during annealing. The imaginary part of the permittivity increases below 100 Hz. The permittivities remain in the range of 150–4000, as discussed before, but with a higher *a*-

domain contribution for both the reference and the deformed sample. Interestingly, the reference sample still has higher permittivity values than the deformed samples, as indicated in the NMR data (Figure 5.24a). Despite the annealing, the trend persists, indicating that the domain state is influenced by some intrinsic, temperature-stable defects such as the introduced dislocations.

After poling, the reference sample reaches ε_r'=150 (Figure 5.27b), indicating an almost perfect c-axis domain configuration and the reduction of the domain wall density after poling [6]. Both deformed samples C-1150-20 and C-1150-30-1 are in the range of 670–770, which points either towards a substantial extrinsic contribution with only a slight reduction of the domain wall density of 90° domain walls or to a change in *c/a* ratio. Morozov et al. attribute the dispersion in permittivity to ionic conduction based on oxygen vacancy hopping [196]. Nevertheless, it is unlikely that oxygen hopping could explain the changes here, because no point-defect doping was carried out. Another possibility is strain incompatibility in the sample, caused for example by a dislocation-related *a/c*-domain mismatch, which is discussed in Section 5.2.8.

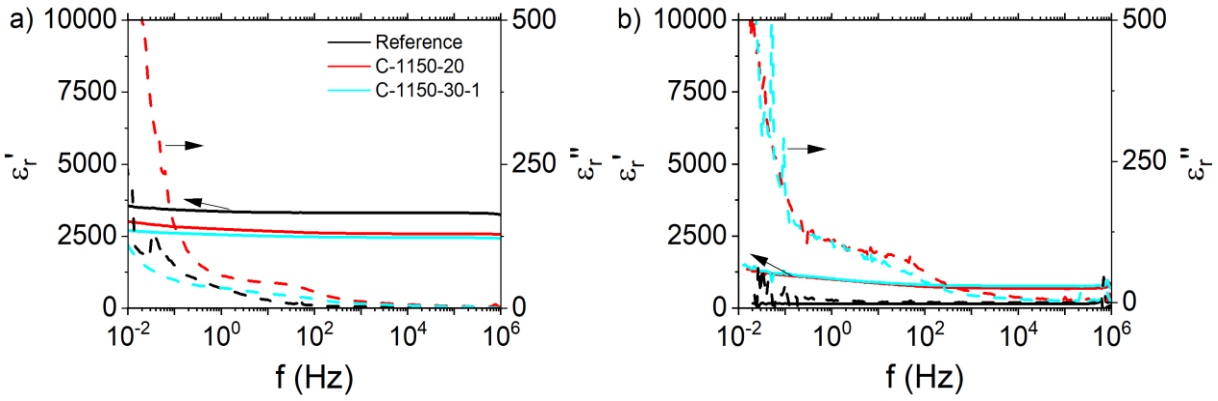

Figure 5.27: Frequency-dependent permittivity at room temperature for (a) unpoled and (b) poled samples. Poled samples were measured at the same day as they were poled.

The dielectric response depends not only on temperature and frequency, but also electric field. This dependence can provide insight into the reversible and irreversible extrinsic domain wall contributions, as briefly discussed in Section 2.2.2.4.

For the field-dependent measurements (Figure 5.28), only poled samples were investigated. As already discussed in Figure 5.27a, the permittivity of the reference sample remains constant while the applied AC electric field increases. None of the samples in Figure 5.28a indicate any changes in permittivity below 15 V/mm, but above this electric field, both deformed samples feature an increase in permittivity, while the reference value does not change. In order to highlight this strong increase, the applied AC field in Figure 5.28b is normalized to the apparent coercive field E_c* (at 1 kV/mm) for each sample, respectively. E_c* corresponds to the coercive field value in the second cycle of the polarization loop at 1 kV/mm, as discussed in the next chapter. The increase in permittivity begins for both deformed samples even before reaching 20% of E_c*.

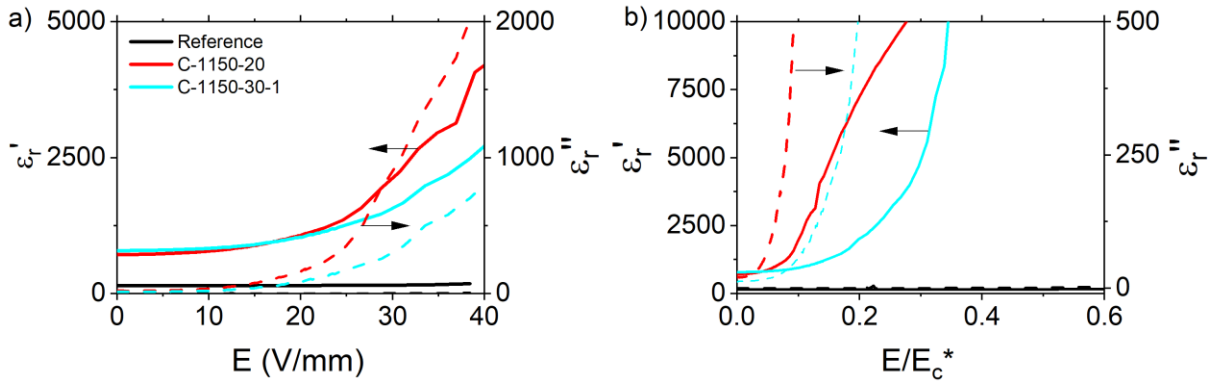

Figure 5.28: AC-field-dependent permittivity of poled reference and two poled deformed samples at 1 kHz, (a) as a function of applied electric field and (b) as a function of the applied electric field normalized to the respective E_c* (apparent coercive field at 1 kV/mm).

The dielectric nonlinearity is a typical feature of ferroelectric materials and is primarily caused by the displacement of domain walls [277]. Hard ferroelectrics (e.g., Fe-doped PZT) exhibit a limited high-field response, while for soft doping (e.g., Nb-doped PZT), the increase is much more pronounced [190]. Nevertheless, the dielectric response increases continuously with increasing electric field. This behavior can be interpreted based on the Rayleigh relation if the point defects are distributed randomly. However, the data in Figure 5.28a and Figure 5.28b corresponds more to an exponential increase. The ideal Rayleigh response (Equation 2-14) requires a random distribution of the pinning centers causing hysteretic behavior due to nonlinear displacement of the domain walls [278, 279]. Hard ferroelectric ceramics in the conventional sense (point-defect doping) do not follow the ideal Rayleigh law, and their potential well is described by only one minimum instead of a random potential with several minima based on the stabilization and pinning of domain walls by stabilized defects [191]. Therefore, the contribution of the domain walls depends on the orientation of the defects. Similar to point defects, line defects also affect the potential landscape and provide pinning centers for domain walls causing a non-typical Rayleigh behavior. Despite this similarity, dislocations will not reorient with an applied electric field, as it is the case for point defects. Neither the pinning force provided by dislocations, nor point defect–domain wall interactions are sufficient to explain the strong increase at a certain field. This indicates that another, stronger force also contributes to the response.

5.2.7 Piezoelectric and Ferroelectric Properties

5.2.7.1 Polarization Loops at Subcoercive Field

Subcoercive field nonlinearity (as displayed in Figure 5.28) and subcoercive field hysteresis are sensitive to defect-mediated effects [190]. In this section, subcoercive field hysteresis loops are used to investigate the field-dependent polarization behavior of an unpoled deformed (Figure 5.29a and Figure 5.29b, C-1150-20) and an unpoled reference sample (Figure 5.29c and Figure 5.29d) at 1 Hz and 1 kHz. The hysteresis loops for the deformed samples at 1 Hz are slim at low electric fields and become more open with increasing electric fields. Such hysteresis represents a substantial domain wall motion contribution and indicates Rayleigh-like behavior, as shown in PZT thin films [280]. The slight asymmetric polarization response to a symmetric

electric field indicates the presence of pinning centers in the material, which causes domain wall motion across an asymmetric energy landscape [281]. At higher frequencies, the polarization loops are pinched. The pinching is more pronounced at 1 kHz and disappears at 1 Hz. Such a pinching is not considered in an ideal Rayleigh behavior and indicates that the pinning centers are not equally distributed, which is a requirement for an ideal Rayleigh behavior [150]. In contrast, the reference sample has a linear field dependence, which is frequency-independent and correlates well with the constant permittivity and increasing electric field, discussed in the previous section. The applied electric field for the reference sample exceeds the critical coercive field for this sample, which is determined in the next section with supercoercive field hysteresis loops. Nevertheless, the sample still indicates a linear relationship between the applied electric field and polarization. Such behavior was detected in several undeformed single crystals before, especially in the first loops of the large-signal hysteresis measurements, indicating a barrier for the "first" domain wall switching, which is not yet fully understood.

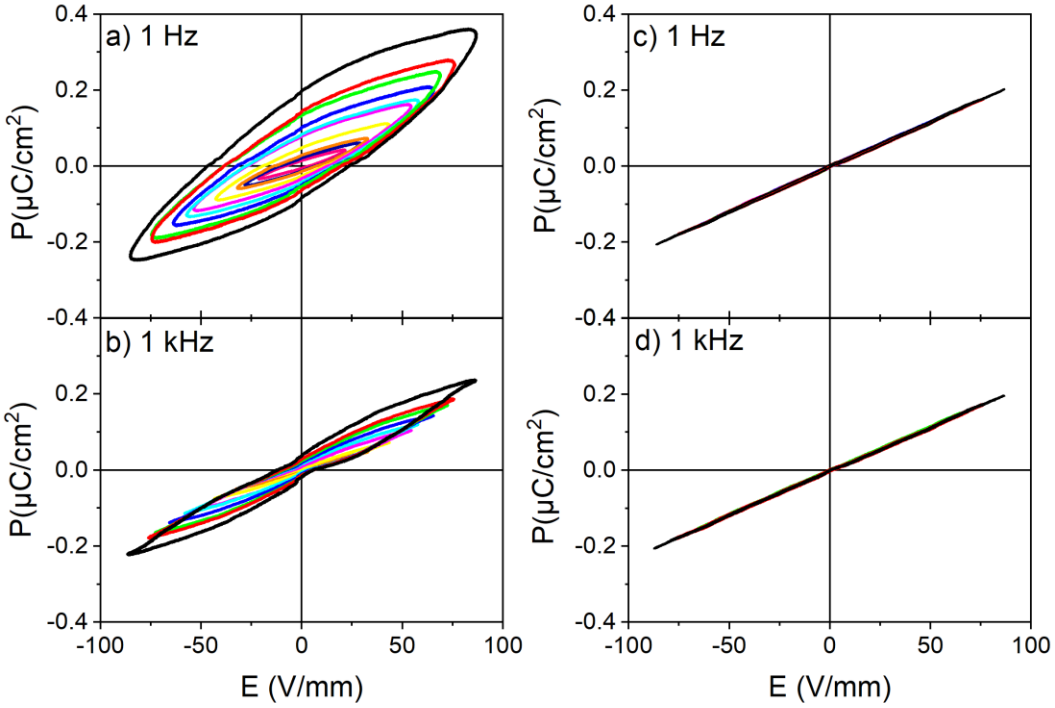

Figure 5.29: Subcoercive field polarization loops for unpoled deformed sample C-1050-20 at 1 Hz (a) and 1 kHz (b) and an unpoled reference sample at 1 Hz (c) and 1 kHz (d).

5.2.7.2 Polarization Loops at Supercoercive Field

Figure 5.30 displays the bipolar polarization and strain measurements at different electric fields for a reference sample (Figure 5.30a) and C-1150-20 (Figure 5.30b). The polarization hysteresis of the reference sample has a well-defined and saturated shape reaching a maximum polarization of 26 μC/cm² and an E_c of 0.06 kV/mm. In the virgin curve (first cycle) the switching of the domains occurs at 0.24 kV/mm. In the second cycle and for all further measurements, the apparent switching field corresponds to the given E_c* value. Typical butterfly loops are depicted for the bipolar strain loop measurements of the reference sample, with a slight asymmetry between the left and right wing. The polarization hysteresis loops after

deformation differ considerably from the reference loops. With increasing electric field, the E_c, P_{max} and P_r increase as well, and a pronounced asymmetry appears in the strain loops. Strain exceeding 0.6% is reached for the negative applied field. The reference sample is already saturated at 0.5 kV/mm, but the deformed sample still has substantially lower P_{max} values with 13.8 μC/cm². Since the loops of deformed samples are not saturated at any measured field, the E_c, P_{max} and P_r will be described as apparent E_c*, P_{max}* and P_r* (marked with * in the following discussion).

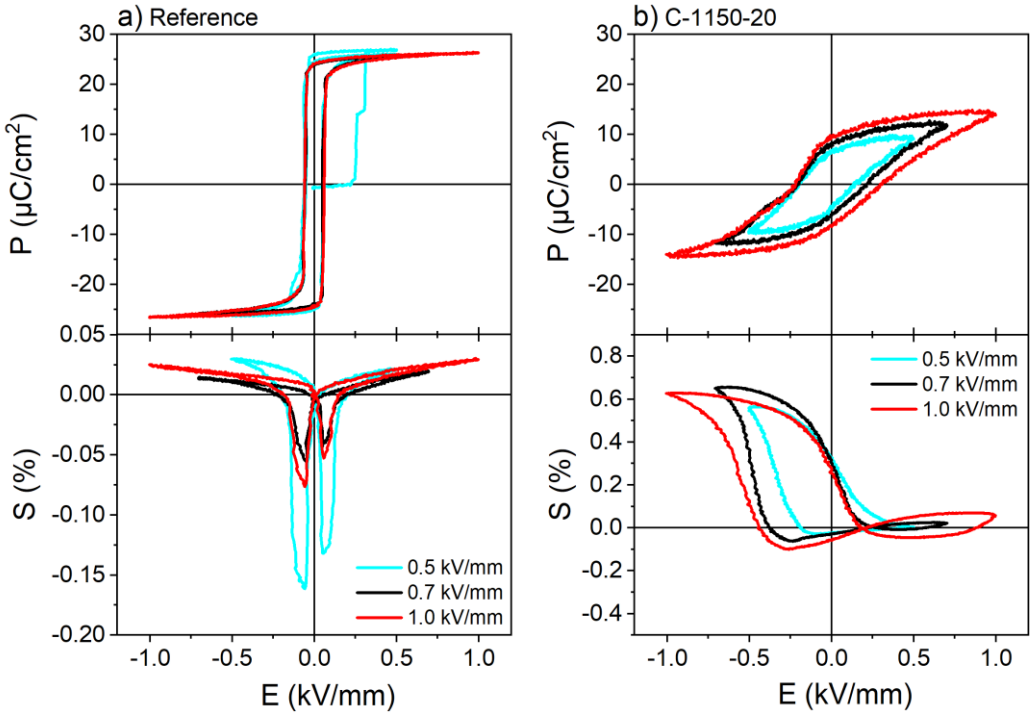

Figure 5.30: Large signal hysteresis for (a) reference and (b) deformed C-1150-20 sample, measured at 1 Hz.

For several reference samples and some of the deformed samples in Figure 5.31, E_c*, P_{max}* and P_r* are listed. Note that "Reference B" was the sample used as a reference for all electrical measurements. Reference 1150 °C was thermally treated to ensure no influence of the temperature on the deformed samples. All reference samples have an electric-field-independent E_c*, P_{max}* and P_r*, in contrast to the deformed samples, which indicate an increase in E_c*, P_{max}* and P_r* with increasing electric field. For the latter, E_c* at 1 kV/mm was used as normalization value for the other electric measurements (e.g., Figure 5.28b).

The ratio between P_{max}* and P_r* points towards a strong domain back-switching, and reaches a four-fold increase for the C-1150-20 sample, as compared to Reference B, indicating a restoring force acting on the switched domains. The lower maximum polarization and the increase in apparent coercive field values of all deformed samples imply domain wall pinning.

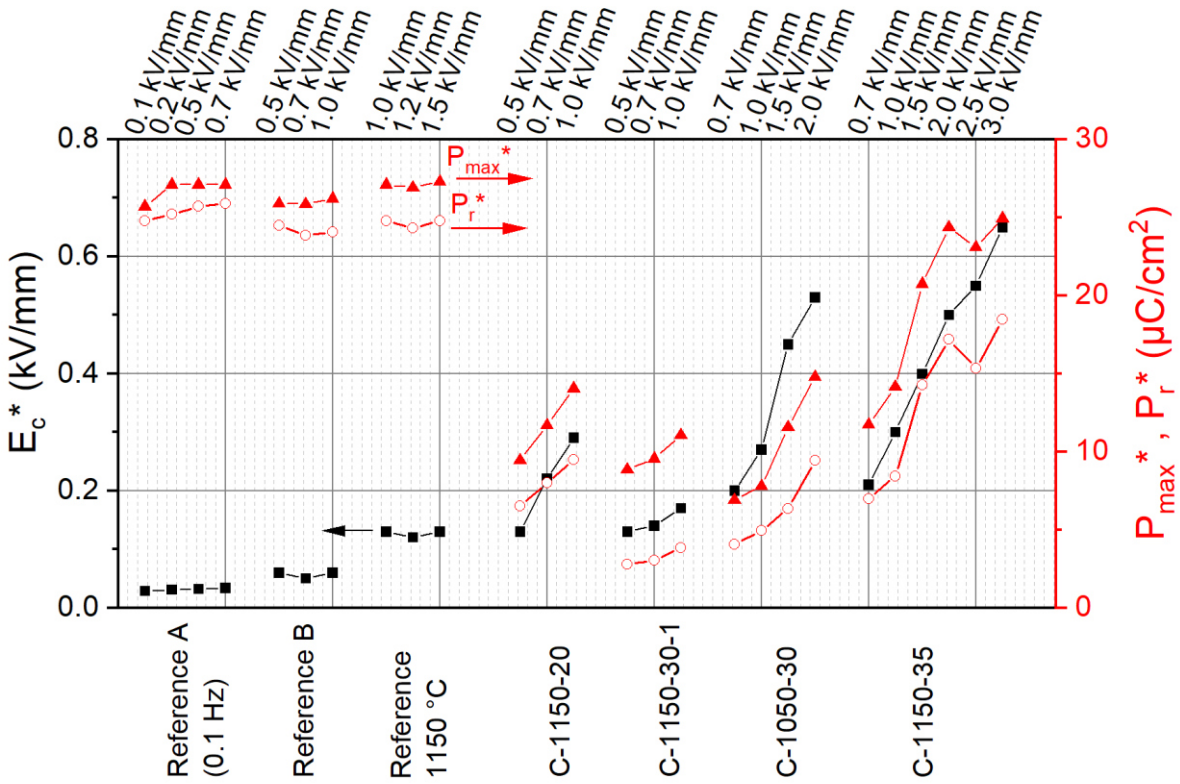

Figure 5.31: Comparison of the large-signal polarization behavior of the reference and selected deformed samples to visualize the trend in E_c*, P_{max}* and P_r*. All measurements were carried out at 1 Hz, if not otherwise mentioned. The presented values correspond to the second cycle. The electric fields on top correspond to the amplitude of the triangular applied electric field. The E_c* at 1 kV/mm is used as a normalization value for some of the other electrical measurements.

For all deformed samples, the apparent coercive field increases with increasing applied maximum electric field. The maximum theoretical polarization of 26 μC/cm² was only reached in the range of 3 kV/mm for the deformed samples, as presented in Figure 5.32. Both P_{max}* and E_c* for Reference B are marked with dashed lines in Figure 5.32. All reference samples depict E_c* independent of the supercoercive field. The deformed samples have a broad distribution of local coercive fields, which probably depend on the local variation in the dislocation density, resulting in a skewed polarization loop and a high portion of back-switching. This behavior makes E_c* and P_{max}* dependent on the electric field.

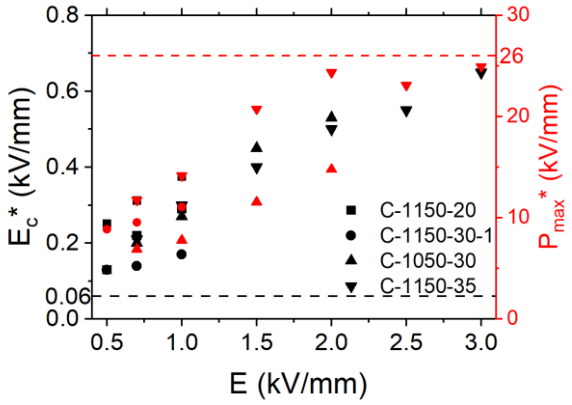

Figure 5.32: Trend for E_c* and P_{max}* for selected deformed samples.

5.2.7.3 Piezoelectric Coefficient

The large signal d_{33}^* was determined for a poled reference sample (Figure 5.33) in the range from 0 to 50 V/mm, corresponding to 83% of E_c^* (E_c^* = 60 V/mm). The electric field presented in Figure 5.33 is normalized to this E_c^*, while the original fields are attached in the appendix (Figure 7.6), together with ε_r. With a d_{33}^* in the range of 100 pm/V, the reference value agrees well with reported experimental values of 85.6 pm/V [282], 90 pm/V [271] and 128 pm/V [283], along with those predicted by the Landau–Ginzburg–Devonshire approach (86.3 pC/N [284], 99.8 pC/N [201]). In general, d_{33}^* has linear and non-linear lattice and domain wall contributions. A small increase in d_{33}^* with increasing electric field (98 pm/V up to 103 pm/V) indicates only a limited linear contribution. No evidence of nonlinear contribution is found, indicating that 90° domain wall motion does not occur at such low fields. This finding corresponds well to the results of the subcoercive and supercoercive polarization measurements. The linear contributions to the piezoelectric coefficient are a combination of intrinsic effects (lattice), reversible domain wall motion and a linear coupling mechanism between electrical conductivity and piezoelectricity (e.g., Maxwell-Wagner effects) [285-288]. Due to the limited linear response, a strong contribution of this mechanism is excluded, and only 180° domain walls are assumed to respond to the field, if at all. Nevertheless, it should be mentioned that the corresponding ε_r indicates an increase with field and a strong hysteresis while reducing the electric field (see appendix, Figure 7.6b), which could point towards a reorientation of defect dipoles. These changes are not reflected in the d_{33}^* behavior.

To investigate the field-dependent nonlinearity of the deformed sample, the d_{33}^* was measured after poling at several positions on the samples and on both electrode-covered surfaces (Figure 5.33a). The electric field is normalized to E_c^* (290 V/mm) in both subfigures, while the non-normalized data of the deformed sample is presented in the appendix (Figure 7.7). After poling, the d_{33}^* fluctuates in a position-dependent manner from 65 pm/V to 138 pm/V and exhibits a field-independent behavior until approximately $0.1E/E_c^*$ (20 V/mm). Above $0.1E/E_c^*$, a strong increase in d_{33}^* occurs. While the first measurement (A, position 1) reaches a value of d_{33}^* = 1901 pm/V at $0.17E/E_c^*$, values at other positions vary between 511 pm/V and 2734 pm/V, indicating that the measurements are sensitive to positioning and poling conditions. The measurements were performed with increasing and decreasing electric fields, resulting in a slim d_{33}^*-hysteresis. Note that ε_r values demonstrate similar slim hysteresis behavior (Figure 7.8). The piezoelectric nonlinearity, in combination with the hysteresis loop, implies a certain degree of irreversible 90° domain wall motion and suggests a rearrangement of pinning centers [287]. Nevertheless, the slim d_{33}^* hysteresis indicates a predominantly reversible domain wall motion. Otherwise the loop would be substantially broader. The increase in d_{33}^* with field additionally points towards an increased number of 90° domain walls compared to the reference sample, which can occur for several reasons, such as dislocations acting as nucleation sites or insufficient poling of some 90° domain walls. Figure 5.31 makes obvious that the deformed single crystals have not reached a fully poled state, which resulted in a certain percentage of non-switched 90° domain walls. Nevertheless, the pinning of the domain walls at dislocations is suggested as a reason for the non-saturated poling condition.

The results presented in Figure 5.33 indicate a position-dependency, which remains even after annealing and re-poling (Figure 5.33b). Indeed, the decrease in d_{33}^* after re-poling indicates that the 90° domain wall switching contribution differs between the two poling steps. The

position-dependency persists after re-poling, as well, pointing to a heterogeneous domain distribution beneath the surface. As shown in Section 5.1.3 for $KNbO_3$, slip planes are not homogeneously distributed over the whole sample. Therefore, local variation in the properties is likely, which explains the position-dependency in the sample. Additionally, in the previous sections, it was shown that the 90° domain wall density increases due to the smaller domain sizes. Wada et al. [23] identify that d_{33} is inversely proportional to the domain size. Therefore, the local domain size can indeed affect the d_{33}* values, especially since not all domains were either aligned during poling or switched back after poling. This partially poled state is indicated in Figure 5.31 with a four-fold domain back-switching ($\Delta P = P_{max}$*–P_r*), suggesting a macroscopic restoring force acting on the domain walls. Due to the restoring force, some of the domains back-switch which increases the reversible behavior. Furthermore, it may indicate that some domains are pinned at dislocations [32].

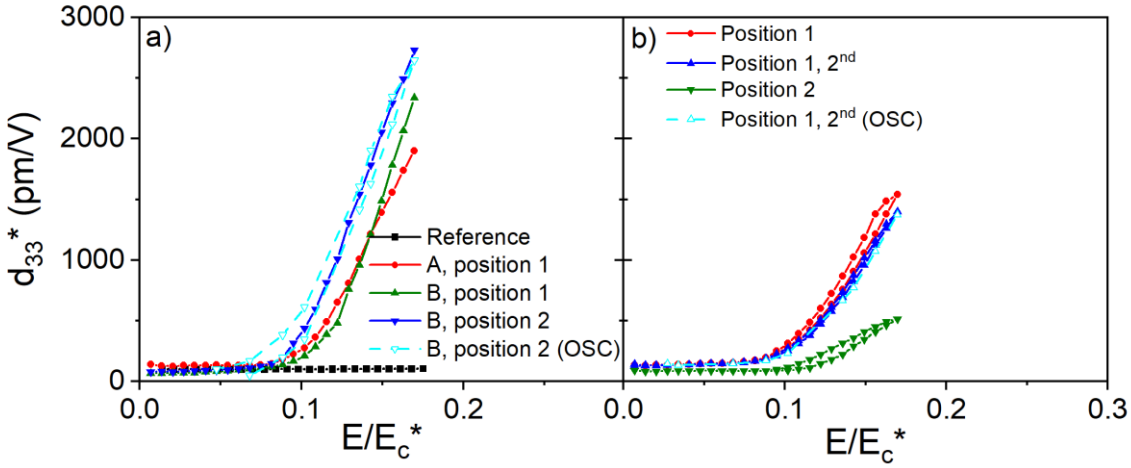

Figure 5.33: d_{33}* of a poled reference sample and the poled deformed C-1150-20 sample, measured at 1 kHz. a) The reference data are presented together with the first poling of the deformed sample. b) Afterwards, the deformed sample was annealed and re-poled to test the reproducibility. A and B correspond to the two electroded surfaces of the deformed sample. OSC marks the measurements, which were read out with the oscilloscope, while a lock-in amplifier was used for all other measurements. 2nd indicates that position 1 was measured several times to investigate the stability of the values. All electric fields are normalized to the apparent coercive field E_c* at 1 kV/mm (Figure 5.31). The non-normalized data of d_{33}* and the corresponding permittivity are presented in the appendix for the reference sample in Figure 7.6 and for the deformed sample in Figure 7.7 and Figure 7.8.

5.2.8 Discussion: Dislocation-Based Functionality

This section primarily demonstrates that dislocations have been introduced and that they can act as nucleation and pinning sites for domain walls, as simulated by Kontsos and Landis [32]. In addition, the changes in electromechanical properties on the macroscopic scale are discussed, and the underlying mechanism is explained.

Uniaxial compression at high temperatures activates dislocation-creep along the {101}⟨101⟩ slip system. This mechanical imprint changes the macroscopic domain structure from a conventional to a rhombic alignment with cloudy and clear regions in a multidomain state. The preference for *a*-*c*-domain configurations after deformation was confirmed by NMR spectroscopy, indicating a preferred alignment of the spontaneous polarization vectors relative to the four slip planes with a Schmid factor of 0.5. These results provide indirect but strong indications of dislocations as possible sources of the observed changes in microstructure.

In-situ TEM was carried out by Xiaoli Tan and his team to investigate the nucleation and pinning behavior of domains at a curved dislocation. A TEM-sample, prepared from the deformed C-1150-20 sample, was heated to 220 °C ($T_c = 130$ °C), and the domain nucleation was investigated during cooling. Shortly after the temperature was cooled below T_c, the first domain wall (I) nucleated at the lower segment of the curved dislocation, as indicated in Figure 5.34a with a blue arrow. While domain I grew (Figure 5.34b) until it was pinned at the upper dislocation segment, a second domain wall (II, black arrow) was formed (Figure 5.34c). Domain I was pinned at the upper segment for almost 40 seconds until it was able to cross the dislocation barrier (Figure 5.34d). In the meantime, other domains were formed (Figure 5.34e). At room temperature, most domains crossed the dislocation barrier and formed a typical zig-zag domain wall pattern (Figure 5.34f).

The in-situ temperature-dependent TEM images provide a visualization of the nucleation and pinning potential of the dislocations and form a complementary viewpoint to the electric-field-dependent TEM investigations of Gao et al. [35] in $Pb(Zr,Ti)O_3$ thin films and phase-field simulations [32].

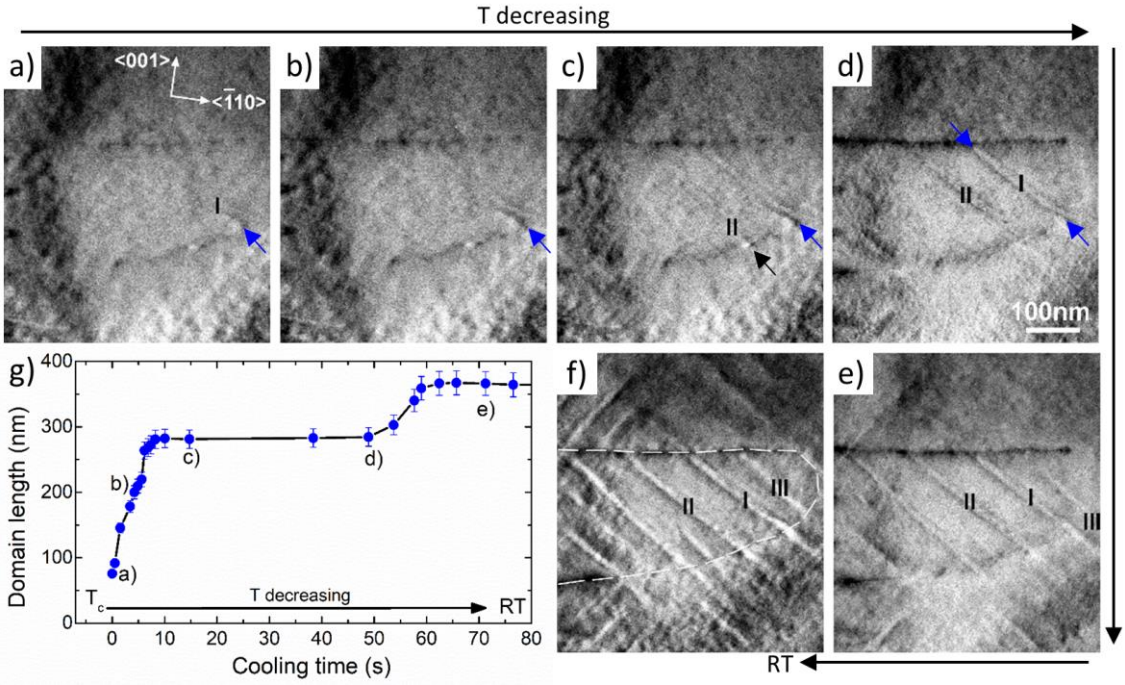

Figure 5.34: In-situ TEM study of the domain nucleation and domain growth on a curved dislocation line during cooling through T_c. A (110) TEM-sample of the deformed C-1150-20 sample was heated to 220 °C and cooled to room temperature. a) At T_c, domain I nucleates at the curved dislocation. During cooling (a–f) further domains are formed at the dislocation and grow until they reach the upper dislocation segment. Subfigures (a–f) are arranged clockwise by cooling time to enable a direct comparison between neighboring TEM images. g) The domain growth of domain I is documented as a function of the cooling time. The letters in (g) correspond to the subfigures (a–e). Domain I is marked with blue arrows in subfigures (a-d), and domain II is indicated with a black arrow in (c). The dashed white line in (f) indicates the dislocation line at room temperature.

Macroscopically, the deformed unpoled sample had a higher density of *c*-domains than *a*-domains (NMR-data, Figure 5.24), resulting in a reduced permittivity due to the anisotropy of the dielectric tensor (Figure 5.26 and Figure 5.27). Poling inverted the permittivity response. While the undeformed poled reference sample achieved a permittivity of 150, corresponding to a nearly perfect *c*-domain configuration [273](Figure 5.35a), the permittivity of the deformed sample was at least five times higher. This increase can be explained by the NMR data in Figure 5.35a. The deformed sample had a much larger contribution from the a_2-domains, leading to the higher permittivity. A schematic representation of the altered domain structure upon poling and deformation is given in Figure 5.35b. The reference sample was fully-poled, while *a*-domains were still pinned at the dislocations in the deformed single crystal. Note that the arrangement of the domains does not necessarily coincide with the real domain structure; rather, it is meant to symbolize the distribution of the a_1, a_2 and *c*-domains and the pinning of the domains at the dislocations. The dislocation density presented in Figure 5.35b is significantly overestimated for better visualization.

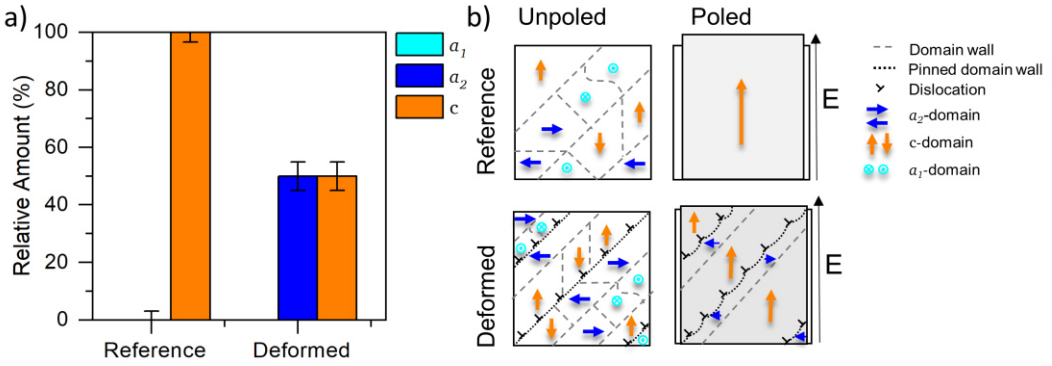

Figure 5.35: a) Domain state after poling at 1 kV/mm for a reference sample and a deformed sample (C-1150-20) measured with NMR by Pedro Groszewicz and co-workers. b) Schematic of the domain wall and dislocation arrangement for the reference and the deformed samples in the unpoled and poled state.

Nevertheless, the domain distribution in Figure 5.35a and the domain back-switching from P_{max}* to P_r* in the large-signal polarization hysteresis curves (summarized in Figure 5.31) suggest a strong macroscopic axial restoring force, acting as the driving force for the back-switching. The increase in the coercive field points towards pinning of the domains at the dislocations, as observed in the TEM (Figure 5.34) and discussed in Section 2.3.2, resulting in a switching of the domains in higher electric fields.

In the intermediate or subcoercive field range, the dislocations have an impact on the reversibility of the electromechanical and dielectric properties, shown as a function of the normalized electric field E/E_c* in Figure 5.36 for C-1150-20 and a reference sample. The strong increase in permittivity and d_{33}* to $\varepsilon_r' \approx 5810$ and $d_{33}^* \approx 1900$ pm/V at $0.17E/E_c$*, starting at $0.1E/E_c$*, emphasize strong domain wall vibration. The absolute value of the increase varies with position and poling cycle (1st or 2nd), as indicated in Figure 5.33. These changes are most likely due to the inhomogeneous distribution of the slip systems and dislocations in the sample. Below E_c* the electromechanical behavior of the deformed sample not only is reversible but also indicates only a small hysteretic behavior between the increasing and decreasing electric field cycle (Figure 5.33). These results support the existence of a macroscopic restoring force in addition to the local pinning force of the dislocations.

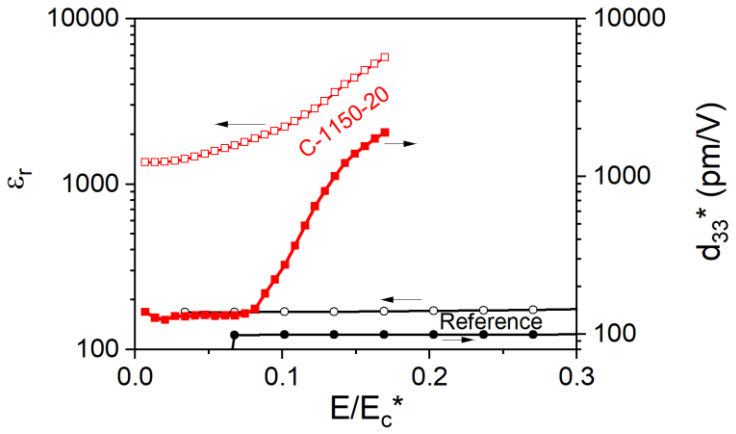

Figure 5.36: Field-dependent permittivity and d_{33}* of the poled reference and deformed samples (C-1150-20).

The origin of electromechanical property changes can be understood by examining the pinning force of dislocations. Domains are pinned to dislocations until the applied electric field overcomes the critical electric pinning field (E_{pin}). The strength of the pinning is proportional to E_{pin} and correlates with the magnitude of the Peach–Koehler force F_{PK}, given in Equation 5-1 [64]. F_{PK} provides an estimation of the force acting between the dislocation and the domain wall. Only if the applied force is higher than F_{PK} can the domain wall overcome the pinning. The phase-field simulation equivalent of F_{PK} is the line force F_{pin}. F_{pin} is given in Equation 5-2 as a function of the critical pinning electric field E_{pin}, the spontaneous polarization P_s and the dislocation density ρ_{DLS} [186] ($\rho_{DLS} = 1/L$; with L as phase field cell height). Dividing $F_{pin} = 0.078\frac{N}{m}$ by L (120 nm)[4] yields a normal stress in the range of 0.7 MPa acting on the domain wall.

$$F_{PK} = \sigma_{xy}\left|\vec{b}\right| \tag{5-1}$$

$$F_{pin} = \frac{2E_{pin}P_s}{\rho_{DLS}} \tag{5-2}$$

This pinning stress depends strongly on the spacing between dislocation lines. Therefore, domains pinned at slip planes with low dislocation density overcome pinning earlier, while others are pinned to higher electric fields at slip planes with high dislocation density. In addition to pinning at the dislocations, there is another consequence for the domains. Since some of the domains back-switch to the more stable initial domain configuration after poling, the samples still have an *a*-*c*-domain configuration, as highlighted with NMR spectroscopy. Consequently, applying a new electric field cycle (e.g., subcoercive, Figure 5.36) leads to a strain incompatibility between the pinned *a*-domains and the surrounding *c*-domains. This incompatibility hinders the expansion and switching of additional domains, providing a restoring force that acts against the applied electric field. The macroscopic restoring force is best described by an in-plane strain condition (Equation 5-3) in the bulk material. This in-plane strain depends on the Young modulus, *Y*, the Poisson ratio, ν, and the mechanical strain, *S* (with $Y = 67$ GPa [289], $\nu = 0.3$). The mechanical strain, caused in the intermediate electric field region, is calculated according to Equation 5-4. In the intermediate field of Figure 7.7a ("A, position 1"; E_2=45.3 V/mm and d_{33}*=1741 pm/V; E_1=25.6 V/mm and d_{33}*=263 pm/V) the corresponding strain is $S = 19.8 \cdot 10^{-6}$.

$$\sigma = \frac{Y}{1-\nu^2}S \tag{5-3}$$

$$S = \int_{E_1}^{E_2} d_{33}^*(E)dE \tag{5-4}$$

$$\sigma = \frac{67\ GPa}{1-0.3^2}19.8 \cdot 10^{-6} = 1.45\ MPa \tag{5-5}$$

Thus, the strain incompatibility causes a macroscopic restoring force of 1.45 MPa, which opposes the applied electric field.

[4] Phase-field data were provided by Xiandong Zhou, (MFM, TU Darmstadt)

The strain incompatibility caused by domain wall pinning at the dislocations is phenomenologically similar to the orthogonal poling approach of Li et al. [24, 290]. Li et al. tailored the domain structure by periodical orthogonal poling and achieved reversible non-180° domain switching, resulting in an actuation strain of 0.6%. They suggested that strain incompatibilities between the differently poled regions in the material were the cause of this high strain [290]. However, they provided a different explanation for the origin of the strain incompatibility [24, 290] than we do. In our case, the changes are related to the mechanical imprint rather than the poling effect. Note that some preliminary results on the cycling stability and bipolar strain loops of our samples suggest a time-dependence for the dislocation-based mechanism, which needs to be further investigated in future work.

As well as the promising reversible electromechanical properties of the mechanically imprinted samples, the variability and the reproducibility of the results should be discussed briefly. As indicated in Figure 5.31, with the broad distribution of the local coercive fields and the high proportion of back-switching, the hysteresis depends on the maximal applied electric field. Furthermore, the piezoelectric coefficient varies with position and poling state between 511 pm/V and 2734 pm/V, suggesting inhomogeneous behavior. This behavior may be related to the mechanical imprint methodology itself. During deformation, the local stress states close to and inside the sample can vary due to lateral constraints, internal defects or alignment issues. With platinum foils and centering tools, the constraints and inhomogeneous stress centers were reduced, resulting in several of the single crystals exhibiting the rhombic structure (Figure 5.20), which is the first indication of a successful deformation. Nevertheless, the concept of the mechanical imprint is based on the predefined slip systems, and an inhomogeneous dislocation distribution is therefore inherent. Samples for electrical measurements were cut out from the middle of the deformed sample. Thus, special care was taken to cut them such that the probability of measuring some dislocations on a slip band is high. The slip planes are not homogeneously distributed, as already discussed for $KNbO_3$ (Section 5.1). In $BaTiO_3$ the dislocation density is only increased locally, and fewer slip planes are expected compared to $KNbO_3$ due to the limited deformation degree and the drawback that the use of Pt eliminates any possible statement about the deformation process. Hence, the probability of measuring the same number of dislocations or slip planes with each electrical measurement is limited. Nevertheless, the resulting restoring force indeed affects a larger region, which can explain the relative increase of the d_{33}* at several positions.

In summary, the mechanical imprint approach affects the electromechanical properties and structure by combining the concept of strain incompatibilities, as is known from orthogonal poling [290], with local dislocation pinning, previously demonstrated by numerical simulations [32]. Therefore, the methodology of dislocation-based functionality is a valid option to tailor the functional properties of ferroelectric bulk materials.

Some of these results were published in a modified way in Ref. [291].

5.3 Outlook on the Deformation of <110>-Oriented $BaTiO_3$

The plastic deformability of ⟨110⟩-oriented $BaTiO_3$ single crystals was investigated at high temperatures to determine the stress necessary to reach the plastic regime and pave the way for further deformation and dislocation-based functionality studies on $BaTiO_3$. Unlike the previous sections, this section focused on plastic deformation, and thus dislocation-based functionality was not addressed. The risk of cracking was taken into account, in order to ensure a higher accuracy of the mechanical data. Therefore, no platinum protection foils were used during deformation, with the consequence that most of the samples were not usable for subsequent electrical measurements. The sample size was limited to $2\times2\times4$ mm³ to ensure that the maximum force limit of the load frame was not reached. In addition, the smaller geometry allowed the testing of a larger number of samples.

Beauchesne and Poirier claimed that "crystals with perovskite structure do not constitute an isomechanical group", meaning that their creep or plastic deformation behavior is not necessarily similar [47]. Therefore, in this section, the plastic deformation behavior of ⟨110⟩-oriented $BaTiO_3$ single crystals is compared to that of $SrTiO_3$ single crystals to address the question whether at least these two perovskite materials behave similarly. The $SrTiO_3$ single crystal deformation results were provided by Lukas Porz.

5.3.1 Orientation Dependence

In Figure 5.37a, high-temperature plastic deformation experiments performed on ⟨001⟩- and ⟨110⟩-oriented $BaTiO_3$ single crystals are compared. The relationship between the applied compressive stress and strain rate is presented in Figure 5.37b. The ⟨100⟩-oriented single crystal deformed elastically until reaching 760 MPa and non-elastic behavior sets in ($R_{p0.2}$ = 930 MPa); fracture occured at 1044 MPa. The strain rate of the ⟨100⟩ orientation in the linear range above 100 MPa remained constant at $\sim10^{-5}$ 1/s, emphasizing a reduced stiffness constant at 1150 °C (Figure 5.37b). Note that below 100 MPa the strain rate is substantially lower. The plastic deformation regime of the ⟨110⟩-oriented $BaTiO_3$ single crystal started at $R_{p0.2}$ = 110 MPa. The strain rate increased to $8\cdot10^{-4}$ 1/s in the non-linear range until the sample fails (Figure 5.37b). In contrast to the ⟨100⟩ orientation, the ⟨110⟩ sample reached the plastic regime and a continuous increase in strain rate was observed up to $8\cdot10^{-4}$ 1/s with increasing load. The measurement was terminated at 9.2% deformation. The plastic deformation stress of the {101}⟨101⟩ slip system was not reached with 2 N/s for the ⟨100⟩ direction, whereas the ⟨110⟩ orientation with the {100}⟨100⟩ slip system was plastically deformable at 1150 °C.

These results show that $BaTiO_3$ has a similar qualitative trend as $SrTiO_3$ at high temperatures, with the {100}⟨100⟩ slip system requiring lower applied stress to reach the yield stress than the {101}⟨101⟩ slip system [88, 94]. For $SrTiO_3$, 1150 °C is close to the brittle region of the ductile-to-brittle-to-ductile transition. Such a transition has not been reported for $BaTiO_3$, but it is likely that at higher temperatures, the yield stresses are also reduced for both slip systems, following the trend of $SrTiO_3$ in the high-temperature ductile region. The presence of a ductile region in $BaTiO_3$ at RT, like in $SrTiO_3$ and $KNbO_3$, can be excluded because both ⟨110⟩- and ⟨001⟩-oriented $BaTiO_3$ fracture at RT under the same loading conditions (2 N/s) and the same sample geometry.

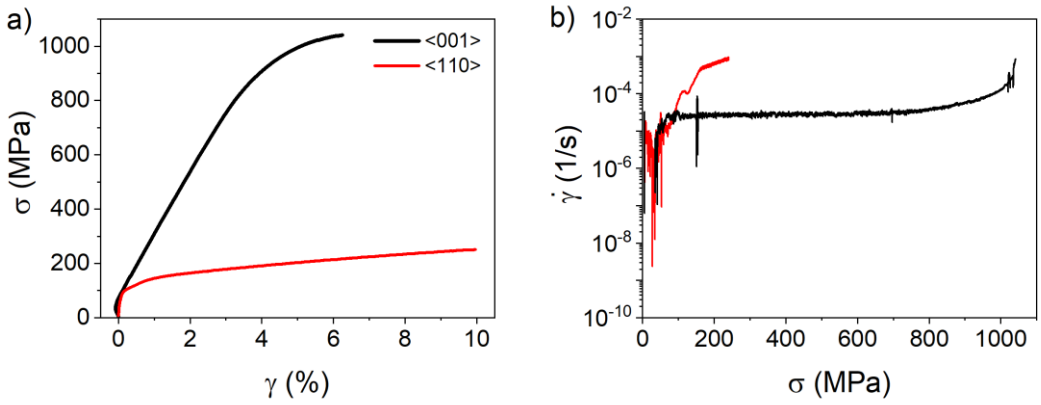

Figure 5.37: a) Compressive stress as a function of deformation strain for ⟨001⟩- and ⟨110⟩-oriented $BaTiO_3$ single crystals at 1150 °C and the resulting strain rate as a function of deformation stress curve (b). Both measurements were conducted at 2 N/s without a protective layer. Absolute strains were averaged over 100 data points before strain rates were calculated to smooth the curves in (b).

Consequently, plastic deformation of ⟨110⟩-oriented $BaTiO_3$ at 1150 °C is the preferred orientation to study isomechanical similarities of deformation processes between $SrTiO_3$ and $BaTiO_3$. $KNbO_3$ is neglected here, because such experiments are not possible due to the volatility of potassium [292] and the low melting temperature [293]. It should be mentioned that the loading conditions, in particularly the loading rate, are crucial parameters and significantly affect the critical applied stress. Both types of deformation experiments, initially strain rate controlled [88, 294] and load controlled [295, 296], have been described in the literature, and the correlation between them is given by the following equation [295]:

$$\frac{d\sigma}{d\gamma} = \frac{d\sigma}{dt}\left(\frac{d\gamma}{dt}\right)^{-1} \qquad 5\text{-}6$$

Using Equation 5-6 and the total length of mobile dislocations per crystal volume, magnitude of the Burgers vector, geometric constant ς and average dislocation velocity $\bar{\xi}$, a prediction of the stress-strain curve is possible:

$$\frac{d\sigma}{d\gamma} = \frac{1}{\varsigma\rho_{DLS}|\vec{b}|\bar{\xi}}\frac{d\sigma}{dt} \qquad 5\text{-}7$$

Considering that the dislocation velocity of screw and edge dislocations is associated with the resolved shear stress, as it has been shown for LiF and MgO, and that the average dislocation velocity is proportional to the screw velocity (slowest type), Equation 5-8 gives a direct relationship between the stress-strain curve and applied shear stress [239, 295].

$$\frac{d\sigma}{d\gamma} = \frac{1}{\rho_{DLS}|\vec{b}|\xi_0\left(\frac{\tau}{\tau_0}\right)^{\eta}}\frac{d\sigma}{dt} \qquad 5\text{-}8$$

τ_0 and η are constants. Experimentally, it has been shown that as the loading-rate decreases, the slope of the stress-strain curve decreases for the same strain [295], making it difficult to identify the critical stress. Strain-rate-controlled experiments indeed provide a more pronounced kink between the linear-elastic and plastic regimes. Nevertheless, lower initial

strain rates reduce the stress level required to reach the plastic deformation regime [294], suggesting that the system has more time to respond.

The combination of orientation, mechanical loading conditions and temperature range is crucial for a successful deformation without failure. However, this specific issue has not been addressed in the literature for single crystalline $BaTiO_3$. The few existing studies focus on creep experiments and the resulting dislocation structures obtained between 1150 °C and 1570 °C and stresses up to 25 MPa [46, 113]. Therefore, the behavior of ⟨110⟩-oriented $BaTiO_3$ single crystals at temperatures between 1100 °C and 1170 °C and stresses above 25 MPa will be addressed in the next subsection.

5.3.2 Influence of Temperature and Loading Conditions

Compressive stress interval tests at constant stress rate allow the determination of the achievable strain rate at given stress and temperature. Using the slope of the strain rate at given stress, the activation volume and activation energy for different temperatures can be studied. With this knowledge, suitable parameters for different types of compression tests such as strain rate controlled or load controlled can be identified, providing an economical and effective way to obtain information about the deformation behavior of the material.

The ⟨110⟩-oriented $BaTiO_3$ single crystals exhibit a temperature-dependent deformation behavior as shown in Figure 5.38 for 1100 °C, 1150 °C and 1170 °C. The temperature-dependent behavior was investigated with stress-intervals from 25 MPa to 200 MPa and the achieved strain rate was evaluated as a function of the applied stress. The strain rate increased from 10^{-6} 1/s to $3{\cdot}10^{-4}$ 1/s with increasing temperature and stress. The strain rate fluctuated at 1100 °C for stresses below 100 MPa; at higher temperatures, the strain rate stabilizes already at stresses of approximately 50 MPa. As the stress increases, the strain rates of all samples reached values of 10^{-4} 1/s or higher. The circles in Figure 5.38b correspond to the strain rate of the stress plateaus, emphasizing that the deformation is purely plastic without any linear-elastic contribution. This is particularly important at low stresses, where it is uncertain whether the yield stress has already been reached.

Diagrams of the strain rate as a function of stress are useful for estimating the strain rate and stress limits of the sample but can only be obtained for load-controlled loading conditions. The results in Figure 5.38 indicate that the strain-rate-controlled experiments can be performed at 10^{-4} 1/s without severe damage to the sample. Moreover, stresses above 50 MPa are recommended to obtain stable and reliable strain rates. Two types of control experiments were conducted at 1150 °C to ensure that the stress-interval method does not significantly affect the strain rate result: load-controlled experiments at 0.5 N/s and 1 N/s, and strain-rate-controlled experiments at 10^{-5} 1/s and 10^{-4} 1/s. The corresponding strain rates for the load-controlled mechanism and the achieved stresses (corresponding to $R_{p0.2}$ and 3% total strain) for the strain-rate-controlled method are plotted in Figure 5.38b to confirm that both loading paths results in similar strain rate as a function of stress plots under certain boundary conditions. The corresponding stress-strain curves are shown in the appendix Figure 7.9. Both stress-controlled measurements reach the $R_{p0.2}$ in the range of 50 MPa and a strain rate of $2–4{\cdot}10^{-5}$ 1/s but do not reach 3% strain until after reaching 100 MPa. The strain-rate-controlled experiments reached $R_{p0.2}$ at 18 MPa for 10^{-5} 1/s and 105 MPa for 10^{-4} 1/s and the 3% strain at compressive

stresses of 45 MPa and 118 MPa. This indicates that lower strain rates require less stress to reach the plastic deformation state. All data points above 50 MPa agree well with the stress interval curve at 1150 °C.

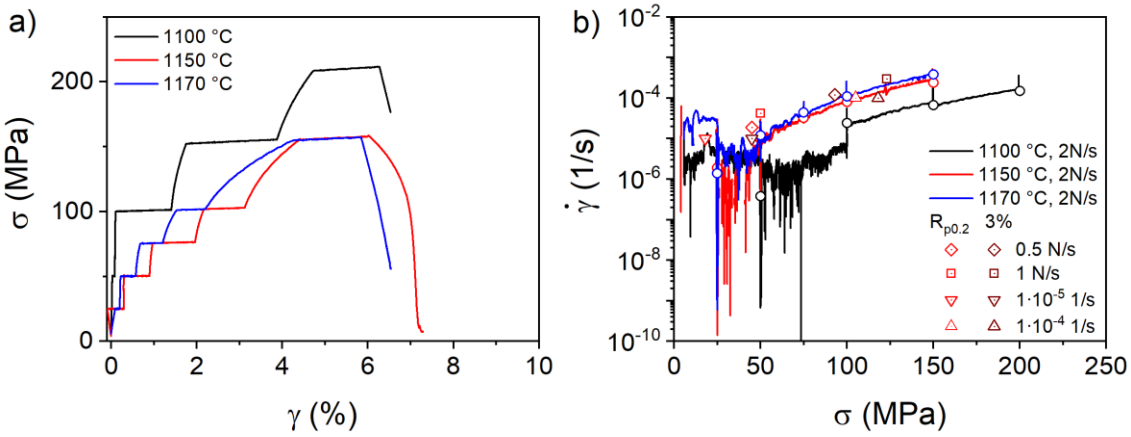

Figure 5.38: Temperature dependent deformation of ⟨110⟩-oriented $BaTiO_3$ single crystals at 1100 °C, 1150 °C and 1170 °C depicted as (a) stress-strain curve and (b) strain rate as a function of applied stress. Uniaxial compression experiments were performed with a loading rate of 2 N/s. The holding time at individual stress intervals was shortened with increasing temperature and stress to avoid sample fracture. The circles (in b) correspond to the calculated strain rate of the stress plateaus in (a). The $R_{p0.2}$ and the stress at 3% total deformation ($\sigma(3\%)$) are given for different loading conditions as a function of the strain rate, all measured at 1150 °C. Note that both values ($R_{p0.2}$ and 3%) have the same symbol but different color, the one at lower stress corresponds to $R_{p0.2}$, the one at higher stress to $\sigma(3\%)$.

The activation energy of the deformation mechanism was determined using Equation 2-6 for the step-interval measurements in the temperature ranges of 1100 °C to 1150 °C and 1150 °C to 1170 °C at the stress levels of 50 MPa, 75 MPa, 100 MPa and 150 MPa, shown in Figure 5.39. The activation energy of 1042 kJ/mol for the 50 MPa at 1100–1150 °C is 2.5 times larger than that of 405 kJ/mol at 150 MPa and even five times larger than that of 203 kJ/mol at 50 MPa at 1150–1170 °C; see Figure 5.39b. Beauchesne and Poirier reported an activation energy of 469 ± 27 kJ/mol for the stress range of 9–25 MPa and 1150–1570 °C and interpreted the results as climb-controlled dislocation creep mechanism limited by diffusion of the slowest species. The reduced activation energy at 150 MPa suggests a more readily activated dislocation mechanism, which could indicate slip deformation or kink-pair mechanism. Therefore, the activation volume is estimated according to Equation 5-9:

$$V(\tau) = k_B T \left(\frac{\partial \ln(\dot{\gamma})}{\partial \tau}\right)_T \qquad 5\text{-}9$$

The resulting values for the {100}⟨100⟩ slip system and $|\vec{b}| = 0.56\,nm$ are presented in Figure 5.39c as a function of temperature and stress. At 150 MPa, the activation volume is in the range of $6b^3$, which is in the same range as 1–20 b^3 reported for deformed $SrTiO_3$ single crystals exhibiting the kink-pair mechanism [64, 88]. Taeri et al. observed a temperature-dependent activation volume for the ⟨110⟩-oriented $SrTiO_3$ single crystals, which was not observed in Figure 5.39c. This could mean that the temperature range of 1100–1170 °C is too narrow or that $BaTiO_3$ does not have such a pronounced temperature dependence. The activation enthalpy according to Equation 2-9 is 487 kJ/mol (1150 °C–1170 °C; 150 MPa), which is slightly higher

than that of the {100}⟨100⟩ slip system in $SrTiO_3$ with 193–290 kJ/mol (2–3 eV) in the same temperature range [88].

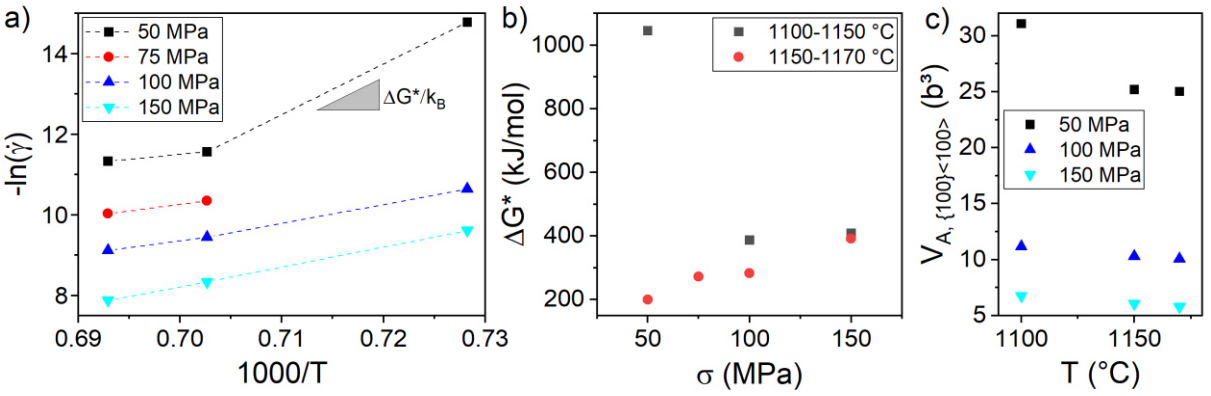

Figure 5.39: Determination of the activation energy. a) Logarithmic strain rate as a function of temperature, (b) activation energy as a function of applied stress and (c) the resulting activation volume as a function of temperature.

A direct comparison between ⟨110⟩-oriented $BaTiO_3$ and $SrTiO_3$ single crystals, as presented in Figure 5.40, illustrates a similar trend for both perovskite materials. At low stresses the slope of the strain rate as a function of stress curve is steep and becomes flat at high stresses, indicating a change in the deformation mechanism. As the temperature increases, the strain rates increase for both materials. $BaTiO_3$ achieves slightly lower strain rates than $SrTiO_3$ at the same temperature and stress, but the trend of the slope at a given stress is similar, indicating comparable activation energy and deformation process. Various publications have discussed the stress range below 50 MPa and reported a wide range of activation energies, indicating different diffusion- and dislocation-based mechanisms [46, 136, 137]. This range of different mechanisms supports the assessment that no isomechanical group can be identified from creep results of perovskites at low stresses, even at high temperatures [47]. Nevertheless, a trend towards a similar slope is identified at high stresses. Therefore, the results obtained from ⟨110⟩-oriented perovskite single crystals presented here show not only similar deformation behavior but also indicate isomechanical behavior at high stresses. As a consequence, a kink-pair mechanism is speculated to be the rate-limiting mechanism for the deformation of ⟨110⟩-oriented $BaTiO_3$ at stresses above 100 MPa and at 1150 °C, as has been proposed for $SrTiO_3$ [90].

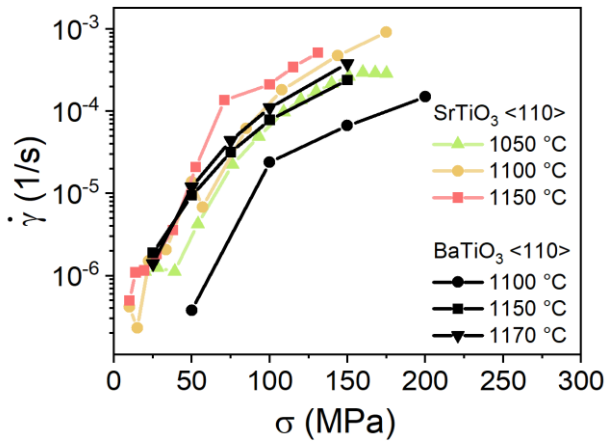

Figure 5.40: Comparison between $BaTiO_3$ and $SrTiO_3$ strain rates as a function of applied stress.

5.3.3 Summary

$BaTiO_3$ single crystals were deformed at 1150 °C in the ⟨001⟩ and ⟨110⟩ orientations. The ⟨001⟩ orientation withstands seven times higher stresses until the sample reaches the non-linear regions and fractures. Plastic deformability of the ⟨110⟩ orientation was tested at 1100 °C, 1150 °C and 1170 °C for different stress-intervals to determine the corresponding strain rates. Above 100 MPa, stable strain rates up to several 10^{-4} 1/s are achieved. Initial strain-rate-controlled and load-controlled experiments confirmed that $BaTiO_3$ is deformable at 1150 °C, which underlines a certain reproducibility of the data. As a result, less-destructive deformation with lower yield stresses was achieved at lower strain rates and loading rates. Finally, $BaTiO_3$ single crystals behave similarly to $SrTiO_3$ at 1150 °C and stresses above 100 MPa, suggesting a kink-pair mechanism and isomechanical behavior.

5.4 From Single Crystals to Polycrystalline $BaTiO_3$

The transfer of the knowledge on dislocation-domain wall interactions obtained from single crystals to polycrystalline $BaTiO_3$ is critical. The latter is preferred from the application and economic point of view. The introduction of dislocations into polycrystals is limited not only by the Taylor criterion. It is also strongly influenced by other competing mechanisms, such as diffusion processes, grain boundary sliding, abnormal grain growth at high temperatures [297], twinning [298] and cracking. In addition to grain size [74, 136, 137], experimental conditions, non-stoichiometry [140] and defect chemistry must also be considered. Most creep studies on polycrystalline $BaTiO_3$ focus on the microstructural changes from a geological point of view [46] and investigate the behavior of the lower earth mantle, or they proceed from a microstructural point of view [133, 136, 142]. The link between creep-induced microstructural changes and the macroscopic dielectric, piezoelectric and ferroelectric properties is still missing. Therefore, this chapter aims to provide a methodology for using high-temperature creep to influence functional properties.

Prior to the investigation of creep-based functionality, the relevant creep regimes are identified (Section 5.4.1), followed by microstructural investigations for the specified regimes (Section 5.4.2). In Section 5.4.3, the functionality is investigated and the polycrystalline creep approach is discussed (Section 5.4.4)

5.4.1 Identification of the Creep Regimes

The temperature and stress ranges for the creep regimes are grain size dependent. Therefore the first step is to identify the relevant creep parameters and develop a map of the deformation mechanism. For this purpose, stepwise creep experiments were performed at 950 °C, 1000 °C, 1050 °C and 1100 °C. The corresponding stress-strain curves are presented in Figure 5.41.

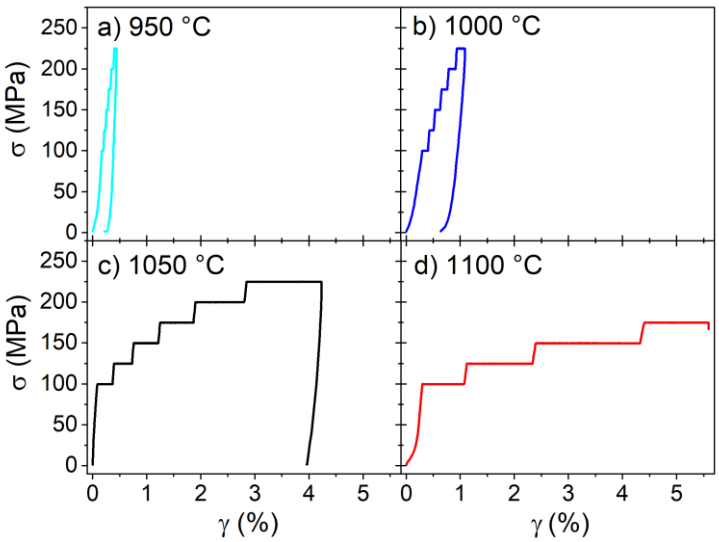

Figure 5.41: Stress-strain curves are given for fine-grained polycrystalline samples deformed at (a) 950 °C, (b) 1000 °C, (c) 1050 °C and (d) 1100 °C. Each plateau corresponds to a holding time of 30 min at a certain stress step. At 950 °C, 1000 °C and 1050 °C stress plateaus are at 100 MPa, 125 MPa, 150 MPa, 175 MPa, 200 MPa and 225 MPa. At 1100 °C the stress plateaus are at 100 MPa, 125 MPa, 150 MPa and 175 MPa (Adapted from Ref. [227]).

The stress level was sustained for 30 min at each step. The strain increases with increasing temperature and stress. While only 0.13% strain is obtained in the 200 MPa plateau at 1000 °C (Figure 5.41b), a six-times higher strain of 0.86% is gained at 1050 °C at the same stress level.

The strain behavior as a function of time is exemplified for 100 MPa and 200 MPa in Figure 5.42a and Figure 5.42b, respectively. The time-dependent strain (Figure 5.42c) provides information on whether the strain rate is constant and, thus, whether the steady-state creep region has been reached.

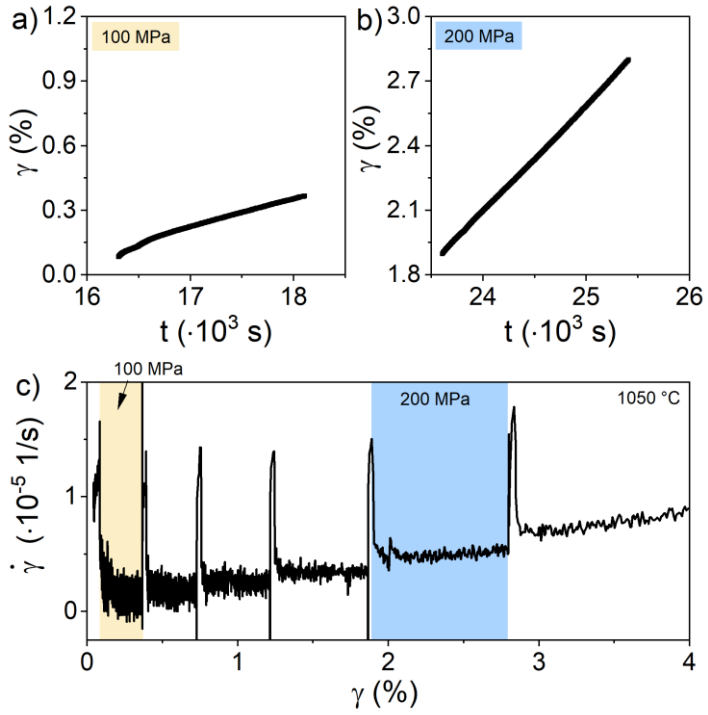

Figure 5.42: Determination of the steady-state creep regime at 1050 °C. Strain as a function of time for (a) 100 MPa and (b) 200 MPa. c) Strain rate as a function of strain to determine the constant strain rate. The stress regions of (a) 100 MPa and (b) 200 MPa are highlighted in (c) (Adapted from [227]).

While the strain rate at 100 MPa varies by an order of magnitude, the deviation in the data at 200 MPa is much smaller. The strain rates are more stable at higher stresses and temperatures. The threshold strain at which a constant strain rate is reached was identified at 0.15% deformation strain. Therefore, the first data points at 950 °C and at 1000 °C were neglected, since the steady-state region was not reached. The power-law creep Equation 2-16 was applied for all other measurement points, assuming that the grain size is constant, as will be demonstrated subsequently in the microstructure analysis.

The assumptions that the grain size and temperature are constant and that the activation energy is independent of the applied stress result in the logarithmic plots in Figure 5.43. The slopes of the segments between the data points represent the stress exponents n.

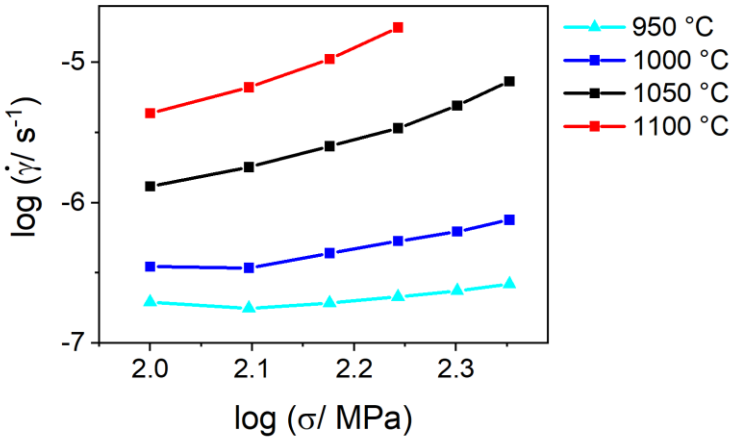

Figure 5.43: Determination of the stress exponent. The slopes of the double logarithmic plots for 950 °C, 1000 °C, 1050 °C and 1100 °C correspond to the stress exponent of the power-law creep Equation 2-16.

Table 5.2: Mean stress values and stress exponents for the slopes in Figure 5.43.

	950 °C	**1000 °C**	**1050 °C**	**1100 °C**
σ_{mean} (MPa)	**n**	**n**	**n**	**n**
112.5			1.4	1.9
137.5	0.5	1.3	1.9	2.5
162.5	0.7	1.3	1.9	3.3
187.5	0.7	1.2	2.8	
212.5	0.9	1.6	3.4	

Based on these stress exponents, as listed in Table 5.2, the deformation map in Figure 5.44 was developed. The stress values of the data points in Figure 5.44 represent the average of two stresses (given in Table 5.2) between which the stress exponent was determined. The shapes of the symbols and the colored background correlate with the linear range (n < 1, green), the diffusion range (n =1-3, yellow) and the dislocation creep range (n > 3, blue) [106, 107]. At this point, some of the competing mechanisms such as grain boundary sliding and kink-pair mechanism have not been considered in the classification of creep regimes. They will be discussed later. Based on this deformation map, the parameters for the single-stress-temperature samples were chosen.

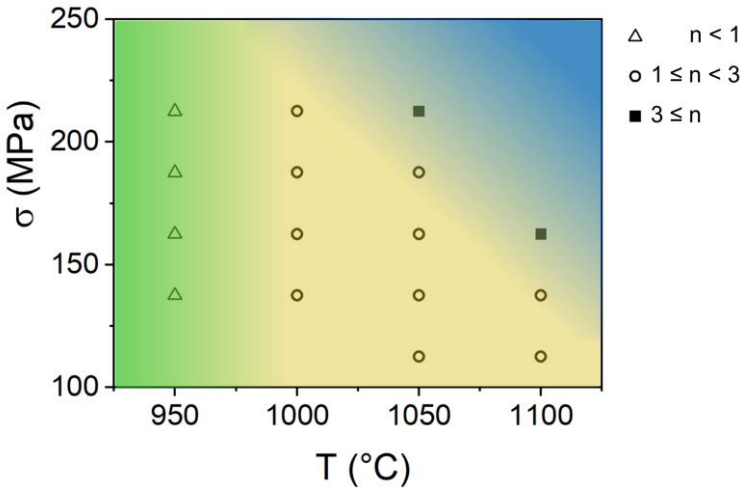

Figure 5.44: Deformation mechanism map for polycrystalline $BaTiO_3$ (grain size 1–2 μm). The data points correspond to the mean of two stress values and the stress exponents classified according to the definition given next to the symbols. All values are listed in Table 5.2. The colored background highlights the linear range (green, open triangles), diffusion creep range (yellow, open circles) and dislocation creep range (blue, filled squares) (Adapted from [227]).

5.4.2 Creep-Based Microstructural Changes

Individual creep experiments were carried out at 200 MPa in the linear regime of the deformation map (Figure 5.44) at 1000 °C for 15 min (PC-1000-15) and in the dislocation creep regime at 1050 °C for 15, 22 and 30 min, denoted PC-1050-15, PC-1050-22 and PC-1050-30. The transition between diffusion and dislocation creep regimes occurs around 1050 °C and approximately 180 MPa, as indicated by the color change from blue to yellow in Figure 5.44. Therefore, choosing 1050 °C (and 200 MPa) was the best compromise to avoid high temperatures that could lead to abnormal grain growth or extensive twinning. PC-1000-15 achieved much lower deformation strains, at 0.29%, than did PC-1050-15, at 0.6%; PC-1050-22, at 1.06%; and PC-1050-30, at 1.29% strain. All samples had an average grain size in the range of 1.4–1.7 μm (see Figure 5.45). Thus, the grain size is considered constant. The total plastic strain was kept below 2% to avoid microcracking and fracture of the samples. The SEM images in Figure 5.46 support that this objective was achieved. No cracks are visible and no increase in twinning was observed for the deformed samples. Twinning often occurs in $BaTiO_3$ during sintering [298] or mechanical compression [299]. Extensive twinning during creep experiments was avoided due to the temperature difference between the sintering temperature (1350 °C) and the much lower deformation temperature (1000–1050 °C). While twin boundaries have a negligible effect on diffusion [144], they can act as barriers for dislocation movement [105] and contribute to strains [300] in the material.

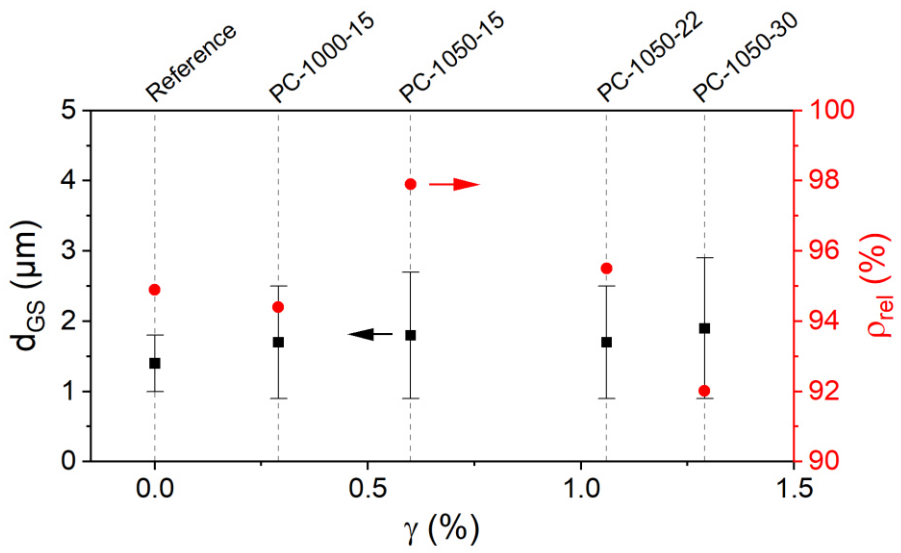

Figure 5.45: Relation between grain size, relative density and deformation strain for the reference and deformed sample.

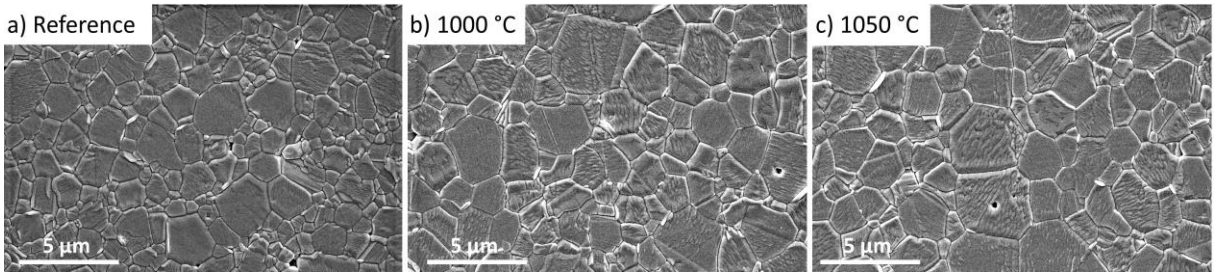

Figure 5.46: Grain size determination with SEM for (a) reference sample, (b) sample deformed at 1000 °C and (c) sample deformed at 1050 ° C (Adapted from Ref. [227]).

Nevertheless, for the PC-1050-15 and PC-1050-22, the relative density was found to increase from 94.9% after sintering to 97.9% and 95.5%, respectively, with increasing deformation temperature and time. This indicates increased diffusion, as also previously reported for hot forging [301] and hot pressing [135]. The decrease in density for the sample PC-1050-30 to 92.1% indicates additional microstructural changes in the sample, such as cavitation formation or microcracks [302].

TEM analysis was used to reveal the domain structure and microstructural features for the different deformation map regimes. The main features in the reference samples are domain walls and grain boundaries, as indicated in Figure 5.47a and Figure 5.47b, while cracks and extensive porosity are absent. On the other hand, both deformed samples contain further artifacts, such as cavitations (Figure 5.47c and Figure 5.47e) and dislocations (Figure 5.47d and Figure 5.47f). Cavitations at grain boundaries are indications of grain boundary sliding. Stress centers form at irregularities, such as second phases, precipitates, and deformation ledges [303], or at contact points between grains, where obstacles prevent adjacent grains from sliding against each other [304]. These stress centers transform into cavitations or triple-point cracking when the stresses are released, due to the loss of grain boundary interlocking [304].

Cavitation formation was found at 1000 °C and 1050 °C, suggesting that grain boundary sliding is present as a competing creep mechanism for both diffusion creep and dislocation creep, but may have different origins. While Raj and Ashby [305] have concluded that “Nabarro-Herring and Coble creep, […][are] identical with grain boundary sliding with diffusional

accommodation," Watanabe [303] and Perry [304] focus on grain boundary sliding mechanisms in relation to dislocation movement. The increased number of cavitations in Figure 5.47c suggests that grain boundary sliding is among the main creep mechanisms at 1000 °C, while it is not as pronounced at 1050 °C.

The dislocation loops at 1000 °C are similar to those found by Doukhan and Doukhan for a $BaTiO_3$ single crystal creeping at 1400 °C [113]. The dot-like dislocation structure in Figure 5.47f is similar to the coffee-bean-like structure or black-dot contrast, reported for $BaTiO_3$-based polycrystalline materials [133, 140, 142, 306]. The formation of such coffee bean structures is based on the agglomeration of point defects, such as oxygen vacancies and the condensation of vacancies. Therefore, they are closely related to non-stoichiometry [133, 140]. Moreover, these dislocations act as metastable sinks for vacancies [133, 140] and have been described as vacancy-like partial dislocations with either TiO_2 deficiency or BaO deficiency [133]. Suzuki et al. argue that such dislocation loops are electrostatically neutral, but they decorate domain walls, indicating a possible effect on ferroelectric properties [140].

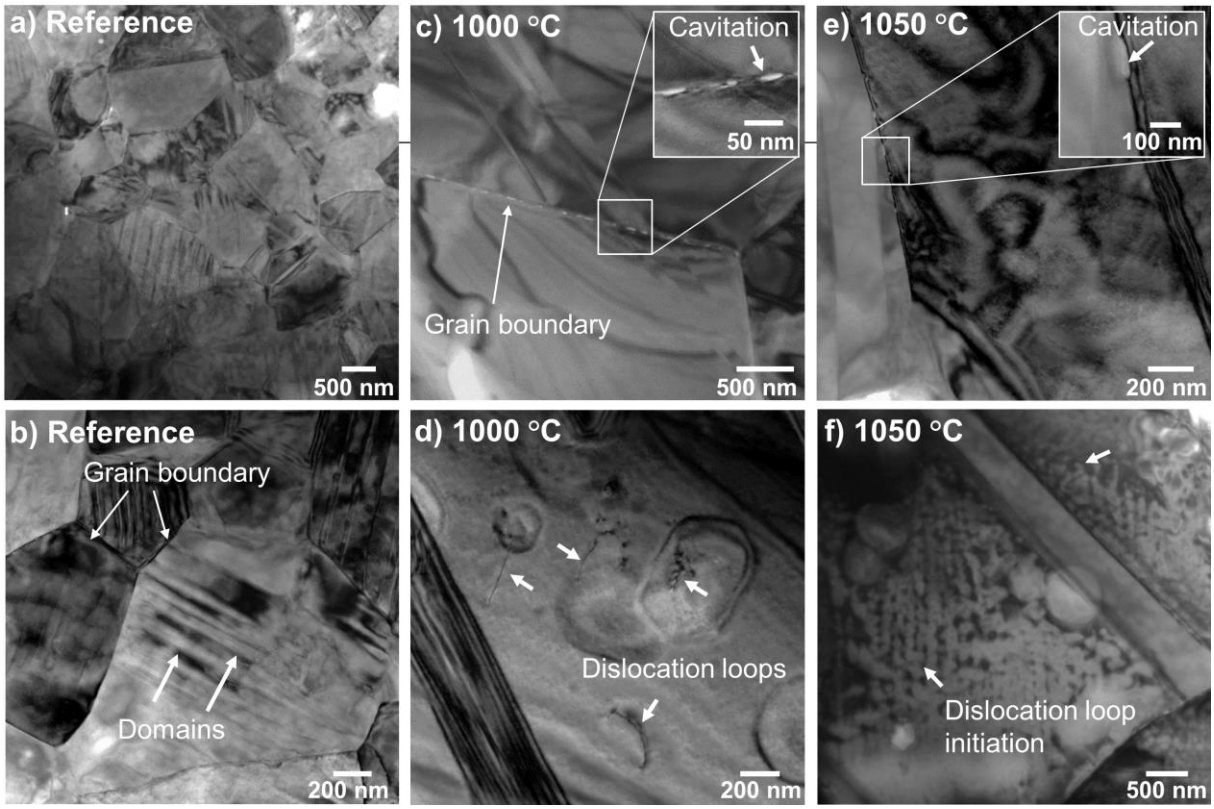

Figure 5.47: Bright-field transmission electron microscopy images facilitate insights into the local microstructural features of the reference sample (a, b) and the samples deformed at 1000 °C (c, d) and at 1050 °C (e, f) (Adapted from Ref. [227]).

One possible influence of dislocations is the change in domain size, which has already been found for $KNbO_3$ single crystals (Section 5.1.4). Therefore, PFM was performed for the samples presented in this thesis and a domain size in the range of 115–154 nm was found, with no obvious deviation between the reference sample and the deformed sample (published in Ref. [227]]). The domain size is in the same range as reported by Hoshina et al. [307] with 100 nm for $d_{GS} = 1.1\ \mu m$ and 150–300 nm for $d_{GS} = 2–4\ \mu m$ [308]. It should be noted that an external influence of pre-stress (1.2–1.3 MPa) on the domain size during cooling could be excluded, as

no change in domain size was observed with PFM in a reference experiment. Moreover, such low stress should not affect the switching behavior of domains in fine-grained $BaTiO_3$ and, thus, should not affect the piezoelectric properties [309, 310].

5.4.3 Creep-Mediated Changes in Dielectric and Electromechanical Response

The dielectric constant and dielectric loss were quantified as measures caused by creep. The undeformed reference sample reaches $\varepsilon_r'(RT) \approx 3100$ at RT, which is in good agreement with values reported for fine-grained $BaTiO_3$ ($d_{GS} \approx 1\,\mu m$) [311]. With $\varepsilon_r'(RT) \approx 3600–3750$, the permittivity of the deformed samples is higher. At T_c, the peak of the deformed samples shifts to higher temperatures and a broadening of the peaks occurs (see Figure 5.48a). In the ferroelectric phase, tanδ is less than 0.03 for all samples, drops at T_c and increases dramatically in the range of 170–180 °C (Figure 5.48b). All samples behave similarly, except PC-1050-30, which has a slightly higher *tanδ*. The trends for $\varepsilon_r'(RT)$ and $\varepsilon_r'(max)$ and T_c are summarized in Figure 5.48c and Figure 5.48d as a function of deformation strain.

The increase in $\varepsilon_r'(RT)$ to 3700 for the deformed samples (Figure 5.48c), indicates a slightly greater stress contribution. Grain boundary sliding may cause this increase in stress contribution. The creep-induced amplification of microstrains was identified as reason for the broadening of the permittivity peak at T_c [227]. Dislocations, twinning, grain boundaries and domains contribute to microstrains [312], but the influence of the last three was ruled out by X-ray investigations above T_c [227] (no domains) and SEM analysis, indicating similar grain size and twinning for all fine-grained samples. Therefore, dislocations (including partial dislocations and stacking faults) are the most likely cause of the microstrains and thus of the broadening and shifting of the permittivity in the deformed samples. The combination of increased stress distribution, microstrains and altered defect chemistry leads to a broadening and reduction in $\varepsilon_r'(max)$ and an increase in T_c with increasing plastic deformation (Figure 5.48c and Figure 5.48d). A change in defect concentration at the grain boundary is possible, but a contribution of impurities to the observed changes was ruled out as all samples were prepared from the same starting powder and the permittivity shift trend is opposite for the majority of point defect dopants [145].

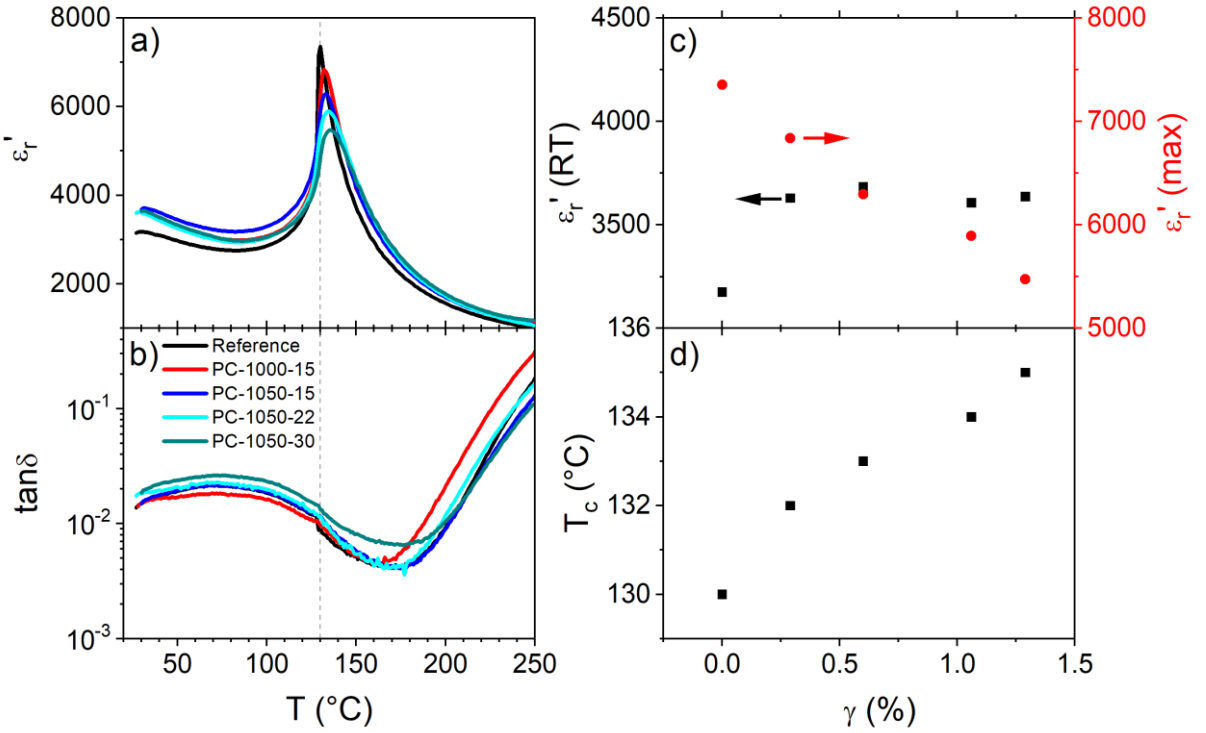

Figure 5.48: Creep-mediated changes in permittivity (a) and dielectric loss (b) as a function of temperature at 1 kHz. The dashed line indicates T_c of the reference sample. c) $\varepsilon_r'(RT)$ and $\varepsilon_r'(max)$ and (d) T_c as a function of the deformation strain γ (Adapted from [227]).

As illustrated in Figure 5.47, creep can produce cavitation at the grain boundaries but also dislocations in the bulk. Therefore, impedance spectroscopy was performed at 400 °C to separate the bulk and grain boundary contributions. In Figure 5.49, the imaginary part of the impedance ($-Z''$) is plotted against the real part (Z'). The large semicircle in Figure 5.49 is correlated to the grain boundary response [313]. The inset in Figure 5.49 indicates the beginning of a small semicircle correlated with the bulk response. The grain boundary resistivities of the deformed samples are reduced, while the bulk resistivity is almost unaffected at 400 °C. Such a reduction in resistivity indicates that the grain boundaries are more affected by creep than is the bulk region. This could point to either an accumulation of point defects such as oxygen vacancies at the grain boundary due to diffusion during creep or towards large cavities. The effect of the dislocations on the bulk resistivity appears to be negligible (Figure 5.49).

Although dislocations in bulk materials can act as vacancy sinks, e.g., for $V_O^{\cdot\cdot}$ [75, 140], Suzuki et al. have pointed out that they are still electrically neutral [140] with lower oxygen ion mobility near the dislocation core, as compared to the bulk [75]. This finding is contrary to the enhanced dislocation-based ionic conductivity identified for TiO_2 [30] and the electrically charged dislocations in alkali halides [10]. Recently, Porz and Frömling et al. clarified that the ability of dislocations to tailor electrical conductivity in ceramics involves a complex interplay between the mesoscopic structure (dislocation type, density and arrangement) [114, 314], the core structure (partial, dipoles, dissociated) [71, 315] and the space charge zone (depleted, enriched, accumulated) [30, 316] of the dislocations [242].

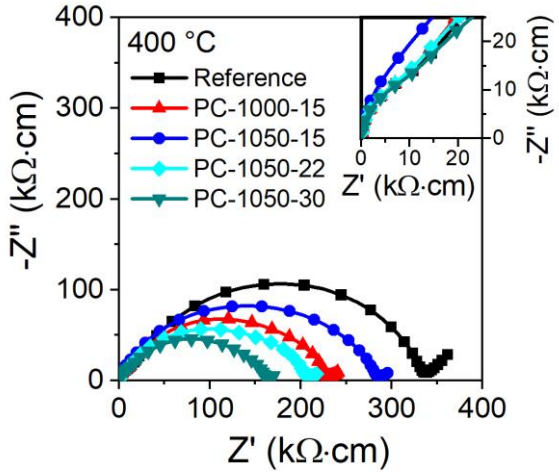

Figure 5.49: Impedance plot for the reference and deformed samples at 400 °C. The inset emphasizes the smaller semicircle at higher frequencies, related to the bulk response (Adapted from [227]).

Unipolar polarization and strain loops were measured to estimate the creep-induced changes in the extrinsic domain wall contribution. Since no evidence of changes in crystallographic structure or composition was found, the intrinsic contribution to strain is assumed to be the same for all samples.

The unipolar polarization curves in Figure 5.50a show consistent field-dependent behavior with a slight decrease in P_{max} with increasing deformation temperature and time. The differences in the unipolar strain loop (Figure 5.50b) are more evident. While the reference sample and PC-1000-15 are almost identical, there is a clear trend towards lower S_{max} in the 1050 °C samples, as depicted in Figure 5.50c. P_{max} and S_{max} (Figure 5.50c) are reduced by 10% and 30%, respectively, with increasing creep strain. This ratio indicates a stronger influence of deformation on the 90° domain walls than on the 180° domain walls. Neither the grain size nor the porosity are responsible for the changes, as grain size remained constant and as porosity would lead to a simultaneous decrease in strain and polarization, which is not observed here [317]. Considering that domain size was not considerably affected by deformation, the reduced strain indicates a decrease in the ferroelectric domain wall mobility of mainly non-180° domains. This reduced mobility is indicative of domain wall pinning at defects [184] due to electrostatic or elastic pinning [32, 186], resulting in electromechanical hardening [7, 200]. The slightly increased *tanδ* at room temperature suggests changes in dielectric loss contribution, but cannot justify the observed 30% changes. Cavities identified for most creep samples behave similarly to anisometric pores and can cause a reduction in the local electric field [317] and lead to a decrease in strain contribution. Therefore, a combination of a dislocation-related and cavitation contribution is a likely reason for the changes in strain.

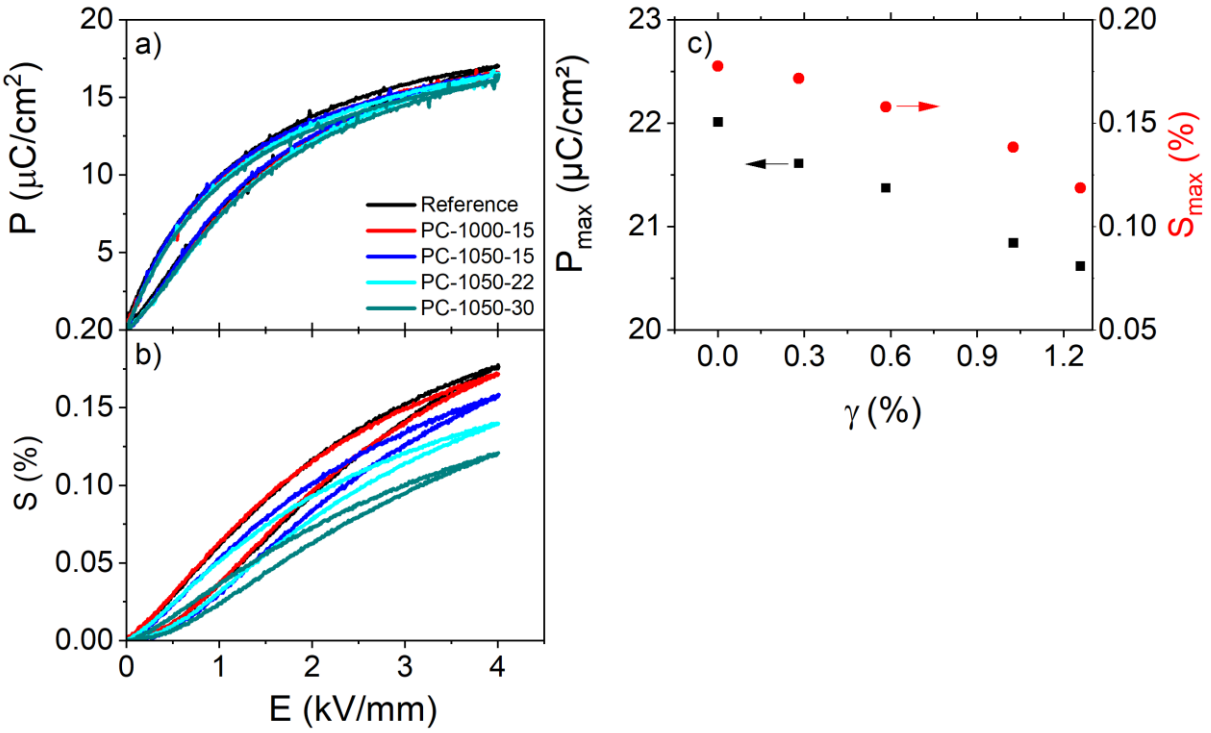

Figure 5.50: Unipolar (a) polarization and (b) strain at 10 Hz. P_{max} and S_{max} are presented as a function of the deformation strain in (c) (Adapted from [227]).

5.4.4 Discussion: Creep in Polycrystalline $BaTiO_3$

The creep mechanisms were identified using the power-law creep equation. Grain boundary sliding was not considered in the stress-exponent determination for the creep map. This assumption was disproven in the following experiments, indicating that grain boundary sliding has a significant effect on the microstructure and on functional properties; and it can also reach $n=3.5$ [106].

The activation energy was determined using the Arrhenius-type relationship in Equation 2-16 and the assumption that the proportionality factor $\dot{\gamma}_0$ is independent of the temperature. In the yellow region (Figure 5.44), interpreted as the diffusion creep regime, an activation energy of 350 kJ/mol is obtained for 950–1050 °C at 150 MPa and $n \approx 1$. The dislocation creep regime (blue region in Figure 5.44) gives an activation energy of 837 kJ/mol for 1000 °C at 212.5 MPa and $n = 3.38$. At slightly higher temperature (1050 °C) but lower stress (162.5 MPa), a similar value of 843 kJ/mol was obtained, with m ≈ 3.3.

The activation energy of 350 kJ/mol is in the same range as the activation enthalpy of the diffusion processes in pressureless-sintered $BaTiO_3$ ($\Delta H = 396 \pm 16$ kJ/mol) [134] and hot-pressing ($\Delta H = 400$ kJ/mol) [135]. The activation energy for oxygen diffusion is significantly lower, about 44–53 kJ/mol [318, 319]. The values in this work agree well with ^{131}Ba diffusion at 350 kJ/mol, suggesting that Ba is the dominant and rate-controlling cation species, as is the case in hot pressing and pressure-less sintering [134, 135]. The activation energy in the identified dislocation-creep regime is 840 kJ/mol for $n = 3.3$, which is twice as large as the activation energy in the diffusion regime and corresponds well to the results of volume-diffusion-creep in coarse-grained $BaTiO_3$ at 720 kJ/mol [137] and superplasticity in fine-

grained $BaTiO_3$ (800 kJ/mol) [136]. Notably, grain sizes, applied compressive stresses and temperature vary in the above-mentioned studies, as indicated in Table 7.1. Nonetheless, they indicate a diffusion-contribution even at 1050 °C, originally defined as the onset of the dislocation-creep regime. This diffusion contribution could be related either to non-conservative dislocation motion (climb controlled) or the diffusion creep remaining the dominant process at higher temperatures and stresses. For creep studies in polycrystalline $BaTiO_3$ [46, 137], including the samples deformed at 1050 °C in this work, the activation energies are higher than for single crystalline $BaTiO_3$ with $\Delta H = 469 \pm 27$ kJ/mol, which has been interpreted as a climb-controlled dislocation-based creep mechanism involving Ba^{2+} diffusion [46]. These studies illustrate that dislocation-based and diffusion-based processes occur in similar energy ranges, making it difficult to classify the processes unambiguously.

The stress-exponent approach and the determination of the activation energies are suitable for an initial estimation of the creep regimes and the processes involved, as long as microstructural investigations are performed in parallel to support and interpret the results. In this study, cavitation formation, variably shaped dislocations and no grain growth were observed, suggesting a superposition of competing creep mechanisms, including grain boundary sliding as a likely reason for the cavities. This superposition emphasizes, that the assumed stress exponent definition for diffusion and dislocation creep is too simple and requires further grain-size-dependent studies to refine it. Fine-grained $BaTiO_3$ offers a large grain-boundary-to-volume ratio that facilitates grain-boundary-related processes. Larger grain sizes may reduce the risk of cavitation but increase the risk of twinning [137]. In this work, the temperature of 1050 °C is on the limit of the dislocation creep mechanism regime, and therefore, a slightly higher temperature might be sufficient to introduce appropriate dislocation-based plastic deformation for fine-grained $BaTiO_3$. Park et al. have identified the temperature range of 1200–1300 °C and strain rates of $5 \cdot 10^{-7}$ to $4 \cdot 10^{-6}$ 1/s as most suitable for diffusion-creep of coarse-grained $BaTiO_3$ to avoid fracture or extensive cavitation [137]. This finding suggests that even higher temperatures or stresses are necessary to achieve the dislocation creep regime. However, higher temperatures could also cause glassy phases [320] at the grain boundaries [134]. To solve this problem, a grain-size-dependent study in similar temperature and stress ranges can provide the necessary information to obtain a more meaningful deformation map.

Based on the determined creep map, deformation parameters within the diffusion creep (200 MPa, 1000 °C) and the dislocation creep (200 MPa, 1050 °C) regimes were selected. The resulting microstructures indicated only slight variations in grain size but more pronounced variations in the relative density (92.1–97.9%), indicating that microcracks and pores in the sample with highest deformation of 1.29% occurred. No substantial pore formation, microcracking or extensive twinning were detected with SEM. Different dislocation structures were identified inside the grains, varying from curved dislocations to coffee-bean like dislocations [113, 140, 142]. This variety of dislocations points toward a partly successful dislocation creep process, causing microstrains in the system, as identified with X-ray investigations [227].

An increase in $\varepsilon_r'(RT)$ and a 5 °C shift in $\varepsilon_r'(max)$ to higher T_c values for the deformed samples compared to the reference sample illustrate that creep, indeed, induces changes in the dielectric properties. The peak broadening of the permittivity at T_c is correlated with microstrains, indicating additional stress contribution [227]. Thus, the number of twins and the domain size were not affected after creep. These two factors are negligible as sources of microstrain. The

existence of dislocations has been demonstrated using TEM, so it is likely that they contribute to the microstrains. Cavities at grain boundaries indicate local stress centers, and therefore, grain boundaries contribute to the microstrains in the material. A shift from $\Delta T_c = 5$ °C to higher temperature is in contrast to the effect of most point defect dopants such as Fe-doped $BaTiO_3$. Independently, a similar trend ($\Delta T_c = 5$-10 °C) has been demonstrated for uniform compressive stresses of 100 MPa-200 MPa for polycrystalline $BaTiO_3$ [321]. It should be mentioned that the creep-induced increase in T_c for polycrystalline $BaTiO_3$ is in contrast to the behavior of the single crystalline $BaTiO_3$, as discussed in Section 5.2.6, where a slightly decreased T_c was observed after creep. This suggests that the Taylor criterion, the grain boundaries and the differently oriented grains do indeed affect the material behavior.

Grain size is essential not only for the creep mechanisms but also for the extrinsic domain wall contribution to the electromechanical properties. Fine-grained $BaTiO_3$ samples often have smaller domain sizes than coarse-grained $BaTiO_3$ [268]. Contrary to the results presented in Section 5.1 for $KNbO_3$ single crystals, no obvious deviation between the reference sample and the deformed sample of the polycrystalline $BaTiO_3$ samples were found (published in Ref. [227]). The domain size is, at 115–154 nm, in the same range as reported values of 100 nm for $d_{GS} = 1.1\,\mu$m [307] and 150–300 nm for $d_{GS} = 2$–$4\,\mu$m [308]. Even more critical for domain wall-dislocation investigations, fine-grained $BaTiO_3$ tends to have weaker domain wall activity [309], which complicates the identification of a domain wall pinning; and hinders a comprehensive rationalization of dislocation-based functionality.

Electromechanically, a reduction of 10% for P_{max} and 30% for S_{max} was observed with increasing deformation strain, suggesting that the ferroelastic switching or the 90° domain wall motion is more affected than the 180° domain walls. Thus, the extrinsic contribution is directly affected by the creep deformation process. The intrinsic contribution is excluded because the bulk crystallographic structure is unchanged during the creep experiments. Cavities are similar to anisometric pores [317], which also reduce polarization and electromechanical strain, but their contribution seems to be rather small. The grain size remains constant, and porosity would lead to a simultaneous decrease in strain and polarization, so such microstructural features are also excluded in this particular case [317]. Since the electromechanical properties in polycrystalline $BaTiO_3$ [268] are generally grain size dependent, further creep studies on different grain sizes (e.g., coarse-grained $BaTiO_3$) are suggested.

Several sintering approaches based on non-stoichiometry [133, 140], flash-sintering [322, 323] or hot forging [324] achieve increased initial dislocation densities, which are also interesting for the dislocation-based functionality studies. The dislocation loops of high-temperature-deformed single crystalline and polycrystalline $BaTiO_3$ often have a ⟨010⟩ type Burgers vector, suggesting that the {100}⟨100⟩ slip systems contribute significantly to the deformation at high temperatures. In the case of the single crystal studies of Beauchesne and Poirier [46] and Doukhan and Doukhan [113], the activation of the {100}⟨100⟩ slip systems is a consequence of the initial single crystal orientation of ⟨110⟩ and the corresponding Schmid factor of 0.5. Nevertheless, it is possible that the {100}⟨100⟩ slip systems dominate in $BaTiO_3$, as is the case for $SrTiO_3$ [88, 113, 133, 140]. In consequence, certain preliminary results on the plastic deformation of ⟨110⟩-oriented $BaTiO_3$ single crystals are presented in Section 5.3 to illustrate the deformation behavior and anticipate further investigations.

Some of these results were published in a modified way in Ref. [227].

6 Conclusions and Outlook

This work investigated the introduction of dislocations and their influence on the ferroelectric domain structure and the dielectric and electromechanical behavior for $KNbO_3$ and $BaTiO_3$ single crystals, and a transfer to polycrystalline $BaTiO_3$ was presented.

As a starting point, [010] and [101] oriented $KNbO_3$ was mechanically deformed in the orthorhombic phase, and a plastic strain of 4.6% was obtained. A critical resolved shear stress of 26–30 MPa for the $\{110\}\langle 1\bar{1}0\rangle$ slip system shows that $KNbO_3$ not only is deformable at room temperature, but also exhibits similar behavior to $SrTiO_3$, which is a model material for dislocation-based functionality in the brittle perovskite family. With increasing plastic deformation, the slip bands, consisting of parallel slip planes, became wider, formed surface steps, and were inhomogeneously distributed throughout the sample. TEM studies illustrated that only single dislocations were distributed in the sample at deformation levels below 0.2%. However, at higher deformation levels, multiple slip bands with different edge dislocations were found, confirming the activation of the $\{110\}\langle 1\bar{1}0\rangle$ slip system with a Schmid factor of 0.5. The ferroelectric domain thickness was reduced from 1.8 μm to 0.5 μm after deformation inside slip bands. Field-dependent piezoresponse force microscopy studies emphasized that the domain structure changes into locally interrupted domain structures, indicating nucleation and pinning of the domains at the dislocations.

In contrast to $KNbO_3$, the focus of dislocation-based functionality study in $BaTiO_3$ single crystals is, besides of deformability investigations, on tailoring the electromechanical response by dislocations. $BaTiO_3$ is one of the model materials for ferroelectric applications and is well-studied in the context of defect engineering and domain wall engineering. The introduction of dislocations into $BaTiO_3$ single crystals requires the use of elevated temperatures. Platinum foils have been used as a protection layer to prevent cracking and allow creep deformation in the range of 1050 °C to 1170 °C to activate the $\{101\}\langle 10\bar{1}\rangle$ slip system in [001]-oriented single crystals. Mechanical imprinting by the creep methodology led to a rhombic domain structure and a preference for *a*-*c*-domains after deformation, indicating an alignment of the domain walls relative to the slip planes with a Schmid factor of 0.5. The rhombic structure consisted of cloudy regions with a high domain wall density and clear regions with a less dense multidomain structure. Although the degree of deformation was lower than in $KNbO_3$, a local change in the domain wall density was found. ECCI and TEM investigations confirmed that the $\{101\}\langle 10\bar{1}\rangle$ slip system was activated and provided evidence for nucleation and pinning of domains to dislocations during a temperature-dependent in-situ TEM study. NMR analysis enabled macroscopic insight into the poled and unpoled bulk samples and elucidated the changes in permittivity caused by the altered domain structure and the dielectric anisotropy. The reversible motion of the 90° *a*-*c*-domain walls in the subcoercive field led to a large increase in the piezoelectric coefficient in the intermediate AC electric field region. This reversible motion, in combination with a large back-switching of the domain walls after poling, led to a variation of the apparent coercive field. Mechanistically, the behavior was explained by a combined action of a pinning force, provided by the dislocations, and a mechanical restoring force opposing the domain wall motion due to strain incompatibilities. While the origin of the pinning force is related to the Peach–Koehler force between the dislocation and the domain wall, the macroscopic restoring force is caused by strain incompatibilities due to the mismatch between *c*- and *a*-domains. This combination of a local pinning force and a macroscopic restoring force

opens a new branch of dislocation-based investigations in ferroelectric materials. Studies of the time, temperature and cycling stability of these mechanisms are suggested to provide further insights for future applications.

Knowledge about the plastic deformability of perovskite materials is still limited, and there is no general agreement on the isomechanical behavior of perovskites. Plastic deformation experiments using compression at temperatures ranging from 1100 °C to 1170 °C were performed to address the deformability of [110]-oriented $BaTiO_3$ and to pave the way for further dislocation-based functionality studies on the {100}⟨100⟩ slip system. Above 100 MPa, [110]-oriented $BaTiO_3$ crystals show a similar trend to $SrTiO_3$ crystals and approach a maximum strain rate with increasing stress. This suggests that perovskite materials may indeed form an isomechanical group, but only when the applied stress and temperature are high enough to switch from a multi-mechanism deformation region to a single-mechanism region (e.g., the kink-pair mechanism). Note that $KNbO_3$ single crystals could not be considered in this comparison, due to the volatility of potassium and the risk of melting due to the near melting temperature.

We suggest the use of ⟨110⟩-oriented $BaTiO_3$ single crystals for further deformation experiments and the investigation of the interaction between the dislocations of the {100}⟨100⟩ slip system and the ferroelectric domain walls. The major advantages of the ⟨110⟩ orientation compared to the ⟨100⟩ orientation at high temperatures are easier deformability, increased dislocation density and no need for Pt protection plates. For a detailed understanding of the interaction between dislocations and domain walls, a deeper knowledge of the dislocation formation, type (edge, screw), structure (partial, dipoles) and local dislocation density are necessary for both slip systems. Similar to the different domain wall orientations, it is likely that the dislocation properties also determine the interaction. Furthermore, the dislocation core charge and the resulting space charge layer, as well as the charged domain walls, should be investigated. Moreover, a comparison between the influence of the $\{101\}\langle 10\bar{1}\rangle$ and the {100}⟨100⟩ slip systems on the electromechanical properties would allow the investigation of the anisotropic behavior not only in terms of the single crystal orientation but also in terms of the domain wall-dislocation pinning force and the resulting macroscopic restoring force.

Transferring the dislocation-based functionality from single crystals to polycrystalline materials extends the challenges regarding the introduction of dislocations. In addition to the Taylor criterion, competing creep mechanisms, diffusion processes and grain boundaries must also be considered. Before the creep study, the individual creep regimes for fine-grained $BaTiO_3$ were identified using stepwise creep experiments between 950 °C and 1100 °C. Assuming power-law creep, stress exponents from 0.5 to 3.3 were observed, indicating the linear regime (< 1), diffusion regime (1–3) and dislocation creep regime (≥ 3). Parameters in the diffusion and dislocation creep regimes were then selected, and compression experiments were performed at discrete temperatures and stresses. The diffusion creep sample reached a deformation of 0.29%, and the deformation of the dislocation creep samples varied from 0.6% to 1.29% over time. Density, grain size and twinning were evaluated and were excluded as reasons for the observed changes, whereas the observed cavitation formation at the grain boundaries may be partially related to the property changes. Dislocation structures were found in both diffusion and dislocation creep samples, but the shape varied from curved dislocations to coffee bean-like dislocations in the dislocation creep regime.

A 5 °C increase in T_c, a 30% decrease in electromechanical strain, and a 10% decrease in maximum polarization indicate that increasing deformation substantially affects the electromechanical behavior. Several competing mechanisms, such as grain boundary sliding combined with diffusion processes and dislocation creep, influence the microstructure, which results in changed electromechanical properties and resistivity. As a consequence, future investigations should consider using high-purity $BaTiO_3$ powder with less than 0.6% impurities, as was used in this study. In addition, a set of samples with different grain sizes could provide more-accurate information about the grain size dependence of the creep regimes in the deformation map. Moreover, the combination of stress exponents, activation energies and microstructural investigations with TEM and SEM is suitable to enclose the options for the active deformation mechanisms and to interpret the electromechanical changes. Furthermore, the use of materials with higher initial dislocation density, as in flash-sintered samples, can support the creep approach.

This work provides a proof of concept for the use of a dislocation-based functionality approach in bulk ferroelectrics and paves the way for further investigations into the tunability of the electromechanical properties and the plastic deformability of perovskites.

7 Appendix

7.1 Room Temperature Deformation

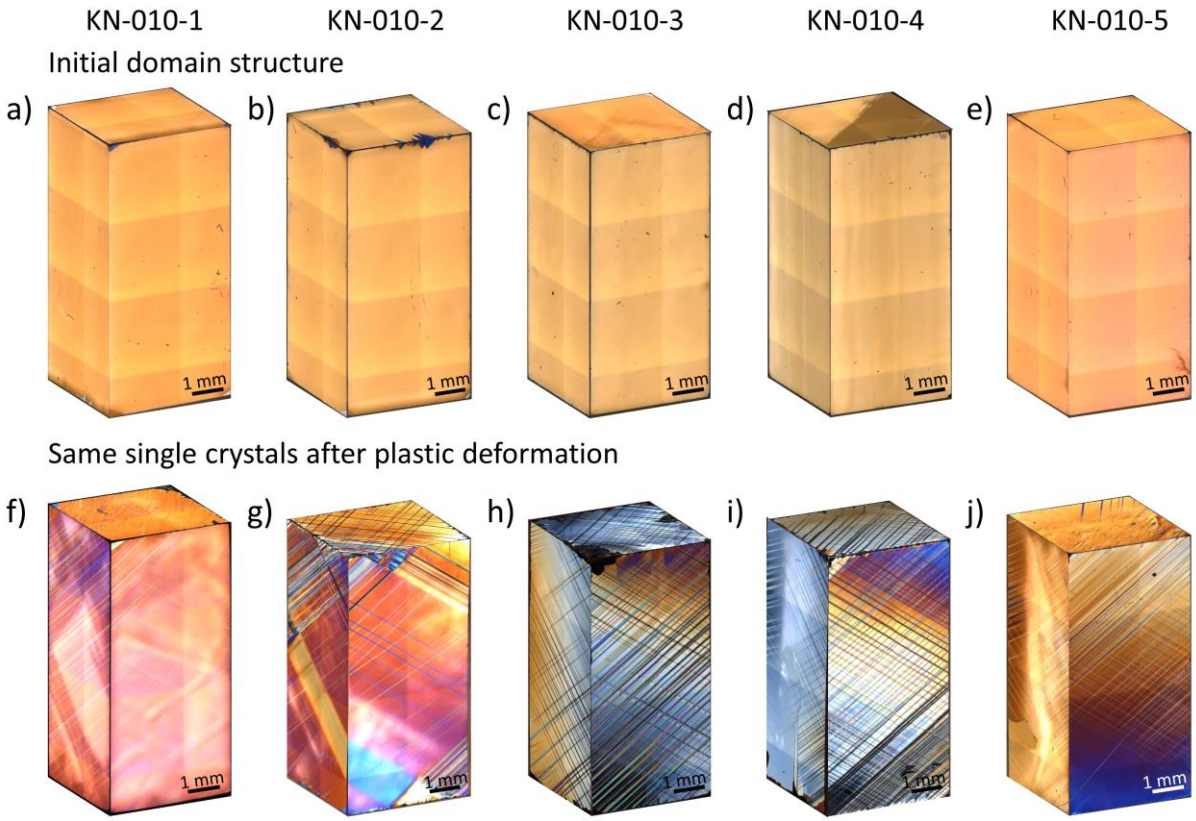

Figure 7.1: Comparison of the domain structure of ⟨010⟩-oriented $KNbO_3$ single crystals before (a-e) and after plastic deformation at room temperature (f-j). The images were acquired in the DIC mode of the Laser microscope (LEXT). Each subfigure consists of three images that were stitched together to obtain a perspective view of the single crystals. Special care was taken to match the edges as closely as possible, but due to the tilting of some samples, a slight mismatch between this representation and the actual single crystal is likely.

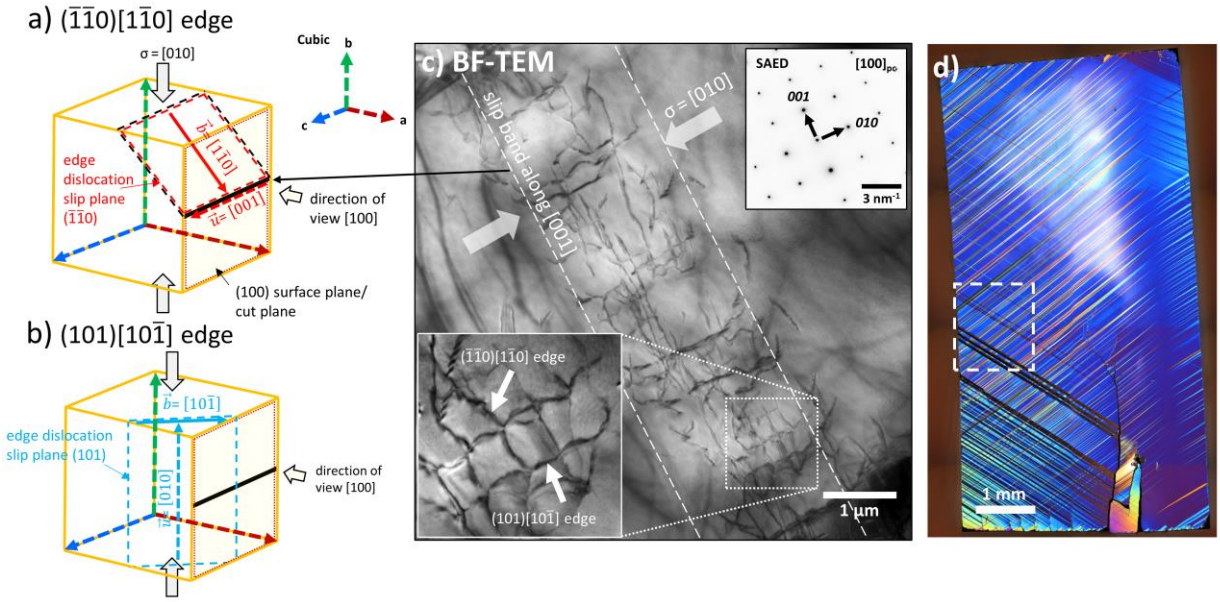

Figure 7.2: Orientation of the edge dislocations in the deformed $KNbO_3$ single crystal. Schematic representation of the slip planes of (a) $(\bar{1}\bar{1}0)[1\bar{1}0]$ and (b) $(101)[10\bar{1}]$-oriented edge dislocations identified in the slip band in (c). TEM-sample was prepared from sample material in the marked region (dashed line) of the tilted sample in (d).

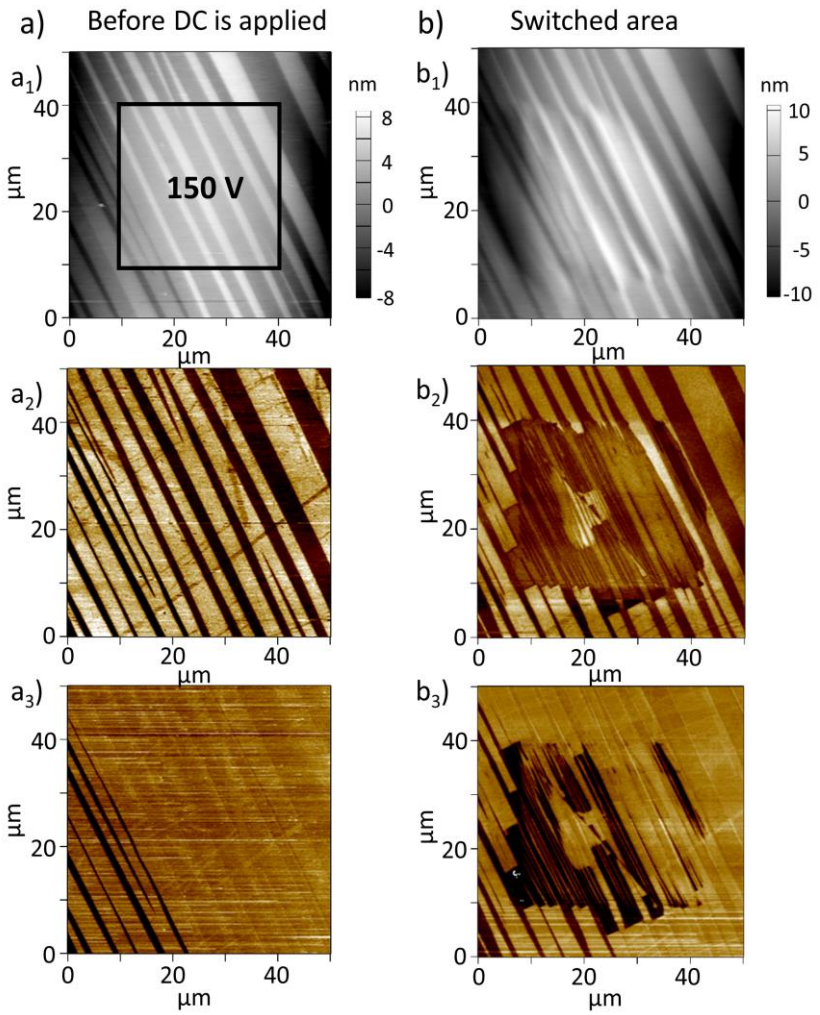

Figure 7.3: Piezoresponse force microscopy: DC switching experiment on an undeformed $KNbO_3$ single crystal (KN-010-4 before deformation). The topography (a_1), amplitude (a_2) and phase (a_3) are given before the application of the DC field and afterwards (b_1-b_3, respectively; after 15 min). The DC field of 150 V was applied in a rectangle with the dimensions 30×30 μm^2, as indicated in the topography in a_1.

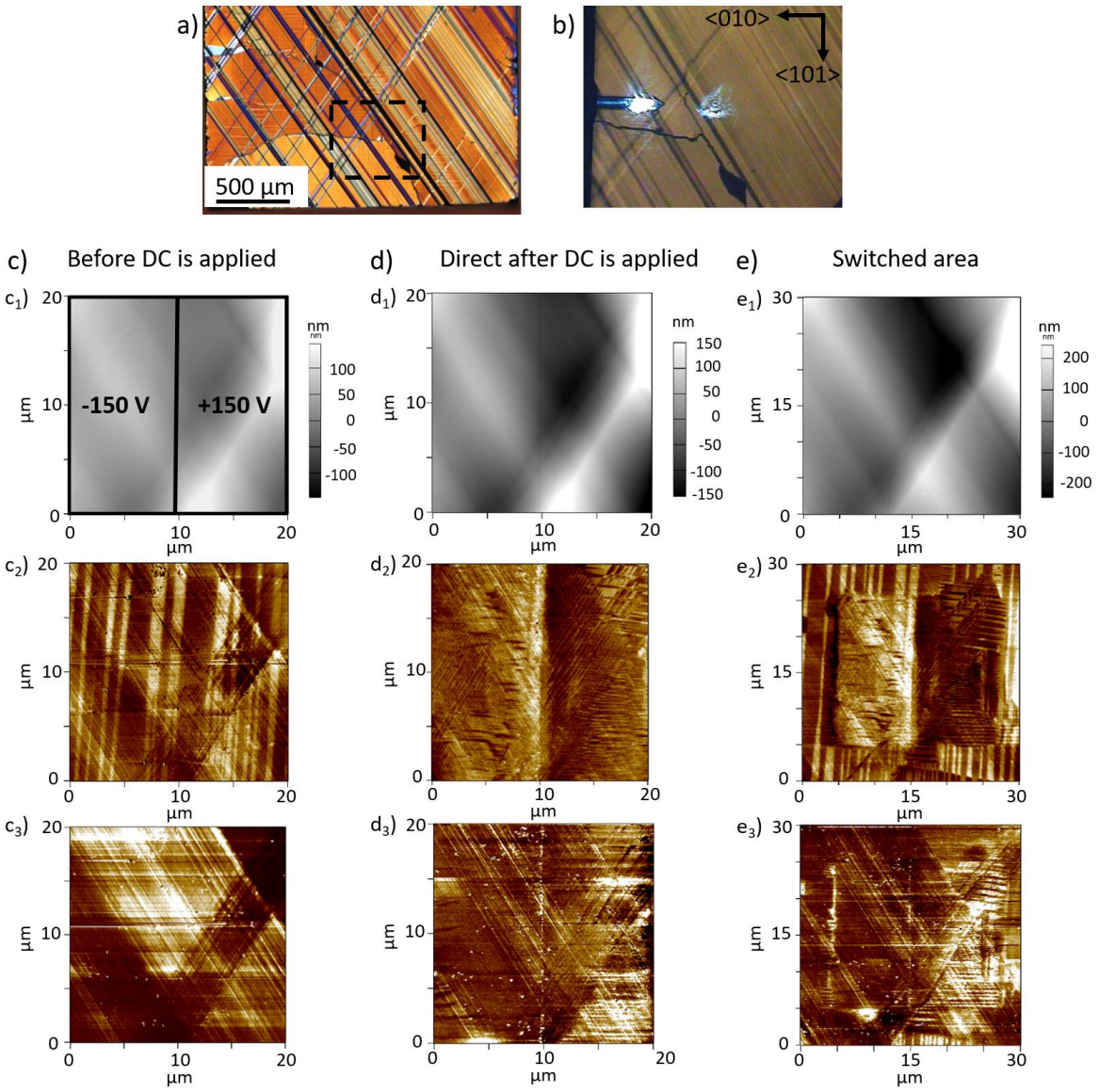

Figure 7.4: DC switching experiment on sample KN-010-2 in a region with pronounced slip band structure as indicated by DIC-OLM in (a) and near the local PFM region in (b). In this experiment, the entire region given in (c) is exposed to the applied DC field of ±150 V, leading to domain switching (d) and a significant difference between inside and outside of the DC field region, as demonstrated in (e). The topography (c_1, d_1, e_1), amplitude (c_2, d_2, e_2) and phase (c_3, d_3, e_3) are provided for all domain states.

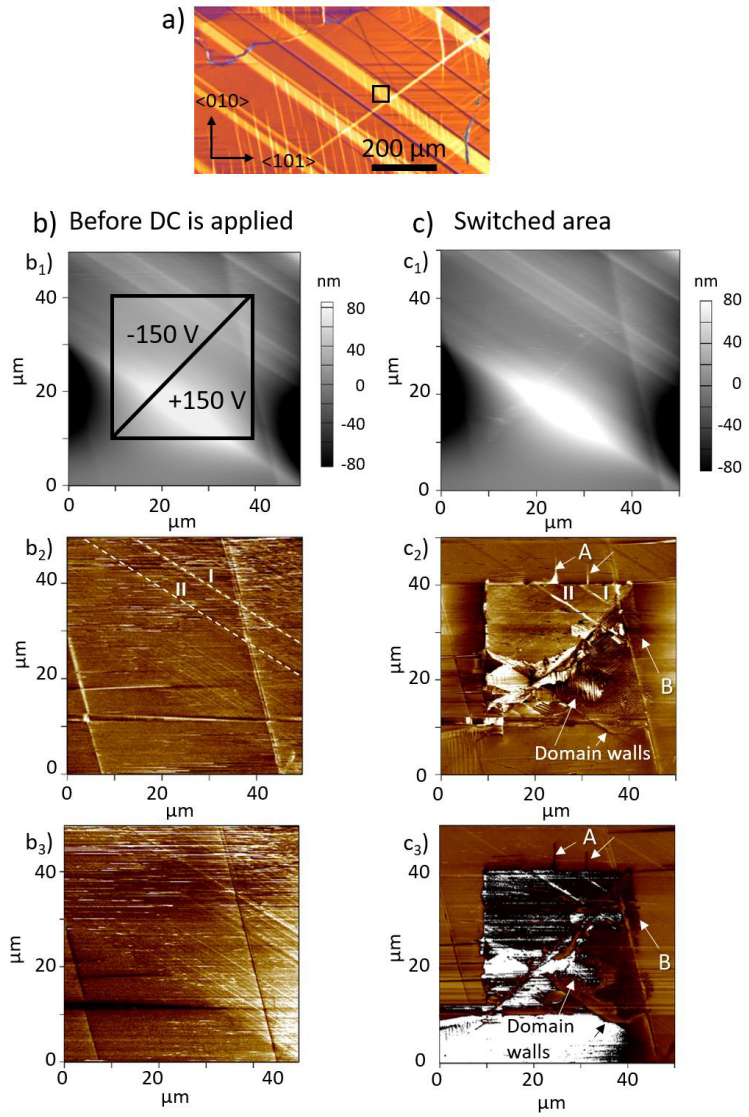

Figure 7.5: DC switching experiment in piezoresponse force microscopy to investigate the local domain structure within a slip band (b) before and (c) 15 min after applying a DC field of ±150 V. **a)** DIC-OLM image of the domain structure for the deformed single crystal KN-010-4. In (b_1-b_3) the topography, amplitude and phase are given for the selected region before a DC field is applied. The two triangles in b_1 indicate the respective DC regions, where ±150 V is applied. After turning of the electric field, the topography remained the same (c_1), but the domains rearrange, which is visible in the amplitude (c_2) and phase (c_3). Arrows point to domain walls that either appear outside the DC region (A, B) or emphasize the fragmented domain structure. Two slip planes **(I, II)** are highlighted with a dashed line in **(b_2)** and marked in **(c_2)** with **I** and **II.**

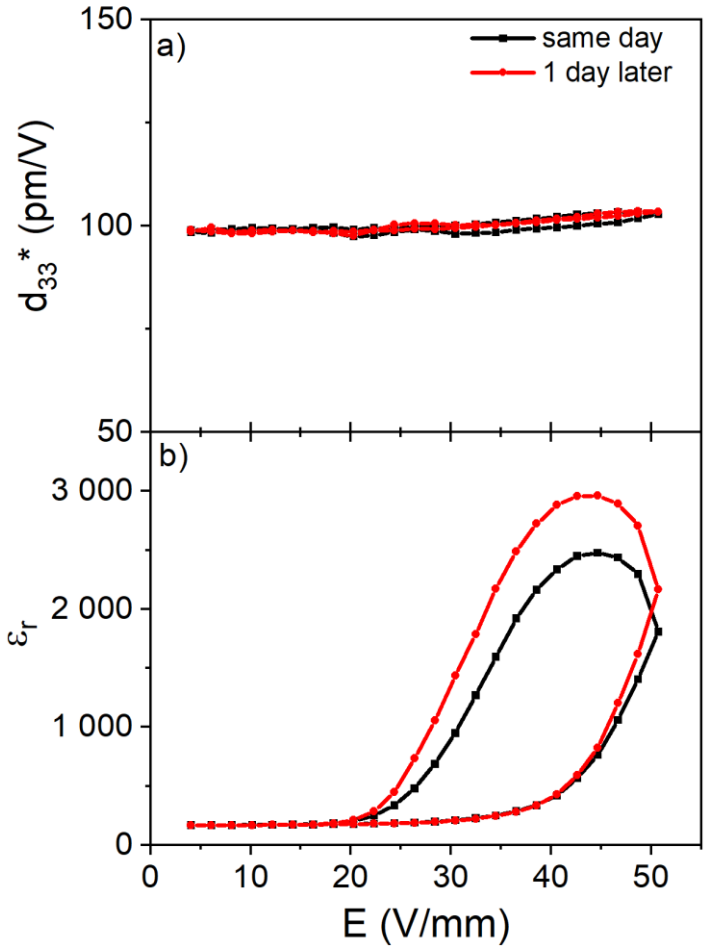

Figure 7.6: d_{33}^* (a) and ε_r (b) of a [001]-oriented $BaTiO_3$ reference single crystal at 1 kHz as a function of the applied subcoercive electric field.

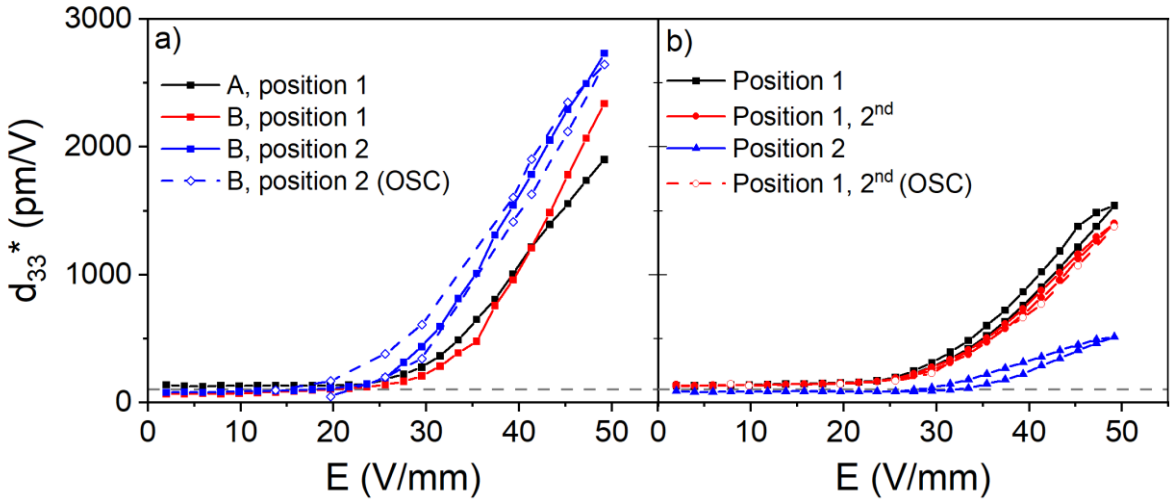

Figure 7.7: d_{33}* of a deformed [001]-oriented $BaTiO_3$ single crystal at 1 kHz as a function of the applied subcoercive electric field. a) Measured after poling at 0.5 kV/mm at different positions and both electrode surfaces. The sample was afterwards annealed and poled again (b).

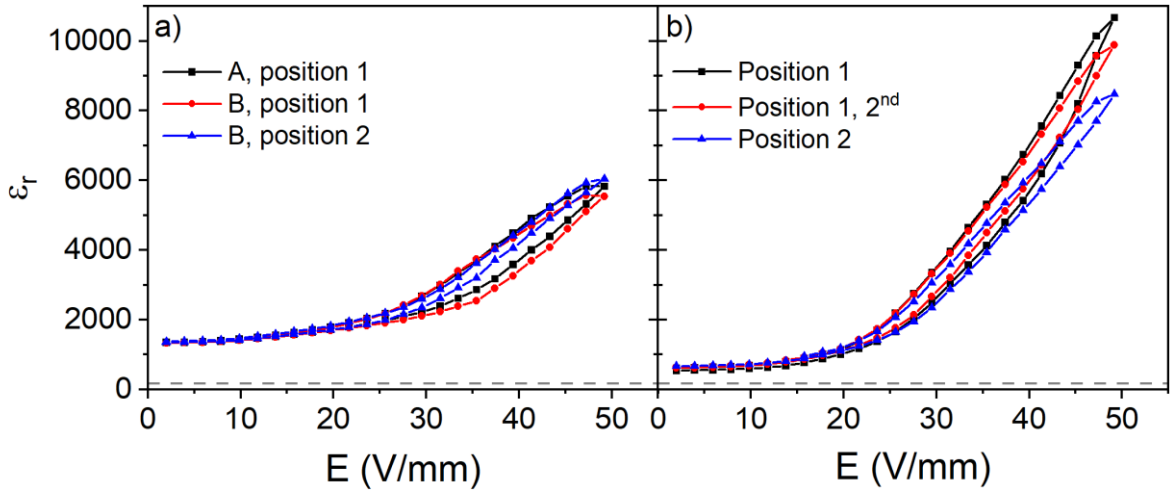

Figure 7.8: ε_r of a deformed [001]-oriented $BaTiO_3$ single crystal at 1 kHz as a function of the applied subcoercive electric field. a) Measured after poling at 0.5 kV/mm at different positions and both electrode surfaces. The sample was afterwards annealed and poled again (b).

7.3 <110>-Oriented $BaTiO_3$ Single Crystals

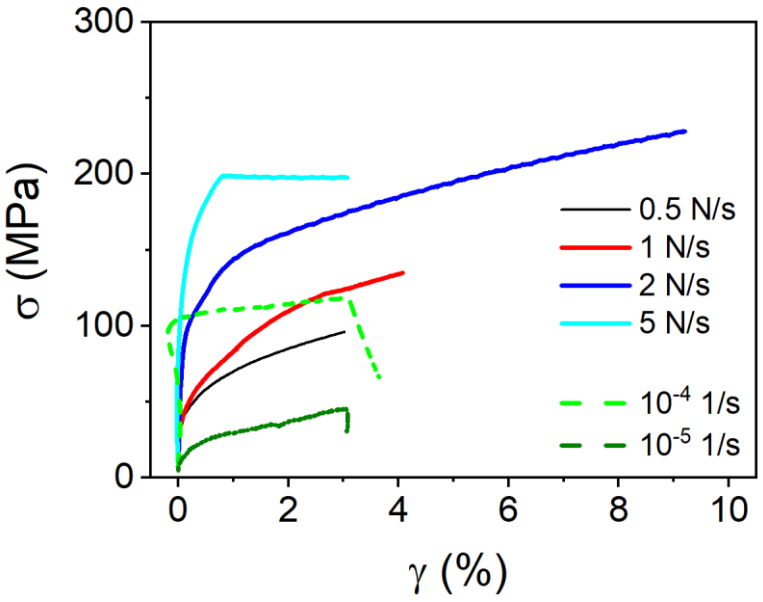

Figure 7.9: Stress-strain curves at different loading conditions for a compression experiment on ⟨110⟩-oriented $BaTiO_3$ at 1150 °C.

7.4 Polycrystalline Creep

Table 7.1: Summary of activation energies and relevant creep parameters for creep studies and activation enthalpies of several non-creep mechanisms and diffusion processes in $BaTiO_3$.

Material, d_{GS}	**m**	**Temperature (°C)**	**Compressive Stress (MPa)**	**Activation energy (kJ/mol)**	**Reference, comment**
$BaTiO_3$, 1-2 μm	≈1	950-1050	150	350 kJ/mol	This work
$BaTiO_3$, 1-2 μm	≈3.38	1000	212.5	837	This work
$BaTiO_3$, 1-2 μm	≈3.3	1050	212.5	843	This work
$BaTiO_3$, 19.3-52.4 μm	≈1	1200-1300	0.25-5	720±70	Creep, diffusion [137]
$BaTiO_3$, 0.45 μm	≈2.5	1150-1250	5-60	1200-800	Creep, superplasticity [136]
$BaTiO_3$ single crystal glide on {**100**}⟨**100**⟩	3.6	1150-1570	9-25	469±27	Climb-controlled by diffusion of slowest species [46])
Non-creep mechanisms		**T (°C)**		**Activation enthalpy ΔH (kJ/mol)**	**Reference, comment**
$BaTiO_3$		1050 °C	2.3-27.6	400	Hot-pressing [135]
$BaTiO_3$				750±80	Sintering, Grain-growth study [325]
$BaTiO_3$ with TiO2-excess				522±130	Pressureless-sintering [134]
$BaTiO_3$ with BaO-excess				396±16	Pressureless-sintering [134]
Diffusion		**T (°C)**		**ΔH (kJ/mol)**	**Reference, comment**
Barium in $BaTiO_3$		884-1180		372	Diffusion of ^{131}Ba in $BaTiO_3$[326]
Oxygen in $BaTiO_3$				44 kJ/mol	[319]
Oxygen		900-1100		53 kJ/mol	Self-diffusion [318]
Titanium				293	Self-diffusion [318]

List of Tables

List of Figures

Bibliography

[1] J.H. Haeni, P. Irvin, W. Chang, R. Uecker, P. Reiche, Y.L. Li, S. Choudhury, W. Tian, M.E. Hawley, B. Craigo, A.K. Tagantsev, X.Q. Pan, S.K. Streiffer, L.Q. Chen, S.W. Kirchoefer, J. Levy, D.G. Schlom, Room-Temperature Ferroelectricity in Strained $SrTiO_3$, Nature 430(7001), 758-761, (2004).

[2] K.J. Choi, M. Biegalski, Y.L. Li, A. Sharan, J. Schubert, R. Uecker, P. Reiche, Y.B. Chen, X.Q. Pan, V. Gopalan, L.Q. Chen, D.G. Schlom, C.B. Eom, Enhancement of Ferroelectricity in Strained $BaTiO_3$ Thin Films, Science 306(5698), 1005-1009, (2004).

[3] R.S. Beach, J.A. Borchers, A. Matheny, R.W. Erwin, M.B. Salamon, B. Everitt, K. Pettit, J.J. Rhyne, C.P. Flynn, Enhanced Curie Temperatures and Magnetoelastic Domains in Dy/Lu Superlattices and Films, Phys. Rev. Lett. 70(22), 3502-3505, (1993).

[4] I. Bozovic, G. Logvenov, I. Belca, B. Narimbetov, I. Sveklo, Epitaxial Strain and Superconductivity in $La_{2-x}Sr_xCuO_4$ Thin Films, Phys. Rev. Lett. 89(10), 4, (2002).

[5] K. Carl, K.H. Härdtl, Electrical Aftereffects in $Pb(Ti,Zr)O_3$ Ceramics, Ferroelectrics 17(3-4), 473-486, (1978).

[6] G. Arlt, D. Hennings, G. Dewith, Dielectric Properties of Fine-Grained Barium Titanate Ceramics, J. Appl. Phys. 58(4), 1619-1625, (1985).

[7] K.V. Lalitha, L.M. Riemer, J. Koruza, J. Rödel, Hardening of Electromechanical Properties in Piezoceramics Using a Composite Approach, Appl. Phys. Lett. 111(2), 022905, (2017).

[8] B. Dam, J.M. Huijbregtse, F.C. Klaassen, R.C.F. van der Geest, G. Doornbos, J.H. Rector, A.M. Testa, S. Freisem, J.C. Martinez, B. Stauble-Pumpin, R. Griessen, Origin of High Critical Currents in $YBa_2Cu_3O_7$-Delta Superconducting Thin Films, Nature 399(6735), 439-442, (1999).

[9] S.I. Kim, K.H. Lee, H.A. Mun, H.S. Kim, S.W. Hwang, J.W. Roh, D.J. Yang, W.H. Shin, X.S. Li, Y.H. Lee, Dense Dislocation Arrays Embedded in Grain Boundaries for High-Performance Bulk Thermoelectrics, Science 348(6230), 109-114, (2015).

[10] R.W. Whitworth, Charged Dislocations in Ionic Crystals, Adv. Phys. 24(2), 203-304, (1975).

[11] M. Johanning, L. Porz, J. Dong, A. Nakamura, J.-F. Li, J. Rödel, Influence of Dislocations on Thermal Conductivity of Strontium Titanate, Appl. Phys. Lett. 117(2), 021902, (2020).

[12] A. Nakamura, K. Matsunaga, J. Tohma, T. Yamamoto, Y. Ikuhara, Conducting Nanowires in Insulating Ceramics, Nat. Mater. 2(7), 453-456, (2003).

[13] T. Nakagawa, A. Nakamura, I. Sakaguchi, N. Shibata, K.P.D. Lagerlof, T. Yamamoto, H. Haneda, Y. Ikuhara, Oxygen Pipe Diffusion in Sapphire Basal Dislocation, J. Ceram. Soc. Jpn. 114(1335), 1013-1017, (2006).

[14] K.K. Adepalli, M. Kelsch, R. Merkle, J. Maier, Influence of Line Defects on the Electrical Properties of Single Crystal TiO_2, Adv. Funct. Mater. 23(14), 1798-1806, (2013).

[15] K. Uchino, Advanced Piezoelectric Materials - Science and Technology Woodhead Publishing Ltd., 2017.

[16] M.E. Lines, A.M. Glass, Principles and Applications of Ferroelectrics and Related Materials, Oxford University Press, 2001.

[17] R. Guo, L.E. Cross, S.E. Park, B. Noheda, D.E. Cox, G. Shirane, Origin of the High Piezoelectric Response in $PbZr_{1-x}Ti_xO_3$, Phys. Rev. Lett. 84(23), 5423-5426, (2000).

[18] X.B. Ren, Large Electric-Field-Induced Strain in Ferroelectric Crystals by Point-Defect-Mediated Reversible Domain Switching, Nat. Mater. 3(2), 91-94, (2004).

[19] G.L. Messing, S. Poterala, Y. Chang, T. Frueh, E.R. Kupp, B.H. Watson, R.L. Walton, M.J. Brova, A.-K. Hofer, R. Bermejo, R.J. Meyer, Texture-Engineered Ceramics–Property Enhancements Through Crystallographic Tailoring, J. Mater. Res. 32(17), 3219-3241, (2017).

[20] Y. Saito, H. Takao, T. Tani, T. Nonoyama, K. Takatori, T. Homma, T. Nagaya, M. Nakamura, Lead-Free Piezoceramics, Nature 432(7013), 84-87, (2004).

[21] J. Li, Z. Shen, X. Chen, S. Yang, W. Zhou, M. Wang, L. Wang, Q. Kou, Y. Liu, Q. Li, Z. Xu, Y. Chang, S. Zhang, F. Li, Grain Orientation Engineered Multilayer Ceramic Capacitors for Energy Storage Applications, Nat. Mater. 19, 999–1005, (2020).
[22] S. Wada, K. Yako, T. Muraishi, H. Kakemoto, T. Tsurumi, Development of Lead-Free Piezoelectric Materials Using Domain Wall Engineering, Key Eng. Mat. 320, 151-154, (2006).
[23] S. Wada, K. Yako, K. Yokoo, H. Kakemoto, T. Tsurumi, Domain Wall Engineering in Barium Titanate Single Crystals for Enhanced Piezoelectric Properties, Ferroelectrics 334, 17-27, (2006).
[24] Q. Wang, F. Li, Large Actuation Strain over 0.3% in Periodically Orthogonal Poled $BaTiO_3$ Ceramics and Multilayer Actuators via Reversible Domain Switching, J. Phys. D Appl. Phys. 51(25), 255301, (2018).
[25] Y.A. Genenko, J. Glaum, M.J. Hoffmann, K. Albe, Mechanisms of Aging and Fatigue in Ferroelectrics, Mater. Sci. Eng. B-Adv. 192, 52-82, (2015).
[26] D. Lupascu, J. Rödel, Fatigue In Bulk Lead Zirconate Titanate Actuator Materials, Adv. Eng. Mater. 7(10), 882-898, (2005).
[27] K.W. Plessner, Ageing of the Dielectric Properties of Barium Titanate Ceramics, P. Phys. Soc. Lond. B 69(12), 1261-1268, (1956).
[28] S. Hirose, M. Aoyagi, Y. Tomikawa, S. Takahashi, K. Uchino, High Power Characteristics at Antiresonance Frequency of Piezoelectric Transducers, Ultrasonics 34(2-5), 213-217, (1996).
[29] M. Slabki, J. Wu, M. Weber, P. Breckner, D. Isaia, K. Nakamura, J. Koruza, Anisotropy of the High-Power Piezoelectric Properties of $Pb(Zr,Ti)O_3$, J. Am. Ceram. Soc. 102(10), 6008-6017, (2019).
[30] K.K. Adepalli, J. Yang, J. Maier, H.L. Tuller, B. Yildiz, Tunable Oxygen Diffusion and Electronic Conduction in $SrTiO_3$ by Dislocation-Induced Space Charge Fields, Adv. Funct. Mater. 27(22), 1700243 (1-9), (2017).
[31] L. Qi, C. Jun, L. Bing-Liang, F. Duan, The Interactions Between Dislocations and Ferroelectric Domains in $KNbO_3$ Crystals, Radiat. Eff. 74(1-4), 307-313, (1983).
[32] A. Kontsos, C.M. Landis, Computational Modeling of Domain Wall Interactions with Dislocations in Ferroelectric Crystals, Int. J. Solids Struct. 46(6), 1491-1498, (2009).
[33] Y.L. Li, S.Y. Hu, S. Choudhury, M.I. Baskes, A. Saxena, T. Lookman, Q.X. Jia, D.G. Schlom, L.Q. Chen, Influence of Interfacial Dislocations on Hysteresis Loops of Ferroelectric Films, J. Appl. Phys. 104(10), 104110, (2008).
[34] Y. Zheng, B. Wang, C.H. Woo, Effects of Interface Dislocations on Properties of Ferroelectric Thin Films, J. Mech. Phys. Solids 55(8), 1661-1676, (2007).
[35] P. Gao, C.T. Nelson, J.R. Jokisaari, S.H. Baek, C.W. Bark, Y. Zhang, E.G. Wang, D.G. Schlom, C.B. Eom, X.Q. Pan, Revealing the Role of Defects in Ferroelectric Switching with Atomic Resolution, Nat. Commun. 2(591), 1-6, (2011).
[36] H.H. Wu, J. Wang, S.G. Cao, L.Q. Chen, T.Y. Zhang, Micro-/Macro-Responses of a Ferroelectric Single Crystal with Domain Pinning and Depinning by Dislocations, J. Appl. Phys. 114(16), 164108, (2013).
[37] H.H. Wu, J. Wang, S.G. Cao, L.Q. Chen, T.Y. Zhang, The Unusual Temperature Dependence of the Switching Behavior in a Ferroelectric Single Crystal with Dislocations, Smart Mater. Struct. 23(2), 7, (2014).
[38] H.H. Wu, J. Wang, S.G. Cao, T.Y. Zhang, Effect of Dislocation Walls on the Polarization Switching of a Ferroelectric Single Crystal, Appl. Phys. Lett. 102(23), 232904, (2013).
[39] A.F. Mark, M. Castillo-Rodríguez, W. Sigle, Unexpected Plasticity of Potassium Niobate During Compression Between Room Temperature and 900 Degrees C, J. Eur. Ceram. Soc. 36(11), 2781-2793, (2016).
[40] T. Suzuki, S. Takeuchi, H. Yoshinaga, Dislocation Dynamics and Plasticity, Springer-Verlag Berlin Heidelberg, 1991.
[41] G.E. Dieter, Mechanical Metallurgy, McGraw-Hill, 1986.
[42] R.W.K. Honeycombe, The Plastic Deformation of Metals, Butler & Tanner, 1985.
[43] Y. Gaillard, A.H. Macias, J. Munoz-Saldana, M. Anglada, G. Trapaga, Nanoindentation of $BaTiO_3$: Dislocation Nucleation and Mechanical Twinning, J. Phys. D-Appl. Phys. 42(8), 085502, (2009).

[44] Y. Gaillard, C. Tromas, J. Woirgard, Study of the Dislocation Structure Involved in a Nanoindentation Test by Atomic Force Microscopy and Controlled Chemical Etching Acta Mater. 51(4), 1059-1065, (2003).
[45] T. Scholz, K.K. McLaughlin, F. Giuliani, W.J. Clegg, F.J. Espinoza-Beltran, M.V. Swain, G.A. Schneider, Nanoindentation Initiated Dislocations in Barium Titanate ($BaTiO_3$), Appl. Phys. Lett. 91(6), 062903, (2007).
[46] S. Beauchesne, J.P. Poirier, Creep of Barium Titanate Perovskite: A Contribution to a Systematic Approach to the Viscosity of the Lower Mantle, Phys. Earth Planet. Inter. 55(1), 187-199, (1989).
[47] S. Beauchesne, J.P. Poirier, In Search of a Systematics for the Viscosity of Perovskites: Creep of Potassium Tantalate and Niobate, Phys. Earth Planet. Int. 61(3), 182-198, (1990).
[48] R. Skulski, P. Wawrzala, The Results of Computerized Simulation of the Influence of Dislocations on the Degree of Phase Transition Diffusion in $BaTiO_3$, Physica B 233(2), 173-178, (1997).
[49] S.Y. Hu, Y.L. Li, L.Q. Chen, Effect of Interfacial Dislocations on Ferroelectric Phase Stability and Domain Morphology in a Thin Film - A Phase-Field Model, J. Appl. Phys. 94(4), 2542-2547, (2003).
[50] N.A. Pertsev, G. Arlt, A.G. Zembilgotov, Prediction of a Giant Dielectric Anomaly in Ultrathin Polydomain Ferroelectric Epitaxial Films, Phys. Rev. Lett. 76(8), 1364-1367, (1996).
[51] N.A. Pertsev, A.Y. Emelyanov, Stability Diagram for Elastic Domains in Epitaxial Ferroelectric Thin Films, Phys. Solid State 39(1), 109-115, (1997).
[52] A.Y. Emelyanov, N.A. Pertsev, Abrupt Changes and Hysteretic Behavior of 90 Degrees Domains in Epitaxial Ferroelectric Thin Films with Misfit Dislocations, Phys. Rev. B 68(21), 10, (2003).
[53] M.W. Chu, I. Szafraniak, R. Scholz, C. Harnagea, D. Hesse, M. Alexe, U. Gosele, Impact of Misfit Dislocations on the Polarization Instability of Epitaxial Nanostructured Ferroelectric Perovskites, Nat. Mater. 3(2), 87-90, (2004).
[54] H.P. Sun, W. Tian, X.Q. Pan, J.H. Haeni, D.G. Schlom, Evolution of Dislocation Arrays in Epitaxial $BaTiO_3$ Thin Films Grown on (100) $SrTiO_3$, Appl. Phys. Lett. 84(17), 3298-3300, (2004).
[55] M.W. Chu, I. Szafraniak, D. Hesse, M. Alexe, U. Gosele, Elastic Coupling Between 90 Degrees Twin Walls and Interfacial Dislocations in Epitaxial Ferroelectric Perovskites: A Quantitative High-Resolution Transmission Electron Microscopy Study, Phys. Rev. B 72(17), 5, (2005).
[56] I.B. Misirlioglu, A.L. Vasiliev, M. Aindow, S.P. Alpay, Strong Degradation of Physical Properties and Formation of a Dead Layer in Ferroelectric Films due to Interfacial Dislocations, Integr. Ferroelectrics 71, 67-80, (2005).
[57] V. Nagarajan, C.L. Jia, H. Kohlstedt, R. Waser, I.B. Misirlioglu, S.P. Alpay, R. Ramesh, Misfit Dislocations in Nanoscale Ferroelectric Heterostructures, Appl. Phys. Lett. 86(19), 192910, (2005).
[58] S. Zlotnik, D.M. Tobaldi, P. Seabra, J.A. Labrincha, P.M. Vilarinho, Alkali Niobate and Tantalate Perovskites as Alternative Photocatalysts, Chem. Phys. Chem. 17(21), 3570-3575, (2016).
[59] M. Zgonik, R. Schlesser, I. Biaggio, E. Voit, J. Tscherry, P. Gunter, Materials Constants of $KNbO_3$ Relevant for Electrooptics and Acoustooptics, J. Appl. Phys. 74(2), 1287-1297, (1993).
[60] S. Trolier-McKinstry, C.A. Randall, Movers, Shakers, and Storers of Charge: The Legacy of Ferroelectricians L. Eric Cross and Robert E. Newnham, J. Am. Ceram. Soc. 100(8), 3346-3359, (2017).
[61] J.B. Wachtman, W.R. Cannon, M.J. Matthewson, Mechanical Properties of Ceramics, John Wiley & Sons Inc., 2009.
[62] J. Pelleg, Mechanical Properties of Ceramics, Springer, 2014.
[63] J. Pelleg, Creep in Ceramics, Springer International Publishing, 2017.
[64] U. Messerschmidt, Dislocation Dynamics During Plastic Deformation, Springer Series in Materials Science, Springer Berlin Heidelberg, 2010.

[65] D. Hull, D.J. Bacon, Introduction to Dislocations, Elsevier, 2011.
[66] M. Tanaka, G. Honjo, Electron Optic Studies of Barium Titanate Single Crystal Films, J. Phys. Soc. Jpn. 19(6), 954-970, (1964).
[67] T. Bretheau, J. Castaing, J. Rabier, P. Veyssiere, Summary- Dislocation-Motion and High-Temperature Plasticity of Binary and Ternary Oxides, Adv. Phys. 28(6), 829-834, (1979).
[68] J. Rösler, H. Harders, M. Baeker, Mechanical Behaviour of Engineering Materials. Metals, Ceramics, Polymers, and Composites, Springer-Verlag Berlin Heidelberg, 2007.
[69] J.-P. Poirier, Creep of Crystals: High-Temperature Deformation Processes in Metals, Ceramics and Minerals, Cambridge University Press, 1985.
[70] R.W. Whitworth, The Sweep-up Model of Charged Dislocations in Ionic-Crystals, Philos. Mag. A 51(6), 857-863, (1985).
[71] K. Szot, C. Rodenbücher, G. Bihlmayer, W. Speier, R. Ishikawa, N. Shibata, Y. Ikuhara, Influence of Dislocations in Transition Metal Oxides on Selected Physical and Chemical Properties, Crystals 8(6), 241, (2018).
[72] C.L. Jia, A. Thust, K. Urban, Atomic-Scale Analysis of the Oxygen Configuration at a $SrTiO_3$ Dislocation Core, Phys. Rev. Lett. 95(22), 225506, (2005).
[73] J.P. Buban, M. Chi, D.J. Masiel, J.P. Bradley, B. Jiang, H. Stahlberg, N.D. Browning, Structural Variability of Edge Dislocations in a $SrTiO_3$ Low-Angle [001] Tilt Grain Boundary, J. Mater. Res. 24(7), 2191-2199, (2009).
[74] K.K. Adepalli, M. Kelsch, R. Merkle, J. Maier, Enhanced Ionic Conductivity in Polycrystalline TiO_2 by "One-Dimensional Doping", Phys. Chem. Chem. Phys. 16(10), 4942-4951, (2014).
[75] D. Marrocchelli, L. Sun, B. Yildiz, Dislocations in $SrTiO_3$: Easy To Reduce but Not so Fast for Oxygen Transport, J. Am. Ceram. Soc. 137(14), 4735-4748, (2015).
[76] C.-L. Jia, M. Lentzen, K. Urban, High-Resolution Transmission Electron Microscopy Using Negative Spherical Aberration, Microsc. Microanal. 10(2), 174-184, (2004).
[77] Z. Zhang, W. Sigle, M. Rühle, Atomic and Electronic Characterization of the [100] Dislocation Core in $SrTiO_3$, Phys. Rev. B 66(9), 094108, (2002).
[78] R.A. De Souza, J. Fleig, J. Maier, O. Kienzle, Z. Zhang, W. Sigle, M. Rühle, Electrical and Structural Characterization of a Low-Angle Tilt Grain Boundary in Iron-Doped Strontium Titanate, J. Am. Ceram. Soc. 86(6), 922-928, (2003).
[79] Y. Furushima, A. Nakamura, E. Tochigi, Y. Ikuhara, K. Toyoura, K. Matsunaga, Dislocation Structures and Electrical Conduction Properties of Low Angle Tilt Grain Boundaries in $LiNbO_3$, J. Appl. Phys. 120(14), 142107, (2016).
[80] V. Metlenko, A.H.H. Ramadan, F. Gunkel, H. Du, H. Schraknepper, S. Hoffmann-Eifert, R. Dittmann, R. Waser, R.A. De Souza, Do Dislocations Act as Atomic Autobahns for Oxygen in the Perovskite Oxide $SrTiO_3$?, Nanoscale 6(21), 12864-12876, (2014).
[81] J. Chen, T. Sekiguchi, J. Li, S. Ito, Investigation of Dislocations in Nb-Doped (100) $SrTiO_3$ Single Crystals and Their Impacts on Resistive Switching, Superlattice Microst. 99, 182-185, (2016).
[82] T. Matsunaga, H. Saka, Transmission Electron Microscopy of Dislocations in $SrTiO_3$, Philos. Mag. Lett. 80(9), 597-604, (2000).
[83] T. Suzuki, S. Takeuchi, Lattice Defects in Ceramics: Proceedings of the Japan-France Seminar on Lattice Defects in Ceramics Publication Office, Jpnn. J. Appl. Phys., (1989).
[84] Y. Kamimura, K. Edagawa, S. Takeuchi, Experimental Evaluation of the Peierls Stresses in a Variety of Crystals and Their Relation to the Crystal Structure, Acta Mater. 61(1), 294-309, (2013).
[85] G. Gottstein, Physikalische Grundlagen der Materialkunde, Springer, 2007.
[86] D. Brunner, Low-Temperature Plasticity and Flow-Stress Behaviour of Strontium Titanate Single Crystals, Acta Mater. 54(19), 4999-5011, (2006).
[87] G. Schoeck, The Activation Energy of Dislocation Movement, Phys. Status. Solidi B 8(2), 499-507, (1965).
[88] S. Taeri, D. Brunner, W. Sigle, M. Rühle, Deformation Behaviour of Strontium Titanate Between Room Temperature and 1800 K Under Ambient Pressure, Z. Metallk. 95(6), 433-446, (2004).

[89] M. Castillo-Rodríguez, W. Sigle, The Kink-Pair Mechanism and Low-Temperature Flow-Stress Behaviour of Strontium Titanate Single Crystals, Scr. Mater. 64(3), 241-244, (2011).
[90] D. Brunner, Can the Kink-Pair Theory Apply for the Yield Stress of Single Crystalline $SrTiO_3$ at High Temperatures?, Mater. Sci. Eng. A 483–484, 521-524, (2008).
[91] J.F. Nye, Physical Properties of Crystals. Their Representation by Tensors and Matrices, Oxford University Press, 1967.
[92] D. German Institute for Standardization, Testing of Metallic Materials; Tensile Test, Beuth Verlag GmbH, 1975.
[93] D. Brunner, S. Taeri-Baghbadrani, W. Sigle, M. Rühle, Surprising Results of a Study on the Plasticity in Strontium Titanate, J. Am. Ceram. Soc. 84(5), 1161-1163, (2001).
[94] P. Gumbsch, S. Taeri-Baghbadrani, D. Brunner, W. Sigle, M. Rühle, Plasticity and an Inverse Brittle-to-Ductile Transition in Strontium Titanate, Phys. Rev. Lett. 87(8), 085505, (2001).
[95] P. Hirel, A.F. Mark, M. Castillo-Rodríguez, W. Sigle, M. Mrovec, C. Elsässer, Theoretical and Experimental Study of the Core Structure and Mobility of Dislocations and Their Influence on the Ferroelectric Polarization in Perovskite $KNbO_3$, Phys. Rev. B 92(21), 12, (2015).
[96] J.J. Gilman, W.G. Johnston, Dislocations in Lithium Fluoride Crystals, in: F. Seitz, D. Turnbull (Ed.), Solid State Physics, Academic Press Inc, 1962, pp. 147-222.
[97] S.O. Kucheyev, J.E. Bradby, J.S. Williams, C. Jagadish, M.V. Swain, Mechanical Deformation of Single-Crystal ZnO, Appl. Phys. Lett. 80(6), 956-958, (2002).
[98] T.H. Sung, J.C. Huang, J.H. Hsu, S.R. Jian, T.G. Nieh, Yielding and Plastic Slip in ZnO, Appl. Phys. Lett. 100(21), 211903, (2012).
[99] S. Koubaïti, J.J. Couderc, C. Levade, G. Vanderschaeve, Vickers Indentation on the {001} Faces of ZnS Sphalerite under UV Illumination and in Darkness. Crack Patterns and Rosette Microstructure, Acta Mater. 44(8), 3279-3291, (1996).
[100] Y. Oshima, A. Nakamura, K. Matsunaga, Extraordinary Plasticity of an Inorganic Semiconductor in Darkness, Science 360(6390), 772-774, (2018).
[101] F.-Z. Dai, Y. Zhou, Reducing the Ideal Shear Strengths of ZrB_2 by High Efficient Alloying Elements (Ag, Au, Pd and Pt), Sci. Rep. 7(1), 43416, (2017).
[102] C.H. Woo, M.P. Puls, An Improved Method of Calculating the Lattice Friction Stress Using an Atomistic Model, J. Phys. C Solid State Phys. 9(2), L27-L31, (1976).
[103] W. Skrotzki, P. Haasen, Hardening Mechanisms of Ionic-Crystals on (110) and (100) Slip Planes, J Phys-Paris Journal De Physique 42, 3119-3148, (1981).
[104] E.A. Patterson, M. Major, W. Donner, K. Durst, K.G. Webber, J. Rödel, Temperature-Dependent Deformation and Dislocation Density in $SrTiO_3$ (001) Single Crystals, J. Am. Ceram. Soc. 99(10), 3411-3420, (2016).
[105] Z. Wang, S.-i. Karato, K. Fujino, High Temperature Creep of Single Crystal Strontium Titanate ($SrTiO_3$): A Contribution to Creep Systematics in Perovskites, Phys. Earth Planet. In. 79(3), 299-312, (1993).
[106] W.R. Cannon, T.G. Langdon, Creep of Ceramics .1. Mechanical Characteristics, J. Mater. Sci. 18(1), 1-50, (1983).
[107] W.R. Cannon, T.G. Langdon, Creep of Ceramics 2. An Examination of Flow Mechanisms, J. Mater. Sci. 23(1), 1-20, (1988).
[108] W. Blum, P. Eisenlohr, F. Breutinger, Understanding Creep - A Review, Metall. Mater. Trans. A 33(2), 291-303, (2002).
[109] C. Herring, Diffusional Viscosity of a Polycrystallien Solid, J. Appl. Phys. 21(5), 437-445, (1950).
[110] R.L. Coble, A Model for Boundary Diffusion Controlled Creep in Polycrystalline Materials, J. Appl. Phys. 34(6), 1679-1682, (1963).
[111] T.G. Langdon, Deformation Mechanism Maps for Applications at High Temperatures, Ceramurgia Int. 6(1), 11-18, (1980).
[112] W. Blum, High-Temperature Deformation and Creep of Crystalline Solids, in: R.W. Cahn, P. Haasen, E.J. Kramer (Ed.), Materials Science and Technology, Wiley-VCH Verlag GmbH & Co. KGaA, 2006, pp. 360-403.

[113] N. Doukhan, J.C. Doukhan, Dislocations in Perovskites $BaTiO_3$ and $CaTiO_3$, Phys. Chem. Minerals 13(6), 403-410, (1986).
[114] L. Jin, X. Guo, C.L. Jia, TEM Study of <110>-Type 35.26 Degrees Dislocations Specially Induced by Polishing of $SrTiO_3$ Single Crystals, Ultramicroscopy 134, 77-85, (2013).
[115] Z.H. Sun, K.W. White, Nanoindentation-Induced Plastic Deformation and Fracture Behavior Difference Between a- and c-Domains of $BaTiO_3$ Single Crystal, J. Appl. Phys. 104(10), 103506, (2008).
[116] D. Liu, M. Chelf, K.W. White, Indentation Plasticity of Barium Titanate Single Crystals: Dislocation Influence on Ferroelectric Domain Walls, Acta Mater. 54(17), 4525-4531, (2006).
[117] F. Javaid, E. Bruder, K. Durst, Indentation Size Effect and Dislocation Structure Evolution evolution in (001) Oriented $SrTiO_3$ Berkovich Indentations: HR-EBSD and Etch-Pit Analysis, Acta Mater. 139, 1-10, (2017).
[118] J.P. Poirier, J. Peyronneau, J.Y. Gesland, G. Brebec, Viscosity and Conductivity of the Lower Mantle; an Experimental Study on a $MgSiO_3$ Perovskite Analogue, $KZnF_3$, Phys. Earth Planet. In. 32(3), 273-287, (1983).
[119] J. Amodeo, S. Merkel, C. Tromas, P. Carrez, S. Korte-Kerzel, P. Cordier, J. Chevalier, Dislocations and Plastic Deformation in MgO Crystals: A Review, Crystals 8(6), 240, (2018).
[120] P. Hirel, P. Marton, M. Mrovec, C. Elsässer, Theoretical Investigation of {110} Generalized Stacking Faults and Their Relation to Dislocation Behavior in Perovskite Oxides, Acta Mater. 58(18), 6072-6079, (2010).
[121] Y.B. Wang, J.P. Poirier, R.C. Liebermann, Dislocation Dissociation in $CaGeO_3$ Perovskites, Phys. Chem. Miner. 16(7), 630-633, (1989).
[122] P. Besson, J.P. Poirier, G.D. Price, Dislocations in $CaTiO_3$ Perovskite Deformed at High-Temperature: A Transmission Electron Microscopy Study, Phys. Chem. Miner. 23(6), 337-344, (1996).
[123] S.P. Alpay, I.B. Misirlioglu, V. Nagarajan, R. Ramesh, Can Interface Dislocations Degrade Ferroelectric Properties?, Appl. Phys. Lett 85(11), 2044-2046, (2004).
[124] M.-H. Lin, H.-Y. Lu, Collinear Partial Dislocations in Barium Titanate Perovskite, Mater. Sci. Eng. A 333(1–2), 41-44, (2002).
[125] Z.L. Zhang, W. Sigle, W. Kurtz, M. Ruhle, Electronic and Atomic Structure of a Dissociated Dislocation in $SrTiO_3$, Phys. Rev. B 66(21), 7, (2002).
[126] J.P. Hirth, J. Lothe, Theory of Dislocations, John Wiley & Sons, Inc., 1982.
[127] D. Ferré, P. Carrez, P. Cordier, Peierls Dislocation Modelling in Perovskite ($CaTiO_3$): Comparison with Tausonite ($SrTiO_3$) and $MgSiO_3$ Perovskite, Phys. Chem. Miner. 36(4), 233-239, (2009).
[128] B. Baufeld, B.V. Petukhov, M. Bartsch, U. Messerschmidt, Transition of Mechanisms Controlling the Dislocation Motion in Cubic ZrO_2 Below 700 °C, Acta Mater. 46(9), 3077-3085, (1998).
[129] K.-H. Yang, N.-J. Ho, H.-Y. Lu, Kink-Pair Mechanism in $SrTiO_3$ Single Crystal Compression-Deformed at Room Temperature, Jpn. J. Appl. Phys. 50(10R), 105601, (2011).
[130] A. Reisman, S. Triebwasser, F. Holtzberg, Phase Diagram of the System $KNbO_3$-$KTaO_3$ by the Methods of Differential Thermal and Resistance Analysis, J. Am. Chem. Soc. 77(16), 4228-4230, (1955).
[131] J.P. Poirier, Beauchesne, S. and Guyot, F, Deformation Mechanisms of Crystals With Perovskite Structure, in: A. Navrotsky, D.J. Weidner (Ed.), Perovskite: A Structure of Great Interest to Geophysics and Materials Science, American Geophysical Union, 1989, pp. 119-123.
[132] O. Eibl, P. Pongratz, P. Skalicky, H. Schmelz, Dislocations in $BaTiO_3$ Ceramics, Phys. Status Solidi A 108(2), 495-502, (1988).
[133] Y.C. Wu, C.Y. Chen, H.Y. Lu, D.E. McCauley, M.S.H. Chu, Dislocation Loops in Pressureless-Sintered Undoped $BaTiO_3$ ceramics, J. Am. Ceram. Soc. 89(7), 2213-2219, (2006).

[134] M.-H. Lin, J.-F. Chou, H.-Y. Lu, The Rate-Determining Mechanism in the Sintering of Undoped Nonstoichiometric Barium Titanate, J. Eur. Ceram. Soc. 20(4), 517-526, (2000).
[135] L.A. Xue, Y. Chen, E. Gilbart, R.J. Brook, The Kinetics of Hot-Pressing for Undoped and Donor-Doped $BaTiO_3$ Ceramics, J. Mater. Sci. 25(2), 1423-1428, (1990).
[136] C. Carry, A. Mocellin, Superplastic Creep of Fine-Grained $BaTiO_3$ in a Reducing Environment, J. Am. Ceram. Soc. 69(9), C-215-C-216, (1986).
[137] E. Park, P. Nash, J. Wolfenstine, K. Goretta, J. Routbort, High-Temperature Creep of Polycrystalline $BaTiO_3$, J. Mater. Res. 14(2), 523-528, (1999).
[138] J.-K. Liou, H.-Y. Lu, Deformed Microstructure in Pressureless-Sintered Barium Titanate, Ceram. Int. 31(1), 1-9, (2005).
[139] S.Y. Cheng, N.J. Ho, H.Y. Lu, Dissociation of the < 001 > Dislocations and Their Interactions with Dislocation Loops in Tetragonal $BaTiO_3$, J. Am. Ceram. Soc. 89(5), 1659-1667, (2006).
[140] T. Suzuki, M. Ueno, Y. Nishi, M. Fujimoto, Dislocation Loop Formation in Nonstoichiometric (Ba,Ca)TiO_3 and $BaTiO_3$ Ceramics, J. Am. Ceram. Soc. 84(1), 200-206, (2001).
[141] M.H. Lin, H.Y. Lu, Dislocation Substructures in CO_2-Laser-Sintered Barium Titanate, Phys. Status Solidi A-Appl. Mat. 191(1), 58-66, (2002).
[142] C. Metzmacher, K. Albertsen, Microstructural Investigations of Barium Titanate-Based Material for Base Metal Electrode Ceramic Multilayer Capacitor, J. Am. Ceram. Soc. 84(4), 821-826, (2001).
[143] E.C. Buck, Effects of Electron-Irradiation of Barium-Titanate, Radiat. Eff. Defect S. 133(1), 15-25, (1995).
[144] P. Li, S.-i. Karato, Z. Wang, High-Temperature Creep in Fine-Grained Polycrystalline $CaTiO_3$, an Analogue Material of (Mg, Fe)SiO_3 Perovskite, Phys. Earth Planet. In. 95(1), 19-36, (1996).
[145] B. Jaffe, W.R. Cook, H. Jaffe, Piezoelectric Ceramics, Academic Press, 1971.
[146] A.J. Moulson, J.M. Herbert, Electroceramics: Materials, Properties, Applications, John Wiley & Sons Ltd, 2003.
[147] R.E. Newnham, Properties of Materials: Anisotropy, Symmetry, Structure, Oxford Univ. Press, 2005.
[148] R. Waser, U. Böttger, S. Tiedke, Polar Oxides - Properties, Characterization, and Imaging, WILEY-VCH Verlag GmbH & Co.KGaA, 2005.
[149] C. Kittel, S. Hunklinger, Einführung in die Festkörperphysik, De Gruyter Oldenbourg, 2013.
[150] D. Damjanovic, Ferroelectric, Dielectric and Piezoelectric Properties of Ferroelectric Thin Films and Ceramics, Rep. Prog. Phys. 61(9), 1267-1324, (1998).
[151] J. Valasek, Piezo-Electric and Allied Phenomena in Rochelle Salt, Phys. Rev. 17(4), 475-481, (1921).
[152] A. von Hippel, R.G. Breckenridge, F.G. Chesley, L. Tisza, High Dielectric Constant Ceramics, Ind. Eng. Chem. 38(11), 1097-1109, (1946).
[153] G.H. Haertling, Ferroelectric Ceramics: History and Technology, J. Am. Ceram. Soc. 82(4), 797-818, (1999).
[154] K.M. Rabe, C.H. Ahn, J.-M. Triscone, Physics of Ferroelectrics, Springer Berlin Heidelberg, 2007.
[155] S. Roberts, Dielectric and Piezoelectric Properties of Barium Titanate, Phys. Rev. 71(12), 890-895, (1947).
[156] H.F. Kay, P. Vousden, Symmetry Changes in Barium Titanate at Low Temperatures and their Relation to its Ferroelectric Properties, Philos. Mag. 40(309), 1019-1040, (1949).
[157] A.G. Kalinichev, J.D. Bass, C.S. Zha, P.D. Han, D.A. Payne, Elastic Properties of Orthorhombic $KNbO_3$ Single Crystals by Brillouin-Scattering, J. Appl. Phys. 74(11), 6603-6608, (1993).
[158] Wiesendanger E, Dielectric, Mechanical and Optical-Properties of Orthorhombic $KNbO_3$, Ferroelectrics 6(3-4), 263-281, (1974).
[159] S. Triebwasser, Behavior of Ferroelectric $KNbO_3$ in the Vicinity of the Cubic-Tetragonal Transition, Phys. Rev. 101(3), 993-997, (1956).

[160] IEEE Standard Definitions of Primary Ferroelectric Terms, ANSI/IEEE Std 180-1986, 0-1, (1986).
[161] A. Pramanick, A.D. Prewitt, J.S. Forrester, J.L. Jones, Domains, Domain Walls and Defects in Perovskite Ferroelectric Oxides: A Review of Present Understanding and Recent Contributions, Crit. Rev. Solid State Mat. Sci. 37(4), 243-275, (2012).
[162] J. Fousek, V. Janovec, The Orientation of Domain Walls in Twinned Ferroelectric Crystals, J. Appl. Phys. 40(1), 135-142, (1969).
[163] E. Wiesendanger, Domain Structures in Orthorhombic $KNbO_3$ and Characterisation of Single Domain Crystals, Czech. J. Phys. B 23(1), 91-99, (1973).
[164] E. Wood, Polymorphism in Potassium Niobate, Sodium Niobate, and other ABO_3 Compounds, Acta Cryst. 4(4), 353-362, (1951).
[165] K.G. Deshmukh, S.G. Ingle, Interferometric Studies of Domain Structures in Potassium Niobate Single Crystals, J. Phys. D: Appl. Phys. 4(1), 124, (1971).
[166] J. Hirohashi, K. Yamada, H. Kamio, M. Uchida, S. Shichijyo, Control of Specific Domain Structure in $KNbO_3$ Single Crystals by Differential Vector Poling Method, J. Appl. Phys. 98(3), 034107, (2005).
[167] A.K. Tagantsev, L.E. Cross, J. Fousek, Domains in Ferroic Crystals and Thin Films, Springer New York, 2010.
[168] W. Heywang, K. Lubitz, W. Wersing, R. Hull, R.M. Osgood, J. Parisi, Piezoelectricity: Evolution and Future of a Technology, Springer-Verlag, 2008.
[169] S. Hunklinger, Festkörperphysik, Oldenbourg, 2011.
[170] J.A. Howell, M.D. Vaudin, R.F. Cook, Orientation, Stress, and Strain in an (001) Barium Titanate Single Crystal with 90° Lamellar Domains Determined Using Electron Backscatter Diffraction, J. Mater. Sci. 49(5), 2213-2224, (2014).
[171] L. Lian, T.C. Chong, H. Kumagai, M. Hirano, L. Taijing, S.C. Ng, Temperature Evolution of Domains in Potassium Niobate Single Crystals, J. Appl. Phys. 80(1), 376-381, (1996).
[172] W.N. Lawless, 180° Domain Wall Energies in $BaTiO_3$, Phys. Rev. 175(2), 619-624, (1968).
[173] W. Kinase, H. Okayama, A. Yoshikawa, N. Taguchi, On the 90°-Type Domain Wall of $BaTiO_3$ Crystal, J. Phys. Soc. Jpn. 28, 383–S385, (1970).
[174] D.A. Hall, P.J. Stevenson, High Field Dielectric Behaviour of Ferroelectric Ceramics, Ferroelectrics 228(1), 139-158, (1999).
[175] D. Damjanovic, M. Demartin, The Rayleigh Law in Piezoelectric Ceramics, J. Phys. D Appl. Phys. 29(7), 2057-2060, (1996).
[176] D. Damjanovic, M. Demartin, Contribution of the Irreversible Displacement of Domain Walls to the Piezoelectric Effect in Barium Titanate and Lead Zirconate Titanate Ceramics, J. Phys.-Condens. Mat. 9(23), 4943-4953, (1997).
[177] D. Damjanovic, Contributions to the Piezoelectric Effect in Ferroelectric Single Crystals and Ceramics, J. Am. Ceram. Soc. 88(10), 2663-2676, (2005).
[178] S. Trolier-McKinstry, N.B. Gharb, D. Damjanovic, Piezoelectric Nonlinearity due to Motion of 180° Domain Walls in Ferroelectric Materials at Subcoercive Fields: A Dynamic Poling Model, Appl. Phys. Lett. 88(20), 202901, (2006).
[179] J. Schultheiß, L. Liu, H. Kungl, M. Weber, L. Kodumudi Venkataraman, S. Checchia, D. Damjanovic, J.E. Daniels, J. Koruza, Revealing the Sequence of Switching Mechanisms in Polycrystalline Ferroelectric/Ferroelastic Materials, Acta Mater. 157, 355-363, (2018).
[180] L. Eric Cross, Ferroelectric Ceramics: Tailoring Properties for Specific Applications, in: N. Setter, E.L. Colla (Ed.), Ferroelectric Ceramics (Proceedings of the Centro Stefano Franscini, Ascona), Birkhäuser Basel, 1993, pp. 1-85.
[181] D.V. Taylor, D. Damjanovic, Evidence of Domain Wall Contribution to the Dielectric Permittivity in PZT Thin Films at Sub-Switching Fields, J. Appl. Phys. 82(4), 1973-1975, (1997).
[182] A. Pramanick, D. Damjanovic, J.E. Daniels, J.C. Nino, J.L. Jones, Origins of Electro-Mechanical Coupling in Polycrystalline Ferroelectrics During Subcoercive Electrical Loading, J. Am. Ceram. Soc. 94(2), 293-309, (2011).
[183] M. Acosta, N. Novak, V. Rojas, S. Patel, R. Vaish, J. Koruza, G.A. Rossetti, J. Rödel, $BaTiO_3$-Based Piezoelectrics: Fundamentals, Current Status, and Perspectives, Appl. Phys. Rev. 4(4), 041305, (2017).

[184] T.J. Yang, V. Gopalan, P.J. Swart, U. Mohideen, Direct Observation of Pinning and Bowing of a Single Ferroelectric Domain Wall, Phys. Rev. Lett. 82(20), 4106-4109, (1999).
[185] R. Mueller, D. Gross, D.C. Lupascu, Driving Forces on Domain Walls in Ferroelectric Materials and Interaction with defects, Comput. Mater. Sci. 35(1), 42-52, (2006).
[186] Y. Su, C.M. Landis, Continuum Thermodynamics of Ferroelectric Domain Evolution: Theory, Finite Element Implementation, and Application to Domain Wall Pinning, J. Mech. Phys. Solid 55(2), 280-305, (2007).
[187] V.S. Postnikov, V.S. Pavlov, S.K. Turkov, Internal Friction in Ferroelectrics Due to Interaction of Domain Boundaries and Point Defects, J. Phys. Chem. Solids 31(8), 1785, (1970).
[188] R.-A. Eichel, Defect Structure of Oxide Ferroelectrics - Valence State, Site of Incorporation, Mechanisms of Charge Compensation and Internal Bias Fields J. Electroceramics 19(1), 11-23, (2007).
[189] A. Chandrasekaran, D. Damjanovic, N. Setter, N. Marzari, Defect Ordering and Defect–Domain-Wall Interactions in $PbTiO_3$: A First-Principles Study, Phys. Rev. B 88(21), (2013).
[190] M. Morozov, D. Damjanovic, N. Setter, The Nonlinearity and Subswitching Hysteresis in Hard and Soft PZT, J. Eur. Ceram. Soc. 25(12), 2483-2486, (2005).
[191] U. Robels, G. Arlt, Domain Wall Clamping in Ferroelectrics by Orientation of Defects, J. Appl. Phys. 73(7), 3454-3460, (1993).
[192] H.S. Han, J. Koruza, E.A. Patterson, J. Schultheiss, E. Erdem, W. Jo, J.S. Lee, J. Rödel, Hardening Behavior and Highly Enhanced Mechanical Quality Factor in $(K_{0.5}Na_{0.5})NbO_3$-Based Ceramics, J. Eur. Ceram. Soc. 37(5), 2083-2089, (2017).
[193] S. Zhang, F. Li, F. Yu, X. Jiang, H.-Y. Lee, J. Luo, T.R. Shrout, Recent Developments in Piezoelectric Crystals, J. Korean Ceram. Soc 55(5), 419-439, (2018).
[194] M.I. Morozov, M.A. Einarsrud, J.R. Tolchard, P.T. Geiger, K.G. Webber, D. Damjanovic, T. Grande, In-Situ Structural Investigations of Ferroelasticity in Soft and Hard Rhombohedral and Tetragonal PZT, J. Appl. Phys. 118(16), 7, (2015).
[195] X.L. Zhang, Z.X. Chen, L.E. Cross, W.A. Schulze, Dielectric and Piezoelectric Properties of Modified Lead Titanate Zirconate Ceramics from 4.2 to 300 K, J Mater Sci 18(4), 968-972, (1983).
[196] M.I. Morozov, D. Damjanovic, Charge Migration in $Pb(Zr,Ti)O_3$ Ceramics and its Relation to Ageing, Hardening, and Softening, J. Appl. Phys. 107(3), 034106, (2010).
[197] T. Rojac, D. Damjanovic, Domain Walls and Defects in Ferroelectric Materials, Jpn J Appl Phys 56(10), (2017).
[198] S.J. Zhang, F. Li, High Performance Ferroelectric Relaxor-$PbTiO_3$ Single Crystals: Status and Perspective, J. Appl. Phys. 111(3), (2012).
[199] S.E. Park, T.R. Shrout, Ultrahigh Strain and Piezoelectric Behavior in Relaxor Based Ferroelectric Single Crystals, J. Appl. Phys. 82(4), 1804-1811, (1997).
[200] F. Li, L. Wang, L. Jin, D. Lin, J. Li, Z. Li, Z. Xu, S. Zhang, Piezoelectric Activity in Perovskite Ferroelectric Crystals, IEEE Trans. Ultrason. Ferroelectr. Freq. Control 62(1), 18-32, (2015).
[201] A.J. Bell, Phenomenologically Derived Electric Field-Temperature Phase Diagrams and Piezoelectric Coefficients for Single Crystal Barium Titanate Under Fields Along Different Axes, J. Appl. Phys. 89(7), 3907-3914, (2001).
[202] M. Davis, D. Damjanovic, D. Hayem, N. Setter, Domain Engineering of the Transverse Piezoelectric Coefficient in Perovskite Ferroelectrics, J. Appl. Phys. 98(1), (2005).
[203] M. Davis, M. Budimir, D. Damjanovic, N. Setter, Rotator and Extender Ferroelectrics: Importance of the Shear Coefficient to the Piezoelectric Properties of Domain-Engineered Crystals and Ceramics, J. Appl. Phys. 101(5), 10, (2007).
[204] M. Budimir, D. Damjanovic, N. Setter, Piezoelectric Anisotropy–Phase Transition Relations in Perovskite Single Crystals, J. Appl. Phys. 94(10), 6753-6761, (2003).
[205] J. Koruza, H.R. Liu, M. Höfling, M.H. Zhang, P. Veber, $(K,Na)NbO_3$-Based Piezoelectric Single Crystals: Growth Methods, Properties, and Applications, J. Mater. Res. 35(8), 990-1016, (2020).

[206] S. Wada, H. Kakemoto, T. Tsurumi, Enhanced Piezoelectric Properties of Piezoelectric Single Crystals by Domain Engineering, Mater. Trans. 45(2), 178-187, (2004).
[207] S. Wada, T. Muraishi, K. Yokoh, K. Yako, H. Kamemoto, T. Tsurumi, Domain Wall Engineering in Lead-Free Piezoelectric Crystals, Ferroelectrics 355, 37-49, (2007).
[208] X.-H. Du, Q.-M. Wang, U. Belegundu, A. Bhalla, K. Uchino, Crystal Orientation Dependence of Piezoelectric Properties of Single Crystal Barium Titanate, Mater. Lett. 40(3), 109–113, (1999).
[209] S. Wada, K. Yako, H. Kakemoto, T. Tsurumi, T. Kiguchi, Enhanced Piezoelectric Properties of Barium Titanate Single Crystals with Different Engineered-Domain Sizes, J. Appl. Phys. 98(1), (2005).
[210] S. Wada, T. Tsurumi, Enhanced Piezoelectricity of Barium Titanate Single Crystals with Engineered Domain Configuration, Brit. Ceram. T. 103(2), 93-96, (2004).
[211] R.C. Bradt, G.S. Ansell, Dislocations and 90 Degrees Domains in Barium Titanate, J. Appl. Phys. 38(13), 5407-5408, (1967).
[212] D. Balzar, H. Ledbetter, P.W. Stephens, E.T. Park, J.L. Routbort, Dislocation-Density Changes Upon Poling of Polycrystalline $BaTiO_3$, Phys. Rev. B 59(5), 3414-3420, (1999).
[213] X. Tan, J.K. Shang, Partial Dislocations at Domain Intersections in a Tetragonal Ferroelectric Crystal, J. Phys. Condens. Mat. 16(8), 1455-1466, (2004).
[214] Z.R. Dai, Z.L. Wang, X.F. Duan, J. Zhang, Link-Up of 90° Domain Boundaries with Interface Dislocations in $BaTiO_3/LaAlO_3$, Appl. Phys. Lett. 68(22), 3093-3095, (1996).
[215] N. Setter, D. Damjanovic, L. Eng, G. Fox, S. Gevorgian, S. Hong, A. Kingon, H. Kohlstedt, N.Y. Park, G.B. Stephenson, I. Stolitchnov, A.K. Taganstev, D.V. Taylor, T. Yamada, S. Streiffer, Ferroelectric Thin Films: Review of Materials, Properties, and Applications, J. Appl. Phys. 100(5), 051606, (2006).
[216] K. Lee, S. Baik, Ferroelastic Domain Structure and Switching Epitaxial Ferroelectric Thin Films Annu. Rev. Mater. Res. 36(1), 81-116, (2006).
[217] S.G. Ingle, M.V. Kokate, Switching of $KNbO_3$ Single-Crystals under Steady Electric-Field Conditions, J. Phys. D Appl. Phys. 16(6), 1115-1121, (1983).
[218] S.G. Ingle, S.C. Joshi, A Dislocation Model for Nucleation of Domain Walls in $KNbO_3$ Single Crystals, J. Phys. D: Appl. Phys. 17(10), 2065, (1984).
[219] S.G. Ingle, H.S. Dutta, A.P. David, Domain-Wall Nucleation by Impurity Ions in $KNbO_3$ Single Crystals, J. Appl. Phys. 64(9), 4640-4645, (1988).
[220] M. Tanaka, Y. Himiyama, Observation of Interaction between Domains and Dislocations in $KNbO_3$, Acta Crystallogr. A 31, 264, (1975).
[221] N.A. Pertsev, G. Arlt, Dislocation Method for Calculation of Internal Stresses in Polycrystalline Ferroelectrics, Sov. Phys. Solid State 33(10), 1738-44, (1991).
[222] M.B. Mishra, S.G. Ingle, Domain-Impurities Interaction in $KNbO_3$ Single-Crystals, J. Appl. Phys. 45(12), 5152-5155, (1974).
[223] S.P. Alpay, A.L. Roytburd, Thermodynamics of Polydomain Heterostructures. III. Domain Stability Map, J. Appl. Phys. 83(9), 4714-4723, (1998).
[224] N. Li, R. Zhu, X. Cheng, H.-J. Liu, Z. Zhang, Y.-L. Huang, Y.-H. Chu, L.-Q. Chen, Y. Ikuhara, P. Gao, Dislocation-Induced Large Local Polarization Inhomogeneity of Ferroelectric Materials, Scr. Mater. 194, (2021).
[225] I.B. Misirlioglu, A.L. Vasiliev, S.P. Alpay, M. Aindow, R. Ramesh, Defect Microstructures in Epitaxial $PbZr_{0.2}Ti_{0.8}O_3$ Films Grown on (001)$SrTiO_3$ by Pulsed Laser Deposition, J. Mater. Sci. 41(3), 697-707, (2006).
[226] J.W. Matthews, Epitaxial Growth, Academic Press, 1975.
[227] P.R. Ren, M. Hoefling, J. Koruza, S. Lauterbach, X.J. Jiang, T. Fromling, D.K. Khatua, C. Dietz, L. Porz, R. Ranjan, H.J. Kleebe, J. Rödel, High Temperature Creep-Mediated Functionality in Polycrystalline Barium Titanate, J. Am. Ceram. Soc. 103(3), 1891-1902, (2020).
[228] J. Chakrabarty, Applied Plasticity, Springer, 2010.
[229] R. Danz, P. Gretscher, C–DIC: A New Microscopy Method for Rational Study of Phase Structures in Incident Light Arrangement, Thin Solid Films 462-463, 257-262, (2004).
[230] C. Trager-Cowan, F. Sweeney, P.W. Trimby, A.P. Day, A. Gholinia, N.H. Schmidt, P.J. Parbrook, A.J. Wilkinson, I.M. Watson, Electron Backscatter Diffraction and Electron

Channeling Contrast Imaging of Tilt and Dislocations in Nitride Thin Films, Phys. Rev. B 75(8), 085301, (2007).
[231] S. Zaefferer, N.-N. Elhami, Theory and Application of Electron Channelling Contrast Imaging under Controlled Diffraction Conditions, Acta Mater. 75, 20-50, (2014).
[232] N. Balke, I. Bdikin, S.V. Kalinin, A.L. Kholkin, Electromechanical Imaging and Spectroscopy of Ferroelectric and Piezoelectric Materials: State of the Art and Prospects for the Future, J. Am. Ceram. Soc. 92(8), 1629-1647, (2009).
[233] D.B. Williams, C.B. Carter, The Transmission Electron Microscope, in: D.B. Williams, C.B. Carter (Ed.), Transmission Electron Microscopy: A Textbook for Materials Science, Springer US, 1996, pp. 3-17.
[234] B. Subramanian, X. Jian Bin, M. Jian Xing, G. Sarveswaran, W. Ian Howard, Surface Morphology of Ferroelectric Domains in $BaTiO_3$ Single Crystals: An Atomic Force Microscope Study, Jpn J Appl Phys 36(9R), 5566, (1997).
[235] V.C.S. Prasad, E.C. Subbarao, Deformation and Relaxation Behavior in Ferroelectric $KNbO_3$ Single-Crystals, Mater. Sci. Eng. A 10(5), 297-299, (1972).
[236] T.G. Langdon, J.A. Pask, Effect of Microstructure on Deformation of Polycrystalline MgO, J. Am. Ceram. Soc. 54(5), 240-246, (1971).
[237] W.S. Rothwell, Etch Pits in $BaTiO_3$ Single Crystals, J. Am. Ceram. Soc. 47(8), 409-411, (1964).
[238] W.G. Johnston, J.J. Gilman, Dislocation Multiplication in Lithium Fluoride Crystals, J. Appl. Phys. 31(4), 632-643, (1960).
[239] W.G. Johnston, J.J. Gilman, Dislocation Velocities, Dislocation Densities, and Plastic Flow in Lithium Fluoride Crystals, J. Appl. Phys. 30(2), 129-144, (1959).
[240] A.F. Brown, Surface Effects in Plastic Deformation of Metals, Adv. Phys. 1(4), 427-479, (1952).
[241] F.R.N. Nabarro, Z.S. Basinski, D.B. Holt, The Plasticity of Pure Single Crystals, Adv. Phys. 13(50), 193-323, (1964).
[242] L. Porz, T. Frömling, A. Nakamura, N. Li, R. Maruyama, K. Matsunaga, P. Gao, H. Simons, C. Dietz, M. Rohnke, J. Janek, J. Rödel, Conceptual Framework for Dislocation-Modified Conductivity in Oxide Ceramics Deconvoluting Mesoscopic Structure, Core, and Space Charge Exemplified for $SrTiO_3$, ACS Nano in print, (2020).
[243] A. Nakamura, K. Yasufuku, Y. Furushima, K. Toyoura, K.P.D. Lagerlof, K. Matsunaga, Room-Temperature Plastic Deformation of Strontium Titanate Crystals Grown From Different Chemical Compositions, Crystals 7(11), (2017).
[244] P. Lukas, L. Kunz, J. Krejci, Effect of Slip Planarity on the Cycling Stress-Strain Cuve, Dislocation-Structure and Surface Relief in FCC Single Crystals, Scr. Metall. Materialia 26(10), 1511-1516, (1992).
[245] J.W. Mitchell, Elementary Processes in the Formation of Slip Bands in Single-Crystals of Alpha-Phase Cu-Al Alloys, Phys. Status Solidi A - Appl. Res. 135(2), 455-466, (1993).
[246] A. Weidner, H. Biermann, Case Studies on the Application of High-Resolution Electron Channelling Contrast Imaging – Investigation of Defects and Defect Arrangements in Metallic Materials, Philos Mag Philosophical Magazine 95(7), 759-793, (2015).
[247] G.A. Schneider, T. Scholz, F.J. Espinoza-Beltran, Rosette Screw Arms Created by AC-Domain Structures and Dislocations in Barium Titanate During Nanoindentation, Appl. Phys. Lett. 92(2), 3, (2008).
[248] C. Coupeau, J. Grilhé, Atomic Force Microscopy Observations of In-Situ Deformed Materials: Application to Single Crystals and Thin Films on Substrates, J. Microsc.-Oxf. 203, 99-107, (2001).
[249] J. Fousek, Permissible Domain Walls in Ferroelectric Species, Czechoslov. J. Phys. B 21(9), 955-968, (1971).
[250] W. Sigle, C. Sarbu, D. Brunner, M. Ruhle, Dislocations in Plastically Deformed $SrTiO_3$, Philos. Mag. 86(29-31), 4809-4821, (2006).
[251] M. Castillo-Rodríguez, W. Sigle, Dislocation Dissociation and Stacking-Fault Energy Calculation in Strontium Titanate, Scr. Mater. 62(5), 270-273, (2010).
[252] B.T. Matthias, J.P. Remeika, Dielectric Properties of Sodium and Potassium Niobates, Phys. Rev. 82(5), 727-729, (1951).

[253] H.R. Liu, P. Veber, J. Koruza, D. Rytz, M. Josse, J. Rödel, M. Maglione, Influence of Ta^{5+} Content on the Crystallographic Structure and Electrical Properties of $[001]_{PC}$-Oriented (Li,Na,K)(Nb,Ta)O_3 Single Crystals, Cryst. Eng. Comm. 18(12), 2081-2088, (2016).
[254] A. Bellou, D.F. Bahr, Complementary Characterization Techniques for Identification of Ferroelectric Domains in $KNbO_3$ Single Crystals, Mater. Charact. 59(6), 688-692, (2008).
[255] S. Wada, K. Muraoka, H. Kakemoto, T. Tsurumi, H. Kumagai, Enhanced Piezoelectric Properties of Potassium Niobate Single Crystals with Fine Engineered Domain Configurations, Mater. Sci. Eng.: B 120(1-3), 186–189, (2005).
[256] S.G. Ingle, H.C. Dutta, A.P. David, Domain Wall Nucleation Evidenced on Naturally Grown Surfaces, J. Phys. D: Appl. Phys. 21(7), 1239-1240, (1988).
[257] M. Höfling, M. Trapp, L. Porz, H. Uršič, E. Bruder, H.-J. Kleebe, J. Rödel, J. Koruza, Large plastic deformability of bulk ferroelectric KNbO3 single crystals, J. Eur. Ceram. Soc. 41(7), 4098-4107, (2021).
[258] D. Munz, T. Fett, Ceramics: Mechanical Properties, Failure Behaviour, Materials Selection, Springer-Verlag Berlin Heidelberg, 1999.
[259] J. Bauer, A. Schroer, R. Schwaiger, O. Kraft, Approaching Theoretical Strength in Glassy Carbon Nanolattices, Nature Materials 15(4), 438-443, (2016).
[260] T. Trzepieciński, M. Gromada, Characterization of Mechanical Properties of Barium Titanate Ceramics with Different Grain Sizes, Materials Science-Poland 36(1), 151-156, (2018).
[261] B.M. Park, S.J. Chung, Optical, Electron Microscopic, and X-ray Topographic Studies of Ferroic Domains in Barium Titanate Crystals Grown from High-Temperature Solution, J. Am. Ceram. Soc. 77(12), 3193-3201, (1994).
[262] S.I. Yakunin, Shakmano.Vv, G.V. Spivak, N.V. Vasileva, Microstructure of Domains and Domain Boundaries of $BaTiO_3$ Single Crystalline Films, Fiz. Tverd. Tela 14(2), 373-377, (1972).
[263] H. Liu, P. Veber, A. Zintler, L. Molina-Luna, D. Rytz, M. Maglione, J. Koruza, Temperature-Dependent Evolution of Crystallographic and Domain Structures in (K,Na,Li)(Ta,Nb)O_3 Piezoelectric Single Crystals, IEEE Trans. Ultrason. Ferroelectr. Freq. Control. 65(9), 1508-1516, (2018).
[264] C. Tromas, J.C. Girard, J. Woirgard, Study by Atomic Force Microscopy of Elementary Deformation Mechanisms Involved in Low Load Indentations in MgO Crystals, Philos. Mag. A 80(10), 2325-2335, (2000).
[265] G.A. Schneider, T. Scholz, J. Muñoz-Saldana, M.V. Swain, Domain Rearrangement During Nanoindentation in Single-Crystalline Barium Titanate Measured by Atomic Force Microscopy and Piezoresponse Force Microscopy, Appl. Phys. Lett 86(19), 3, (2005).
[266] F. Javaid, K.E. Johanns, E.A. Patterson, K. Durst, Temperature Dependence of Indentation Size Effect, Dislocation Pile-Ups, and Lattice Friction in (001) Strontium Titanate, J. Am. Ceram. Soc 101(1), 356-364, (2018).
[267] R.J. Kamaladasa, M. Noman, W. Chen, P.A. Salvador, J.A. Bain, M. Skowronski, Y.N. Picard, Dislocation Impact on Resistive Switching in Single-Crystal $SrTiO_3$, J. Appl. Phys. 113(23), 234510, (2013).
[268] G. Arlt, The Influence of Microstructure on the Properties of Ferroelectric Ceramics, Ferroelectrics 104, 217-227, (1990).
[269] K. Kinoshita, A. Yamaji, Grain-Size Effects on Dielectric Properties in Barium Titanate Ceramics, J. Appl. Phys. 47(1), 371-373, (1976).
[270] K. Wu, W.A. Schulze, Aging of the Weak-Field Dielectric Response in Fine- and Coarse-Grain Ceramic $BaTiO_3$, J. Am. Ceram. Soc. 75(12), 3390-3395, (1992).
[271] M. Zgonik, P. Bernasconi, M. Duelli, R. Schlesser, P. Günter, M.H. Garrett, D. Rytz, Y. Zhu, X. Wu, Dielectric, Elastic, Piezoelectric, Electro-Optic, and Elasto-Optic Tensors of $BaTiO_3$ Crystals, Phys. Rev. B 50(9), 5941-5949, (1994).
[272] W.J. Merz, The Dielectric Behavior of $BaTiO_3$ Single-Domain Crystals, Phys. Rev. 75(4), 687-687, (1949).
[273] A. Schaefer, H. Schmitt, A. Dorr, Elastic and Piezoelectric Coefficients of TSSG Barium Titanate Single Crystals, Ferroelectrics 69(1), 253-266, (1986).

[274] T. Hoshina, K. Takizawa, J. Li, T. Kasama, H. Kakemoto, T. Tsurumi, Domain Size Effect on Dielectric Properties of Barium Titanate Ceramics, Jpn. J. Appl. Phys. 47(9), 7607-7611, (2008).
[275] Q.M. Zhang, H. Wang, N. Kim, L.E. Cross, Direct Evaluation of Domain-Wall and Intrinsic Contributions to the Dielectric and Piezoelectric Response and their Temperature Dependence on Lead Zirconate-Titanate Ceramics, J. Appl. Phys. 75(1), 454-459, (1994).
[276] L.N. Bulaevskii, Thermodynamic Theory of Domain Walls in Ferroelectric Materials with the Perovskite Structure Sov. Phys.-Sol. State 5(11), 2329-2332, (1964).
[277] D. Berlincourt, H.H.A. Krueger, Domain Processes in Lead Titanate Zirconate and Barium Titanate Ceramics, J. Appl. Phys. 30(11), 1804-1810, (1959).
[278] M. Morozov, Softening and Hardening Transitions in Ferroelectric Pb(Zr,Ti)O_3 ceramics, Institute of Materials, École polytechnique fédérale de Lausanne, 2005.
[279] D.V. Taylor, D. Damjanovic, Domain Wall Pinning Contribution to the Nonlinear Dielectric Permittivity in Pb(Zr, Ti)O_3 Thin Films, Appl. Phys. Lett. 73(14), 2045-2047, (1998).
[280] D.V. Taylor, D. Damjanovic, N. Setter, Nonlinear Contributions to Dielectric and Piezoelectric Properties in Lead Zirconate Titanate Thin Films, Ferroelectrics 224(1), 299-306, (1999).
[281] G. Tutuncu, D. Damjanovic, J. Chen, J.L. Jones, Deaging and Asymmetric Energy Landscapes in Electrically Biased Ferroelectrics, Phys. Rev. Lett. 108(17), (2012).
[282] D. Berlincourt, H. Jaffe, Elastic and Piezoelectric Coefficients of Single Crystal Barium Titanate, Phys. Rev. 111(1), 143-148, (1958).
[283] S.E. Park, S. Wada, L.E. Cross, T.R. Shrout, Crystallographically Engineered $BaTiO_3$ Single Crystals for High-Performance Piezoelectrics, J. Appl. Phys. 86(5), 2746-2750, (1999).
[284] Y.L. Li, L.E. Cross, L.Q. Chen, A Phenomenological Thermodynamic Potential for $BaTiO_3$ Single Crystals, J. Appl. Phys. 98(6), (2005).
[285] S.P. Li, W.W. Cao, L.E. Cross, The Extrinsic Nature of Nonlinear Behavior Observed in Lead Zirconate Titanate Ferroelectric Ceramic, J. Appl. Phys. 69(10), 7219-7224, (1991).
[286] R.E. Eitel, T.R. Shrout, C.A. Randall, Nonlinear Contributions to the Dielectric Permittivity and Converse Piezoelectric Coefficient in Piezoelectric Ceramics, J. Appl. Phys. 99(12), 124110, (2006).
[287] T. Rojac, H. Ursic, A. Bencan, B. Malic, D. Damjanovic, Mobile Domain Walls as a Bridge between Nanoscale Conductivity and Macroscopic Electromechanical Response, Adv. Funct. Mater. 25(14), 2099-2108, (2015).
[288] D. Damjanovic, M.D. Maeder, P.D. Martin, C. Voisard, N. Setter, Maxwell-Wagner Piezoelectric Relaxation in Ferroelectric Heterostructures, J. Appl. Phys. 90(11), 5708-5712, (2001).
[289] Takahisa Sakakibara, Hiroaki Izu, T. Kura, W. Shinohara, H. Iwata, S. Kiyama, Development of High-Voltage Photovoltaic Micro-Devices for an Energy Supply to Micromachines, 5th International Symposium on Micro Machine and Human Science Proceedings, 1994, p. 71.
[290] F. Li, Q. Wang, H. Miao, Giant Actuation Strain Nearly 0.6% in a Periodically Orthogonal Poled Lead Titanate Zirconate Ceramic via Reversible Domain Switching, J. Appl. Phys. 122(7), 074103, (2017).
[291] M. Höfling, X. Zhou, L.M. Riemer, E. Bruder, B. Liu, L. Zhou, P.B. Groszewicz, F. Zhuo, B.-X. Xu, K. Durst, X. Tan, D. Damjanovic, J. Koruza, J. Rödel, Control of polarization in bulk ferroelectrics by mechanical dislocation imprint, Science 372(6545), 961, (2021).
[292] G. Singh, V.S. Tiwari, P.K. Gupta, Role of Oxygen Vacancies on Relaxation and Conduction Behavior of $KNbO_3$ Ceramic, J. Appl. Phys. 107(6), 064103, (2010).
[293] A. Reisman, F. Holtzberg, Phase Equilibria in the System K_2CO_3-Nb_2O_5 by the Method of Differential Thermal Analysis, J. Am. Ceram. Soc. 77(8), 2115-2119, (1955).
[294] W.G. Johnston, Yield Points and Delay Times in Single Crystals, J. Appl. Phys. 33(9), 2716-2730, (1962).

[295] S.M. Copley, J.A. Pask, Plastic Deformation of MgO Single Crystals up to 1600 °C, J. Am. Ceram. Soc. 48(3), 139-146, (1965).
[296] D.S. Thompson, J.P. Roberts, Flow of Magnesium Oxide Single Crystals, J. Appl. Phys. 31(2), 433-434, (1960).
[297] B.-K. Lee, S.-Y. Chung, S.-J.L. Kang, Grain Boundary Faceting and Abnormal Grain Growth in $BaTiO_3$, Acta Mater 48(7), 1575–1580, (2000).
[298] H. Schmelz, H. Thomann, Grain-Growth in $BaTiO_3$ Ceramics .1. Evidence of Twinning and Exaggerated Grain-Growth Below the Eutectic Temperature, Am. Ceram. Soc. Bull. 61(8), 813-813, (1982).
[299] A. Reichmann, S. Mitsche, A. Zankel, P. Poelt, K. Reichmann, In Situ Mechanical Compression of Polycrystalline $BaTiO_3$ in the ESEM, J. Eur. Ceram. Soc. 34(10), 2211-2215, (2014).
[300] P. Van Houtte, F. Wagner, 11 - Development of Textures by Slip and Twinning, in: H.-R. Wenk (Ed.), Preferred Orientation in Deformed Metal and Rocks, Academic Press, 1985, pp. 233-258.
[301] R.Z. Zuo, E. Aulbach, R.K. Bordia, J. Rödel, Critical Evaluation of Hot Forging Experiments: Case Study in Alumina, J. Am. Ceram. Soc. 86(7), 1099-1105, (2003).
[302] S.G. Yousef, J. Rödel, E.R. Fuller Jr., A. Zimmermann, B.S. El-Dasher, Microcrack Evolution in Alumina Ceramics: Experiment and Simulation, J. Am. Ceram. Soc. 88(10), 2809-2816, (2005).
[303] T. Watanabe, Grain Boundary Sliding and Stress Concentration During Creep, Metall. Trans. A 14(3), 531-545, (1983).
[304] A.J. Perry, Cavitation in Creep, J. Mater. Sci. 9(6), 1016-1039, (1974).
[305] R. Raj, M.F. Ashby, On Grain Boundary Sliding and Diffusional Creep, Metall. Mater. Trans. B 2(4), 1113-1127, (1971).
[306] J.-F. Chou, M.-H. Lin, H.-Y. Lu, Ferroelectric Domains in Pressureless-Sintered Barium Titanate, Acta Mater. 48(13), 3569-3579, (2000).
[307] T. Hoshina, Size Effect of Barium Titanate: Fine Particles and Ceramics, J. Ceram. Soc. Jpn. 121(1410), 156-161, (2013).
[308] W. Cao, C.A. Randall, Grain Size and Domain Size Relations in Bulk Ceramic Ferroelectric Materials, J. Phys. Chem. Solids 57(10), 1499-1505, (1996).
[309] M. Demartin, D. Damjanovic, Dependence of the Direct Piezoelectric Effect in Coarse and Fine Grain Barium Titanate Ceramics on Dynamic and Static Pressure, Appl. Phys. Lett. 68(21), 3046-3048, (1996).
[310] J. Muñoz-Saldaña, G.A. Schneider, L.M. Eng, Stress Induced Movement of Ferroelastic Domain Walls in $BaTiO_3$ Single Crystals Evaluated by Scanning Force Microscopy, Surf. Sci. 480(1-2), L402-L410, (2001).
[311] W.R. Buessem, L.E. Cross, A.K. Goswami, Effect of Two-Dimensional Pressure on the Permittivity of Fine- and Coarse-Grained Barium Titanate, J. Am. Ceram. Soc. 49(1), 36-39, (1966).
[312] T. Ungár, Microstructural Parameters from X-Ray Diffraction Peak Broadening, Scri. Mater. 51(8), 777-781, (2004).
[313] J.T.S. Irvine, D.C. Sinclair, A.R. West, Electroceramics: Characterization by Impedance Spectroscopy, Adv. Mater. 2(3), 132–138, (1990).
[314] R.H. Wang, Y.M. Zhu, S.M. Shapiro, Structural Defects and the Origin of the Second Length Scale in $SrTiO_3$, Phys. Rev. Lett. 80(11), 2370-2373, (1998).
[315] H. Du, C.-L. Jia, L. Houben, V. Metlenko, R.A. De Souza, R. Waser, J. Mayer, Atomic Structure and Chemistry of Dislocation Cores at Low-Angle Tilt Grain Boundary in $SrTiO_3$ Bicrystals, Acta Mater. 89, 344-351, (2015).
[316] H. Schraknepper, T.E. Weirich, R.A. De Souza, The Blocking Effect of Surface Dislocations on Oxygen Tracer Diffusion in $SrTiO_3$, Phys. Chem. Chem. Phys. 20(22), 15455-15463, (2018).
[317] R. Khachaturyan, S. Zhukov, J. Schultheiß, C. Galassi, C. Reimuth, J. Koruza, H. von Seggern, Y.A. Genenko, Polarization-Switching Dynamics in Bulk Ferroelectrics with Isometric and Oriented Anisometric Pores, J. Phys. D: Appl. Phys. 50(4), 045303, (2016).

[318] R. Freer, Self-Diffusion and Impurity Diffusion in Oxides, J. Mater. Sci. 15(4), 803-824, (1980).
[319] S. Shirasaki, H. Yamamura, H. Haneda, K. Kakegawa, J. Moori, Defect Structure and Oxygen Diffusioon in Undoped and La-Doped Polycrystalline Barium-Titanate, J. Chem. Phys. 73(9), 4640-4645, (1980).
[320] J.-K. Liou, M.-H. Lin, H.-Y. Lu, Crystallographic Facetting in Sintered Barium Titanate, J. Am. Ceram. Soc. 85(12), 2931-2937, (2002).
[321] F.H. Schader, E. Aulbach, K.G. Webber, G.A. Rossetti, Influence of Uniaxial Stress on the Ferroelectric-to-Paraelectric Phase Change in Barium Titanate, J. Appl. Phys. 113(17), (2013).
[322] J. Cho, J. Li, H. Wang, Q. Li, Z. Fan, A.K. Mukherjee, W. Rheinheimer, H. Wang, X. Zhang, Study of Deformation Mechanisms in Flash-Sintered Yttria-Stabilized Zirconia by In-Situ Micromechanical Testing at Elevated Temperatures, Mater. Res. Lett. 7(5), 194-202, (2019).
[323] J. Li, J. Cho, J. Ding, H. Charalambous, S.C. Xue, H. Wang, X.L. Phuah, J. Jian, X.J. Wang, C. Ophus, T. Tsakalakos, R.E. Garcia, A.K. Mukherjee, N. Bernstein, C.S. Hellberg, H.Y. Wang, X.H. Zhang, Nanoscale Stacking Fault-Assisted Room Temperature Plasticity in Flash-Sintered TiO_2, Sci. Adv. 5(9), 1-9, (2019).
[324] R.W. Rice, Deformation, Recrystallization, Strength, and Fracture of Press-Forged Ceramic Crystals, J. Am. Ceram. Soc. 55(2), 90-97, (1972).
[325] E.T. Park, Grain Growth of $BaTiO_3$, J. Mater. Sci. Lett. 18(2), 163-165, (1999).
[326] A. Garcia Verduch, R. Lindner, *Selbstdiffusion in Bariummetatitanat, Arkiv for Kemi 5(4), 313-316, (1953).

Acknowledgements

On this occasion I would like to thank all people, who have supported me during my PhD in manifold ways.

First and foremost, I would like to thank my supervisor Prof. Dr. Jürgen Rödel, not only for the great opportunity to write my PhD-thesis in his group but also for his scientific guidance and his extraordinary leadership style, resulting in a well-structured and organized working group and providing a pleasant working environment. Besides, I would like to thank him for the great opportunities he offered to me in my PhD and beyond, to develop own ideas, participate in conferences, get to know other scientific environments and to engage in the materials science community.

I want to thank the Deutsche Forschungsgemeinschaft for the financial support under project grant number 414179371.

Moreover, I want to address my gratitude to Prof. Dr. Hans-Joachim Kleebe for being the second reviewer of this work. Furthermore, I would like to thank Prof. Dr. Karsten Durst and Prof. Dr. Ralf Müller for contributing as examiners.

I especially would like to thank Jurij Koruza, for the thoughtful scientific input and his patient and constructive guidance style. I really appreciate his open mind for scientific and group related discussions, his flexibility, his perfectionistic working style and that I can always count on his scientific feedback.

Furthermore, I would like to thank Daniel Isaia and Patrick Breckner for their technical support and their open ears for technical questions and discussions. A special thanks also to Gila Völzke, her open-door philosophy is one of the most important pillars for the group dynamic in NAW and a place to go for organization and group related questions. Thank you all, for keeping the group running in such a pleasant and smooth way.

I also want to thank Till Frömling, my former master thesis supervisor, for valuable discussions and insights into the scientific work during my master thesis and his support during my PhD.

Apart from scientific discussion with the other group leaders, post-docs, PhD students, students, AvHs and guests, which I really appreciate, I would never like to miss the social and community perspective in NAW. Starting with my office colleagues Sebastian, Michael, Satyanarayan and Maximilian, who always provided a comfortable and supporting atmosphere in our office and continuing with the variety of NAW get-togethers.

A special thanks for Jan, Peter, Sebastian and Lukas as more experienced PhDs for their advice and exchange of experience; but also to the scientifically younger PhDs An-Phuc, Michael and Maximilian and the others for an amazing and productive office and next-door communication culture.

With Michael Scherer and Sophie Bauer, I had the chance to supervise two great students. It was a pleasure to work with you on fascinating tasks. I also would like to thank Nils Winkelmann for his support as Hiwi in the laboratory. He did a great job and I really appreciate his help.
Further, I want to address my gratitude to Pengrong Ren and Fangping Zhuo with whom I had the pleasure to work together on side projects related to my thesis.

Furthermore, I would like to thank all my collaborators for their experimental support and scientific discussion. I especially would like to thank Enrico Bruder, Karsten Durst, Sebastian Bruns and Claudia Wasmund from PhM for carrying out ECCI and EBSD measurements, nanoindentation and the access to the LEXT microscope. I further want to thank Maximilian Trapp, Stefan Lauterbach and Hans-Joachim Kleebe for the TEM investigations on $KNbO_3$ and polycrystalline $BaTiO_3$. Besides, I would like to thank Xiaoli Tan and his group from Iowa State University for the TEM investigations on $BaTiO_3$ single crystals.
A special thanks also to Hana Uršič for her supervision of the PFM investigations, hospitality in Ljubljana and her students Matija Buljan and Mateo Miličevič for the acquisition of PFM images. I want to say thank you to Pedro Groszewicz, Jonas Linz and Felix Dietrich for performing and analyzing NMR. Last but not least, I would like to thank Dragan Damjanovic and Lukas Riemer for their great support and the opportunity to stay at the EPFL in Lausanne for several weeks, doing my research exchange. I learned a lot and I really appreciate the great experimental support and valuable discussions. It was a pleasure to work with all of you.

Besides I would like to thank all my friends for their support and acting as counterpart to the scientific work.

Finally, I would like to thank my parents, my sister and my family for their love and unlimited support.

Publications

- **M. Höfling**, X. Zhou, L.M. Riemer, E. Bruder, B. Liu, L. Zhou, P.B. Groszewicz, F. Zhuo, B.-X. Xu, K. Durst, X. Tan, D. Damjanovic, J. Koruza, J. Rödel, Control of Polarization in Bulk Ferroelectrics by Mechanical Dislocation Imprint. Science 372(6545) 961, (2021).
- X. Fang, H. Bishara, K. Ding, H. Tsybenko, L. Porz, **M. Höfling**, E. Bruder, Y. Li, G. Dehm, K. Durst, Nanoindentation Pop-in in Oxides at Room Temperature: Dislocation Activation or Crack Formation?, J. Am. Ceram. Soc. (2021).
- J. Schultheiß, L. Porz, L. Kodumudi Venkataraman, **M. Höfling**, C. Yildirim, P. Cook, C. Detlefs, S. Gorfman, J. Rödel, H. Simons, Quantitative Mapping of Nanotwin Variants in the Bulk, Scr. Mater. 199, 113878, (2021).
- **M. Höfling**, M. Trapp, L. Porz, H. Uršič , E. Bruder, H.-J. Kleebe, J. Rödel, J. Koruza, Large Plastic Deformability of Bulk Ferroelectric $KNbO_3$ Single Crystals, J. Eur. Ceram. Soc. 41(7), 4098-4107, (2021).
- L. Porz, A.J. Klomp, X. Fang, N. Li, C. Yildirim, C. Detlefs, E. Bruder, **M. Höfling**, W. Rheinheimer, E.A. Patterson, P. Gao, K. Durst, A. Nakamura, K. Albe, H. Simons, J. Rödel, Dislocation-Toughened Ceramics, Materials Horizons 8(5), 1528-1537, (2021).
- J. Koruza, H.R. Liu, **M. Höfling**, M.H. Zhang, P. Veber, (K,Na)NbO_3-Based Piezoelectric Single Crystals: Growth Methods, Properties, and Applications, J. Mater. Res. 35(8), 990-1016, (2020).
- P.R. Ren*, **M. Hoefling***, J. Koruza, S. Lauterbach, X.J. Jiang, T. Frömling, D.K. Khatua, C. Dietz, L. Porz, R. Ranjan, H.J. Kleebe, J. Rödel, High Temperature Creep-Mediated Functionality in Polycrystalline Barium Titanate, J. Am. Ceram. Soc. 103(3), 1891-1902, (2020). * contributed equally
- **M. Höfling**, S. Steiner, A.-P. Hoang, I.-T. Seo, T. Frömling, Optimizing the Defect Chemistry of $Na_{1/2}Bi_{1/2}TiO_3$-Based Materials: Paving the Way for Excellent High Temperature Capacitors, J. Mater. Chem. C 6(17), 4769-4776, (2018).
- S. Flege, R. Hatada, **M. Hoefling**, A. Hanauer, A. Abel, K. Baba, W. Ensinger, Modification of Diamond-Like Carbon Films by Nitrogen Incorporation via Plasma Immersion Ion Implantation, Nucl. Instrum. Meth. B 365, 357-361, (2015).